Chemical Engineering Science 63 (2008) 3120 – 3140

Contents lists available at ScienceDirect

Chemical Engineering Science

journal homepage: www.elsevier.com/locate/ces

Onsager coefficients for binary mixture diffusion in nanopores

R. Krishna*, J.M. van Baten

Van't Hoff Institute for Molecular Sciences, University of Amsterdam, Nieuwe Achtergracht 166, 1018 WV Amsterdam, The Netherlands

ARTICLE INFO

Article history:
Received 24 January 2008
Received in revised form 7 March 2008
Accepted 11 March 2008
Available online 16 March 2008

Keywords:
Zeolites
Nanomaterials
Carbon nanotubes
Titanosilicates
Metal–organic frameworks
Molecular dynamics
Onsager coefficients
Coupling
Loading dependence
Correlation effects
Diffusion
Binary mixture

ABSTRACT

This paper presents a critical appraisal of current estimation methods for the Onsager coefficients L_{11}, L_{22}, and L_{12} for binary mixture diffusion inside nanopores using pure component diffusivity data inputs. The appraisal is based on extensive sets of molecular dynamics (MD) simulation data on L_{ij} for a variety of mixtures in zeolites (MFI, AFI, TON, FAU, CHA, DDR, MOR, and LTA), carbon nanotubes (CNTs: armchair and zig-zag configurations), titanosilicates (ETS-4), and metal–organic frameworks (IRMOF-1, CuBTC). The success of the L_{ij} predictions is crucially dependent on the estimates of the degree of correlations in molecular jumps for different guest–host combinations; these correlations are captured in Maxwell–Stefan approach by the exchange coefficients $Đ_{ij}$. Three limiting scenarios for correlation effects have been distinguished; for each of these scenarios appropriate expressions for the L_{ij} are presented. For CNTs, correlation effects are dominant and the interaction factor, defined by $\alpha_{12} = L_{12}/\sqrt{L_{11}L_{22}}$, is close to unity. For cage-type zeolites such as LTA, CHA, and DDR with narrow windows separating cages, correlation effects are often, but not always, negligibly small and the assumption of uncoupled diffusion, i.e., $\alpha_{12} = 0$, is a reasonable approximation provided the occupancies are not too high. In other cases such as zeolites with one-dimensional channel structures (AFI, TON), intersecting channels (MFI), cage-type zeolite with large windows (FAU), ETS-4, CuBTC, and in IRMOF-1, it is essential to have a reliable estimation of the $Đ_{ij}$; MD simulations underline the wide variety of factors that influence the $Đ_{ij}$.
We also highlight two situations where estimations of the L_{ij} fail completely; in both cases the failure is caused due to *segregated* adsorption. In adsorption of CO_2–bearing mixtures in LTA and DDR zeolites, CO_2 is preferentially lodged at the narrow window regions and this hinders the diffusion of partner molecules between cages. The second situation arises in MOR zeolite that has one-dimensional channels connected to side pockets. Some molecules such as methane, get preferentially lodged in the side pockets and do not freely participate in the molecular thoroughfare. Current phenomenological models do not cater for segregation effects on mixture diffusion.

1. Introduction

Nanoporous materials such as zeolites (crystalline aluminosilicates), carbon nanotubes (CNTs), carbon molecular sieves (CMS), metal–organic frameworks (MOFs), and titanosilicates (such as ETS-4, and ETS-10) offer considerable potential for use in separation of a variety of gaseous mixtures (Arora and Sandler, 2005; Chen and Sholl, 2004; Chen et al., 1994; Düren and Snurr, 2004; Himeno et al., 2007; Keskin and Sholl, 2007; Krishna and Paschek, 2000; Krishna and van Baten, 2006, 2007a; Kuznicki et al., 2001; Li et al., 2007b; Marathe et al., 2004; Ohta et al., 2007; Snurr et al., 2004; van den Bergh et al., 2007). For the development and design of such processes a proper description of mixture diffusion within the nanopores is required. The pore dimensions in nanomaterials usually vary in the range 0.5–1.5 nm and there is no "bulk" fluid phase to speak of. The molecules inside nanopores are always within the influence of the force field exerted with the wall and we have to reckon with the motion of *adsorbed* molecules; in this respect nanopore diffusion is distinct from Knudsen diffusion and has similarities with surface diffusion (Krishna, 1990). The pore size, pore topology, and connectivity are important in determining the nanopore diffusivity. Fig. 1 illustrates the pore (energy) landscapes, along with snapshots of molecules within eight different zeolites. AFI and TON have one-dimensional (1D) 12-ring and 10-ring channel structures, respectively. In MOR the 12-ring 1D channels are connected with 8-ring side pockets. In MFI the 10-ring straight channels and zig-zag channels intersect at junctions. FAU has a cage structure, with large 12-ring windows separating two cages. LTA, CHA, and DDR also have cage structures, with narrow 8-ring windows separating the cages. The walls of CNTs are considerably smoother than for zeolites; witness the snapshot shown in Fig. 2; this leads to diffusivity values in CNTs

* Corresponding author. Tel.: +31 20 5257007; fax: +31 20 5255604.
E-mail address: r.krishna@uva.nl (R. Krishna).

0009-2509/$ - see front matter © 2008 Elsevier Ltd. All rights reserved.
doi:10.1016/j.ces.2008.03.017

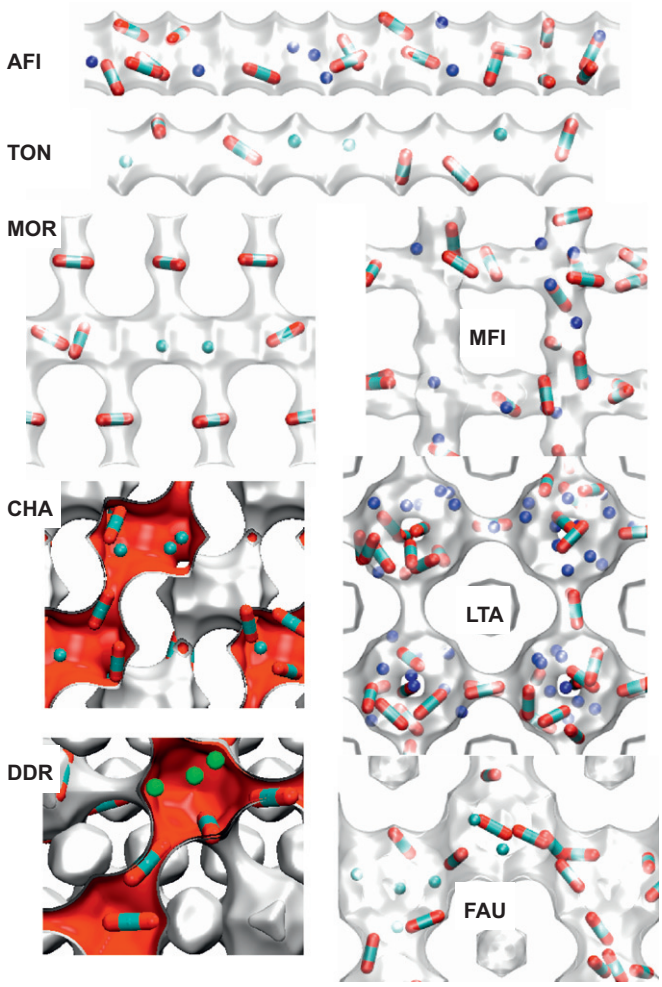

Fig. 1. Snapshots of molecules within the *one-dimensional* channel structure of AFI, TON, and MOR, *intersecting channels* of MFI, *cages separated by large windows* of FAU, and *cages separated by narrow windows* of LTA, CHA, and DDR. Note that the zeolites are not all drawn to the same scale.

about two orders of magnitude higher than for zeolites, and in line with fluid phase diffusion (Chen and Sholl, 2004; Krishna and van Baten, 2006). There are several MOF structures currently being investigated (Snurr et al., 2004); Fig. 2 shows the pore landscapes of IRMOF-1 and CuBTC. ETS-4 has 12-ring main channels that are interconnected with small cages through narrower 8-ring openings (Kuznicki et al., 2001); see Fig. 2. Diffusion in the 12-ring main channels has the characteristics of diffusion in the 1D channels of AFI, whereas the transport of molecules across the 8-ring openings has features similar to intercage hopping of molecules in DDR, LTA and ERI; this can be evidenced from the animations created from molecular dynamics (MD) simulations of molecular motions in various structures (van Baten and Krishna, 2008).

A phenomenological description of diffusion based on the Onsager theory of irreversible thermodynamics is commonly employed in practice (Benes and Verweij, 1999; Chempath et al., 2004; Habgood, 1958; Kärger and Ruthven, 1992; Skoulidas et al., 2003a; Sundaram and Yang, 2000; Yang et al., 1991). For binary mixtures the flux of any component is related to the chemical potential gradients by the 2×2 dimensional matrix equation:

$$(N) = -\rho \frac{1}{RT}[L]\frac{\mathrm{d}(\mu)}{\mathrm{d}x} \tag{1}$$

where L_{ij} are the Onsager coefficients. The Onsager reciprocal relations are

$$L_{12} = L_{21} \tag{2}$$

In contrast to the treatment of diffusion in bulk fluid mixtures where the reference frame is often chosen as the molar average velocity of the mixture (Taylor and Krishna, 1993), for diffusion inside nanopores the reference velocity frame chosen in Eq. (1) is with respect to the framework of the nanoporous material (Krishna and Baur, 2003). The Fick diffusivity matrix $[D]$, required in process design, is related to $[L]$ by introduction of thermodynamic correction factors (Krishna and Baur, 2003; Sanborn and Snurr, 2001). The Onsager coefficients are determined either from experiment, or from molecular simulations (Bell et al., 1997; Chen and Sholl, 2006; Dubbeldam and Snurr, 2007; Jobic and Theodorou, 2006; Kärger and Ruthven, 1992; Kärger et al., 2003; Keil et al., 2000; Sanborn and Snurr, 2000; Sholl, 2006; Theodorou et al., 1996). From a practical engineering point of view it is desirable to have a reliable procedure for estimation of L_{11}, L_{22}, and L_{12} using pure component diffusivities as data inputs. In the related area of adsorption, the ideal adsorbed solution theory (IAST) (Myers and Prausnitz, 1965) allows estimation of multicomponent adsorption using pure component isotherm data inputs. Essentially, we seek an analog of the IAST for mixture diffusion inside nanopores.

In the published literature there are two distinct approaches to estimating the L_{ij}. In the first approach, Sundaram and Yang (2000) have suggested that the diagonal elements L_{ii} can be identified with the pure component L_i; the latter is related to the "corrected" or Maxwell–Stefan (M–S) diffusivity $Đ_i$

$$L_i = q_i Đ_i \tag{3}$$

Furthermore, they quantify the extent of coupling for binary mixtures by defining an interaction factor α_{12}

$$\alpha_{12} = \frac{L_{12}}{\sqrt{L_{11}L_{22}}} \tag{4}$$

For a given guest–host combination, they assume a *constant* value of α_{12} to characterize mixture diffusion, but offer no *a priori* estimation procedures. Wang and LeVan (2007) follow the Sundaram–Yang procedure and interpret their experimental data for diffusion CO_2–CH_4 mixtures in CMS by taking $\alpha_{12} = 0.74$. MD simulations of diffusion of equimolar CH_4/H_2 and N_2/O_2 mixtures in CNTs yield a unity value for α_{12} (Arora and Sandler, 2006; Chen and Sholl, 2004).

The second approach is based on the M–S formulation for mixture diffusion that yields the following expression for the fluxes (Krishna et al., 2008; Krishna and van Baten, 2008b)

$$(N) = -\rho \frac{1}{RT}[\Delta]\begin{bmatrix} q_1 & 0 \\ 0 & q_2 \end{bmatrix}\frac{\mathrm{d}(\mu)}{\mathrm{d}x} \tag{5}$$

The Onsager matrix $[L]$ is related to the M–S matrix $[\Delta]$, which in turn is expressed explicitly in terms of the M–S diffusivities $Đ_i$ and the binary exchange coefficients $Đ_{ij}$, as derived in our earlier publications (Krishna et al., 2008; Krishna and van Baten, 2008b):

$$L_{11} = q_1\Delta_{11} = q_1\frac{Đ_1(1+\theta_1 Đ_2/Đ_{21})}{1+\frac{\theta_1 Đ_2}{Đ_{21}}+\frac{\theta_2 Đ_1}{Đ_{12}}} \tag{6}$$

$$L_{22} = q_2\Delta_{22} = q_2\frac{Đ_2\left(1+\frac{\theta_2 Đ_1}{Đ_{12}}\right)}{1+\frac{\theta_2 Đ_1}{Đ_{12}}+\frac{\theta_1 Đ_2}{Đ_{21}}} \tag{7}$$

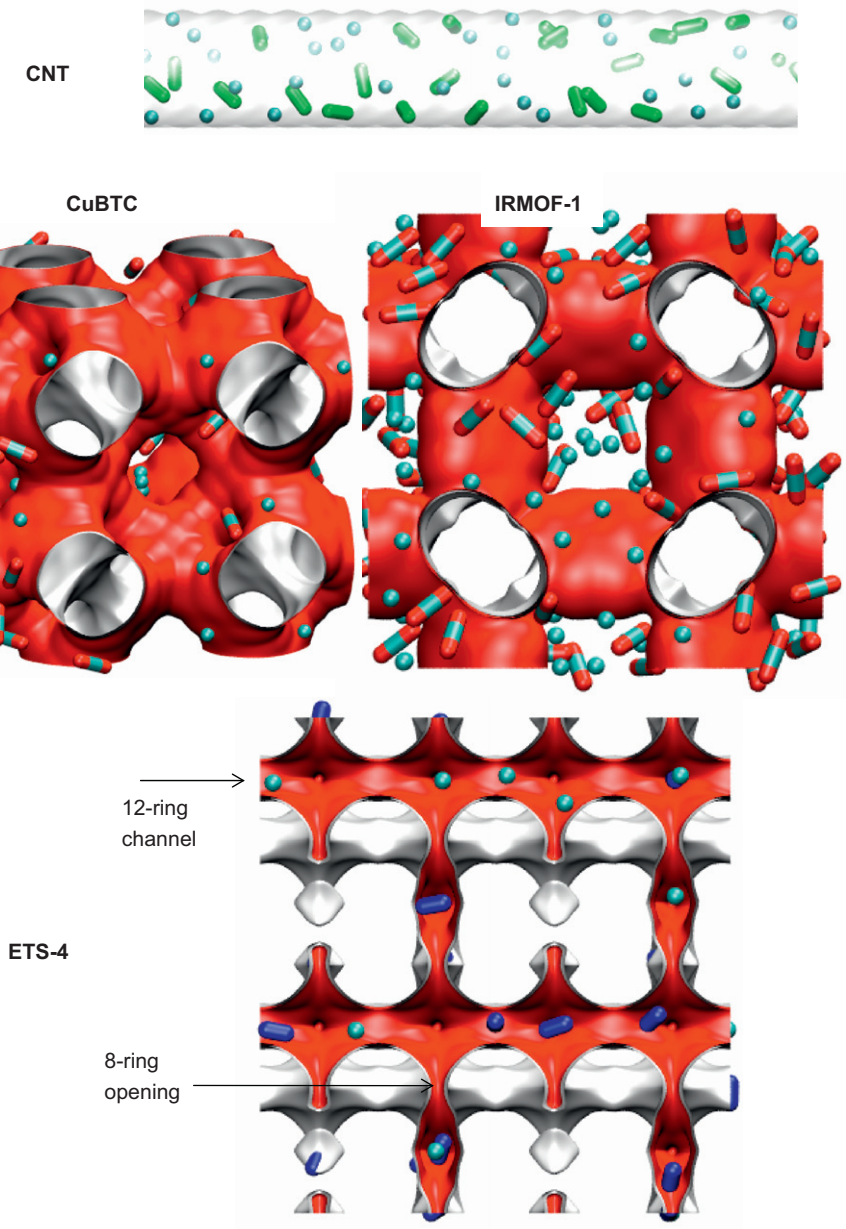

Fig. 2. Snapshots of molecules within CNT (10,10), CuBTC, IRMOF-1, and ETS-4.

$$L_{12} = q_2 \Delta_{12} = q_2 \frac{Đ_1 \frac{\theta_1 Đ_2}{Đ_{21}}}{1 + \frac{\theta_1 Đ_2}{Đ_{21}} + \frac{\theta_2 Đ_1}{Đ_{12}}} \tag{8}$$

$$L_{21} = q_1 \Delta_{21} = q_2 \Delta_{12} = q_1 \frac{Đ_2 \frac{\theta_2 Đ_1}{Đ_{12}}}{1 + \frac{\theta_1 Đ_2}{Đ_{21}} + \frac{\theta_2 Đ_1}{Đ_{12}}} \tag{9}$$

where θ_i are the fractional occupancies

$$\theta_i \equiv q_i / q_{i,\text{sat}}, \quad i = 1, 2, \ldots, n \tag{10}$$

and $q_{i,\text{sat}}$ represents the saturation capacity of species i. Conformity with the Onsager reciprocal relations (2) demands that

$$q_{2,\text{sat}} Đ_{12} = q_{1,\text{sat}} Đ_{21} \tag{11}$$

and so there are three independent diffusivities $Đ_1$, $Đ_2$, and $Đ_{12}$ that need to be estimated. The success of the M–S approach hinges on a good estimation of the degree of correlations between molecular jumps (Kärger et al., 2003); this is embodied in the exchange coefficients $Đ_{ij}$. The $Đ_{ij}$ can be determined from the self-exchange coefficients $Đ_{ii}$ for constituent pure components using an interpolation formula (Chempath et al., 2004; Krishna and van Baten, 2008b; Skoulidas et al., 2003b)

$$\begin{aligned} q_{2,\text{sat}} Đ_{12} &= [q_{2,\text{sat}} Đ_{11}]^{q_1/(q_1+q_2)} [q_{1,\text{sat}} Đ_{22}]^{q_2/(q_1+q_2)} \\ &= q_{1,\text{sat}} Đ_{21} \end{aligned} \tag{12}$$

Eq. (12) has been validated for CH_4–CF_4 and for alkane mixtures in MFI and FAU (Chempath et al., 2004; Krishna and van Baten, 2005; Skoulidas et al., 2003b) but its applicability to other guest–host combinations needs to be established.

The objectives of the present communication are to provide insights into the structure of the Onsager matrix $[L]$ and to examine the accuracy of the two alternative estimation procedures for a variety

of guest molecules in zeolites, CNTs, ETS-4, CuBTC, and in IRMOF-1. Specifically, we aim to provide answers to the following questions:

(1) What does α_{12} reflect? What are the factors that determine α_{12}? Is it justified to take a constant value of α_{12} to describe nanopore diffusion for a particular guest mixture–host combination? Does α_{12} depend on the loading within the nanopores? How do the α_{12} relate with the $Đ_{ij}$? Can we estimate of α_{12} from pure component diffusion data?
(2) Is the result $\alpha_{12}=1$, found in MD simulations for CNTs (Arora and Sandler, 2006; Chen and Sholl, 2004), of generic significance? If so, under what conditions?
(3) Under what conditions can the diagonal elements L_{ii} be identified with the pure component L_i?
(4) Is the basic premise made in the literature (Chempath et al., 2004; Krishna and van Baten, 2008b; Skoulidas et al., 2003b) that the $Đ_i$ in the mixture is the same as that for pure components *always* valid?
(5) Is the interpolation formula (12) valid for nanostructures other than zeolites for which it has been checked thus far?
(6) Which is the better route to follow for estimation of mixture diffusion from pure component diffusion data: Onsager or M–S?

To obtain answers to the above questions we used an extensive database of MD simulations of diffusion in a variety of mixtures in eight different all-silica zeolite structures (MFI, AFI, TON, FAU, CHA, DDR, MOR, and LTA), in CNTs of both zig-zag (20,0) and armchair (10,10) configurations, in ETS-4, IRMOF-1, and CuBTC. This database contains some published data for zeolites and CNTs (Krishna and van Baten, 2005, 2006, 2007b, 2008b, c) and substantially extended in the current study to include a wider variety of mixtures and nanostructures (ETS-4, IRMOF-1, CuBTC) for more critical testing of current estimation methods.

In every case the following simulations were conducted: (1) Monte Carlo simulations in the grand canonical ensemble were performed to determine the pure component adsorption isotherms; these simulations yield the saturation capacities, $q_{i,\text{sat}}$. (2) MD simulations of the pure self-diffusivities $D_{i,\text{self}}$ and M–S diffusivities $Đ_i$; combining these yields information on the self-exchange coefficients $Đ_{ii}$. (3) MD simulations for binary mixtures to determine the elements Δ_{ij}; this allowed calculation of the L_{ij} and α_{ij}. The entire database of simulation results is available in the Supplementary material accompanying this publication; this material includes details of the MD simulation methodology, description of the force fields used, simulation data (pure component isotherms; $D_{i,\text{self}}$; $Đ_i$; $q_{i,\text{sat}}$; $Đ_{ii}$; Δ_{ij}; L_{ij}; α_{ij}), snapshots showing the location of molecules in the structures, derivations of the inter-relationship between the Onsager and M–S formulations, derivations of all of the algebraic formula presented in this paper, along with explicit formulae for backing out the $Đ_1$, $Đ_2$, and $Đ_{12}$ from the MD simulated Δ_{ij}.

2. Onsager coefficients: loading dependencies and correlation effects

In both approaches for estimating L_{ij}, the first step involves characterization of the pure component $Đ_i$ and L_i. The $Đ_i$ exhibits a wide variety of dependencies on the occupancy (Krishna and van Baten, 2008b; Skoulidas and Sholl, 2003); Fig. 3 illustrates this for a variety of guest molecules in AFI, FAU, MFI, LTA, CHA, and DDR zeolites. The assumption of a constant, occupancy independent $Đ_i$ is valid only for Ne, and for low occupancies of other molecules. For a good estimation of mixture diffusion it is essential to have a proper description of the occupancy dependence of $Đ_i$; in earlier work (Krishna and van Baten, 2005, 2008b) we had suggested the Reed and Ehrlich model (Reed and Ehrlich, 1981) for this purpose and the model fits are shown by the continuous solid lines in Fig. 3. There is growing experimental evidence in the literature that verify the $Đ_i$-θ_i trends seen in Fig. 3, albeit qualitatively. Recent work has also demonstrated that a proper $Đ_i$-θ_i description is the key to successful modeling of permeation of gases across zeolite membranes (Krishna and van Baten, 2007b, 2008c; Krishna et al., 2007; Li et al., 2007a, b).

The $Đ_i$ of CH_4, Ar, and Ne in ETS-4, and MOFs are also loading dependent, and are amenable to "empirical" fitting using the Reed and Ehrlich model; for MOFs the loading dependence is complex and deserves further investigation. A further point to note is that the loading dependence of $Đ_i$ may also change with temperature. In the Supplementary material MD data are presented for CH_4 diffusion in LTA at various T in order to illustrate this point; this topic needs further investigation.

The corresponding $L_i - q_i$ dependences for Ne, Ar, and CO_2 in zeolites are shown in Fig. 4; the straight lines represent calculations following the suggestion of Sundaram and Yang (2000) that the values of $Đ_i$ in the limit of zero occupancies can be used in L_i estimations, i.e.,

$$L_i = q_i Đ_i(0) \tag{13}$$

Except for Ne, and for low occupancies of other species, we see that Eq. (13) is a poor approximation and is not recommended for description of diffusion in zeolites, titanosilicates and MOFs.

When the isotherm exhibits a strong inflection, the $Đ_i - q_i$ dependence also shows a corresponding inflection (Chmelik et al., 2008; Jobic et al., 2006) and this behavior is difficult to capture with the Reed and Ehrlich model.

It is convenient to define α_{ii} as the ratios of the diagonal elements L_{ii} to the corresponding pure component L_i values

$$\alpha_{11} = \frac{L_{11}}{L_1}, \quad \alpha_{22} = \frac{L_{22}}{L_2} \tag{14}$$

Explicit expressions for α_{11}, α_{22}, and α_{12} in terms of the $Đ_i$ and $Đ_{ij}$ can be derived:

$$\alpha_{11} = \frac{\left(1+\frac{\theta_1 Đ_2}{Đ_{21}}\right)}{1+\frac{\theta_1 Đ_2}{Đ_{21}}+\frac{\theta_2 Đ_1}{Đ_{12}}} \tag{15}$$

$$\alpha_{22} = \frac{\left(1+\frac{\theta_2 Đ_1}{Đ_{12}}\right)}{1+\frac{\theta_2 Đ_1}{Đ_{12}}+\frac{\theta_1 Đ_2}{Đ_{21}}} \tag{16}$$

and

$$\alpha_{12} = \sqrt{\frac{\left(\frac{\theta_1 Đ_2}{Đ_{21}}\right)\left(\frac{\theta_2 Đ_1}{Đ_{12}}\right)}{\left(1+\frac{\theta_1 Đ_2}{Đ_{21}}\right)\left(1+\frac{\theta_2 Đ_1}{Đ_{12}}\right)}} \tag{17}$$

Even though the $Đ_{12}$ and $Đ_{21}$ are inter-related (cf. Eq. (11)) we shall persist with writing equations including both these exchange coefficients in order to retain the elegant symmetry.

In the M–S approach (Krishna and van Baten, 2008b), the $Đ_i$ in Eqs. (6)–(9) are assumed to be equal to the corresponding *pure component* diffusivity, evaluated at the occupancy of the total mixture

$$\theta = \theta_1 + \theta_2 = \frac{q_1}{q_{1,\text{sat}}} + \frac{q_2}{q_{2,\text{sat}}} \tag{18}$$

This assumption has been verified in earlier work for CH_4–CF_4 and alkane mixtures in MFI and FAU (Chempath et al., 2004; Krishna and van Baten, 2005; Skoulidas et al., 2003b). We now demonstrate its validity for other mixtures. Fig. 5a compares the pure component $Đ_i$ with the values backed-out from MD simulations of [Δ] for methane

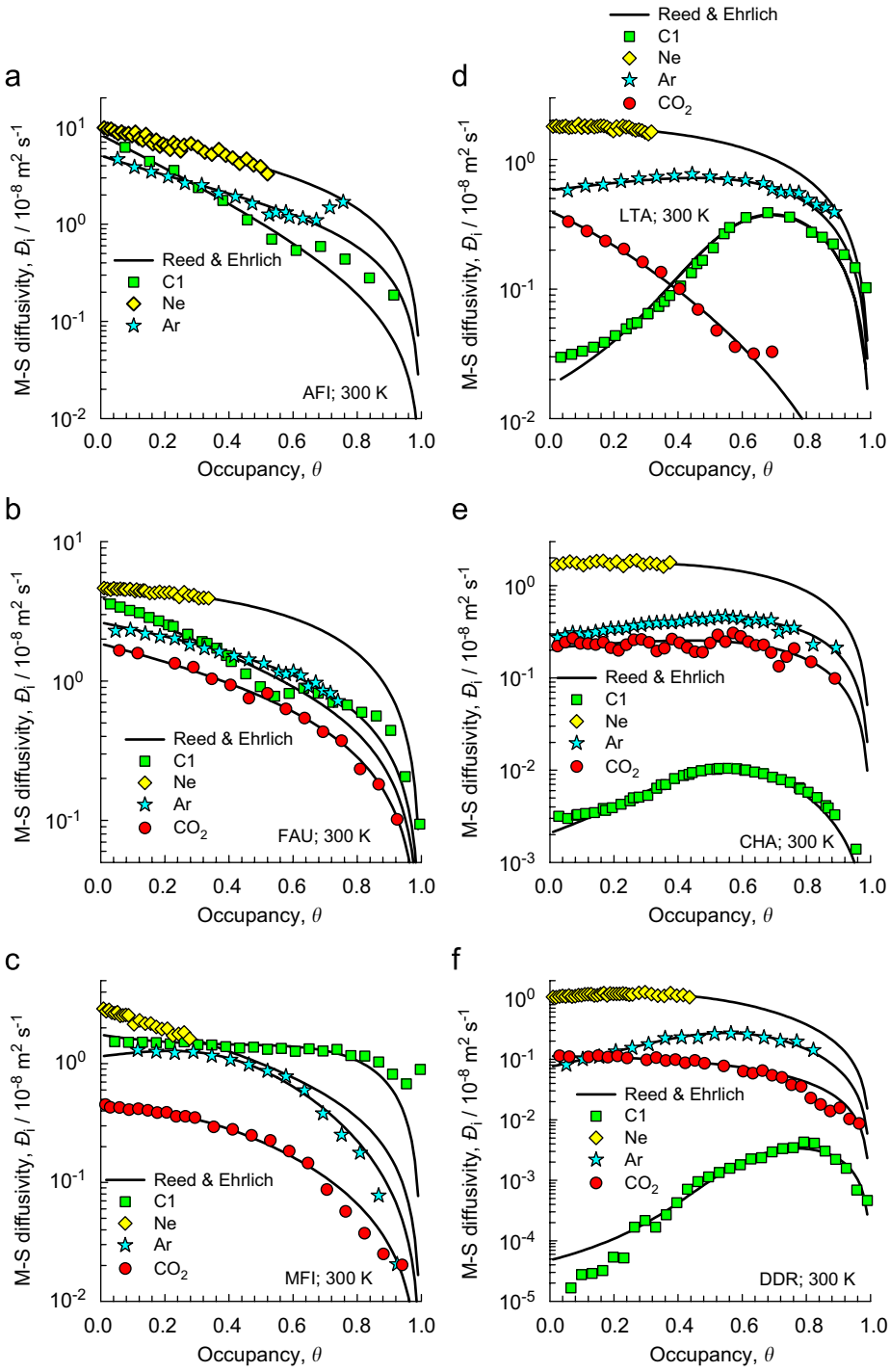

Fig. 3. Dependence of the pure component M–S diffusivity $Đ_i$ on occupancy for a variety of molecules in AFI, FAU, MFI, LTA, CHA, and DDR zeolites. Also shown by the continuous solid lines are the Reed and Ehrlich model fits of the data using the parameters given in the Supplementary material.

(C1)–Ar, C1–ethane (C2), and C1–CO_2 mixtures in FAU. The data sets agree very well with one another. Similar agreement is found for most guest–host combinations investigated in this work; however, some important exceptions in some special cases will be highlighted later in this paper.

Fig. 5b shows the variation of $Đ_{12}$ with occupancy θ for Ne–Ar, C1–Ar, and C1–C2 mixtures in FAU. The symbols represent the $Đ_{12}$ values backed-out from MD simulations of [Δ] for equimolar mixtures. Also shown by the continuous solid lines are the calculations using the interpolation formula (12) using the pure component fits for $Đ_i$ and $Đ_{ii}$; the agreement is very good. Similar good agreement holds for all the guest–host combinations considered in this study and, therefore, we shall consider Eq. (12) as a validated interpolation formula, albeit with an empirical character.

We now examine the significance of α_{12} and the factors that influence it. From Eq. (17) we note that α_{12} is a function of two dimensionless parameters $\theta_1 Đ_2/Đ_{21}$ and $\theta_2 Đ_1/Đ_{12}$, that can be interpreted to reflect the strength of correlations. Invoking Eq. (12) for

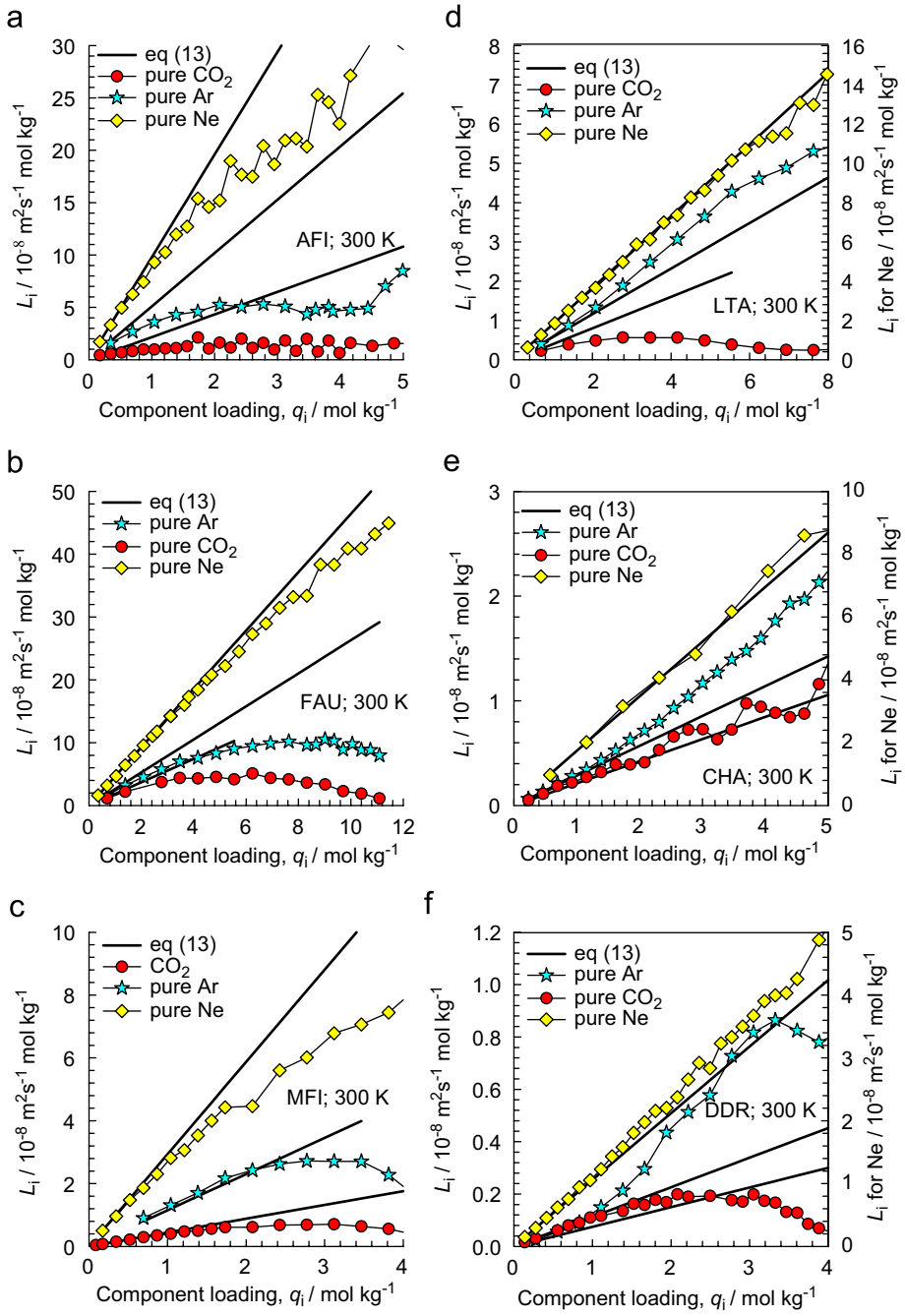

Fig. 4. Dependence of the pure component Onsager coefficient L_i with component loading q_i for Ne, Ar, and CO_2 in AFI, FAU, MFI, LTA, CHA, and DDR zeolites. The symbols represent calculations following Eq. (3), and the straight lines are drawn with Eq. (13) as basic assumption.

equimolar (i.e., $q_1 = q_2$) mixtures we can show

$$Đ_{12}Đ_{21} = Đ_{11}Đ_{22} \tag{19}$$

and a *qualitative* impression of the significance of correlation effects is gained by examining the magnitudes of the *pure component* parameter $\theta_i Đ_i/Đ_{ii}$; Fig. 6a and b present data for Ar in a variety of nanostructures as a function of θ. We note that $\theta_i Đ_i/Đ_{ii}$ varies by about three orders of magnitude in different structures. The mathematical bounds are $0 < \theta_i Đ_i/Đ_{ii} < \infty$ and in all cases the degree of correlation increases with increasing θ as is to be expected intuitively. The highest values of $\theta_i Đ_i/Đ_{ii}$ are for CNTs; correlation effects are *dominant* in this case. Correlation effects are the weakest for LTA, CHA and DDR that consist of cages separated by narrow windows. For AFI, MFI, FAU, ETS-4, CuBTC, and IRMOF-1, $\theta_i Đ_i/Đ_{ii} > 1$ for $\theta > 0.4$ and strong correlation effects are to be expected, especially at high occupancies. For ETS-4 we consider diffusion along the 12-ring channels; and here we note that the correlation effects are practically the same as for AFI. For CuBTC and IRMOF-1 the data show that correlations are comparable to that in FAU.

Fig. 7 shows values of α_{12} for: (a) a variety of mixtures in CNTs and (b) for Ne–Ar mixture in zeolites, CuBTC, IRMOF-1, and ETS-4. These α_{12} were determined from Eq. (4) using MD data on L_{ij}. The α_{12} hierarchy follows that dictated by the $\theta_i Đ_i/Đ_{ii}$ hierarchy, as was anticipated. For $\theta > 0.2$ in CNTs, the approximation $\alpha_{12} \approx 1$ is

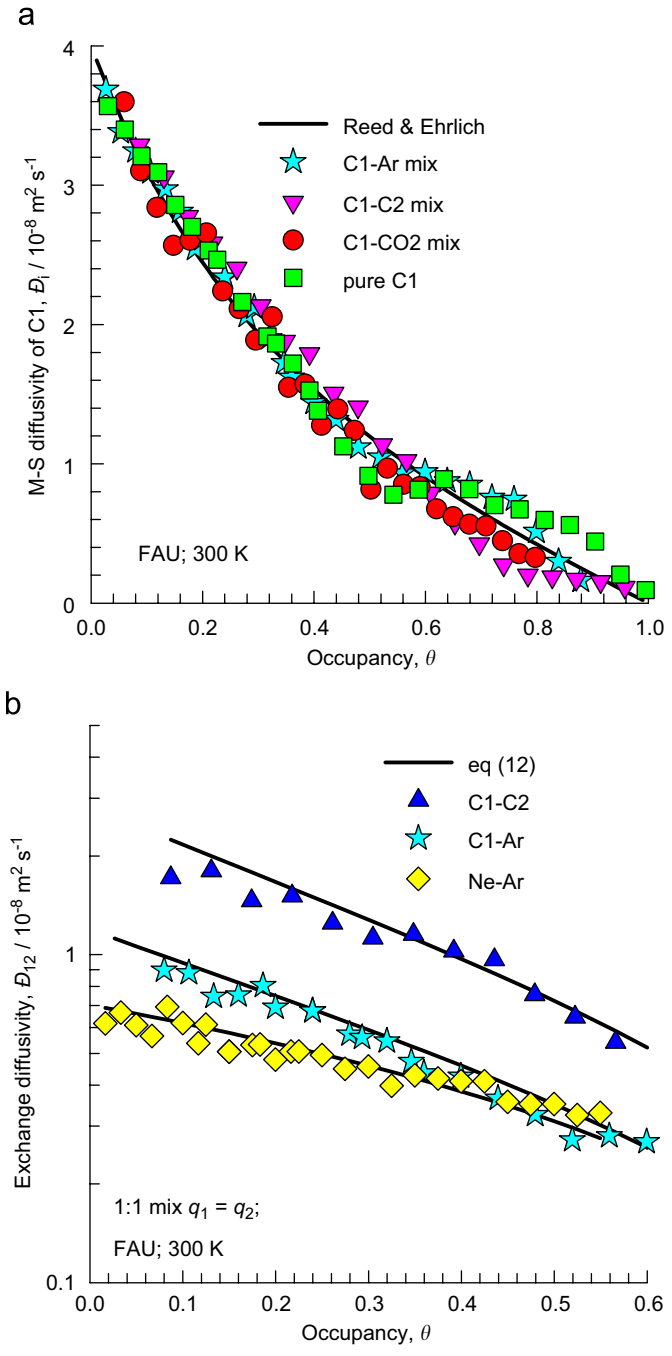

Fig. 5. Variation of (a) $Đ_i$ and (b) $Đ_{12}$ with occupancy θ for a variety of mixtures in FAU. The symbols represent the values backed-out from MD simulations of the M–S matrix [Δ]; the detailed procedure for backing-out is given in the Supplementary material. The continuous solid lines in (b) represent calculations using the interpolation formula (12) using the pure component data fits given in the Supplementary material.

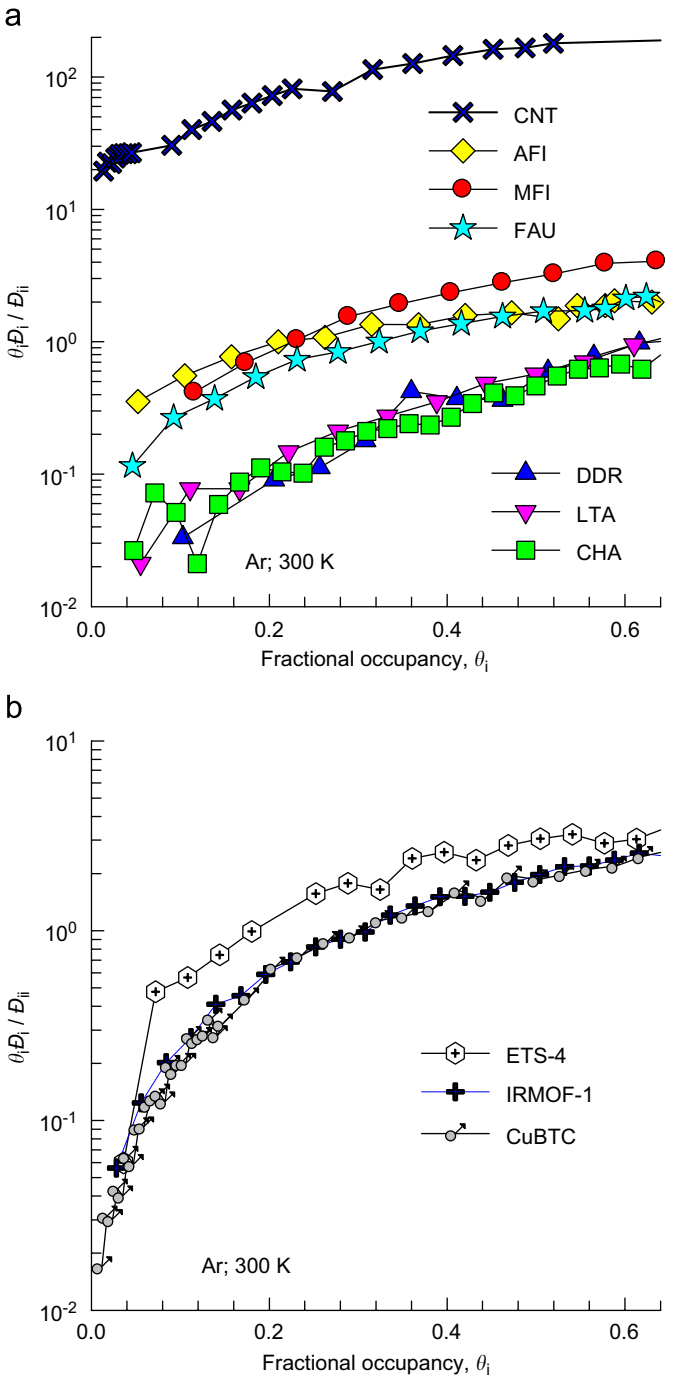

Fig. 6. Variation of $\theta_i Đ_i/Đ_{ii}$ with occupancy, θ for Ar in (a) CNT and zeolites; and (b) ETS-4, IRMOF-1, and CuBTC.

a good one. The α_{12} for ETS-4, CuBTC, IRMOF-1, AFI, MFI, and FAU are higher than in LTA, CHA and DDR, reflecting the higher degree of correlations in these structures.

Correlation effects are not exclusively dictated by the host structure, but are determined by the *combination* of guest molecules and host topology. Fig. 8a compares the $\theta_i Đ_i/Đ_{ii}$ data for Ne, Ar, C1 and Kr in LTA. Here C1 and Kr are the most tightly constrained at the window and these molecules can only hop one molecule at a time between the cages; consequently, correlation effects are negligibly small except at occupancies exceeding about 0.5. For high occupancies intracage motion starts to become rate determining and; consequently, correlation effects become non-negligible. Ne and Ar are smaller molecules and not so tightly constrained at the window, and correlations are much more significant than for C1 and Ar. Eq. (17) anticipates a direct dependence of α_{12} on $\theta_i Đ_j/Đ_{ji}$ and to test this we present MD results for α_{12} in equimolar Ne–Ar, C1–Ar, and Kr–Ar mixtures in LTA zeolite; see Fig. 8b. The α_{12} for C1–Ar and Kr–Ar mixtures are practically the identical, consistent with the $\theta_i Đ_i/Đ_{ii}$ data. The α_{12} for Ne–Ar is significantly higher, reflecting the significantly higher correlations for Ne, that is also reflected in the $\theta_i Đ_i/Đ_{ii}$ data.

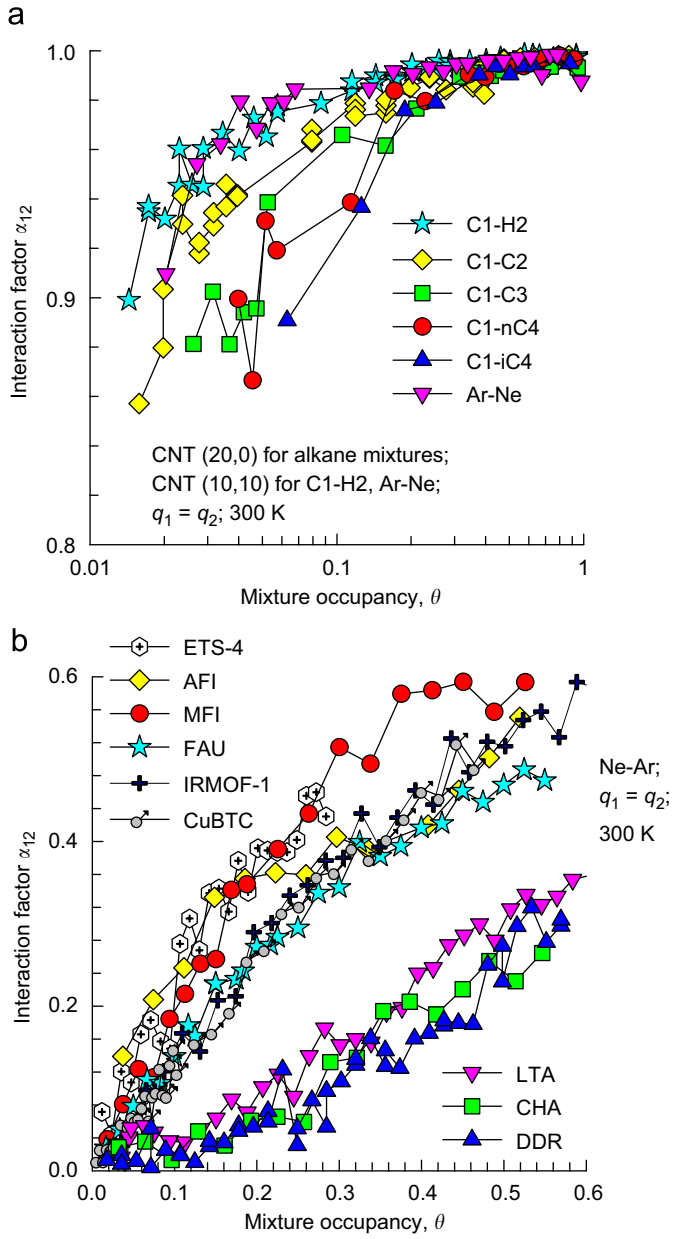

Fig. 7. Interaction factor α_{12} as a function of the mixture occupancy, θ, for (a) a variety of mixtures in CNTs; (b) for Ne–Ar mixture in zeolites, ETS-4, IRMOF-1, and CuBTC.

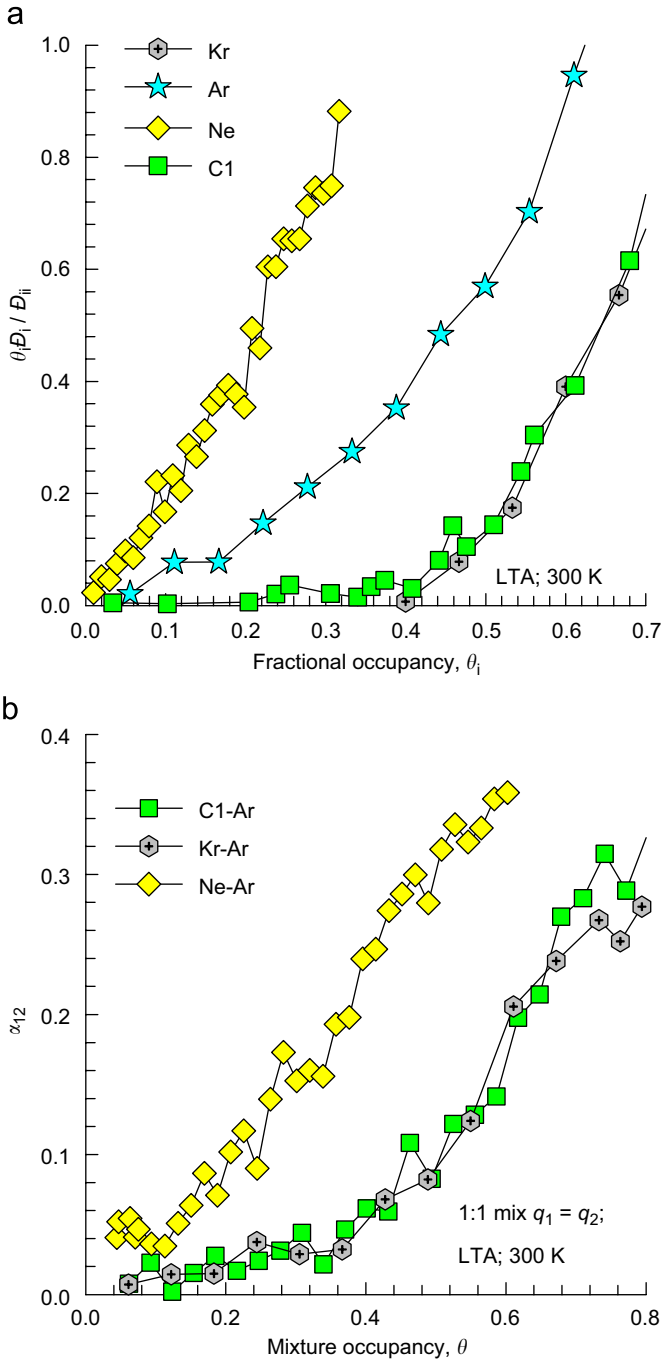

Fig. 8. (a) Variation of $\theta_i Đ_i/Đ_{ii}$ with occupancy, θ for Ne, Ar, C1, and Kr in LTA. (b) Interaction factor $\alpha_{12,}$ determined in equimolar Ne–Ar, C1–Ar, and Kr–Ar mixtures in LTA as a function of the mixture occupancy, θ.

It is also clear from Eq. (17) that $\alpha_{12} \to 0$ as $\theta \to 0$, and so a constant, occupancy independent, value for α_{12} is not a good assumption to make.

3. Negligible correlations scenario

In the limiting scenario in which correlation effects are of negligible importance, $\theta_i Đ_j/Đ_{ji} \to 0$ and we obtain

$$\alpha_{11} = 1, \quad \alpha_{22} = 1, \quad \alpha_{12} = 0 \tag{20}$$

In the early work of Habgood (1958), Eq. (20) was used to model transient uptake of N_2/CH_4 mixtures in LTA. The scenario (20) will be a reasonable one for diffusion of mixtures in which molecules are tightly constrained at the windows of cage-type zeolites; two examples of this have already been seen in Fig. 8b for C1–Ar and Kr–Ar mixtures provided $\theta < 0.4$. A further example is shown in Fig. 9a with data for C1–Ar mixture in CHA; these data show that $\alpha_{ii} \approx 1$, and that the interaction factor $\alpha_{12} < 0.05$, up to values $\theta < 0.5$. Indeed, Li et al. (2007b) and Krishna et al. (2008) were able to model permeation of CO_2/CH_4, CO_2/N_2, CH_4/N_2, Ar/CH_4, and $CO_2/CH_4/N_2$ mixtures across a SAPO-34 (an isotype of CHA zeolite) membrane with success using *uncoupled* Onsager equations, consistent with Eq. (20). Experiments for CO_2/H_2 permeation across the SAPO-34, have, however, shown that correlation effects could not be ignored for this mixture because of the presence of small H_2 molecules (Krishna et al., 2008). These findings can be rationalized by examination of the data in

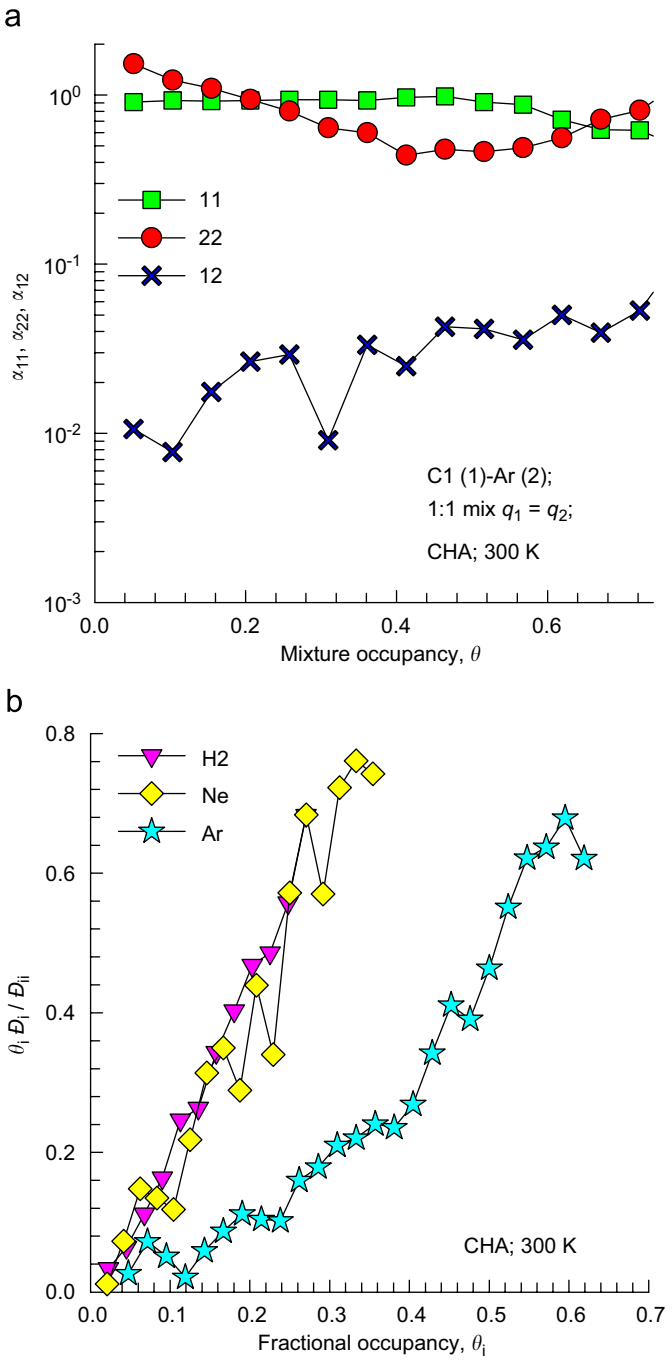

Fig. 9. (a) MD simulation data for α_{11}, α_{22}, and α_{12} in equimolar C1(1)–Ar(2) mixtures in CHA as a function of the mixture occupancy, θ. (b) Variation of $\theta_i Đ_i/Đ_{ii}$ with θ for Ne, H_2, and Ar in CHA.

Fig. 9b for $\theta_i Đ_i/Đ_{ii}$ in CHA. We note that the correlation effects for H_2 are practically the same as for Ne which is equally small in size; for mixtures containing either of these molecules in CHA, correlation effects will be significant and the simplification given by Eq. (20) will not hold.

4. Correlations-dominant scenario

It is useful to derive expressions for the limiting scenario in which correlation effects are dominant, as is the case in CNTs. Imposing the condition $\theta_i Đ_j/Đ_{ji} \gg 1$ we obtain

$$L_{11} = \frac{q_1^2}{\frac{q_1}{Đ_1} + \frac{q_2}{Đ_2}}, \quad L_{22} = \frac{q_2^2}{\frac{q_1}{Đ_1} + \frac{q_2}{Đ_2}}, \quad L_{12} = \frac{q_1 q_2}{\frac{q_1}{Đ_1} + \frac{q_2}{Đ_2}} \tag{21}$$

The corresponding α_{ij} ratios are

$$\alpha_{11} = \frac{1}{1 + \frac{q_2}{q_1}\frac{Đ_1}{Đ_2}}, \quad \alpha_{22} = \frac{1}{1 + \frac{q_1}{q_2}\frac{Đ_2}{Đ_1}}, \quad \alpha_{12} = 1 \tag{22}$$

For the special case in which the component loadings are equimolar, i.e., $q_1 = q_2$, Eq. (21) yields

$$L_{11} = L_{22} = L_{12} = \frac{q_1}{\frac{1}{Đ_1} + \frac{1}{Đ_2}} = \frac{1}{\frac{1}{L_1} + \frac{1}{L_2}} \tag{23}$$

Eqs. (21)–(23) are new, yet remarkably simple, results. It is interesting to note that the expressions for the Onsager coefficients do not contain the hallmark of the M–S formulation: the exchange coefficients $Đ_{12}$ and $Đ_{21}$. Nevertheless, we find it hard to see how the final result could have been obtained without invoking the M–S formalism as a starting point.

The MD data for L_{ij} in equimolar mixtures containing methane (C1)–ethane (C2), C1–propane (C3), C1–*n*-butane (*n*C4), C1–isobutane (*i*C4), C1–hydrogen (H_2), and Ar–Ne mixtures in CNTs are shown in Fig. 10. For all mixtures we note that $L_{11} \approx L_{22} \approx L_{12}$. These results are in agreement with the MD results of Chen and Sholl (2004; 2006) (for H_2–C1 mixtures), and Arora and Sandler (2006) (for N_2–O_2 mixtures) in CNT. Also shown in Fig. 10 are the MD data for pure component L_i. For all mixtures both L_{11} and L_{22} are lowered in the mixture below the corresponding L_1 and L_2 values, respectively. Furthermore, we note that the lowering is more severe for the more mobile species. The continuous solid lines represent the calculations using Eq. (23); the agreement with L_{ij} MD data is good in all cases.

For the C1–H_2 mixture at a total loading $q_1 + q_2 = 1.92$ molecule nm^{-1} in CNT (10,10), the MD data for L_{ij} with varying compositions are compared with the estimations using Eq. (21) in Fig. 11a. The agreement is remarkably good. The good agreement also holds for C1–C2 mixture at a total loading $q_1 + q_2 = 2.6$ molecule nm^{-1} in CNT (20,0), see Fig. 11b. From the results presented in Figs. 10 and 11 we conclude that for correlation dominated systems such as CNTs, the diagonal elements L_{ii} are significantly lower than the pure component L_i.

Eqs. (21)–(23) serve as good *approximations* to describe mixture diffusion in 1D channel zeolites such as AFI and TON provided the occupancies are high enough to ensure significant correlations. To illustrate this we present MD data for L_{ij} for (a) C1–C3 mixture in AFI and (b) C1–C2 mixture in TON; see Fig. 12. We see that $L_{11} \approx L_{22} \approx L_{12}$ for both systems and note that Eq. (23) provides a reasonably good description.

From a practical point of view 1D nanoporous channels are not attractive for separation purposes because the high degree of correlations tends to yield low diffusion selectivities.

5. Finite correlations scenario

We now examine the intermediate scenario between the two extremes considered in the foregoing. It is clear from Eqs. (15) and (16) that for finite correlations we have $\alpha_{ii} < 1$; the diagonal elements L_{ii} are both reduced below the pure component values L_i. The departure of α_{ii} from unity values is dictated by the magnitude of $\theta_i Đ_j/Đ_{ji}$. Put another way, if $\alpha_{12} > 0$, then we *must* have both α_{11} and $\alpha_{22} < 1$; we shall test this conclusion. Fig. 13 presents α_{11}, α_{22}, and α_{12} data for

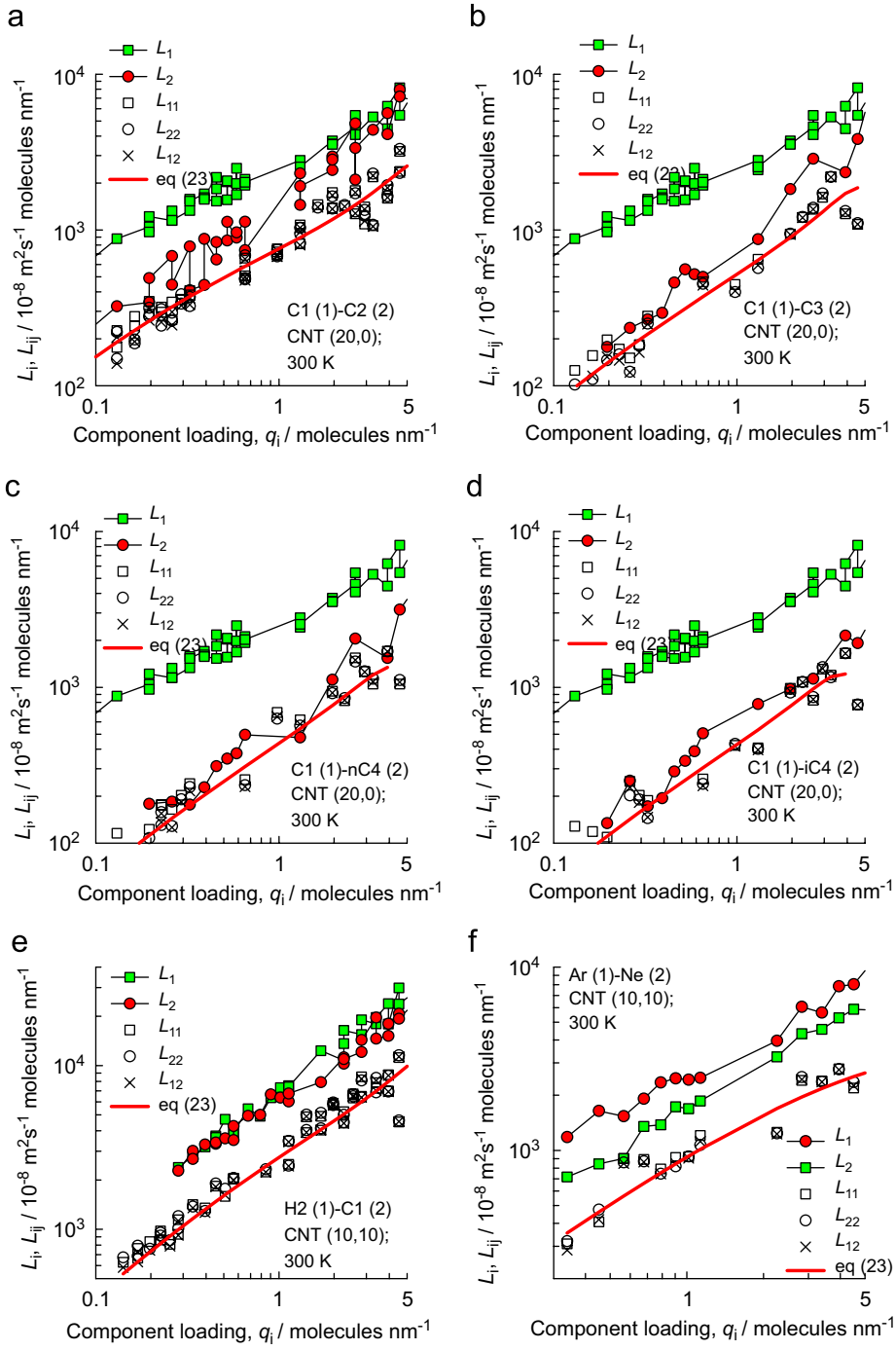

Fig. 10. MD data for L_{ij} (open symbols) in equimolar mixtures (a) C1–C2, (b) C1–C3, (c) C1–*n*C4, (d) C1–*i*C4, (e) C1–H_2, and (f) Ar–Ne mixtures in CNTs at 300 K as a function of the component loadings expressed in molecules per nm. Also shown are the pure component L_i (solid symbols). The estimations using Eq. (23), with the pure component diffusivity data fits given in the Supplementary material, are shown by the continuous solid lines.

equimolar Ne(1)–Ar(2) mixtures in six different zeolites, as a function of occupancy in the mixture, θ. The interaction factor α_{12}, increases as θ increases in all cases. Correlations also tend to have a stronger retarding influence on the more mobile species. In all six zeolites, with increasing θ the α_{11} for the more mobile Ne decreases in values below unity. The sharper the *increase* in α_{12}, the sharper is the corresponding *decrease* in the α_{11}. There is a less pronounced reduction in the corresponding α_{22} of the tardier Ar with θ. In LTA, CHA, and DDR the reduction is negligible and $\alpha_{22} \approx 1$ is a reasonable approximation. A finite, non-zero value for α_{12} is inconsistent with the assumption of unity values for the α_{11} and α_{22}, except for limiting scenario given by Eq. (20). The estimation procedure for the Onsager matrix suggested by Sundaram and Yang (2000) is fundamentally flawed in this respect because it prescribes $\alpha_{ii} = 1$, along with a finite non-zero α_{12}.

From Eq. (17) we note α_{12} is influenced by the occupancies θ_1 and θ_2 of the two species in separate parameters. This suggests that at constant total loading, the α_{12} must vary with the relative proportions of the two species. Fig. 14 presents α_{ij} data for Ne(1)–Ar(2) mixtures at constant total loading, $q_1 + q_2$, as a function of Ar mole fraction, x_2. Indeed, α_{12} is composition dependent for all zeolites. In all cases the progressive increase in the composition of the tardier

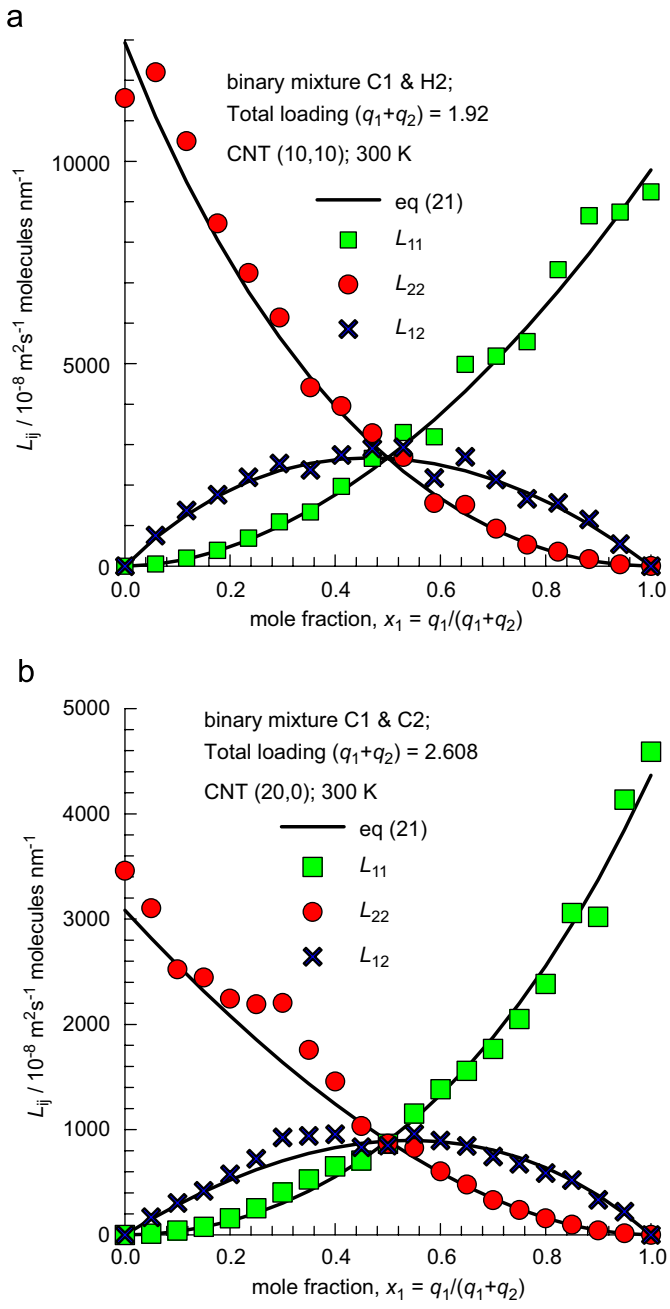

Fig. 11. MD data for L_{ij} (solid symbols) in (a) C1–H_2 and (b) C1–C2 mixtures at constant total loading, $q_1 + q_2$, in CNTs as a function of mixture composition. The estimations using Eq. (21), with the pure component diffusivity data fits given in the Supplementary material, are shown by the continuous solid lines.

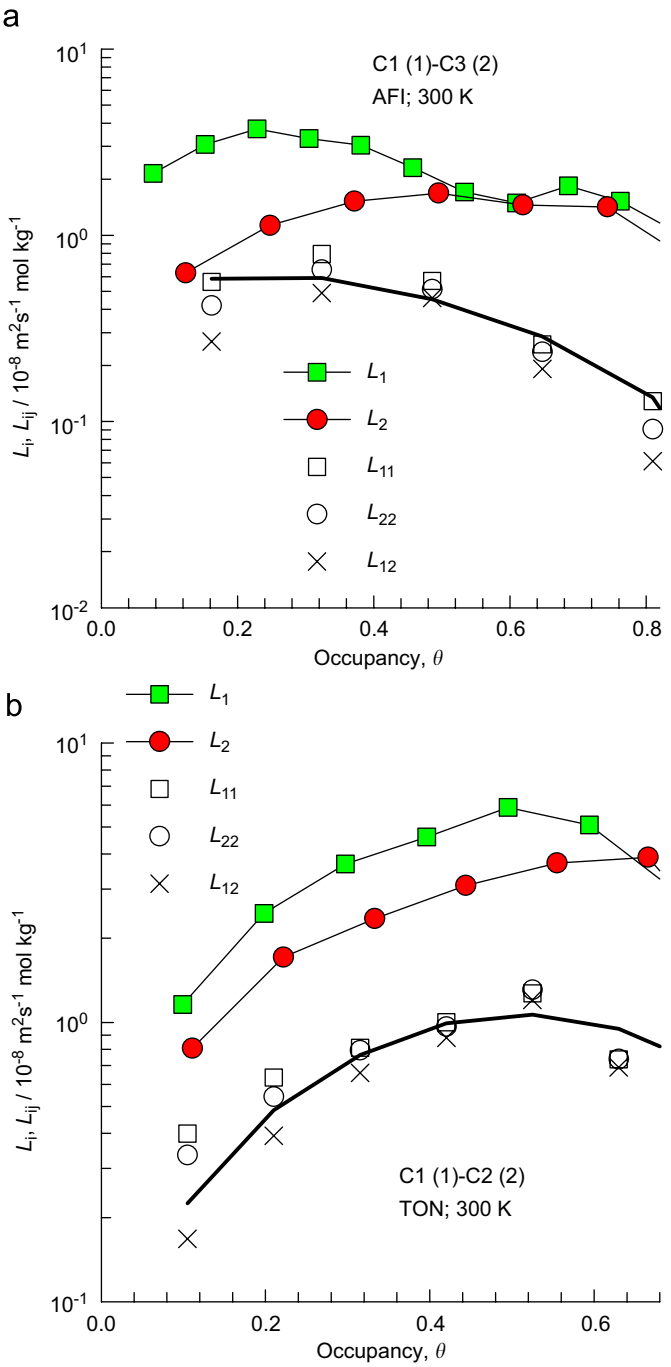

Fig. 12. MD data for L_{ij} (open symbols) in equimolar (a) C1–C3 mixture in AFI; and (b) C1–C2 mixture in TON as a function of the occupancy in the total mixture. Also shown are the pure component L_i (solid symbols). The estimations using Eq. (23) are shown by the continuous solid line.

Ar has a retarding influence on Ne, and α_{11} is progressively reduced with increase in x_2. With increasing proportion of the more mobile Ne, α_{22} of Ar is also reduced below its pure component value in AFI, FAU, and MFI. However for LTA, CHA, and DDR we have $\alpha_{22} \approx 1$ irrespective of the composition; this is a reflection of weak correlations in cage type zeolites with narrow windows.

The continuous solid lines in Figs. 13 and 14, represent calculations using Eqs. (15)–(17) along with the interpolation formula (12); the step-by-step calculation procedure is available in the Supplementary material. There is reasonably good agreement with MD data for α_{11}, α_{22}, and α_{12}. This suggests that (a) the use of *pure component* $Đ_i$ is justified for prediction of the Ne-Ar mixture diffusion and (b) that the interpolation formula (12) is reasonably accurate.

Fig. 15 presents L_{ij} data for Ne–Ar, and C1–Ar mixtures in CuBTC, IRMOF-1, and in the 12-ring channels of ETS-4 (see pore landscapes in Fig. 2). The estimations are in good agreement with MD simulations, suggesting that the procedure developed for zeolites applies equally to titanosilicates and MOFs as well. Due to the wide variety of MOF structures that are available, more work will be required to ascertain whether this conclusion is generic. The diffusion data for ETS-4 was only determined for transport in the 12-ring channels using MD. In practice the rate limiting step will be hopping across the narrow 8-ring windows; the diffusivities for this transport are,

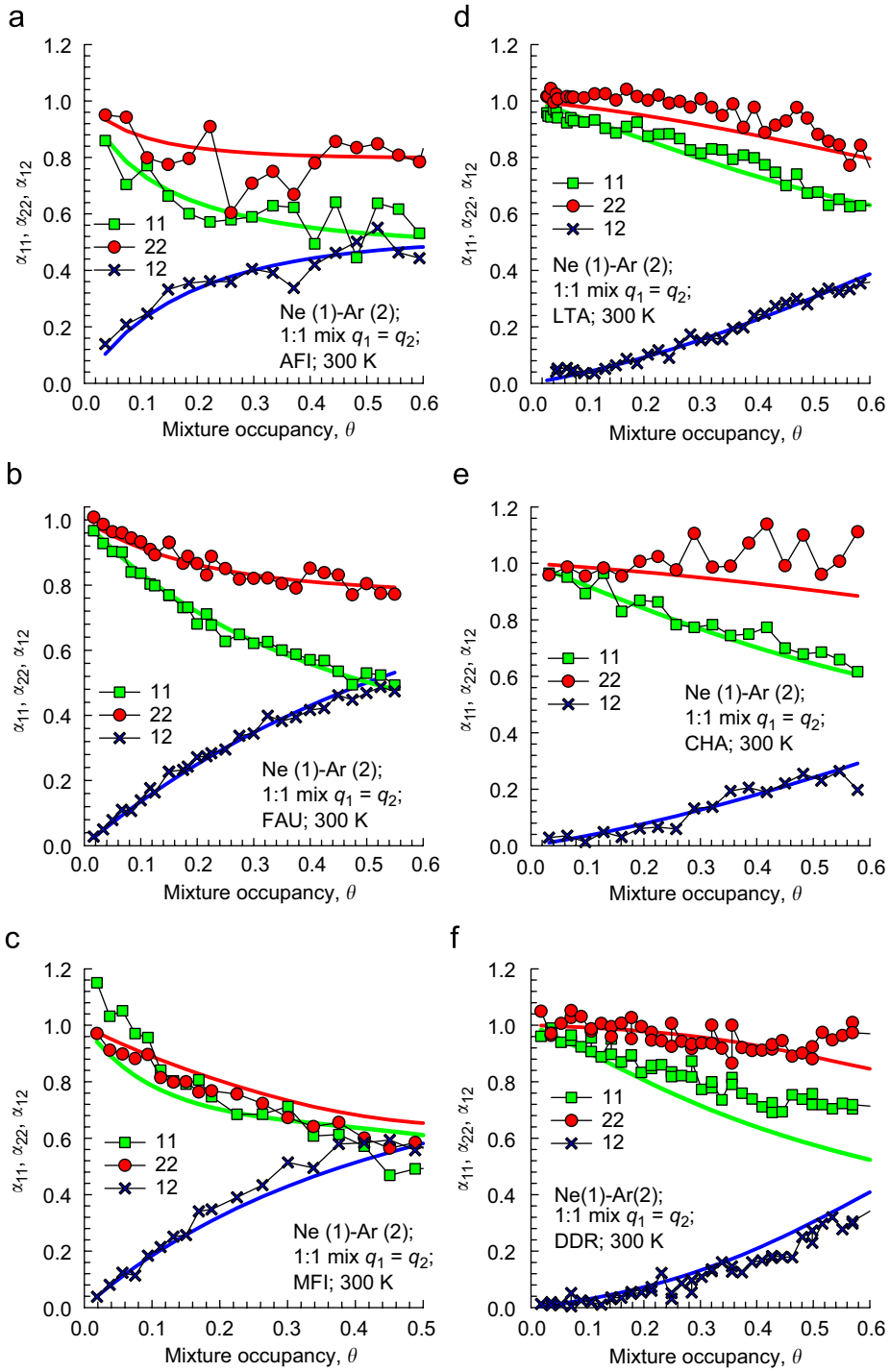

Fig. 13. MD data for α_{11}, α_{22}, and α_{12} in equimolar Ne(1)–Ar(2) mixtures in AFI, FAU, MFI, LTA, CHA, and DDR zeolites as a function of the mixture occupancy, θ. Also shown by the continuous solid lines are the estimations using Eqs. (12), (15)–(17) using the pure component diffusivity data fits given in the Supplementary material.

however, too low to be determined from MD simulations. However, it is to be expected that the transport characteristics will be akin to inter-cage hopping between the cages of DDR and LTA. In this case, therefore, correlation effects will be negligible and mixture diffusion characteristics can be estimated from pure component diffusivity data. Work is currently in progress to seek verification of this conclusion.

6. Binary mixture of identical species

If the two species in the mixture are nearly identical in respect of the pure component $Đ_i$, there is a temptation to assume the off-diagonal element L_{12} vanishes. We investigate this situation and consider a binary mixture of species 1 and 2 where species 2 is identical to species 1; for this case $q_{1,\mathrm{sat}} = q_{2,\mathrm{sat}}$, the $Đ_1 = Đ_2$,

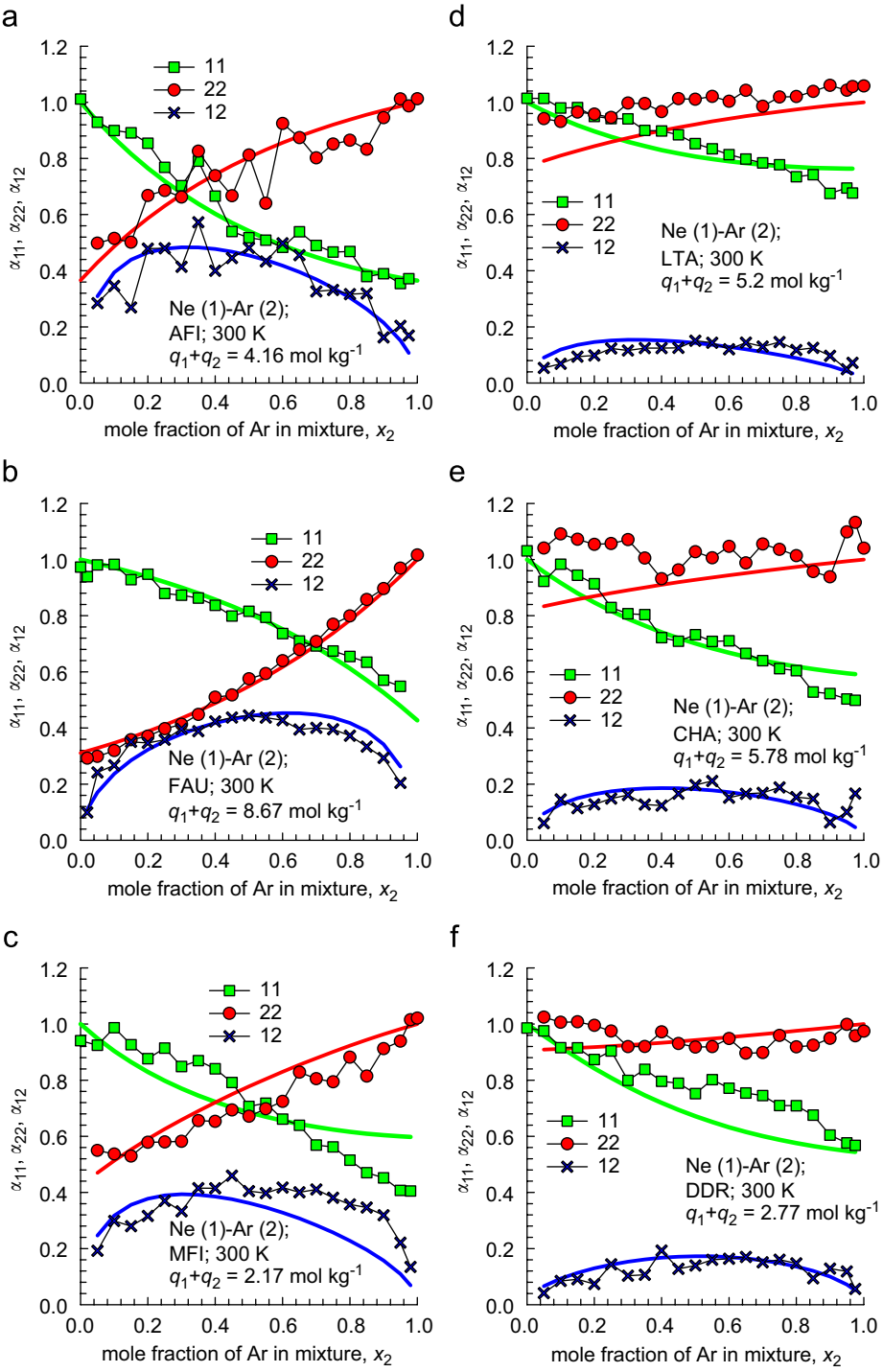

Fig. 14. MD data for α_{11}, α_{22}, and α_{12} in Ne(1)–Ar(2) mixtures at constant total loading, q_1+q_2, in AFI, FAU, MFI, LTA, CHA, and DDR zeolites as a function of Ar mole fraction, x_2. Also shown by the continuous solid lines are the estimations using Eqs. (12), (15)–(17) using the pure component diffusivity data fits given in the Supplementary material.

and $Đ_{12} = Đ_{21} = Đ_{11}$. Eqs. (6)–(8) simplify to yield

$$\Delta_{11} = \frac{Đ_1\left(1+\frac{\theta_1 Đ_1}{Đ_{11}}\right)}{1+\frac{(\theta_1+\theta_2)Đ_1}{Đ_{11}}}, \quad \Delta_{22} = \frac{Đ_1\left(1+\frac{\theta_2 Đ_1}{Đ_{11}}\right)}{1+\frac{(\theta_1+\theta_2)Đ_1}{Đ_{11}}},$$

$$\Delta_{12} = \frac{\left(\frac{\theta_1 Đ_1^2}{Đ_{11}}\right)}{1+\frac{(\theta_1+\theta_2)Đ_1}{Đ_{11}}} = \Delta_{21}\frac{q_1}{q_2} \tag{24}$$

The off-diagonal elements Δ_{12} and Δ_{21} do not vanish. To verify this conclusion we carried out simulations for FAU in which the two species are *both* assigned the force field parameters of Ar, but sampled separately as Ar (1) and Ar (2). The elements Δ_{ii} are determined using the formula

$$\Delta_{ij} = \frac{1}{6}\lim_{\Delta t\to\infty}\frac{1}{n_j}\frac{1}{\Delta t}\left\langle\left(\sum_{l=1}^{n_i}(\mathbf{r}_{l,i}(t+\Delta t)-\mathbf{r}_{l,i}(t))\right)\right.$$
$$\left.\bullet\left(\sum_{k=1}^{n_j}(\mathbf{r}_{k,j}(t+\Delta t)-\mathbf{r}_{k,j}(t))\right)\right\rangle \tag{25}$$

In this expression n_i and n_j represent the number of molecules of species Ar (1) and Ar (2), respectively, and $\mathbf{r}_{l,i}(t)$ is the position vector

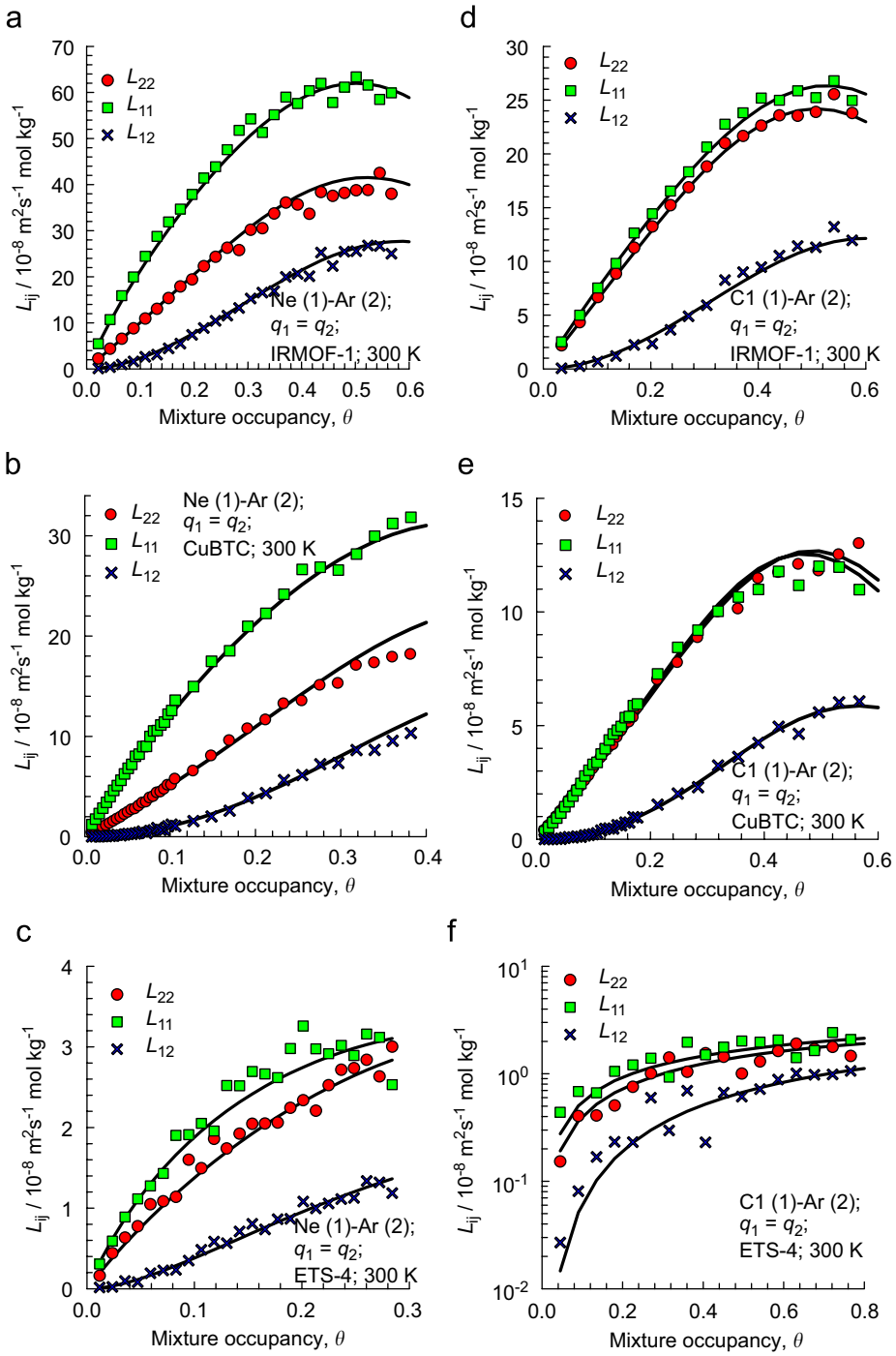

Fig. 15. MD data for L_{ij} (symbols) for (a)–(c) Ne(1)–Ar(2), and (d)–(f) C1(1)–Ar(2) mixtures in CuBTC, IRMOF-1, and ETS-4 at 300 K as a function of the mixture occupancy, θ. Also shown by the continuous solid lines are the estimations using Eqs. (6)–(8) and (12) using the pure component diffusivity data fits given in the Supplementary material. Diffusion in ETS-4 is only considered along the 12-ring channels. Animations can be downloaded from our website (van Baten and Krishna, 2008).

of molecule l of species i at any time t. The Δ_{11}, Δ_{22}, and Δ_{12} data are shown in Fig. 16a, along with the pure component $Đ_i$ data for Ar. We see that Δ_{12} is finite, and non-zero. Furthermore the Δ_{ii} values are significantly lower than the $Đ_i$. Eq. (24) provides a good estimation of the Δ_{ij} data using pure component $Đ_i$ fits.

For *self*-diffusion in a mixture consisting of tagged (1) and untagged (2) species we have a further restriction that the sum of driving forces vanish, because the total number of molecules is held constant in such an "experiment". Also, the sum of the two fluxes is zero. Applying these constraints allows us to derive the following expression for the self-diffusion of tagged component 1 (Krishna and Paschek, 2002):

$$D_{1,\text{self}} = \Delta_{11} - \Delta_{12} = \frac{1}{\frac{1}{Đ_1} + \frac{\theta_1+\theta_2}{Đ_{11}}} \tag{26}$$

From MD simulations of $Đ_i$ and $D_{i,\text{self}}$ for unary systems, Eq. (26) allows us to back out the $Đ_{ii}$; this is the procedure we had adopted to obtain the data presented in Fig. 8.

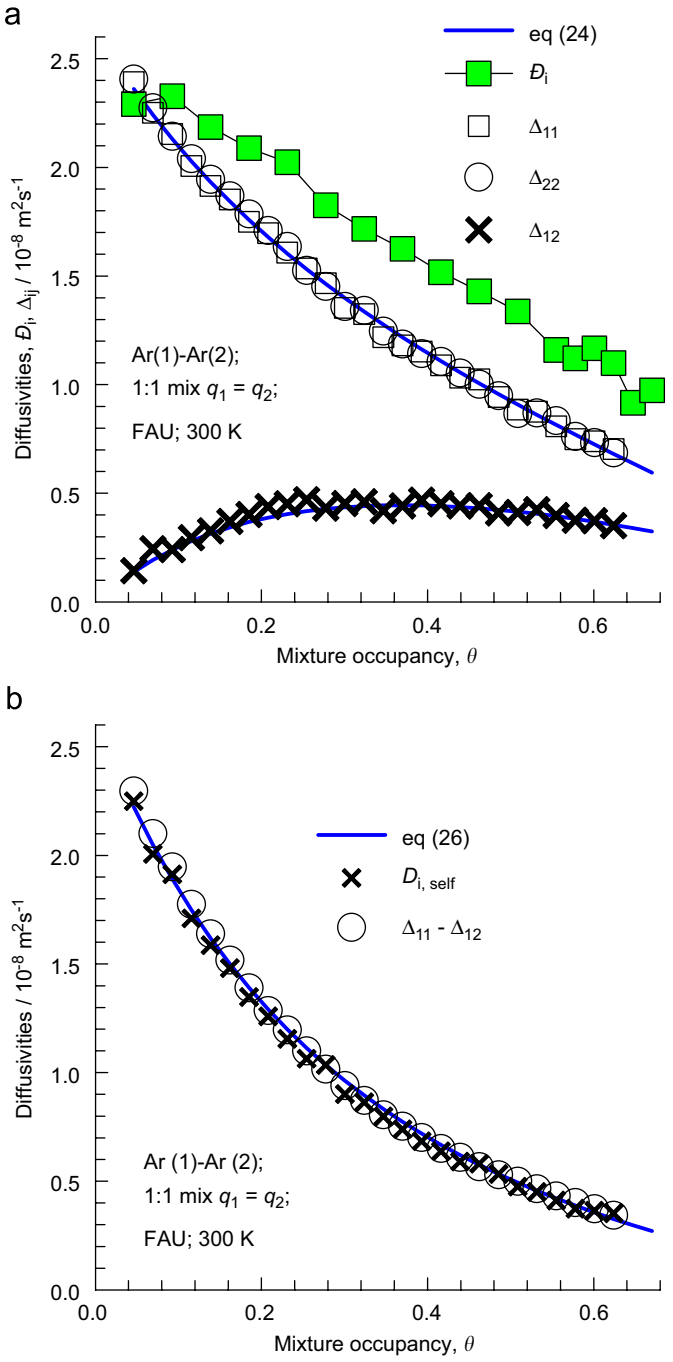

Fig. 16. (a) MD data for Δ_{11}, Δ_{22}, and Δ_{12} in equimolar Ar(1)–Ar(2) mixtures in FAU as a function of the total mixture occupancy. Also shown are the pure component $Đ_i$. The continuous solid line represents the calculations following Eq. (24), using pure component data fits given in the Supplementary material. (b) The self-diffusivities in the mixture, $D_{i,\text{self}}$, are compared with $\Delta_{11} - \Delta_{12}$. The continuous solid line is based on Eq. (26).

For the Ar(1)–Ar(2) equimolar mixture in FAU, the $D_{i,\text{self}}$ were computed by analyzing the mean square displacement of each species i:

$$D_{i,\text{self}} = \frac{1}{6n_i} \lim_{\Delta t \to \infty} \frac{1}{\Delta t} \left\langle \left(\sum_{l=1}^{n_i} (\mathbf{r}_{l,i}(t + \Delta t) - \mathbf{r}_{l,i}(t))^2 \right) \right\rangle \tag{27}$$

Fig. 16b compares $D_{i,\text{self}}$ data with $\Delta_{11} - \Delta_{12}$, determined from Eq. (25); the agreement between the two *independent* sets of simulation results is very good, confirming the validity of Eq. (26). In terms of the Onsager coefficients the expression for $D_{i,\text{self}}$ is

$$D_{1,\text{self}} = \frac{L_{11}}{q_1} - \frac{L_{12}}{q_2} \tag{28}$$

Eq. (28) was originally derived by Ash and Barrer (1967). Our main reason to revisit the classic Eqs. (26) and (28) is to address the sixth question posed in the Introduction. In the Onsager result for self-diffusion, Eq. (28), the cross-coefficient L_{12} $(=q_2\Delta_{12})$ is related to *both* $Đ_1$ *and* the exchange coefficient $Đ_{11}$, making it difficult to directly relate the L_{12} to *correlations* in molecular jumps. In the M–S theory, the $Đ_{11}$ uniquely portrays correlations for unary diffusion. The main coefficient L_{11} in Eq. (28) is also influenced by correlations, and L_{11} does not equal L_1 except for the limiting case of vanishing correlations, $Đ_{11}/Đ_1 \to \infty$. There is no foundation, therefore, for expecting $L_{11} = L_1$ to hold for *binary* mixtures if this equality does not even hold for self-diffusion in *unary* systems. In sharp contrast, the $Đ_1$ is uninfluenced by correlations, and this is the reason that the M–S estimation strategy has been successful in the examples discussed in the foregoing sections. It is difficult, if not impossible, to set up estimation procedures for L_{ij} based purely on the Onsager formulation; the exceptions are the two limiting scenarios of dominant and negligible correlations.

7. Evidence of failure of estimation methods

We now highlight two situations that lead to a complete breakdown of the estimation procedure for the Onsager coefficients. Fig. 17 shows the α_{11}, α_{22}, and α_{12} data for equimolar Ne(1)–CO_2(2) mixtures in LTA, DDR, FAU, and CHA as a function of the mixture occupancy, θ. For FAU and CHA the estimations from pure component diffusivity data, shown by continuous solid lines, are good, as we have become accustomed to expect. The situation with regard to LTA and DDR is different. For these two zeolites, the predictions are good only for α_{22} and α_{12}; α_{11} is overestimated to a significant extent. Since α_{11} portrays the extent to which the L_{11} is lowered below the pure component value L_1, this implies that the actual situation (i.e., portrayed by MD) leads to a more significant lowering of L_1 than anticipated on the basis of correlation effects alone. The deviation between estimations and MD data cannot be ascribed to inadequate predictions of correlations using the interpolation formula (12). If this were to be the case then α_{12} would also be poorly predicted; this is not the case. The inescapable conclusion is that the poor estimations of α_{11} are most likely caused by the assumption, implicit in the entire foregoing discussions, that the $Đ_i$ in the mixture is the same as the pure component value. We shall seek to verify this hypothesis.

Fig. 18 shows data on M–S diffusivities $Đ_i$ of Ne, Ar, N_2, and O_2 in LTA, and in DDR as a function of the occupancy. In each case the pure component values are compared with the values backed-out from MD data on Δ_{ij} for a variety of equimolar mixtures. Consider, for example the diffusivity of Ar in LTA. We see from Fig. 18b that the pure component $Đ_i$ is in good agreement with the values backed out for Ar–Ne, and Ar–C1 mixtures. However, for Ar–CO_2 mixtures, the backed-out diffusivity for Ar is lower than the pure component value by about one order of magnitude at high θ. The same story holds for other molecules Ne, N_2, and O_2 in both LTA and DDR, i.e., the pure component $Đ_i$ are in good agreement with values in mixtures, provided these do not contain CO_2. Fig. 18 also shows that in CO_2-bearing mixtures the $Đ_i$ are lowered below the pure component value by increasing extents as the θ increases. This reduction is due to the fact that CO_2 gets preferentially, and strongly, adsorbed at the narrow windows of these zeolites, hindering the diffusion of partner

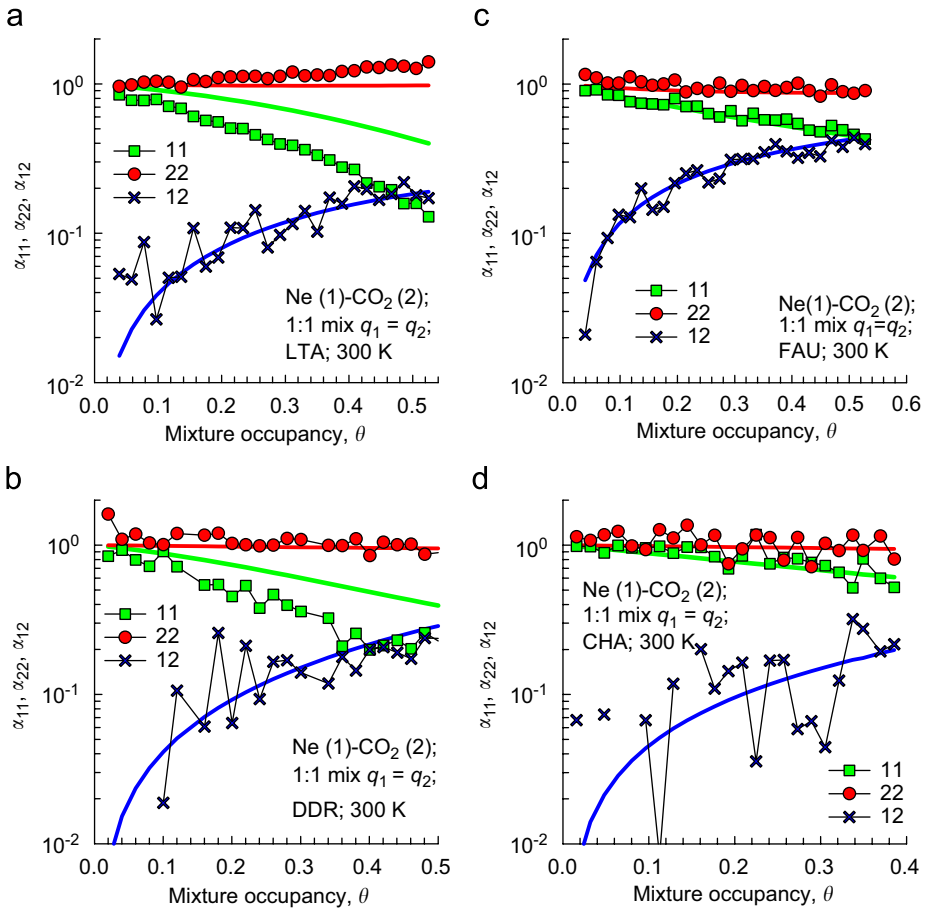

Fig. 17. MD data for α_{11}, α_{22}, and α_{12} in equimolar Ne(1)–CO$_2$(2) mixtures in (a) LTA, (b) DDR, (c) FAU, and (d) CHA as a function of the mixture occupancy, θ. Also shown by the continuous solid lines are the estimations using Eqs. (12), (15)–(17) using the pure component diffusivity data fits given in the Supplementary material.

molecules; this was shown in an earlier study on *self*-diffusion in CO$_2$-bearing mixtures in cage-type zeolites such as LTA, DDR and ERI (Krishna and van Baten, 2008c). An appreciation of the hindrance effect exerted by CO$_2$ at the window regions can be gained from the animations of intercage hopping of molecules (van Baten and Krishna, 2008).

While CO$_2$ hinders the diffusion of partner molecules in LTA, and DDR, it is uninfluenced by the presence of its partners and the M–S diffusivity of CO$_2$ in CO$_2$-bearing mixtures remains the same as for pure component; this is demonstrated by the data presented for DDR in Fig. 19a.

The hindrance effect gets increasingly severe as the proportion of CO$_2$ in the mixtures increases. To demonstrate this we present results for M–S diffusivities of Ne, Ar, N$_2$, and O$_2$ in DDR in CO$_2$-bearing mixtures where the total loading, $q_1 + q_2$, is held constant; see Fig. 19b. Since the mixture occupancy θ is practically unchanged in this case, the classical M–S estimation procedure anticipates practically no reduction in the $Đ_i$ values of Ne, Ar, N$_2$, and O$_2$; the MD results, however, show that there is about an order of magnitude reduction in the $Đ_i$ when the CO$_2$ mole fraction approaches unity. Interestingly, for Ar, N$_2$, and O$_2$ the $Đ_i$ values are lowered to values below that of the "tardier" CO$_2$.

Experimental evidence of window blocking can be obtained from a re-analysis of the published DDR permeation data for CO$_2$–CH$_4$ and CO$_2$–N$_2$ mixtures (van den Bergh et al., 2007, 2008). Fig. 20a compares the membrane transport coefficients, $\rho Đ_i/\delta$, for pure CH$_4$ with those of CH$_4$ in mixtures with CO$_2$, and with N$_2$. When compared at the same occupancy θ, there is a dramatic reduction in the transport coefficient due to the presence of CO$_2$, most likely due to window blocking. Fig. 20b shows a similar strong reduction in the transport coefficient for N$_2$ in CO$_2$–N$_2$ mixtures. In practical terms the selectivity for permeation of CO$_2$ across a DDR membrane will be significantly higher than anticipated on the basis of the model using the M–S theory (Krishna and van Baten, 2007b, 2008c). In other words, the window blocking by CO$_2$ is a boon in practice and predictions based on the M–S theory will be overly conservative.

The second situation we consider is that of diffusion in MOR, in which the 12-ring 1D channels are connected with 8-ring side pockets; see Fig. 21a. Segregation effects are present during adsorption of C1–C2 mixtures. By sampling 10^4 equilibrium positions of molecules during a Monte Carlo simulation of binary adsorption equilibrium, we determined the % probability of locating C1 and C2 in the side pockets; for C1 this probability is 70% whereas for C2, the value is only 15–20%; see Fig. 21b. The preferential location of C1 in the side pockets can also be observed qualitatively in the snapshot in Fig. 21a. There are consequences of this segregation on diffusion. In Fig. 21c the M–S diffusivity of pure C1 is compared with the value backed-out from C1 to C2 equimolar mixture simulations. We see that the $Đ_{C1}$ value is lower in the mixture by more than one order of magnitude. A similar story holds for $Đ_{C1}$ in the C1–C3 mixture. The reason for the lower $Đ_{C1}$ in the two mixtures is that the side pockets are *cul-de-sacs* in respect of molecular traffic that is along the 12-ring channels. The only way a C1 molecule located in a side pocket can contribute to the diffusion process is to hop back into the main (12-ring) stream, but this motion is about one order of magnitude tardier. Animations of the molecular traffic demonstrate that

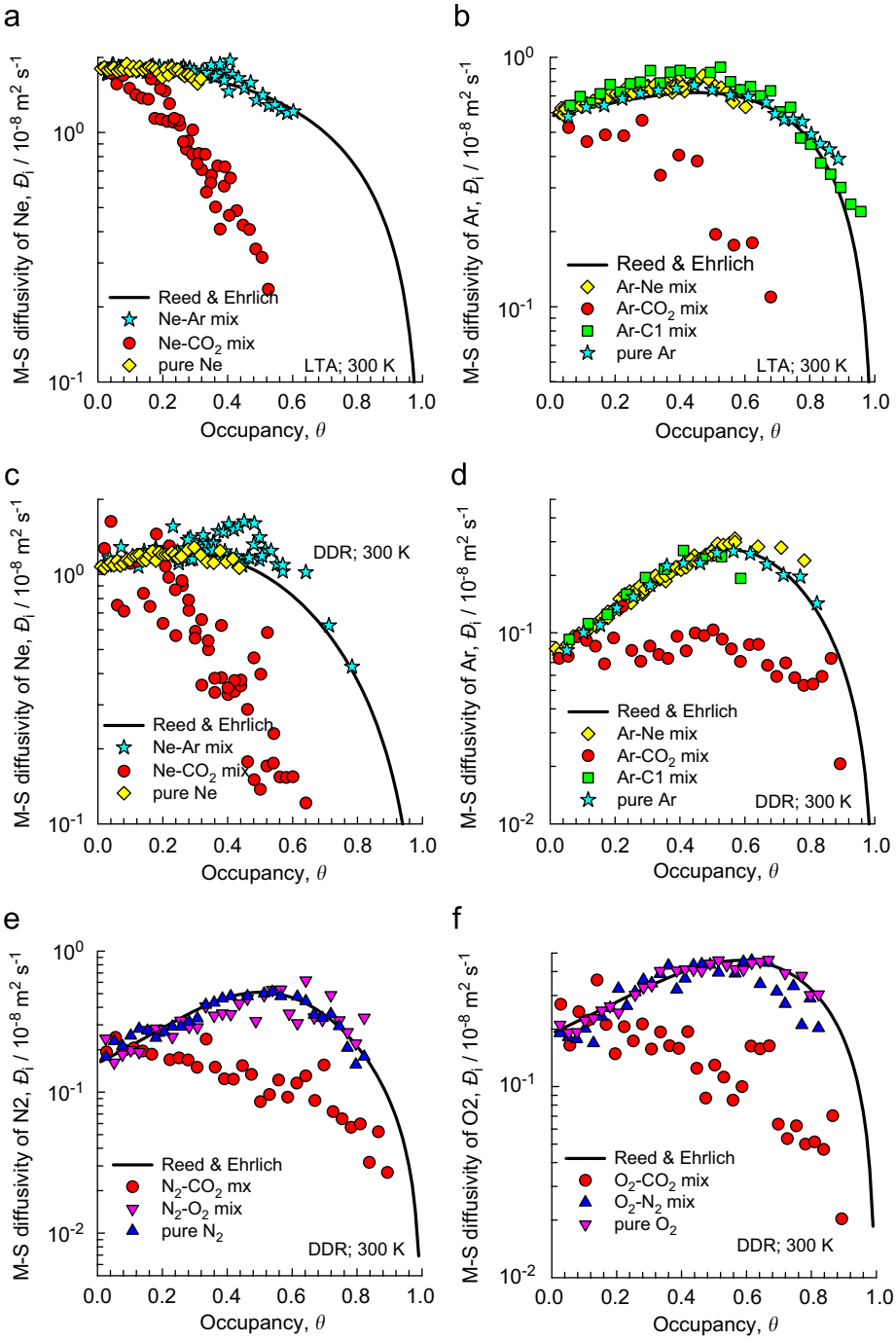

Fig. 18. M–S diffusivities of Ne, Ar, N_2, and O_2 in LTA and DDR zeolites as function of occupancy. In each case the pure component $Đ_i$ are compared with the values backed-out from MD data on $Đ_{ij}$ for equimolar mixtures; the explicit formula for backing-out are given in the Supplementary material.

C1 molecules located in side pockets appear to be "locked in" and do not participate in the main thoroughfare along the 12-ring channels (van Baten and Krishna, 2008). In C1–CO_2 mixtures it is the CO_2 that gets trapped in the side pockets (cf. snapshot in Fig. 1); for this reason MOR is not a good adsorbent choice for CO_2 removal from natural gas (García-Pérez et al., 2007; Krishna and van Baten, 2007a) because of its poor diffusivity.

It is interesting to note that when strong segregation effects occur in adsorption, the IAST theory fails at a *quantitative* level to describe multicomponent equilibria (Chen and Sholl, 2007; Krishna and Paschek, 2001; Krishna and van Baten, 2007b, 2008a, c; Murthi and Snurr, 2004); this bodes a corresponding failure of the M–S approach to adequately predict mixture diffusion. The IAST and M–S suffer failures for analogous reasons. Another interesting point to note is that when segregation occurs the M–S estimation procedure fails badly by an order of magnitude; the corresponding failure in the IAST is less significant (Krishna and van Baten, 2008c). Adjusting the exchange coefficients $Đ_{ij}$ will not be successful in capturing the mixture diffusion characteristics when segregation occurs.

8. Conclusions

By careful examination of a vast data base of MD simulations for mixture diffusion we have obtained answers to the set of six

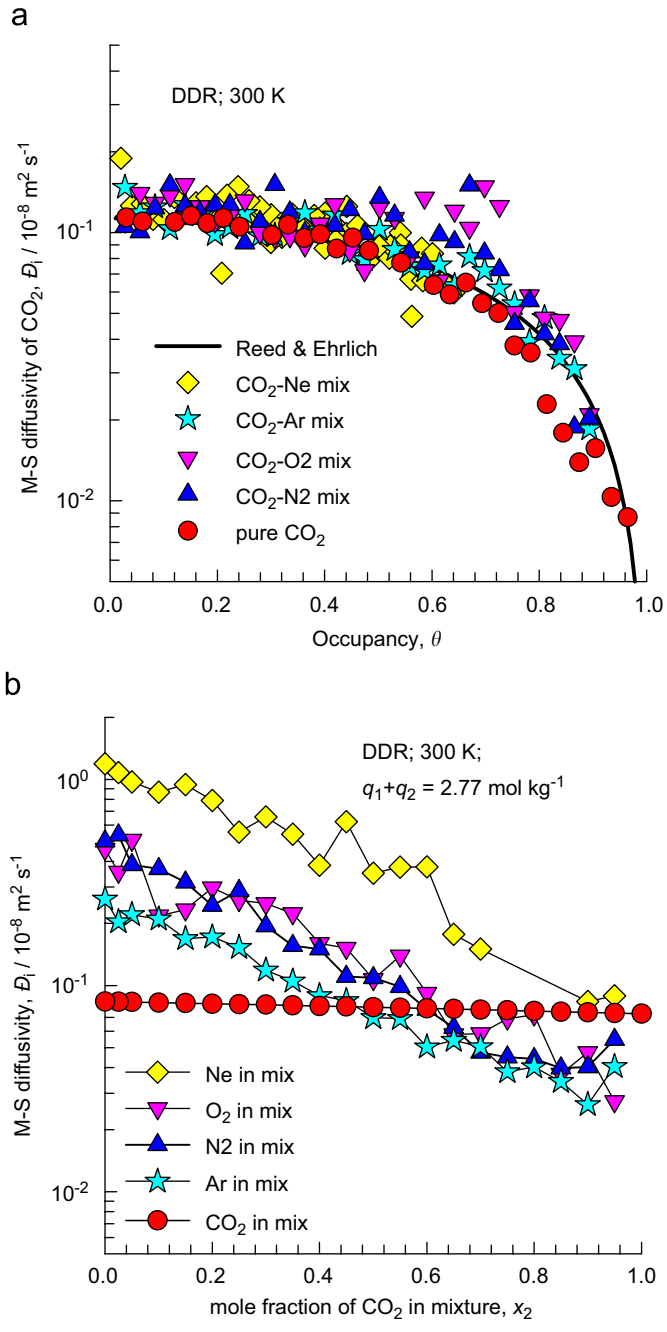

Fig. 19. (a) M–S diffusivity of CO_2 in CO_2-bearing mixtures in DDR as a function of occupancy. Also shown are the data for pure CO_2 along with the Reed and Ehrlich fit of this pure $Đ_i$ data. (b) M–S diffusivities of Ne, Ar, N_2, and O_2 in CO_2-bearing mixtures in DDR as a function of CO_2 mole fraction, x_2. The CO_2 diffusivity in these mixtures is practically independent of composition. The symbols in (a) and (b) represent values backed-out from MD data on $Đ_{ij}$.

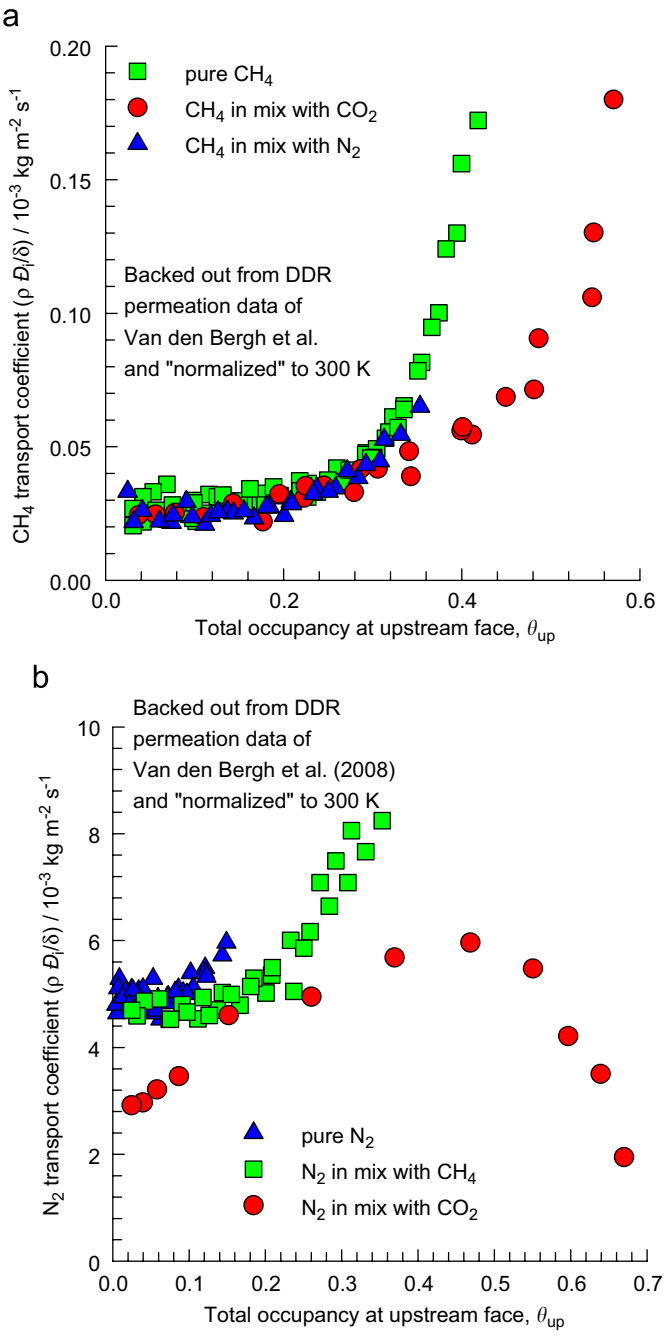

Fig. 20. Comparison of transport coefficients, $\rho Đ_i/\delta$, for (a) CH_4 and (b) N_2 backed-out from unary and binary mixture permeation data across DDR membrane (van den Bergh et al., 2007, 2008). The data for N_2 is backed out from CO_2–air mixture permeation; we consider N_2 and O_2 to have equal diffusivities. The backing-out is done with the pure component adsorption and diffusion data presented in earlier work (Krishna and van Baten, 2008c), using the procedure described earlier (Krishna and van Baten, 2008b). The data at different temperatures have been normalized to 300 K, by using the diffusion activation energy.

questions posed in the Introduction.

(1) The α_{12} is a function of two dimensionless factors parameters reflecting correlations: $\theta_1 Đ_2/Đ_{21}$ and $\theta_2 Đ_1/Đ_{12}$; Eq. (17) allows its estimation from pure component diffusion parameters by invoking the interpolation formula (12). A constant value of α_{12} is never a good assumption for mixture diffusion except when (a) correlations are negligibly small giving $\alpha_{12} = 0$ or (b) correlations are dominant. For all other cases α_{12} depends on occupancy θ and on composition of the mixture.

(2) The result $\alpha_{12} = 1$ is valid only for systems in which correlation effects dominate such as in CNTs; in all other cases we have the bounds $0 < \alpha_{12} < 1$.

(3) The diagonal elements L_{ii} can be identified with the pure component L_i only when correlation effects are negligibly small; in this case Eq. (20) holds and $\alpha_{12} = 0$. A non-zero finite value for α_{12} necessarily implies $L_{ii} < L_i$.

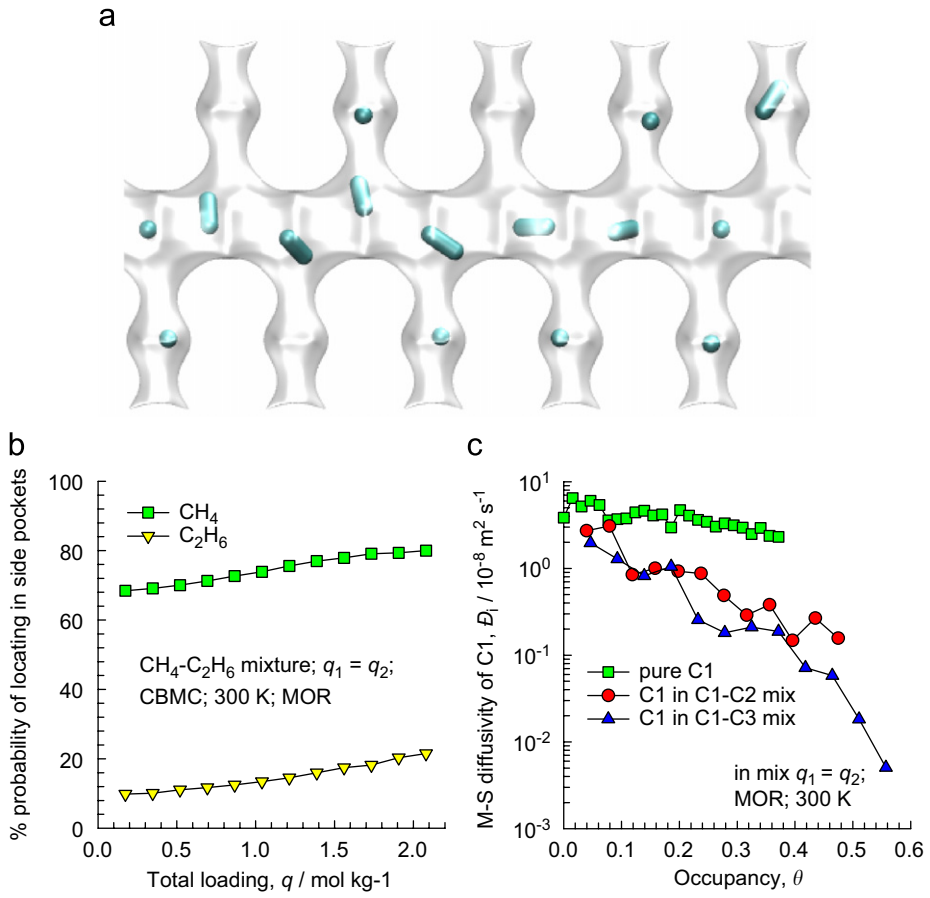

Fig. 21. (a) Snapshot of equimolar C1–C2 mixture in MOR. (b) % probabilities of locating C1 and C2 in the side pockets of MOR. (c) M–S diffusivities as a function of the occupancy: pure component C1, C1 in C1–C2 mixture, and C1 in C1–C3 mixture in MOR.

(4) The assumption that the M–S diffusivity $Đ_i$ in the mixture is the same as that for pure components is violated in cases where we have strongly segregated adsorption. For CO_2-bearing mixtures, the preponderance of CO_2 in the window regions of cage-type zeolites with narrow windows such as LTA and DDR has the effect of slowing down the partner molecules far more than anticipated by the M–S diffusion theory. This hindering effect cannot be captured by the exchange coefficient $Đ_{ij}$. In MOR zeolite the preferential location of C1 in the side-pockets tends to lower the $Đ_{C1}$ in mixtures with C2 or C3. There is a need for developing reliable estimation procedures for cases where segregation effects occur.

(4) For all the guest–host combinations considered in the present study, the interpolation formula (12) provides good estimates of the exchange coefficients. Nevertheless, this formula has an empirical character with no theoretical foundation.

(5) For correlation dominated systems such as CNTs simple expressions are obtained using the Onsager approach: Eqs. (21)–(23). For systems in which correlation effects are negligible, both Onsager and M–S approaches are equally potent. For the general case with finite correlations, the M–S approach is to be preferred.

Notation

$[D]$	matrix of Fick diffusivities, $m^2\,s^{-1}$
$Đ_i$	Maxwell–Stefan diffusivity of species i, $m^2\,s^{-1}$
$Đ_i(0)$	zero-loading Maxwell–Stefan diffusivity of species i, $m^2\,s^{-1}$
$Đ_{ii}$	self-exchange diffusivity of species, $m^2\,s^{-1}$
$Đ_{ij}$	binary exchange diffusivity, $m^2\,s^{-1}$
$D_{i,\mathrm{self}}$	self-diffusivity, $m^2\,s^{-1}$
L_i	Onsager coefficients of pure species i, $mol\,kg^{-1}$ $m^2\,s^{-1}$
L_{ij}	Onsager coefficients in binary mixture, $mol\,kg^{-1}$ $m^2\,s^{-1}$
n_i	number of molecules of species i in simulation box, dimensionless
N_i	molar flux of species i, $mol\,m^{-2}\,s^{-1}$
q_i	loading of species i, $mol\,kg^{-1}$
$q_{i,\mathrm{sat}}$	saturation loading of species i, $mol\,kg^{-1}$
$\mathbf{r}_{l,i}(t)$	position vector for molecule l of species i at any time t, m
R	gas constant, $8.314\,J\,mol^{-1}\,K^{-1}$
t	time, s
T	absolute temperature, K
x	spatial distance, m

Greek letters

α_{ii}	ratios defined by Eq. (14), dimensionless
α_{12}	interaction factor defined by Eq. (4), dimensionless
δ	thickness of membrane, m
$[\Delta]$	matrix of Maxwell–Stefan diffusivities, $m^2\,s^{-1}$
θ	total occupancy of mixture, dimensionless
θ_i	fractional occupancy of component i, dimensionless

μ_i molar chemical potential, J mol^{-1}
ρ framework density, kg m^{-3}

Subscripts

i, j components in mixture
sat referring to saturation conditions

Vector and matrix notation

( ) vector
[ ] square matrix

Acknowledgment

R.K. acknowledges the grant of a TOP subsidy from the Netherlands Foundation for Fundamental Research (NWO-CW) for intensification of reactors.

Appendix A. Supplementary data

Supplementary data associated with this article can be found in the online version at doi: 10.1016/j.ces.2008.03.017.

References

Arora, G., Sandler, S.I., 2005. Air separation by single wall carbon nanotubes: thermodynamics and adsorptive selectivity. Journal of Chemical Physics 123, 044705.
Arora, G., Sandler, S.I., 2006. Air separation by single wall carbon nanotubes: mass transport and kinetic selectivity. Journal of Chemical Physics 124, 084702.
Ash, R., Barrer, R.M., 1967. Mechanisms of surface flow. Surface Science 8, 461–466.
Bell, A.T., Maginn, E.J., Theodorou, D.N., 1997. Molecular simulation of adsorption and diffusion in zeolites. In: Ertl, G., Knözinger, H., Weitkamp, J. (Eds.), Handbook of Heterogeneous Catalysis, vol. 3. VCH, Weinheim, pp. 1165–1188.
Benes, N., Verweij, H., 1999. Comparison of macro- and microscopic theories describing multicomponent mass transport in microporous media. Langmuir 15, 8292–9299.
Chempath, S., Krishna, R., Snurr, R.Q., 2004. Nonequilibrium MD simulations of diffusion of binary mixtures containing short *n*-alkanes in faujasite. Journal of Physical Chemistry B 108, 13481–13491.
Chen, H., Sholl, D.S., 2007. Examining the accuracy of ideal adsorbed solution theory without curve-fitting using transition matrix Monte Carlo simulations. Langmuir 23, 6431–6437.
Chen, H.B., Sholl, D.S., 2004. Rapid diffusion of CH_4/H_2 mixtures in single-walk carbon nanotubes. Journal of The American Chemical Society 126, 7778–7779.
Chen, H.B., Sholl, D.S., 2006. Predictions of selectivity and flux for CH_4/H_2 separations using single walled carbon nanotubes as membranes. Journal of Membrane Science 269, 152–160.
Chen, Y.D., Yang, R.T., Uawithya, P., 1994. Diffusion of oxygen nitrogen and their mixtures in carbon molecular-sieve. American Institute of Chemical Engineers Journal 40, 577–585.
Chmelik, C., Heinke, L., Kärger, J., Shah, D.B., Schmidt, W., van Baten, J.M., Krishna, R., 2008. Inflection in the loading dependence of the Maxwell–Stefan diffusivity of iso-butane in MFI zeolite. Chemical Physics Letters, submitted for publication.
Dubbeldam, D., Snurr, R.Q., 2007. Recent developments in the molecular modeling of diffusion in nanoporous materials. Molecular Simulation 33, 15–30.
Düren, T., Snurr, R.Q., 2004. Assessment of isoreticular metal–organic frameworks for adsorption separations: a molecular simulation study of methane/*n*-butane mixtures. Journal of Physical Chemistry B 108, 15703–15708.
García-Pérez, E., Parra, J.B., Ania, C.O., García-Sánchez, A., van Baten, J.M., Krishna, R., Dubbeldam, D., Calero, S., 2007. A computational study of CO_2, N_2 and CH_4 adsorption in zeolites. Adsorption-Journal of the International Adsorption Society 13, 469–476.
Habgood, H.W., 1958. The kinetics of molecular sieve action. Sorption of nitrogen-methane mixtures by Linde molecular sieve 4A. Canadian Journal of Chemistry 36, 1384–1397.
Himeno, S., Tomita, T., Suzuki, K., Nakayama, K., Yoshida, S., 2007. Synthesis and permeation properties of a DDR-type zeolite membrane for separation of CO_2/CH_4 gaseous mixtures. Industrial & Engineering Chemistry Research 46, 6989–6997.
Jobic, H., Laloué, C., Laroche, C., van Baten, J.M., Krishna, R., 2006. Influence of isotherm inflection on the loading dependence of the diffusivities of *n*-hexane and *n*-heptane in MFI zeolite. Quasi-elastic neutron scattering experiments supplemented by molecular simulations. Journal of Physical Chemistry B 110, 2195–2201.
Jobic, H., Theodorou, D.N., 2006. Quasi-elastic neutron scattering and molecular dynamics simulation as complementary techniques for studying diffusion in zeolites. Microporous and Mesoporous Materials 102, 21–50.
Kärger, J., Ruthven, D.M., 1992. Diffusion in Zeolites and Other Microporous Solids. Wiley, New York.
Kärger, J., Vasenkov, S., Auerbach, S.M., 2003. Diffusion in zeolites. In: Auerbach, S.M., Carrado, K.A., Dutta, P.K. (Eds.), Handbook of Zeolite Science and Technology. Marcel Dekker, New York, pp. 341–422 (Chapter 10).
Keil, F.J., Krishna, R., Coppens, M.O., 2000. Modeling of diffusion in zeolites. Reviews in Chemical Engineering 16, 71–197.
Keskin, S., Sholl, D.S., 2007. Screening metal–organic framework materials for membrane-based methane/carbon dioxide separations. Journal of Physical Chemistry C 111, 14055–14059.
Krishna, R., 1990. Multicomponent surface diffusion of adsorbed species—a description based on the generalized Maxwell–Stefan equations. Chemical Engineering Science 45, 1779–1791.
Krishna, R., Baur, R., 2003. Modelling issues in zeolite based separation processes. Separation and Purification Technology 33, 213–254.
Krishna, R., Paschek, D., 2000. Separation of hydrocarbon mixtures using zeolite membranes: a modelling approach combining molecular simulations with the Maxwell–Stefan theory. Separation and Purification Technology 21, 111–136.
Krishna, R., Paschek, D., 2001. Molecular simulations of adsorption and siting of light alkanes in silicalite-1. Physical Chemistry Chemical Physics 3, 453–462.
Krishna, R., Paschek, D., 2002. Self-diffusivities in multicomponent mixtures in zeolites. Physical Chemistry Chemical Physics 4, 1891–1898.
Krishna, R., van Baten, J.M., 2005. Diffusion of alkane mixtures in zeolites. Validating the Maxwell–Stefan formulation using MD simulations. Journal of Physical Chemistry B 109, 6386–6396.
Krishna, R., van Baten, J.M., 2006. Describing binary mixture diffusion in carbon nanotubes with the Maxwell–Stefan equations. An investigation using molecular dynamics simulations. Industrial & Engineering Chemistry Research 45, 2084–2093.
Krishna, R., van Baten, J.M., 2007a. Using molecular simulations for screening of zeolites for separation of CO_2/CH_4 mixtures. Chemical Engineering Journal 133, 121–131.
Krishna, R., van Baten, J.M., 2007b. Influence of segregated adsorption on mixture diffusion in DDR zeolite. Chemical Physics Letters 446, 344–349.
Krishna, R., van Baten, J.M., 2008a. Diffusion of hydrocarbon mixtures in MFI zeolite: influence of intersection blocking. Chemical Engineering Journal ⟨http://dx.doi.org/10.1016/j.cej.2007.11.026⟩.
Krishna, R., van Baten, J.M., 2008b. Insights into diffusion of gases in zeolites gained from molecular dynamics simulations. Microporous and Mesoporous Materials 109, 91–108.
Krishna, R., van Baten, J.M., 2008c. Segregation effects in adsorption of CO_2 containing mixtures and their consequences for separation selectivities in cage-type zeolites. Separation and Purification Technology ⟨http://dx.doi.org/10.1016/j.seppur.2007.12.003⟩.
Krishna, R., van Baten, J.M., García-Pérez, E., Calero, S., 2007. Incorporating the loading dependence of the Maxwell–Stefan diffusivity in the modeling of CH_4 and CO_2 permeation across zeolite membranes. Industrial & Engineering Chemistry Research 46, 2974–2986.
Krishna, R., Li, S., van Baten, J.M., Falconer, J.L., Noble, R.D., 2008. Investigation of slowing-down and speeding-up effects in binary mixture permeation across SAPO-34 and MFI membranes. Separation and Purification Technology 60, 230–236.
Kuznicki, S.M., Bell, V.A., Nair, S., Hillhouse, H.W., Jacubinas, R.M., Braunbarth, C.M., Toby, B.H., Tsapatsis, M., 2001. A titanosilicate molecular sieve with adjustable pores for size-selective adsorption of molecules. Nature 412, 720–724.
Li, S., Falconer, J.L., Noble, R.D., Krishna, R., 2007a. Modeling permeation of CO_2/CH_4, CO_2/N_2, and N_2/CH_4 mixtures across SAPO-34 membrane with the Maxwell–Stefan equations. Industrial & Engineering Chemistry Research 46, 3904–3911.
Li, S., Falconer, J.L., Noble, R.D., Krishna, R., 2007b. Interpreting unary, binary and ternary mixture permeation across a SAPO-34 membrane with loading-dependent Maxwell–Stefan diffusivities. Journal of Physical Chemistry C 111, 5075–5082.
Marathe, R.P., Mantri, K., Srinivasan, M.P., Farooq, S., 2004. Effect of ion exchange and dehydration temperature on the adsorption and diffusion of gases in ETS-4. Industrial & Engineering Chemistry Research 43, 5281–5290.
Murthi, M., Snurr, R.Q., 2004. Effects of molecular siting and adsorbent heterogeneity on the ideality of adsorption equilibria. Langmuir 20, 2489–2497.
Myers, A.L., Prausnitz, J.M., 1965. Thermodynamics of mixed gas adsorption. American Institute of Chemical Engineers Journal 11, 121–130.
Ohta, Y., Takaba, H., Nakao, S., 2007. A combinatorial dynamic Monte Carlo approach to finding a suitable zeolite membrane structure for CO_2/N_2 separation. Microporous and Mesoporous Materials 101, 319–323.
Reed, D.A., Ehrlich, G., 1981. Surface diffusion, atomic jump rates and thermodynamics. Surface Science 102, 588–609.
Sanborn, M.J., Snurr, R.Q., 2000. Diffusion of binary mixtures of CF_4 and *n*-alkanes in faujasite. Separation and Purification Technology 20, 1–13.
Sanborn, M.J., Snurr, R.Q., 2001. Predicting membrane flux of CH_4 and CF_4 mixtures in faujasite from molecular simulations. American Institute of Chemical Engineers Journal 47, 2032–2041.
Sholl, D.S., 2006. Understanding macroscopic diffusion of adsorbed molecules in crystalline nanoporous materials via atomistic simulations. Accounts of Chemical Research 39, 403–411.
Skoulidas, A.I., Sholl, D.S., 2003. Molecular dynamics simulations of self, corrected, and transport diffusivities of light gases in four silica zeolites to assess influences of pore shape and connectivity. Journal of Physical Chemistry A 107, 10132–10141.

Skoulidas, A.I., Bowen, T.C., Doelling, C.M., Falconer, J.L., Noble, R.D., Sholl, D.S., 2003a. Comparing atomistic simulations and experimental measurements for CH_4/CF_4 mixture permeation through silicalite membranes. Journal of Membrane Science 227, 123–136.

Skoulidas, A.I., Sholl, D.S., Krishna, R., 2003b. Correlation effects in diffusion of CH_4/CF_4 mixtures in MFI zeolite. A study linking MD simulations with the Maxwell–Stefan formulation. Langmuir 19, 7977–7988.

Snurr, R.Q., Hupp, J.T., Nguyen, S.T., 2004. Prospects for nanoporous metal–organic materials in advanced separations processes. American Institute of Chemical Engineers Journal 50, 1090–1095.

Sundaram, N., Yang, R.T., 2000. Binary diffusion of unequal sized molecules in zeolites. Chemical Engineering Science 55, 1747–1754.

Taylor, R., Krishna, R., 1993. Multicomponent Mass Transfer. John Wiley, New York.

Theodorou, D.N., Snurr, R.Q., Bell, A.T., 1996. Molecular dynamics and diffusion in microporous materials. In: Alberti, G., Bein, T. (Eds.), Comprehensive Supramolecular Chemistry, vol. 7. Pergamon Press, Oxford, pp. 507–548.

van Baten, J.M., Krishna, R., 2008. MD Animations of Diffusion in Nanoporous Materials. University of Amsterdam, Amsterdam. ⟨http://www.science.uva.nl/research/cr/animateMD/⟩ (3 February 2008).

van den Bergh, J., Zhu, W., Groen, J.C., Kapteijn, F., Moulijn, J.A., Yajima, K., Nakayama, K., Tomita, T., Yoshida, S., 2007. Natural gas purification with a DDR zeolite membrane; permeation modelling with Maxwell–Stefan equations. Studies in Surface Science and Catalysis 170, 1021–1027.

van den Bergh, J., Zhu, W., Kapteijn, F., Gascon, J., Moulijn, J. A., 2008. Separation and permeation characteristics of a DD3R zeolite membrane. Journal of Membrane Science ⟨http://dx.doi.org/10.1016/j.memsci.2007.12.051⟩.

Wang, Y., LeVan, M.D., 2007. Mixture diffusion in nanoporous adsorbents: development of Fickian flux relationship and concentration-swing frequency response method. Industrial & Engineering Chemistry Research 46, 2141–2154.

Yang, R.T., Chen, Y.D., Yeh, Y.T., 1991. Prediction of cross-term coefficients in binary diffusion: diffusion in zeolite. Chemical Engineering Science 46, 3089–3099.

Supplementary Material to accompany:

Onsager coefficients for binary mixture diffusion in nanopores

R. Krishna*, J.M. van Baten

Van 't Hoff Institute for Molecular Sciences, University of Amsterdam, Nieuwe Achtergracht 166,

1018 WV Amsterdam, The Netherlands

Appendix A1. Inter-relationships between Onsager and Maxwell-Stefan formulations; step-by-step procedure for estimation of Onsager coefficients; backing-out $Đ_i$, and $Đ_{ij}$ from Δ_{ij}.

Appendix A2. Molecular simulation methodology for zeolites, ETS-4, IRMOF-1, and CuBTC; pure component fits for $Đ_i$, and $Đ_{ii}$.

Appendix A3. GCMC and MD simulation results (pure component isotherms; $D_{i,self}$, $Đ_i$, $q_{i,sat}$, $Đ_{ii}$) in different zeolites, ETS-4, IRMOF-1, and CuBTC.

Appendix A4. MD simulations results ($D_{i,self}$, Δ_{ij}, L_{ij}, and α_{ij}) for mixture diffusion in zeolites, ETS-4, IRMOF-1, and CuBTC.

Appendix A5. GCMC and MD simulation results (pure component isotherms; $Đ_i$, $q_{i,sat}$, Δ_{ij}) for CNTs.

Appendix A1: Inter-relationship between Onsager and Maxwell-Stefan formulations; Estimations; Backing-out of M-S $Đ_i$ and $Đ_{ij}$

1. Onsager vs M-S

The Onsager theory of irreversible thermodynamics provides the fundamental basis for mixture diffusion[1-7]; for *n*-component mixtures, for example, the flux of any component is related to the chemical potential gradients by

$$N_i = -\rho \frac{1}{RT} \sum_{j=1}^{n} L_{ij} \frac{d\mu_j}{dx}; \quad i = 1,2...n \tag{1}$$

where L_{ij} are the Onsager coefficients. The Onsager reciprocal relations are

$$L_{ij} = L_{ji} \tag{2}$$

For unary systems, $n = 1$, eq (1) simplifies to

$$N_i = -\rho L_i \frac{1}{RT} \frac{d\mu_i}{dx} \tag{3}$$

By introducing the thermodynamic factor Γ_i

$$\frac{q_i}{RT} \frac{d\mu_i}{dx} = \Gamma_i \frac{dq_i}{dx}; \quad \Gamma_i \equiv \frac{\partial \ln f_i}{\partial \ln q_j} = \frac{q_i}{f_i} \frac{\partial f_i}{\partial q_i}; \quad \text{unary system} \tag{4}$$

we may re-write eq (3) for a unary system as

$$N_i = -\rho L_i \frac{1}{q_i} \Gamma_i \frac{dq_i}{dx} \tag{5}$$

For unary diffusion the Fick diffusivity, D_i, and the Maxwell-Stefan (M-S) or "corrected" diffusivity, $Đ_i$, are defined by

$$N_i = -\rho D_i \frac{dq_i}{dx} = -\rho \frac{q_i}{RT} Đ_i \frac{d\mu_i}{dx} \tag{6}$$

and the Onsager coefficient may be related to the Fick and M-S diffusivities

$$L_i = q_i Đ_i = q_i D_i / \Gamma_i \tag{7}$$

In the M-S formulation [8] the chemical potential gradients are related to the fluxes in an inverse manner

$$-\rho \frac{\theta_i}{RT} \frac{d\mu_i}{dx} = \sum_{\substack{j=1 \\ j \neq i}}^{n} \frac{q_j N_i - q_i N_j}{q_{i,sat} q_{j,sat} Đ_{ij}} + \frac{N_i}{q_{i,sat} Đ_i}; \quad i = 1,2,..n \tag{8}$$

where θ_i are the fractional occupancies

$$\theta_i \equiv q_i / q_{i,sat} \quad i = 1,2,...n \tag{9}$$

and $q_{i,sat}$ represents the saturation capacity of species *i*.

Equation (8) *defines* two types of M-S diffusivities: $Đ_i$ and $Đ_{ij}$. The binary exchange coefficients $Đ_{ij}$ reflect *correlation* effects in mixture diffusion[6-8]. For mixture diffusion the $Đ_{ij}$ tends to slow down the more mobile species and speed up the relatively sluggish ones. A lower value of the exchange coefficient $Đ_{ij}$ implies *stronger* correlation effects. When $Đ_{ij} \to \infty$, correlation effects vanish; the first member on the right of eq (8) is absent.

Conformity with the Onsager Reciprocal Relations (2) demands that

$$q_{j,sat} Đ_{ij} = q_{i,sat} Đ_{ji} \tag{10}$$

Equation (8) can be cast into *n*-dimensional matrix notation

$$-\rho \begin{bmatrix} q_1 & 0 & 0 & 0 & 0 \\ 0 & q_2 & 0 & 0 & 0 \\ 0 & 0 & \ddots & 0 & 0 \\ 0 & 0 & 0 & \ddots & 0 \\ 0 & 0 & 0 & 0 & q_n \end{bmatrix} \frac{1}{RT} \frac{d(\mu)}{dx} = [B](N) \tag{11}$$

by defining an n-dimensional square matrix $[B]$ with elements

$$B_{ii} = \frac{1}{Đ_i} + \sum_{\substack{j=1 \\ j \neq i}}^{n} \frac{\theta_j}{Đ_{ij}}; \quad B_{ij} = -\frac{q_{i,sat}}{q_{j,sat}} \frac{\theta_i}{Đ_{ij}}; \quad i, j = 1,2....n \tag{12}$$

We denote the inverse of $[B]$ as $[\Delta]$:

$$[B]^{-1} \equiv [\Delta] \tag{13}$$

Comparing equations (1), (11), and (13) we find that $[\Delta]$ is simply related to the Onsager matrix $[L]$

$$[\Delta] \begin{bmatrix} q_1 & 0 & 0 & 0 & 0 \\ 0 & q_2 & 0 & 0 & 0 \\ 0 & 0 & \ddots & 0 & 0 \\ 0 & 0 & 0 & \ddots & 0 \\ 0 & 0 & 0 & 0 & q_n \end{bmatrix} = [L] \tag{14}$$

The elements Δ_{ij} can be determined from MD simulations in each of the three coordinate directions using the formula

$$\Delta_{ij} = \frac{1}{2} \lim_{\Delta t \to \infty} \frac{1}{n_j} \frac{1}{\Delta t} \left\langle \left(\sum_{l=1}^{n_i} \left(\mathbf{r}_{l,i}(t + \Delta t) - \mathbf{r}_{l,i}(t) \right) \right) \bullet \left(\sum_{k=1}^{n_j} \left(\mathbf{r}_{k,j}(t + \Delta t) - \mathbf{r}_{k,j}(t) \right) \right) \right\rangle \tag{15}$$

In this expression n_i and n_j represent the number of molecules of species i and j respectively, and $\mathbf{r}_{l,i}(t)$ is the position of molecule l of species i at any time t. For unary systems eq (15) yields the M-S diffusivity $Đ_i$. The MD simulation strategy is discussed in Appendix A2.

The Onsager reciprocal relations (2) translate to

$$\Delta_{ij} q_j = \Delta_{ji} q_i \tag{16}$$

For binary mixtures, i.e. $n = 2$, the relation between the Onsager matrix $[L]$ and the M-S matrix $[\Delta]$ is

$$\begin{bmatrix} L_{11} & L_{12} \\ L_{21} & L_{22} \end{bmatrix} = \begin{bmatrix} \Delta_{11} q_1 & \Delta_{12} q_2 \\ \Delta_{21} q_1 & \Delta_{22} q_2 \end{bmatrix} \tag{17}$$

For $n = 2$, t the inversion in eq (13) can be carried out explicitly to yield the following expressions that were also published in our earlier papers [8, 9]

$$\Delta_{11} = \frac{Đ_1}{\dfrac{\dfrac{\theta_2 Đ_1}{Đ_{12}}}{1+\dfrac{\theta_1 Đ_2}{Đ_{21}}}} = \frac{Đ_1\left(1+\dfrac{\theta_1 Đ_2}{Đ_{21}}\right)}{1+\dfrac{\theta_1 Đ_2}{Đ_{21}}+\dfrac{\theta_2 Đ_1}{Đ_{12}}} \tag{18}$$

$$\Delta_{22} = \frac{Đ_2}{\dfrac{\dfrac{\theta_1 Đ_2}{Đ_{21}}}{1+\dfrac{\theta_2 Đ_1}{Đ_{12}}}} = \frac{Đ_2\left(1+\dfrac{\theta_2 Đ_1}{Đ_{12}}\right)}{1+\dfrac{\theta_2 Đ_1}{Đ_{12}}+\dfrac{\theta_1 Đ_2}{Đ_{21}}} \tag{19}$$

$$\Delta_{12} = \frac{Đ_1 \dfrac{\theta_1 Đ_2}{Đ_{21}}}{1+\dfrac{\theta_1 Đ_2}{Đ_{21}}+\dfrac{\theta_2 Đ_1}{Đ_{12}}} \tag{20}$$

$$\Delta_{21} = \frac{q_2}{q_1}\Delta_{12} = \frac{Đ_2 \dfrac{\theta_2 Đ_1}{Đ_{12}}}{1+\dfrac{\theta_1 Đ_2}{Đ_{21}}+\dfrac{\theta_2 Đ_1}{Đ_{12}}} \tag{21}$$

We define the ratios

$$\alpha_{11} = \frac{L_{11}}{L_1} = \frac{\Delta_{11}}{Đ_1}; \qquad \alpha_{22} = \frac{L_{22}}{L_2} = \frac{\Delta_{22}}{Đ_2}; \quad \alpha_{12} = \frac{L_{12}}{\sqrt{L_{11}L_{22}}} = \sqrt{\frac{q_2}{q_1}}\,\frac{\Delta_{12}}{\sqrt{\Delta_{11}\Delta_{22}}} \tag{22}$$

From eqs (18), (19), (20), and (21) we obtain

$$\alpha_{11} = \frac{\left(1+\frac{\theta_1 Đ_2}{Đ_{21}}\right)}{1+\frac{\theta_1 Đ_2}{Đ_{21}}+\frac{\theta_2 Đ_1}{Đ_{12}}} \tag{23}$$

$$\alpha_{22} = \frac{\left(1+\frac{\theta_2 Đ_1}{Đ_{12}}\right)}{1+\frac{\theta_2 Đ_1}{Đ_{12}}+\frac{\theta_1 Đ_2}{Đ_{21}}} \tag{24}$$

$$\alpha_{12} = \sqrt{\frac{\left(\frac{\theta_1 Đ_2}{Đ_{21}}\right)\left(\frac{\theta_2 Đ_1}{Đ_{12}}\right)}{\left(1+\frac{\theta_1 Đ_2}{Đ_{21}}\right)\left(1+\frac{\theta_2 Đ_1}{Đ_{12}}\right)}} \tag{25}$$

2. Scenario in which correlations are negligible

In the limiting scenario in which correlations effects are of negligible importance:

$$\frac{\theta_i Đ_j}{Đ_{ji}} \to 0; \quad \text{correlations negligible} \tag{26}$$

we obtain

$$\Delta_{11} = Đ_1; \quad \Delta_{22} = Đ_2 \quad \Delta_{12} = \Delta_{21} = 0; \quad \text{correlations negligible} \tag{27}$$

and

$$\alpha_{11} = 1; \quad \alpha_{22} = 1 \quad \alpha_{12} = 0; \quad \text{correlations negligible} \tag{28}$$

3. Scenario in which correlations are dominant

For the case in which correlation effects are dominant

$$\frac{\theta_i Đ_j}{Đ_{ji}} >> 1; \quad \text{correlations dominant} \tag{29}$$

we get

$$\Delta_{11} = \frac{Đ_1}{1 + \dfrac{\dfrac{\theta_2 Đ_1}{Đ_{12}}}{1 + \dfrac{\theta_1 Đ_2}{Đ_{21}}}} \to \frac{Đ_1}{1 + \dfrac{\dfrac{\theta_2 Đ_1}{Đ_{12}}}{\dfrac{\theta_1 Đ_2}{Đ_{21}}}} = \frac{Đ_1}{1 + \dfrac{\theta_2}{\theta_1}\dfrac{Đ_1}{Đ_2}\dfrac{Đ_{21}}{Đ_{12}}}; \quad \text{correlations dominant} \tag{30}$$

$$\Delta_{22} = \frac{Đ_2}{1 + \dfrac{\dfrac{\theta_1 Đ_2}{Đ_{21}}}{1 + \dfrac{\theta_2 Đ_1}{Đ_{12}}}} \to \frac{Đ_2}{1 + \dfrac{\dfrac{\theta_1 Đ_2}{Đ_{21}}}{\dfrac{\theta_2 Đ_1}{Đ_{12}}}} = \frac{Đ_2}{1 + \dfrac{\theta_1}{\theta_2}\dfrac{Đ_2}{Đ_1}\dfrac{Đ_{12}}{Đ_{21}}}; \quad \text{correlations dominant} \tag{31}$$

$$\Delta_{12} = \frac{Đ_1\left(\dfrac{\theta_1 Đ_2}{Đ_{21}}\right)}{1 + \dfrac{\theta_1 Đ_2}{Đ_{21}} + \dfrac{\theta_2 Đ_1}{Đ_{12}}} \to \frac{Đ_1\left(\dfrac{\theta_1 Đ_2}{Đ_{21}}\right)}{\dfrac{\theta_1 Đ_2}{Đ_{21}} + \dfrac{\theta_2 Đ_1}{Đ_{12}}} = \frac{Đ_1}{1 + \dfrac{\theta_2}{\theta_1}\dfrac{Đ_1}{Đ_2}\dfrac{Đ_{21}}{Đ_{12}}} = \Delta_{11}; \quad \text{correlations dominant} \tag{32}$$

$$\Delta_{21} = 1 + \frac{\theta_1 Đ_2}{Đ_{21}} + \frac{\theta_2 Đ_1}{Đ_{12}} \to \frac{Đ_2\dfrac{\theta_2 Đ_1}{Đ_{12}}}{\dfrac{\theta_1 Đ_2}{Đ_{21}} + \dfrac{\theta_2 Đ_1}{Đ_{12}}} = \frac{Đ_2}{1 + \dfrac{\theta_1}{\theta_2}\dfrac{Đ_2}{Đ_1}\dfrac{Đ_{12}}{Đ_{21}}} = \Delta_{22}; \quad \text{correlations dominant} \tag{33}$$

In the denominators in the extreme right members of eqs (30) and (31) we introduce equation (10), i.e.

$$q_{2,sat} Đ_{12} = q_{1,sat} Đ_{21}; \quad \frac{Đ_{21}}{Đ_{12}} = \frac{q_{2,sat}}{q_{1,sat}}; \quad \frac{Đ_{12}}{Đ_{21}} = \frac{q_{1,sat}}{q_{2,sat}} \tag{34}$$

along with

$$\theta_1 = \frac{q_1}{q_{1,sat}}; \quad \theta_2 = \frac{q_2}{q_{2,sat}} \tag{35}$$

to obtain

$$\Delta_{11} = \frac{Đ_1}{1 + \frac{q_2}{q_1}\frac{Đ_1}{Đ_2}} = \Delta_{12}; \quad \text{correlations dominant} \tag{36}$$

$$\Delta_{22} = \frac{Đ_2}{1 + \frac{q_1}{q_2}\frac{Đ_2}{Đ_1}} = \Delta_{21}; \quad \text{correlations dominant} \tag{37}$$

It is interesting to note that

The elements of the Onsager matrix [L] can be obtained from the M-S matrix [Δ] using eq. (17):

$$L_{11} = \Delta_{11} q_1 = \frac{q_1^2}{\frac{q_1}{Đ_1} + \frac{q_2}{Đ_2}}; \quad \text{correlations dominant} \tag{38}$$

$$L_{22} = \Delta_{22} q_2 = \frac{q_2^2}{\frac{q_1}{Đ_1} + \frac{q_2}{Đ_2}}; \quad \text{correlations dominant} \tag{39}$$

$$L_{12} = \Delta_{12} q_2 = \frac{q_1 q_2}{\frac{q_1}{Đ_1} + \frac{q_2}{Đ_2}}; \quad \text{correlations dominant} \tag{40}$$

The ratios α_{ii} are

$$\alpha_{11} = \frac{1}{1 + \frac{q_2}{q_1}\frac{Đ_1}{Đ_2}}; \quad \text{correlations dominant} \tag{41}$$

$$\alpha_{22} = \frac{1}{1 + \frac{q_1}{q_2}\frac{Đ_2}{Đ_1}}; \quad \text{correlations dominant} \tag{42}$$

$$\alpha_{12} = 1; \quad \text{correlations dominant} \tag{43}$$

4. Scenario in which species 1 and 2 are identical

Let us consider a scenario in which the M-S diffusivities of component 2 is identical to that of component 1.

$$Đ_2 = Đ_1; \quad \text{identical species} \tag{44}$$

From eqs (18), (19), and (20) we obtain

$$\Delta_{11} = \frac{Đ_1\left(1+\frac{\theta_1 Đ_1}{Đ_{11}}\right)}{1+\frac{(\theta_1+\theta_2)Đ_1}{Đ_{11}}}; \quad \text{identical species} \tag{45}$$

$$\Delta_{22} = \frac{Đ_1\left(1+\frac{\theta_2 Đ_1}{Đ_{11}}\right)}{1+\frac{(\theta_1+\theta_2)Đ_1}{Đ_{11}}}; \quad \text{identical species} \tag{46}$$

$$\Delta_{12} = \frac{\left(\frac{\theta_1 Đ_1^2}{Đ_{11}}\right)}{1+\frac{(\theta_1+\theta_2)Đ_1}{Đ_{11}}}; \quad \Delta_{21} = \Delta_{12}\frac{q_2}{q_1}; \quad \text{identical species} \tag{47}$$

The corresponding α_{ii} ratios are

$$\alpha_{11} = \frac{\left(1+\frac{\theta_1 Đ_1}{Đ_{11}}\right)}{1+\frac{(\theta_1+\theta_2)Đ_1}{Đ_{11}}}; \quad \text{identical species} \tag{48}$$

$$\alpha_{22} = \frac{\left(1+\frac{\theta_2 Đ_1}{Đ_{11}}\right)}{1+\frac{(\theta_1+\theta_2)Đ_1}{Đ_{11}}}; \quad \text{identical species} \tag{49}$$

$$\alpha_{12} = \sqrt{\frac{\frac{\theta_1 Đ_1}{Đ_{11}}\frac{\theta_2 Đ_1}{Đ_{11}}}{\left(1+\frac{\theta_1 Đ_1}{Đ_{11}}\right)\left(1+\frac{\theta_2 Đ_1}{Đ_{11}}\right)}}; \quad \text{identical species} \tag{50}$$

Further simplification arises for equimolar mixtures, $q_1 = q_2$; $\theta_1 = \theta_2$;

$$\alpha_{11} = \alpha_{22} = \frac{\left(1+\frac{\theta_1 Đ_1}{Đ_{11}}\right)}{1+\frac{2\theta_1 Đ_1}{Đ_{11}}}; \quad \text{identical species, equimolar} \tag{51}$$

$$\alpha_{12} = \frac{\frac{\theta_1 Đ_1}{Đ_{11}}}{\left(1+\frac{\theta_1 Đ_1}{Đ_{11}}\right)}; \quad \text{identical species, equimolar} \tag{52}$$

5. Estimation of [Δ] from pure component diffusion data

We summarize below the step-by-step procedure we had developed earlier [8] for estimation of the M-S matrix [Δ] and Onsager matrix [L] from pure component diffusion data.

Step 1. The dependence of the pure component M-S diffusivities $Đ_i$ are described using the Reed and Ehrlich model:

$$Đ_i = Đ_i(0)\frac{(1+\varepsilon_i)^{z-1}}{(1+\varepsilon_i/\phi_i)^z}; \varepsilon_i = \frac{(\beta_i - 1 + 2\theta_i)\phi_i}{2(1-\theta_i)}; \quad \beta_i = \sqrt{1-4\,\theta_i(1-\theta_i)(1-1/\phi_i)} \tag{53}$$

The values of the coordination number z and fitted expression for ϕ_i (fitted to MD simulated data for pure component diffusion) are given in Appendix 2, Table 1 for various molecules-zeolites, and in Appendix 5, Table 4, for various molecules-CNT.

Step 2. The self-exchange coefficients $Đ_{ii}$ are obtained from MD simulations of pure component coefficients $D_{i,self}$ and $Đ_i$. The occupancy dependence of $Đ_{ii}$ are fitted using the empirical expression

$$\frac{Đ_{ii}}{Đ_i} = a_i \exp(-b_i \theta_i) \tag{54}$$

The fitted values of a_i and b_i for various guest molecules in a variety of zeolites are given in Table 2 of Appendix 2 for various guest molecules in different zeolites.

Step 3. For a binary mixture with component loadings q_1 and q_2, we estimate the binary exchange coefficients $Đ_{12}$, and $Đ_{21}$ using the interpolation formula suggested earlier[6, 10]

$$q_{2,sat} Đ_{12} = \left[q_{2,sat} Đ_{11}\right]^{q_1/(q_1+q_2)} \left[q_{1,sat} Đ_{22}\right]^{q_2/(q_1+q_2)} = q_{1,sat} Đ_{21} \tag{55}$$

Though the interpolation formula has been validated for a variety of mixtures in several different zeolites [6-8, 10], it must be emphasized that eq (55) is to be regarded "empirical" and is not an integral part of the M-S theory. In applying eq (55) it is to be noted that the self-exchange coefficients $Đ_{11}$, and $Đ_{22}$ are calculated using eq (54) using the occupancy of the total mixture, θ, defined by

$$\theta = \theta_1 + \theta_2 = \frac{q_1}{q_{1,sat}} + \frac{q_2}{q_{2,sat}} \tag{56}$$

Step 4. The M-S diffusivities $Đ_i$ in the mixture are assumed to be the same as the pure component diffusivities, estimated from eq (53) evaluated at the occupancy of the total mixture, given by eq. (56).

Step 5. The elements Δ_{ij} are calculated from eqs (18), (19), (20) and (21) in the general case. For the limiting case of negligible correlations, eq (27) is used. For the correlation-dominant scenario, eqs (43), (41), and (42) are used.

Step 6. The elements of the Onsager matrix [L] are calculated from eq (17).

6. Backing out $Đ_i$ and $Đ_{ij}$ from simulated [Δ] data

In order to test the assumption that whether the M-S diffusivity $Đ_i$ is the same as the value for pure component, at occupancy of the total mixture, θ, we derive formulae for extracting $Đ_1$, $Đ_2$, from simulated values of the M-S matrix [Δ]. From eqs (18) and (20) we derive

$$\frac{\Delta_{11}}{\Delta_{12}} = \frac{\left(1+\frac{\theta_1 Đ_2}{Đ_{21}}\right)}{\frac{\theta_1 Đ_2}{Đ_{21}}}; \quad \frac{Đ_{21}}{\theta_1 Đ_2} = \left(\frac{\Delta_{11}}{\Delta_{12}} - 1\right) \tag{57}$$

Similarly from eqs (19) and (21)

$$\frac{\Delta_{22}}{\Delta_{21}} = \frac{\left(1+\frac{\theta_2 Đ_1}{Đ_{12}}\right)}{\frac{\theta_2 Đ_1}{Đ_{12}}}; \quad \frac{Đ_{12}}{\theta_2 Đ_1} = \left(\frac{\Delta_{22}}{\Delta_{21}} - 1\right) \tag{58}$$

Introducing eqs (57) and (58) into eqs (18) and (19) and re-arranging we get

$$Đ_1 = \frac{\Delta_{11}\left(1+\frac{1}{\left(\frac{\Delta_{11}}{\Delta_{12}}-1\right)}+\frac{1}{\left(\frac{\Delta_{22}}{\Delta_{21}}-1\right)}\right)}{\left(1+\frac{1}{\left(\frac{\Delta_{11}}{\Delta_{12}}-1\right)}\right)} \tag{59}$$

and

$$Đ_2 = \frac{\Delta_{22}\left(1+\frac{1}{\left(\frac{\Delta_{11}}{\Delta_{12}}-1\right)}+\frac{1}{\left(\frac{\Delta_{22}}{\Delta_{21}}-1\right)}\right)}{\left(1+\frac{1}{\left(\frac{\Delta_{22}}{\Delta_{21}}-1\right)}\right)} \tag{60}$$

The exchange coefficients can then be explicitly determined by combining eqs (57) , (58), (59), and (60)

$$Đ_{12} = \theta_2\left(\frac{\Delta_{22}}{\Delta_{21}} - 1\right)\frac{\Delta_{11}\left(1 + \frac{1}{\left(\frac{\Delta_{11}}{\Delta_{12}} - 1\right)} + \frac{1}{\left(\frac{\Delta_{22}}{\Delta_{21}} - 1\right)}\right)}{\left(1 + \frac{1}{\left(\frac{\Delta_{11}}{\Delta_{12}} - 1\right)}\right)} \tag{61}$$

$$Đ_{21} = \theta_1\left(\frac{\Delta_{11}}{\Delta_{12}} - 1\right)\frac{\Delta_{22}\left(1 + \frac{1}{\left(\frac{\Delta_{11}}{\Delta_{12}} - 1\right)} + \frac{1}{\left(\frac{\Delta_{22}}{\Delta_{21}} - 1\right)}\right)}{\left(1 + \frac{1}{\left(\frac{\Delta_{22}}{\Delta_{21}} - 1\right)}\right)} \tag{62}$$

Equations (61) and (62) allow us to test the validity of the interpolation formula (55).

7. Expression for $Đ_{12}\, Đ_{21}$

In calculation of the interaction factor α_{12} using eq (25), we encounter the product $Đ_{12}\, Đ_{21}$ in the numerator. We derive a simple expression relating this product to the product of the self-exchange diffusivities $Đ_{11}\, Đ_{22}$ that arises by use of the interpolation formula (55). We begin by defining the mole fractions x_i

$$x_1 = \frac{q_1}{q_1 + q_2}; \quad x_2 = \frac{q_2}{q_1 + q_2} = 1 - x_1 \tag{63}$$

Invoking eq (34), (55), and (63)

$$Đ_{12}Đ_{21} = \frac{q_{2,sat}}{q_{1,sat}} Đ_{12}Đ_{12} = \left[q_{2,sat}\right]^{2x_1 - 1}\left[q_{1,sat}\right]^{2x_2 - 1}\left[Đ_{11}\right]^{2x_1}\left[Đ_{22}\right]^{2x_2} \tag{64}$$

For equimolar loadings, $x_1 = x_2 = 0.5$,we get the simple result

$$Đ_{12} Đ_{21} = Đ_{11} Đ_{22} \tag{65}$$

which is the product of the self-exchange diffusivities of the individual components.

8. Expression for the Fick diffusivity matrix

For completeness, we present relations for the Fick diffusivity matrix [D] defined by

$$(N) = -\rho[D]\frac{d(q)}{dx} \tag{66}$$

We define matrix of thermodynamic correction factors [Γ]

$$\frac{q_i}{RT}\nabla\mu_i = \sum_{j=1}^{n}\Gamma_{ij}\nabla q_j; \quad \Gamma_{ij} \equiv \frac{q_i}{q_j}\frac{\partial \ln f_i}{\partial \ln q_j} = \frac{q_i}{f_i}\frac{\partial f_i}{\partial q_j}; \quad i, j = 1,..n \tag{67}$$

where f_i represents the fugacity of component i in the bulk fluid phase. The Γ_{ij} can be calculated from knowledge of the multicomponent sorption isotherms using say the Ideal Adsorbed Solution Theory. Combining eqs (11), (13), and (67) we get

$$(N) = -\rho[\Delta][\Gamma]\frac{d(q)}{dx} \tag{68}$$

and so

$$[D] = [\Delta][\Gamma] \tag{69}$$

Other definitions of the thermodynamic factors are used in the literature [6, 10, 11].

9. Notation

a_i	constants describing self-exchange in eq (54), dimensionless
b_i	constants describing self-exchange in eq (54), dimensionless
$[B]$	matrix of inverse Maxwell-Stefan coefficients, m^{-2} s
$D_{i,self}$	self-diffusivity, m^2 s^{-1}
$Đ_i$	Maxwell-Stefan diffusivity of species *i*, m^2 s^{-1}
$Đ_i(0)$	zero-loading M-S diffusivity of species *i*, m^2 s^{-1}
$Đ_{ii}$	self-exchange diffusivity, m^2 s^{-1}
$Đ_{ij}$	binary exchange diffusivity, m^2 s^{-1}
f_i	fugacity of species *i*, Pa
L_{ij}	Onsager coefficients, mol kg^{-1} m^2 s^{-1} in zeolites; molecule nm^{-1} m^2 s^{-1} in CNT
N_i	molar flux of species *i*, mol m^{-2} s^{-1}
n_i	number of molecules of species *i* in simulation box, dimensionless
n	number of species in mixture, dimensionless
q_i	loading of species *i*, mol kg^{-1} in zeolites; molecule nm^{-1} in CNT
$q_{i,sat}$	saturation loading of species *i*, mol kg^{-1} in zeolites; molecule nm^{-1} in CNT
R	gas constant, 8.314 J mol^{-1} K^{-1}
T	absolute temperature, K
x	spatial distance, m
z	coordination number, dimensionless

Greek letters

β_i	Reed-Ehrlich parameter, dimensionless
$[\Gamma]$	matrix of thermodynamic factors, dimensionless
Γ_{ij}	thermodynamic factors, dimensionless
$[\Delta]$	matrix of Maxwell-Stefan diffusivities, m^2 s^{-1}

ε_i	Reed-Ehrlich parameter, dimensionless
ϕ_i	Reed-Ehrlich parameter, dimensionless
θ_i	fractional occupancy of component *i*, dimensionless
μ_i	molar chemical potential, J mol^{-1}
ρ	framework density of zeolite, kg m^{-3}

Subscripts

sat	referring to saturation conditions
i,j	components in mixture

Vector and Matrix Notation

( )	*n* dimensional column matrix
[ ]	$n \times n$ dimensional square matrix

10. Literature cited

[1] H.W. Habgood, The kinetics of molecular sieve action. Sorption of nitrogen-methane mixtures by Linde molecular sieve 4A, Canad. J. Chem. 36 (1958) 1384-1397.

[2] J. Kärger, D.M. Ruthven, Diffusion in zeolites and other microporous solids, John Wiley, New York, 1992.

[3] R.T. Yang, Y.D. Chen, Y.T. Yeh, Prediction of cross-term coefficients in binary diffusion: Diffusion in zeolite, Chem. Eng. Sci. 46 (1991) 3089-3099.

[4] N. Benes, H. Verweij, Comparison of Macro- and Microscopic Theories Describing Multicomponent Mass Transport in Microporous Media, Langmuir 15 (1999) 8292-9299.

[5] N. Sundaram, R.T. Yang, Binary diffusion of unequal sized molecules in zeolites, Chem. Eng. Sci. 55 (2000) 1747-1754.

[6] A.I. Skoulidas, D.S. Sholl, R. Krishna, Correlation effects in diffusion of CH_4/CF_4 mixtures in MFI zeolite. A study linking MD simulations with the Maxwell-Stefan formulation, Langmuir 19 (2003) 7977-7988.

[7] S. Chempath, R. Krishna, R.Q. Snurr, Nonequilibrium MD simulations of difusion of binary mixtures containing short n-alkanes in faujasite, J. Phys. Chem. B 108 (2004) 13481-13491.

[8] R. Krishna, J.M. van Baten, Insights into diffusion of gases in zeolites gained from molecular dynamics simulations, Microporous Mesoporous Mater. 109 (2008) 91-108.

[9] R. Krishna, S. Li, J.M. van Baten, J.L. Falconer, R.D. Noble, Investigation of slowing-down and speeding-up effects in binary mixture permeation across SAPO-34 and MFI membranes, Sep. Purif. Technol. (2008) http://dx.doi.org/10.1016/j.seppur.2007.08.012

[10] R. Krishna, J.M. van Baten, Diffusion of alkane mixtures in zeolites. Validating the Maxwell-Stefan formulation using MD simulations, J. Phys. Chem. B 109 (2005) 6386-6396.

[11] M.J. Sanborn, R.Q. Snurr, Predicting membrane flux of CH_4 and CF_4 mixtures in faujasite from molecular simulations, A.I.Ch.E.J. 47 (2001) 2032-2041.

Appendix A2: Molecular Simulation methodology for zeolites, ETS-4, IRMOF-1, and CuBTC. Pure component diffusivity data fits

Eight different zeolite structures were investigated. Table 1 gives the characteristic sizes of channels or windows for these eight zeolite structures. The pore landscapes, including snapshots of molecules in the pores are presented in Appendix A3. A few simulations were also performed for ETS-4 (pure components: C1, Ar, Ne, and mixtures: C1-Ar, and Ne-Ar), IRMOF-1 (pure components: C1, Ar, Ne and mixtures: C1-Ar, and Ne-Ar), and CuBTC (pure components: C1, Ar, Ne and mixtures: C1-Ar, and Ne-Ar). All simulations were carried out for T = 300 K. For methane (C1) diffusion in LTA, MD simulations were carried out for T = 800, 1000, 1200, 1400, 1600, and 1800 K in order to investigate the loading dependence as a function of T. All simulation data in graphical form are presented in Appendix A3 (for pure components) and Appendix A4 (for binary mixtures).

1. MC simulation methodology

The adsorption isotherms were computed using Monte Carlo (MC) simulations in the grand canonical (GC) ensemble. The crystallographic data are available elsewhere.[1] The zeolite lattices are rigid during simulations, with static atomic charges that are assigned by choosing q_{Si} = +2.05 and q_O = -1.025, following the works of Jaramillo and Auerbach [2] and Calero et al. [3]. CH_4 molecules are described with a united atom model, in which each molecule is treated as a single interaction center.[4] The interaction between adsorbed molecules is described with Coulombic and Lennard-Jones terms. The Coulombic interactions in the system are calculated by Ewald summation for periodic systems[5]. The parameters for CH_4 are taken from Dubbeldam et al[6] and Calero et al.[3]. CO_2 molecules are taken

linear and rigid with bond length C–O of 1.16Å according to the 3LJ3CB.EPM2 model developed by Harris and Young [7]. We use the 2LJ3CB.MSKM model for N_2 dumbbell molecules with a rigid interatomic bond of 1.098Å[8, 9]. The partial charges of N_2 and CO_2 are distributed around each molecule to reproduce experimental quadrupole moment. The interactions between adsorbed molecules and the zeolite are dominated by dispersive forces between the pseudo-atoms and the oxygen atoms of the zeolite [10, 11] and the interactions of silicon and aluminium are considered through an effective potential with only the oxygen atoms. The Lennard-Jones parameters for CH_4-zeolite interactions are taken from Dubbeldam et al.[6]. The Lennard-Jones parameters for CO_2-zeolite and N_2-zeolite interactions are essentially those of Makrodimitris et al.[9]; see also García-Pérez et al.[12]. The force fields for Ne and Ar are taken from the paper by Skoulidas and Sholl[13]. The force field for Kr is from Talu and Myers [14]. The force field for O_2 is taken from the work of Mellot and Lignieres[15]. The force field for H_2 corresponds to that given by Kumar et al.[16] In implementing this force field, quantum effects for H_2 have been ignored because the work of Kumar et al.[16] has shown that quantum effects are of negligible importance for temperatures above 200 K; all our simulations were performed at 300 K. The force field of Kumar et al.[16] is quite similar to that used by Gallo et al. [17].

For simulations with linear and branched alkanes with two or more C atoms, the Configurational-Bias Monte Carlo (CBMC) simulation technique was used. The beads in the chain are connected by harmonic bonding potentials. A harmonic cosine bending potential models the bond bending between three neighboring beads, a Ryckaert-Bellemans potential controls the torsion angle. The beads in a chain separated by more than three bonds interact with each other through a Lennard-Jones potential. The Lennard-Jones potentials are shifted and cut at 12 Å. The CBMC simulation details, along with the force fields have been given in detail in earlier publications[6, 18, 19].

The number of unit cells in the simulation box was chosen such that the minimum length in each of the coordinate directions was larger than 24 Å. Periodic boundary conditions were employed.

The CBMC simulations were performed using the BIGMAC code developed by T.J.H. Vlugt[20] as basis. The code was modified to handle rigid molecular structures and charges. Detailed validation of the force fields used for various molecules is available elsewhere[6, 12, 21-25].

The pure component isotherm data for all molecule-zeolite combinations relevant to our work are summarized in Appendix A3 in graphical form. The isotherm data was used to estimate the saturation capacities required for interpretation of the diffusion data discussed below. The saturation capacity values are reported in Table 5.

Additionally a few GCMC simulations for adsorption of C1, Ar, and Ne were also carried out for ETS-4 using the structural data published by Kuznicki et al. [26]. In our simulations the published lattice parameters for a structure that was dehydrated at a temperature of 423 K, was used. Just as for zeolites, the interactions of molecules with ETS-4 are assumed to be dominated by dispersive forces between the pseudo-atoms and the oxygen atoms of the zeolite. The force fields used was exactly the same as for zeolites. In order to validate this approach, adsorption isotherms of C1 and Ar are compared with the experimental data of Marathe et al.[27] and of Pillai et al.[28]. As can be witnessed by the data given in Appendix A3, the agreement is good in both cases.

For IRMOF-1 simulations we used the structural data, and the force field information published by Dubbeldam et al. [29, 30]. For CuBTC simulations we used the structural data, and the force field information published by Yang and Zhong [31]; the force field information has been supplemented with Ar parameters of Vishnyakov et al. [32]. For both MOFs the intermolecular force field for Ne was taken from Skoulidas and Sholl[13] and Lorentz-Berthelot mixing rules were applied for calculating σ and ε/k_B.

2. MD simulation methodology

Diffusion is simulated using Newton's equations of motion until the system properties, on average, no longer change in time. The Verlet algorithm is used for time integration. A time step of 1 fs was used in all simulations. For each simulation, *initializing* CBMC moves are used to place the molecules in the

domain, minimizing the energy. Next, follows an *equilibration* stage. These are essentially the same as the production cycles, only the statistics are not yet taken into account. This removes any initial large disturbances in the system do not affect statistics. After a fixed number of initialization and equilibrium steps, the MD simulation *production* cycles start. For every cycle, the statistics for determining the mean square displacements (MSDs) are updated. The MSDs are determined for time intervals ranging from 2 fs to 1 ns. In order to do this, an order-*N* algorithm, as detailed in Chapter 4 of Frenkel and Smit[5] is implemented. The Nosé-Hoover thermostat is applied to all the diffusing particles.

The DLPOLY code[33] was used along with the force field implementation as described in the previous section. DL_POLY is a molecular dynamics simulation package written by W. Smith, T.R. Forester and I.T. Todorov and has been obtained from CCLRCs Daresbury Laboratory via the website.[33]

The MD simulations were carried out for a variety of molecular loadings. All simulations were carried out on the LISA clusters of PCs equipped with Intel Xeon processors running at 3.4 GHz on the Linux operating system[34]. Each MD simulation, for a specified loading, was run for 120 h, determined to be long enough to obtain reliable statistics for determination of the diffusivities. In many cases, several independent MD simulations were run and the results averaged.

3. MD simulations for pure components

The self-diffusivities, $D_{\mathrm{i,self}}$, were computed by analyzing the mean square displacement of each species *i* for each of the coordinate directions:

$$D_{i,self} = \frac{1}{2n_i} \lim_{\Delta t \to \infty} \frac{1}{\Delta t} \left\langle \left(\sum_{l=1}^{n_i} \left(\mathbf{r}_{l,i}(t + \Delta t) - \mathbf{r}_{l,i}(t) \right)^2 \right) \right\rangle \qquad (1)$$

In this expression n_{i} represents the number of molecules of species *i* respectively, and $\mathbf{r}_{\mathrm{l,i}}(t)$ is the position of molecule *l* of species *i* at any time *t*. The expression (1) also defines the self-diffusivity in a *n*-component mixture.

For single component diffusion, the Maxwell-Stefan diffusivity was determined for each of the coordinate directions from

$$Đ_i = \frac{1}{2}\lim_{\Delta t\to\infty}\frac{1}{n_i}\frac{1}{\Delta t}\left\langle\left(\sum_{l=1}^{n_i}\left(\mathbf{r}_{l,i}(t+\Delta t)-\mathbf{r}_{l,i}(t)\right)\right)^2\right\rangle \tag{2}$$

For 1D channel structures of AFI, MOR, TON the reported diffusivities are along the z-direction. For ETS-4, only diffusion along the 12-ring channels is considered (z-axis); the diffusivities in the other two directions were too low to be determined accurately. For DDR the reported diffusivities are the averages in x- and y- directions $Đ = \left(Đ_x + Đ_y\right)/2$. For all other cases (MFI, FAU, LTA, CHA, IRMOF-1, CuBTC) the average values calculated according to $Đ = \left(Đ_x + Đ_y + Đ_z\right)/3$ are presented. In all cases reported here, the MSD values were linear in t for t > 10 ps (used in data regression analysis to determine the diffusivities) and we found no evidence of single file diffusion characteristics.

The self-exchange coefficient $Đ_{ii}$ were calculated from

$$Đ_{ii} = \frac{\theta_i}{\dfrac{1}{D_{i,self}} - \dfrac{1}{Đ_i}} \tag{3}$$

where θ_i is the fractional occupancy:

$$\theta_i = \frac{q_i}{q_{i,sat}} \tag{4}$$

The values of the saturation capacities $q_{i,sat}$ were determined from CBMC simulations of the isotherms. For all molecule-zeolite combinations the pure component diffusion data, for $D_{i,self}$, $Đ_i$, and $Đ_{ii}/Đ_i$ are presented in Appendix A3 in graphical form. The data on $Đ_{ii}/Đ_i$ was correlated using

$$\frac{Đ_{ii}}{Đ_i} = a_i \exp(-b_i\theta_i) \tag{5}$$

The fitted values of a_i and b_i for various guest molecules in a variety of zeolites are given in Tables 2 and 3 for zeolites, and Table 4 for CuBTC, IRMOF-1, and ETS-4. It should be noted that in many cases the fits were performed for occupancies lower than about 0.7.

4. Pure component diffusivity data fits

For prediction of the elements of the matrices [Δ] and [L] using pure component diffusion data, it is essential to have a reasonable representation of the $Đ_i$ - θ_i behavior in various zeolite structures. The most convenient and practical physical model to quantify the $Đ_i$ - q_i relation is that developed by Reed and Ehrlich for surface diffusion of adsorbed molecules[35]. In the Reed and Ehrlich model, as applied earlier by Krishna and van Baten [36, 37] for zeolites, the intermolecular interactions *within* a cage is assumed to influence the hopping frequencies of molecules *between* cages, by a factor $\phi_i = \exp(\frac{\delta E_i}{RT})$, where δE_i represents the reduction in the energy barrier for diffusion. The values of δE_i can be estimated from molecular simulations of the free energy profiles [38, 39]. The Reed and Ehrlich model leads to the following expression for the M-S diffusivity as a function of the fractional occupancy, θ_i

$$Đ_i = Đ_i(0)\frac{(1+\varepsilon_i)^{z-1}}{(1+\varepsilon_i/\phi_i)^z} \tag{6}$$

where z is the coordination number, representing the maximum number of nearest neighbors within a cage. From an engineering point of view the precise choice of the value of z is not crucial, as the *combination* of z and ϕ_i prescribes the loading dependence. For FAU, LTA, CHA, DDR, IRMOF-1, and CuBTC we choose a value z = 5 for all molecules. For 1 D structures such as AFI, TON, MOR, and ETS-4 (diffusion along 12-ring channels) we use z = 2. For MFI we use z = 2.5, based on the arguments presented in earlier work[40]. The other parameters are defined as follows (see Krishna et al.[36, 40] for more detailed discussions and derivations)

$$\varepsilon_i = \frac{(\beta_i - 1 + 2\theta_i)\phi_i}{2(1-\theta_i)}; \quad \beta_i = \sqrt{1 - 4\,\theta_i(1-\theta_i)(1-1/\phi_i)} \tag{7}$$

The fitted values of ϕ_i are reported in Tables 5 and 6 for zeolites, and Table 7 for CuBTC, IRMOF-1, and ETS-4.

For methane (C1) diffusion in LTA, MD simulations were carried out for T = 800, 1000, 1200, 1400, 1600, and 1800 K in order to investigate the loading dependence as a function of T. The data are presented in Appendix A3. We note that the $Đ_i$ - q_i behavior changes with T. This implies that the activation energy for diffusion is also loading dependent. This subject needs further investigation.

5. Binary mixture diffusion simulations

For binary mixtures the elements of the matrix [Δ], defined by

$$(N) = -\rho \frac{[\Delta]}{RT} \begin{bmatrix} q_1 & 0 \\ 0 & q_2 \end{bmatrix} \frac{d(\mu)}{dx} = -\rho [\Delta][\Gamma] \frac{d(q)}{dx} \tag{8}$$

are obtained in each coordinate direction from

$$\Delta_{ij} = \frac{1}{2} \lim_{\Delta t \to \infty} \frac{1}{n_j} \frac{1}{\Delta t} \left\langle \left(\sum_{l=1}^{n_i} \left(\mathbf{r}_{l,i}(t + \Delta t) - \mathbf{r}_{l,i}(t) \right) \right) \bullet \left(\sum_{k=1}^{n_j} \left(\mathbf{r}_{k,j}(t + \Delta t) - \mathbf{r}_{k,j}(t) \right) \right) \right\rangle \tag{9}$$

In this expression n_i and n_j represent the number of molecules of species i and j respectively, and $\mathbf{r}_{l,i}(t)$ is the position of molecule l of species i at any time t. In this context we note a typographical error in eq (9) as printed in earlier publications [36, 41, 42] wherein the denominator in the right member had n_i instead of n_j. The simulation results presented in these publications are, however, correct as the proper formula given in eq (9) was used in the calculations.

The matrix of Onsager coefficients [L] are defined by

$$(N) = -\rho \frac{1}{RT} [L] \frac{d(\mu)}{dx} \tag{10}$$

The units of L_{ij} are $m^2\ s^{-1}$ mol kg^{-1} when component molar loadings q_i have the units of mol kg^{-1}. For diffusion in carbon nanotubes the component loadings are expressed in molecule nm^{-1}, and the units of L_{ij} are $m^2\ s^{-1}$ molecule nm^{-1}. The inter-relationship between [Δ] and [L] is

$$\Delta_{ij} q_j = L_{ij} \tag{11}$$

The combination of eqs (9) and (11) allows us to determine the L_{ij} from MD simulations.

The Onsager Reciprocal Relations $L_{ij} = L_{ji}$ imply

$$\Delta_{ij} q_j = \Delta_{ji} q_i; \quad i, j = 1,2,....n \tag{12}$$

For all binary mixture-zeolite combinations the data on $D_{i,self}$ and Δ_{ij} are presented in Appendix A4 in graphical form. Also presented in Appendix A4 are the ratios α_{11} and α_{22}

$$\alpha_{11} = \frac{\Delta_{11}}{Đ_1}; \qquad \alpha_{22} = \frac{\Delta_{22}}{Đ_2} \tag{13}$$

along with the interaction factor α_{12}

$$\alpha_{12} = \frac{L_{12}}{\sqrt{L_{11} L_{22}}} = \alpha_{21} \tag{14}$$

In determining these ratios the Reed and Ehrlich model calculations for $Đ_i$ are carried out at the total *mixture* occupancy calculated from

$$\theta = \theta_1 + \theta_2 = \frac{q_1}{q_{1,sat}} + \frac{q_2}{q_{2,sat}} \tag{15}$$

6. Animations

For visual appreciation of the diffusion phenomena in different zeolites, ETS-4, and IRMOF-1 animations were created on the basis of the MD simulations; these can be viewed by downloading the movies from our website[43].

7. Acknowledgements

We are grateful to T.J.H. Vlugt, Delft, for providing the BIGMAC code. This code was modified to handle rigid molecular structures and charges, with generous assistance and technical inputs from S. Calero, Seville.

For IRMOF-1 and CuBTC simulations we obtained the structural data files from D. Dubbeldam, Northwestern University; for this we are grateful. Additional information on force fields for CuBTC was also provided by S. Calero, Seville.

8. Notation

Same as for Appendix A1, and additionally:

$\mathbf{r}_{l,i}(t)$ position of molecule l of species i at any time t, m

t time, s

Table 1. Characteristic sizes of channels or windows for zeolite structures

Zeolite	**Channel or window size/ Å**
MFI	10-ring intersecting channels of 5.1 – 5.6 Å size
AFI	12-ring 1D channels of 7.3 Å size
TON	10-ring 1D channels of 4.6 Å- 5.7 Å size
FAU	12-ring window of 7.4 Å size
LTA	8-ring window of 4.1 Å size
CHA	8-ring window of 3.8 Å size
DDR	8-ring window of 3.6 Å- 4.4 Å size
MOR	12-ring 1D channels of 6.5 – 7 Å size, connected to 8-ring side pocket of 2.6 Å- 5.7 Å size

Table 2. Correlation parameters a_i and b_i describing self-exchange coefficients $Đ_{ii}$ defined by Eq. (3) for a variety of molecules in AFI, and MOR zeolites, determined from MD simulations of pure component $Đ_i$ and $D_{i,self}$.

Zeolite	Molecule	a_i	b_i
AFI	C1	0.04	-4
AFI	CO2	0.15	-1.4
AFI	Ar	0.15	-1.4
AFI	Ne	0.13	-0.9
MOR	C1	1	2.5
MOR	C2	1.6	1.7
MOR	C3	4	3

Table 3. Correlation parameters a_i and b_i describing self-exchange coefficients $Đ_{ii}$ defined by Eq. (3) for a variety of molecules in FAU, MFI, CHA, DDR zeolites, determined from MD simulations of pure component $Đ_i$ and $D_{i,self}$.

Zeolite	Molecule	a_i	b_i
FAU	C1	0.5	0.9
FAU	C2	0.9	0.2
FAU	CO_2	0.45	0
FAU	Ar	0.38	0.45
FAU	Ne	0.26	1
MFI	C1	0.42	1.3
MFI	CO_2	0.8	2
MFI	Ar	0.27	1
MFI	Ne	0.14	0
LTA	C1	20	4
LTA	CO_2	2	0
LTA	N_2	2.0	2.1
LTA	Ar	2.4	2
LTA	Ne	0.65	1.7
CHA	C1	5	0
CHA	CO_2	1.5	1.3
CHA	Ar	2.6	1.6
CHA	Ne	0.7	1.3
DDR	C1	5	0
DDR	Ne	0.9	2.5
DDR	CO_2	1.6	1.7
DDR	N_2	3.2	4
DDR	O_2	4.0	3.5
DDR	Ar	4	3

The self-exchange coefficients for C1 in CHA and DDR could not be determined accurately from MD, and the value of 5 in the Table is an estimate.

Table 4. Correlation parameters a_i and b_i describing self-exchange coefficients $Đ_{ii}$ defined by Eq. (3) for a variety of molecules in CuBTC, IRMOF-1, and ETS-4 determined from MD simulations of pure component $Đ_i$ and $D_{i,self}$.

Zeolite	Molecule	a_i	b_i
CuBTC	C1	0.5	0.6
CuBTC	Ar	0.5	1.4
CuBTC	Ne	0.23	1.3
IRMOF-1	C1	0.5	0.75
IRMOF-1	Ar	0.27	0
IRMOF-1	Ne	0.25	0.8
ETS-4	C1	0.13	0.6
ETS-4	Ar	0.15	-0.4
ETS-4	Ne	0.12	0

Table 5. Reed-Ehrlich parameters for a variety of molecules in AFI, TON, MOR zeolites.

Zeolite	Molecule	Saturation capacity, $q_{i,sat}$ / mol/kg	$Đ_i(0)$ / 10^{-8} m^2 s^{-1}	z	ϕ_i
AFI	C1	4.55	8.27	2	$0.42\exp(-1.76\theta_i)$
AFI	C3	1.4	4	2	1.07
AFI	CO_2	6	2.16	2	1.32
AFI	Ne	16	9.8	2	0.73
AFI	Ar	6.6	5.1	2	0.56
TON	C1	2.8	3.5	2	$12\exp(-2.76\theta_i)$
TON	C2	2.5	2.64	2	$4.65\exp(-1.0\theta_i)$
MOR	C1	5.6	5.97	2	0.534
MOR	C2	3.6	11.7	2	0.35
MOR	C3	2.8	6.6	2	$2.24\exp(-3.29\theta_i)$

Table 6. Reed-Ehrlich parameters for a variety of molecules in FAU, MFI, CHA, DDR zeolites.

Zeolite	Molecule	Saturation capacity, $q_{i,sat}$ / mol/kg	$Đ_i(0)$ / 10^{-8} m^2 s^{-1}	z	ϕ_i
FAU	C1	11.5	4	5	$0.75\exp(0.12\theta_i)$
FAU	C2	6.24	2.4	5	0.85
FAU	CO2	12	1.85	5	0.92
FAU	Ne	34	4.64	5	1.17
FAU	Ar	15	2.63	5	$0.98\exp(0.06\theta_i)$
MFI	C1	4	1.75	2.5	$1.0\exp(1.0\theta_i)$
MFI	CO2	5.9	0.44	2.5	$1.44\exp(-0.72\theta_i)$
MFI	Ne	20	2.94	2.5	0.68
MFI	Ar	6	1.15	2.5	$3.36\exp(-1.54\theta_i)$
LTA	C1	10.2	0.018	5	$5.9\exp(-0.64\theta_i)$
LTA	CO_2	12	0.4	5	$0.76\exp(-0.5\theta_i)$
LTA	N_2	12.5	0.8	5	$1.5\exp(-0.15\theta_i)$
LTA	Ar	12.5	0.58	5	1.5
LTA	Ne	35	1.83	5	1.22
CHA	C1	8.32	2.1×10^{-3}	5	$4.55\exp(-0.98\theta_i)$
CHA	CO_2	9.71	0.21	5	1.47
CHA	Ar	9.71	0.285	5	1.64
CHA	Ne	27.7	1.74	5	1.31
DDR	C1	4.2	4.76×10^{-5}	5	$6\exp(-0.2\theta_i)$
DDR	Ne	14	1.06	5	$1.63\exp(-0.4\theta_i)$
DDR	CO_2	4.6	0.113	5	1.2
DDR	N_2	5.4	0.16	5	$3.7\exp(-0.95\theta_i)$
DDR	O_2	5.4	0.19	5	$2.25\exp(-0.24\theta_i)$
DDR	Ar	5.4	0.075	5	$3.5\exp(-0.74\theta_i)$

Table 7. Reed-Ehrlich parameters for a variety of molecules in CuBTC, IRMOF-1, and ETS-4.

Zeolite	Molecule	Saturation capacity, $q_{i,sat}$ / mol/kg	$Đ_i(0)$ / 10^{-8} m^2 s^{-1}	z	ϕ_i
CuBTC	C1	25	1.9	5	$2.4\exp(-0.9\theta_i)$
CuBTC	Ar	35	1.9	5	$2.2\exp(-0.7\theta_i)$
CuBTC	Ne	80	5.7	5	$1.6\exp(-0.45\theta_i)$
IRMOF-1	C1	41	3.3	5	$1.5\exp(-0.2\theta_i)$
IRMOF-1	Ar	58	2.65	5	$1.8\exp(-0.5\theta_i)$
IRMOF-1	Ne	104	6.95	5	$1.44\exp(-0.15\theta_i)$
ETS-4	C1	4.5	6.83	2	$0.7\exp(1.0\theta_i)$
ETS-4	Ne	16	7.8	2	$0.7\exp(-0.4\theta_i)$
ETS-4	Ar	5	4.5	2	$1.40\exp(-0.16\theta_i)$

9. References

[1] C. Baerlocher, L.B. McCusker, Database of Zeolite Structures, International Zeolite Association, http://www.iza-structure.org/databases/, 26 June 2001.

[2] E. Jaramillo, S.M. Auerbach, New force field for Na cations in faujasite-type zeolites, J. Phys. Chem. B 103 (1999) 9589-9594.

[3] S. Calero, D. Dubbeldam, R. Krishna, B. Smit, T.J.H. Vlugt, J.F.M. Denayer, J.A. Martens, T.L.M. Maesen, Understanding the role of sodium during adsorption. A force field for alkanes in sodium exchanged faujasites, J. Am. Chem. Soc. 126 (2004) 11377-11386.

[4] J.P. Ryckaert, A. Bellemans, Molecular dynamics of liquid alkanes, Faraday Discuss. Chem. Soc. 66 (1978) 95-106.

[5] D. Frenkel, B. Smit, Understanding molecular simulations: from algorithms to applications, Academic Press, 2nd Edition, San Diego, 2002.

[6] D. Dubbeldam, S. Calero, T.J.H. Vlugt, R. Krishna, T.L.M. Maesen, B. Smit, United Atom Forcefield for Alkanes in Nanoporous Materials, J. Phys. Chem. B 108 (2004) 12301-12313.

[7] J.G. Harris, K.H. Yung, Carbon Dioxide's Liquid-Vapor Coexistence Curve And Critical Properties as Predicted by a Simple Molecular Model, J. Phys. Chem. 99 (1995) 12021-12024.

[8] C.S. Murthy, K. Singer, M.L. Klein, I.R. McDonald, Pairwise additive effective potentials for nitrogen, Mol. Phys. 41 (1980) 1387-1399.

[9] K. Makrodimitris, G.K. Papadopoulos, D.N. Theodorou, Prediction of permeation properties of CO_2 and N_2 through silicalite via molecular simulations, J. Phys. Chem. B 105 (2001) 777-788.

[10] A.G. Bezus, A.V. Kiselev, A.A. Lopatkin, P.Q. Du, Molecular statistical calculation of the thermodynamic adsorption characteristics of zeolites using the atom-atom approximation. Part 1. Adsorption of methane by zeolite sodium-X, J.Chem.Soc., Faraday Trans. II 74 (1978) 367-379.

[11] A.V. Kiselev, A.A. Lopatkin, A.A. Shul'ga, Molecular statistical calculation of gas adsorption by silicalite, Zeolites 5 (1985) 261-267.

[12] E. García-Pérez, J.B. Parra, C.O. Ania, A. García-Sánchez, J.M. Van Baten, R. Krishna, D. Dubbeldam, S. Calero, A computational study of CO_2, N_2 and CH_4 adsorption in zeolites, Adsorption 13 (2007) 469-476.

[13] A.I. Skoulidas, D.S. Sholl, Transport diffusivities of CH_4, CF_4, He, Ne, Ar, Xe, and SF_6 in silicalite from atomistic simulations, J. Phys. Chem. B 106 (2002) 5058-5067.

[14] O. Talu, A.L. Myers, Reference potentials for adsorption of helium, argon, methane and krypton in high-silica zeolites, Colloids Surf., A 187-188 (2001) 83-93.

[15] C. Mellot, J. Lignieres, Monte Carlo SImulations of N_2 and O_2 adsorption in silicalites and CaLSX zeolites, Mol. Simulation 18 (1997) 349-365.

[16] A.V.A. Kumar, H. Jobic, S.K. Bhatia, Quantum effects on adsorption and diffusion of hydrogen and deuterium in microporous materials, J. Phys. Chem. B 110 (2006) 16666-16671.

[17] M. Gallo, T.M. Nenoff, M.C. Mitchell, Selectivities for binary mixtures of hydrogen/methane and hydrogen/carbon dioxide in silicalite and ETS-10 by Grand Canonical Monte Carlo techniques, Fluid Phase Equilib. 247 (2006) 135-142.

[18] D. Dubbeldam, S. Calero, T.J.H. Vlugt, R. Krishna, T.L.M. Maesen, E. Beerdsen, B. Smit, Force Field Parametrization through Fitting on Inflection Points in Isotherms, Phys. Rev. Lett. 93 (2004) 088302.

[19] T.J.H. Vlugt, R. Krishna, B. Smit, Molecular simulations of adsorption isotherms for linear and branched alkanes and their mixtures in silicalite, J. Phys. Chem. B 103 (1999) 1102-1118.

[20] T.J.H. Vlugt, BIGMAC, University of Amsterdam, http://molsim.chem.uva.nl/bigmac/, 1 November 2000.

[21] R. Krishna, J.M. van Baten, Using molecular simulations for screening of zeolites for separation of CO_2/CH_4 mixtures, Chem. Eng. J. 133 (2007) 121-131.

[22] R. Krishna, J.M. van Baten, Influence of segregated adsorption on mixture diffusion in DDR zeolite, Chem. Phys. Lett. 446 (2007) 344-349.
[23] R. Krishna, J.M. van Baten, Insights into diffusion of gases in zeolites gained from molecular dynamics simulations, Microporous Mesoporous Mater. (2007) DOI:10.1016/j.micromeso.2007.04.036
[24] R. Krishna, J.M. van Baten, Segregation effects in adsorption of CO_2 containing mixtures and their consequences for separation selectivities in cage-type zeolites, Sep. Purif. Technol. (2008) http://dx.doi.org/10.1016/j.seppur.2007.12.003
[25] R. Krishna, J.M. van Baten, Diffusion of hydrocarbon mixtures in MFI zeolite: Influence of intersection blocking, Chem. Eng. J. (2008) http://dx.doi.org/10.1016/j.cej.2007.11.026
[26] S.M. Kuznicki, V.A. Bell, S. Nair, H.W. Hillhouse, R.M. Jacubinas, C.M. Braunbarth, B.H. Toby, M. Tsapatsis, A titanosilicate molecular sieve with adjustable pores for size-selective adsorption of molecules, Nature 412 (2001) 720-724.
[27] R.P. Marathe, K. Mantri, M.P. Srinivasan, S. Farooq, Effect of Ion Exchange and Dehydration Temperature on the Adsorption and Diffusion of Gases in ETS-4, Ind. Eng. Chem. Res. 43 (2004) 5281-5290.
[28] R.S. Pillai, S.A. Peter, R.V. Jasra, Adsorption of Carbon dioxide, Methane, Nitrogen, Oxygen and Argon in NaETS-4, Microporous Mesoporous Mater. (2008) http://dx.doi.org/10.1016/j.micromeso.2007.11.042
[29] D. Dubbeldam, K.S. Walton, D.E. Ellis, R.Q. Snurr, Exceptional Negative Thermal Expansion in Isoreticular Metal–Organic Frameworks, Angew. Chem. Int. Ed. 46 (2007) 4496-4499.
[30] D. Dubbeldam, H. Frost, K.S. Walton, R.Q. Snurr, Molecular simulation of adsorption sites of light gases in the metal-organic framework IRMOF-1, Fluid Phase Equilib. 261 (2007) 152-161.
[31] Q. Yang, C. Zhong, Electrostatic-Field-Induced Enhancement of Gas MixtureSeparation in Metal-OrganicFrameworks: A Computational Study, ChemPhysChem 7 (2006) 1417-1421.
[32] A. Vishnyakov, P.I. Ravikovitch, A.V. Neimark, M. Bülow, Q.M. Wang, Nanopore Structure and Sorption Properties of Cu-BTC Metal-Organic Framework, Nano Lett. 3 (2003) 713-718.
[33] W. Smith, T.R. Forester, I.T. Todorov, The DL_POLY Molecular Simulation Package, Warrington, England, http://www.cse.clrc.ac.uk/msi/software/DL_POLY/index.shtml, March 2006.
[34] SARA, Computing & Networking Services, Amsterdam, https://subtrac.sara.nl/userdoc/wiki/lisa/description, 16 January 2008.
[35] D.A. Reed, G. Ehrlich, Surface diffusion, atomic jump rates and thermodynamics, Surf. Sci. 102 (1981) 588-609.
[36] R. Krishna, J.M. van Baten, Diffusion of alkane mixtures in zeolites. Validating the Maxwell-Stefan formulation using MD simulations, J. Phys. Chem. B 109 (2005) 6386-6396.
[37] R. Krishna, J.M. van Baten, Insights into diffusion of gases in zeolites gained from molecular dynamics simulations, Microporous Mesoporous Mater. 109 (2008) 91-108.
[38] E. Beerdsen, D. Dubbeldam, B. Smit, Molecular Understanding of Diffusion in Confinment, Phys. Rev. Lett. 95 (2005) 164505.
[39] E. Beerdsen, D. Dubbeldam, B. Smit, Understanding Diffusion in Nanoporous Materials, Phys. Rev. Lett. 96 (2006) 044501.
[40] R. Krishna, D. Paschek, R. Baur, Modelling the occupancy dependence of diffusivities in zeolites, Microporous Mesoporous Mater. 76 (2004) 233-246.
[41] J.M. van Baten, R. Krishna, Entropy effects in adsorption and diffusion of alkane isomers in mordenite: An investigation using CBMC and MD simulations, Microporous Mesoporous Mater. 84 (2005) 179-191.
[42] R. Krishna, J.M. van Baten, Describing binary mixture diffusion in carbon nanotubes with the Maxwell-Stefan equations. An investigation using molecular dynamics simulations, Ind. Eng. Chem. Res. 45 (2006) 2084-2093.
[43] J.M. van Baten, R. Krishna, MD animations of diffusion in nanoporous materials, University of Amsterdam, Amsterdam, http://www.science.uva.nl/research/cr/animateMD/, 3 February 2008.

Appendix A3

GCMC and MD simulation results for pure component adsorption and diffusion of variety of molecules in different zeolites, ETS-4, IRMOF-1, and CuBTC

AFI (all silica)

12-ring
channel of AFI

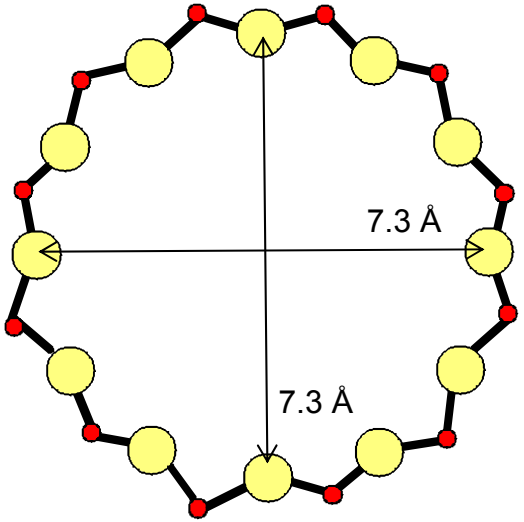

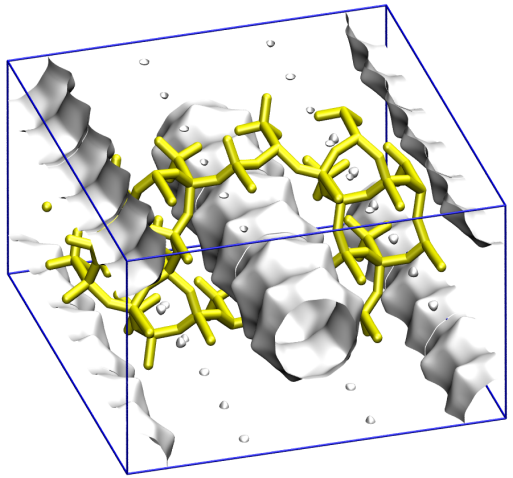

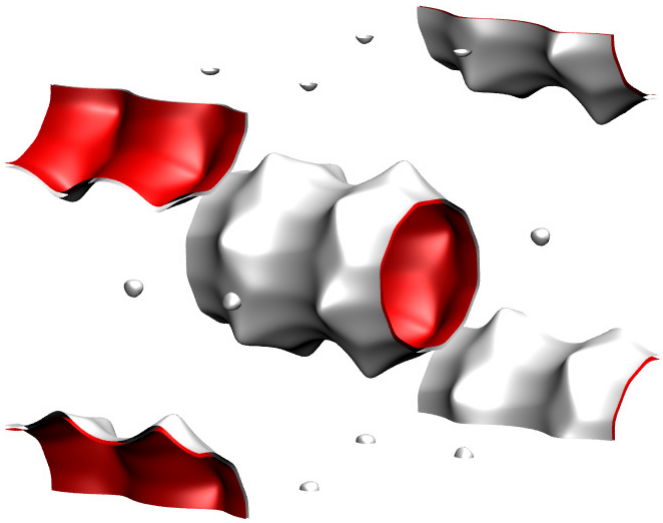

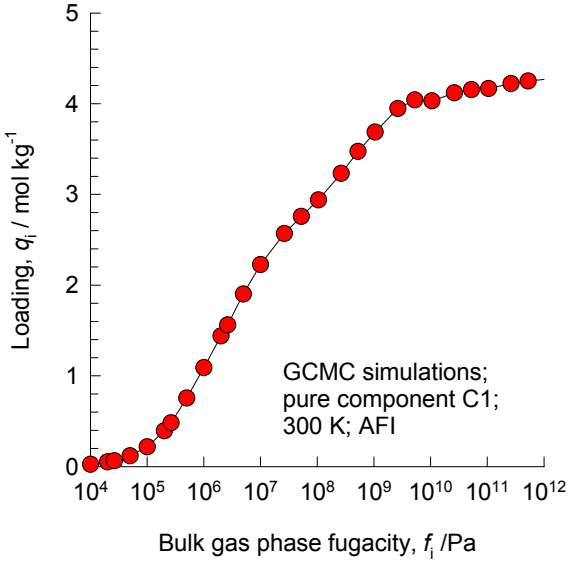
Loading, q_i / mol kg^{-1}
GCMC simulations;
pure component C1;
300 K; AFI
Bulk gas phase fugacity, f_i /Pa

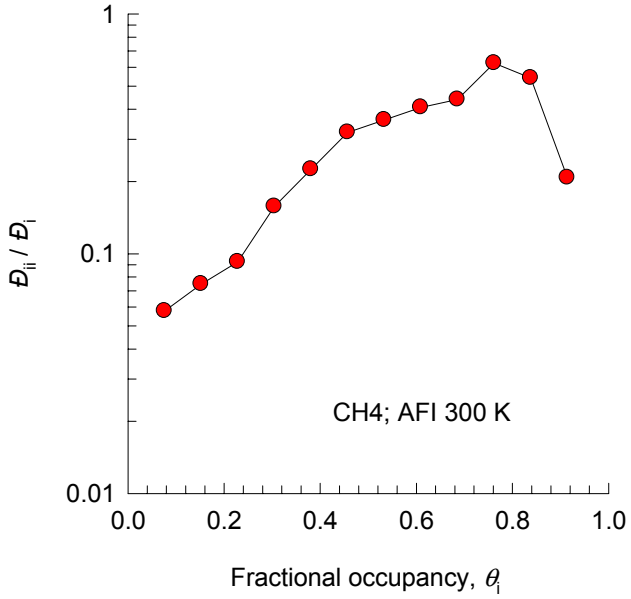
$Đ_{ii}$ / $Đ_i$
CH4; AFI 300 K
Fractional occupancy, θ_i

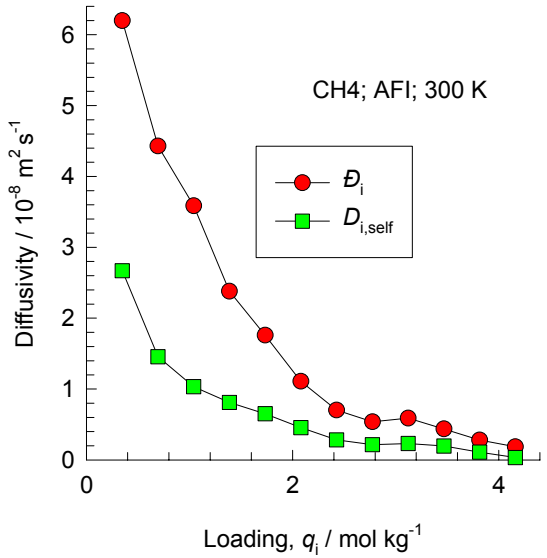
CH4; AFI; 300 K
$Đ_i$
$D_{i,self}$
Diffusivity / 10^{-8} m^2 s^{-1}
Loading, q_i / mol kg^{-1}

AFI, 300 K, CH4

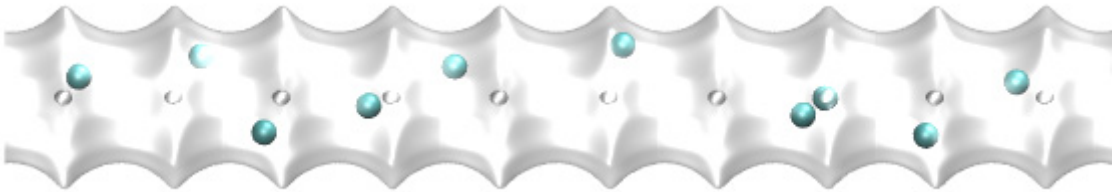

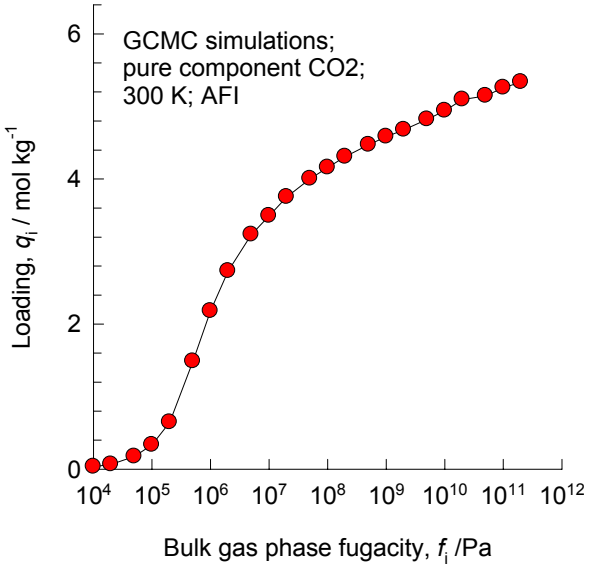
GCMC simulations;
pure component CO2;
300 K; AFI
Loading, q_i / mol kg^{-1}
Bulk gas phase fugacity, f_i /Pa

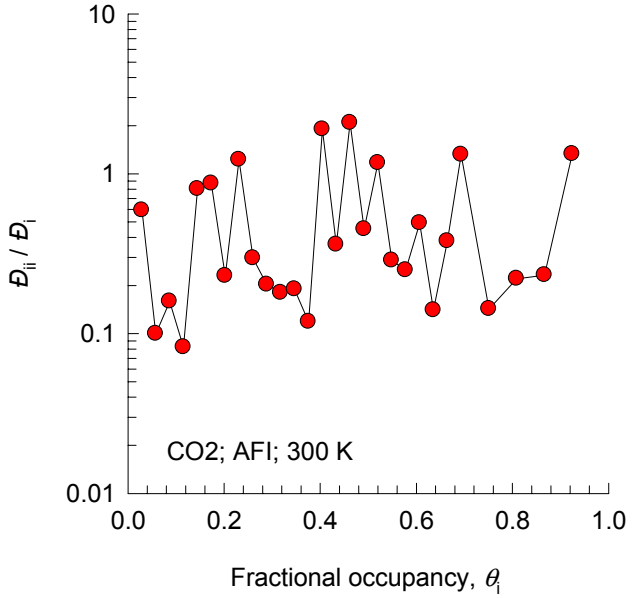
$Đ_{ii}$ / $Đ_i$
CO2; AFI; 300 K
Fractional occupancy, θ_i

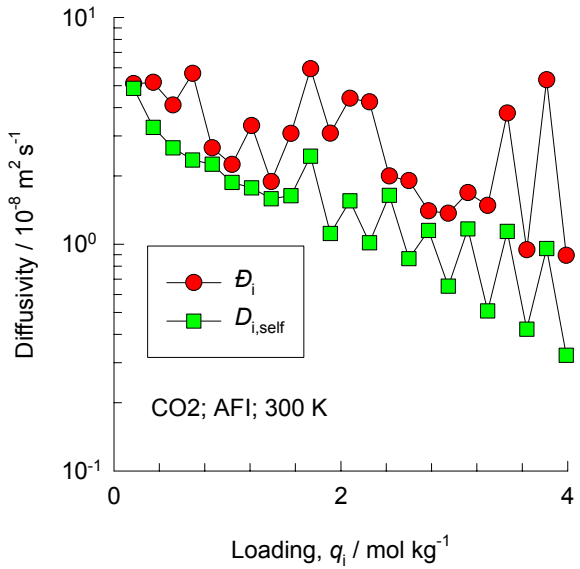
Diffusivity / 10^{-8} m^2 s^{-1}
$Đ_i$
$D_{i,self}$
CO2; AFI; 300 K
Loading, q_i / mol kg^{-1}

AFI, 300 K, CO2

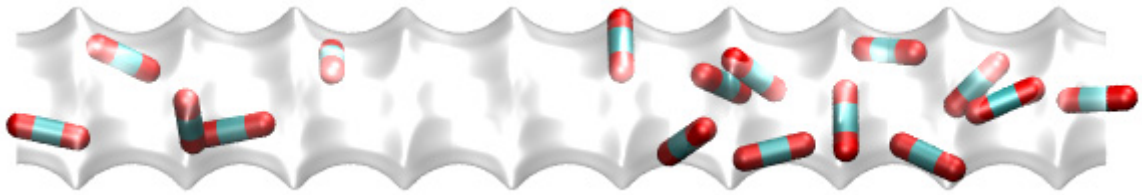

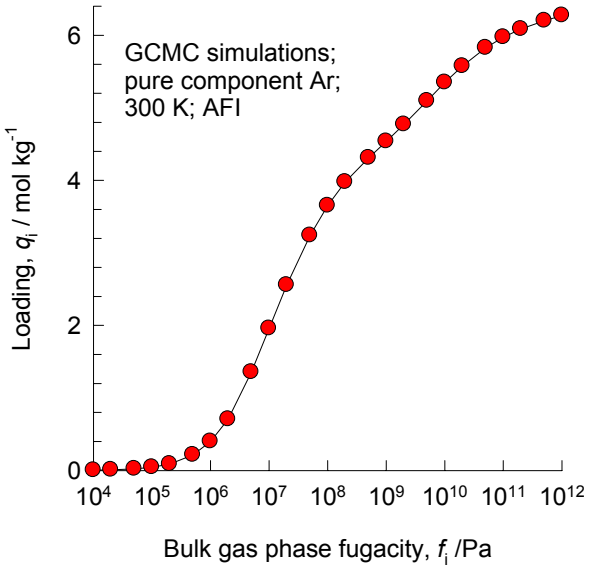
GCMC simulations;
pure component Ar;
300 K; AFI
Loading, q_i / mol kg^{-1}
Bulk gas phase fugacity, f_i /Pa

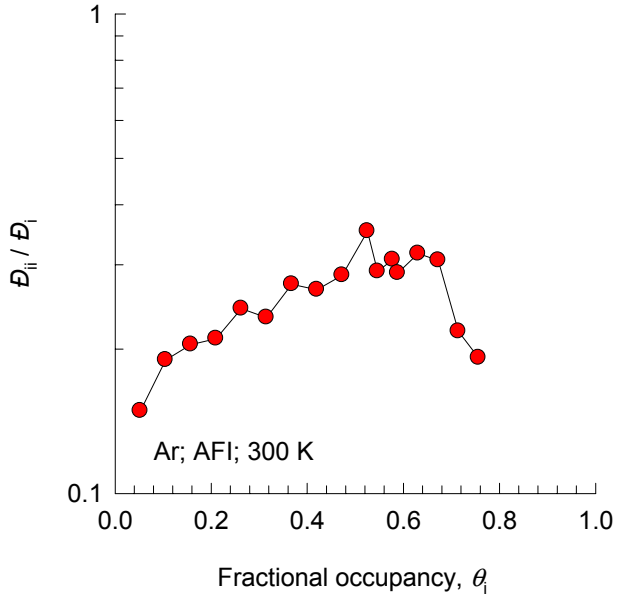
Ar; AFI; 300 K
$Đ_{ii} / Đ_i$
Fractional occupancy, θ_i

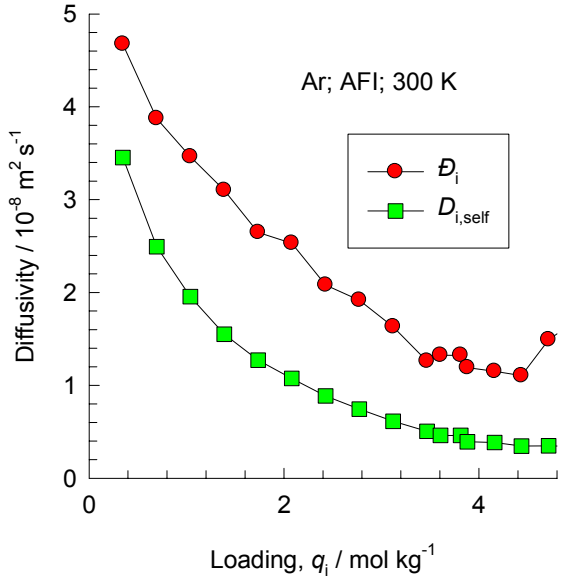
Ar; AFI; 300 K
$Đ_i$
$D_{i,self}$
Diffusivity / 10^{-8} m^2 s^{-1}
Loading, q_i / mol kg^{-1}

AFI, 300 K, Ar

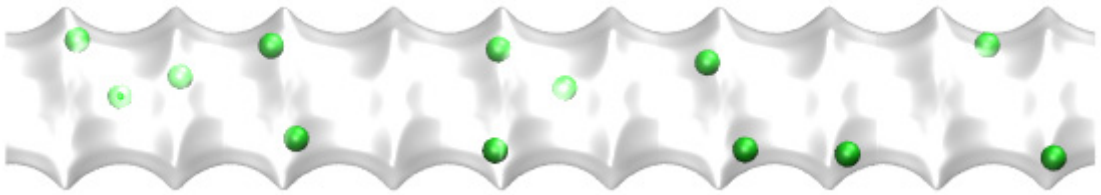

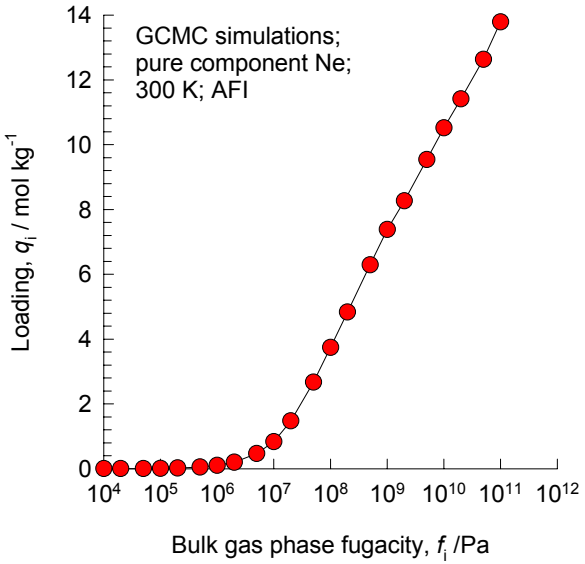
GCMC simulations;
pure component Ne;
300 K; AFI
Loading, q_i / mol kg^{-1}
Bulk gas phase fugacity, f_i /Pa

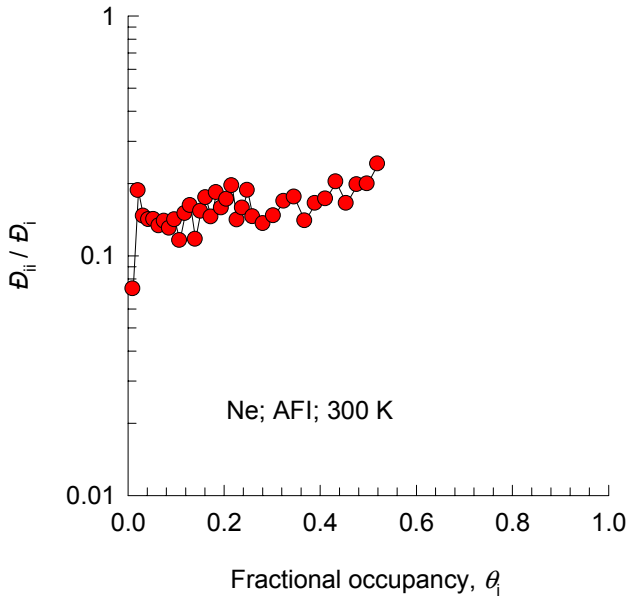
Ne; AFI; 300 K
$Đ_{ii}$ / $Đ_i$
Fractional occupancy, θ_i

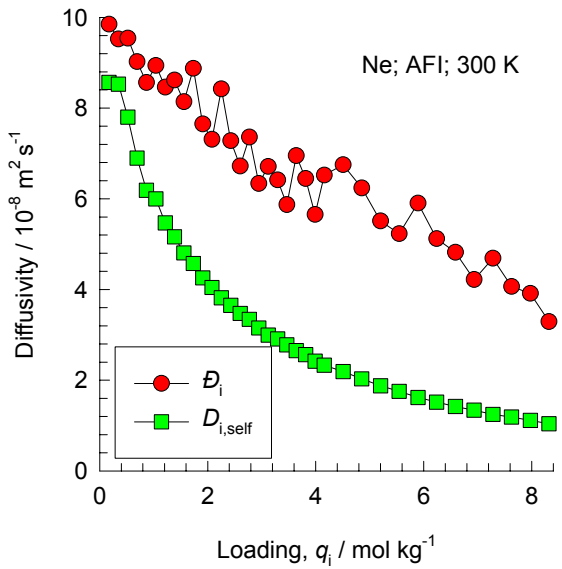
Ne; AFI; 300 K
$Đ_i$
$D_{i,self}$
Diffusivity / 10^{-8} m^2 s^{-1}
Loading, q_i / mol kg^{-1}

AFI, 300 K, Ne

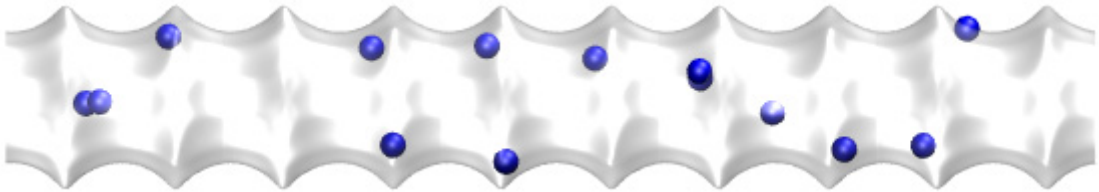

AFI, 300 K, C2

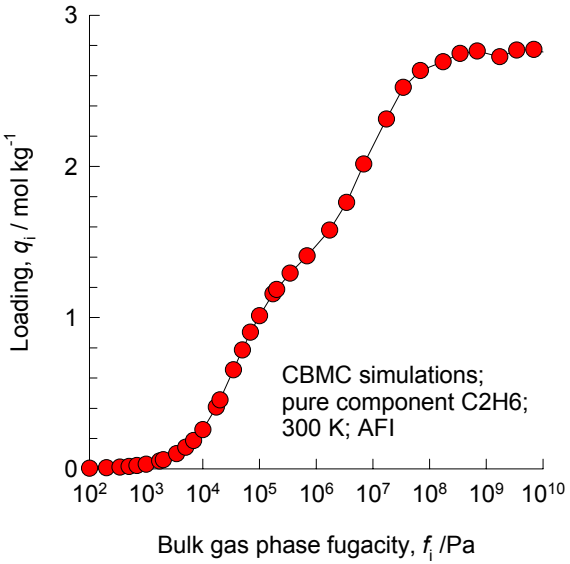
Loading, q_i / mol kg^{-1}
0
1
2
3
10^2 10^3 10^4 10^5 10^6 10^7 10^8 10^9 10^{10}
Bulk gas phase fugacity, f_i /Pa
CBMC simulations;
pure component C2H6;
300 K; AFI

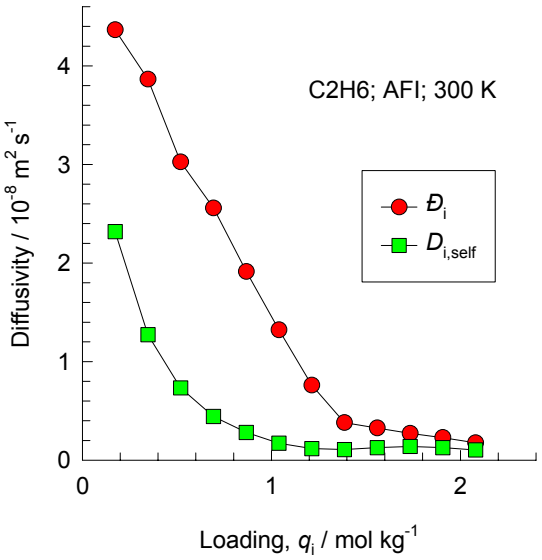
Diffusivity / 10^{-8} m^2 s^{-1}
0
1
2
3
4
0
1
2
Loading, q_i / mol kg^{-1}
C2H6; AFI; 300 K
$Đ_i$
$D_{i,self}$

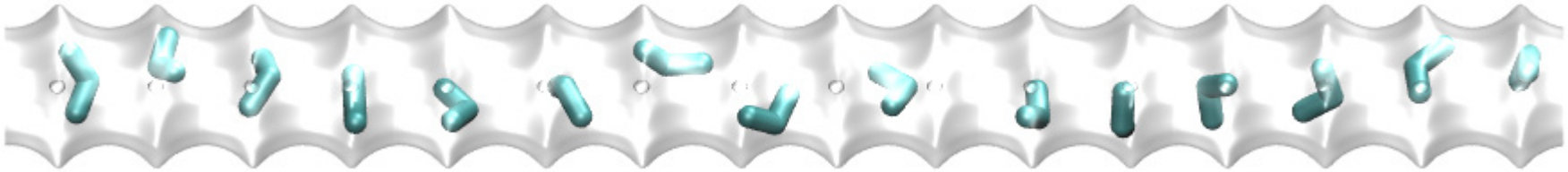

AFI, 300 K, C3

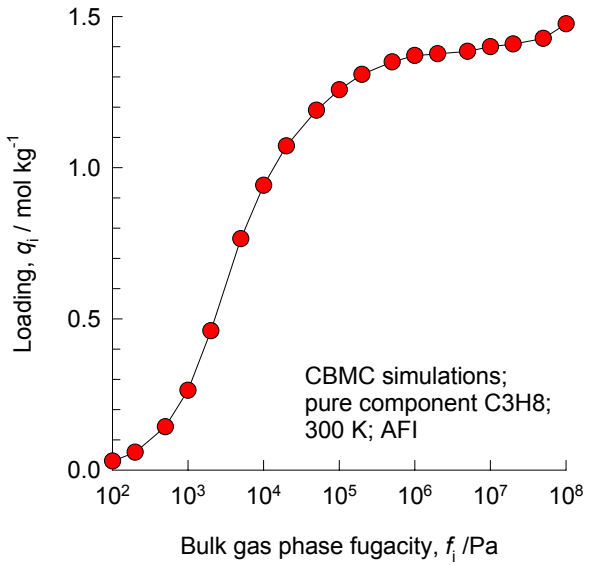
1.5
1.0
0.5
0.0
Loading, q_i / mol kg^{-1}
10^2
10^3
10^4
10^5
10^6
10^7
10^8
Bulk gas phase fugacity, f_i /Pa
CBMC simulations;
pure component C3H8;
300 K; AFI

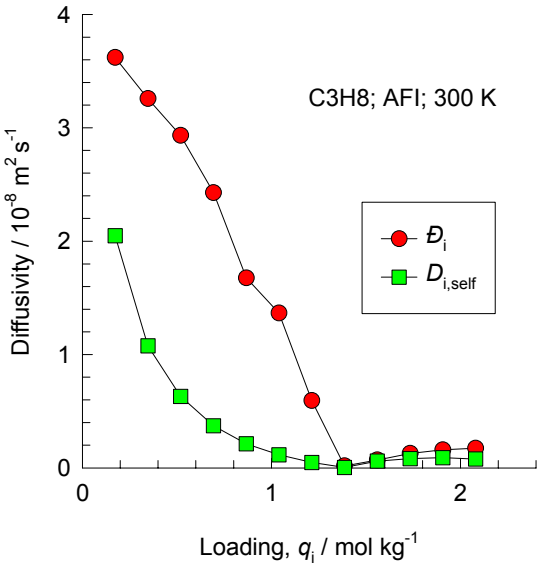
4
3
2
1
0
Diffusivity / 10^{-8} m^2 s^{-1}
0
1
2
Loading, q_i / mol kg^{-1}
C3H8; AFI; 300 K
Đ$_i$
$D_{i,self}$

FAU (all silica)

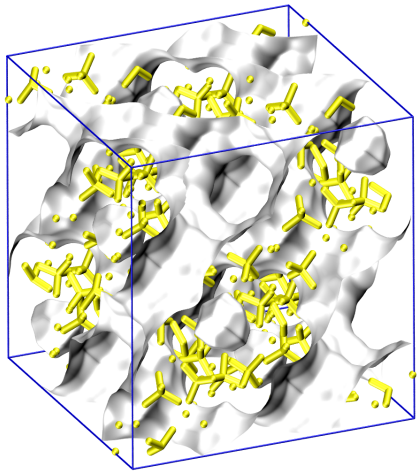

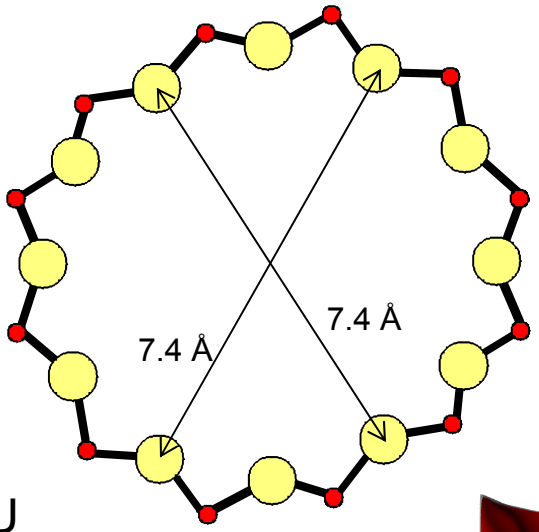

12-ring
window of FAU

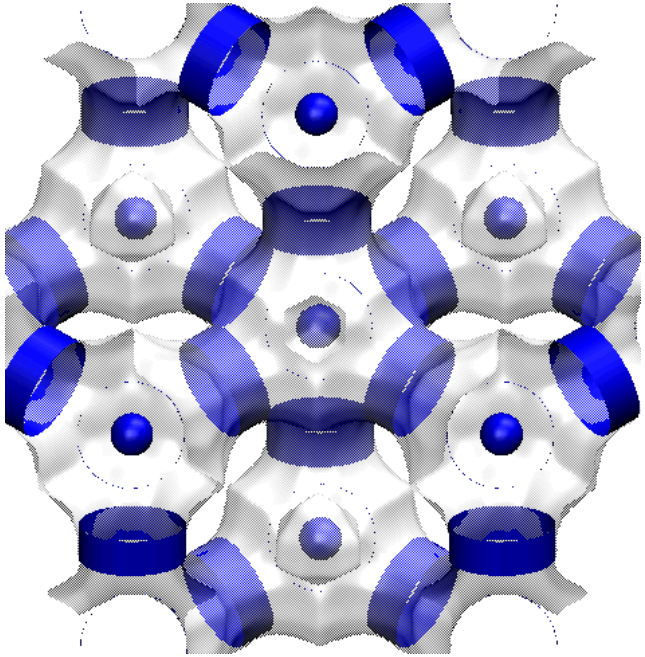

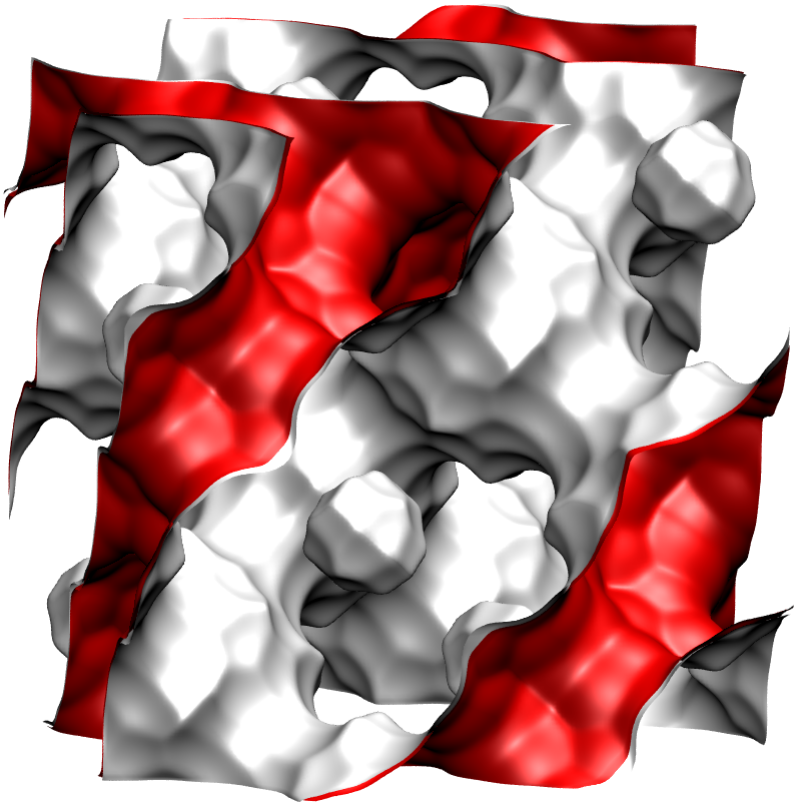

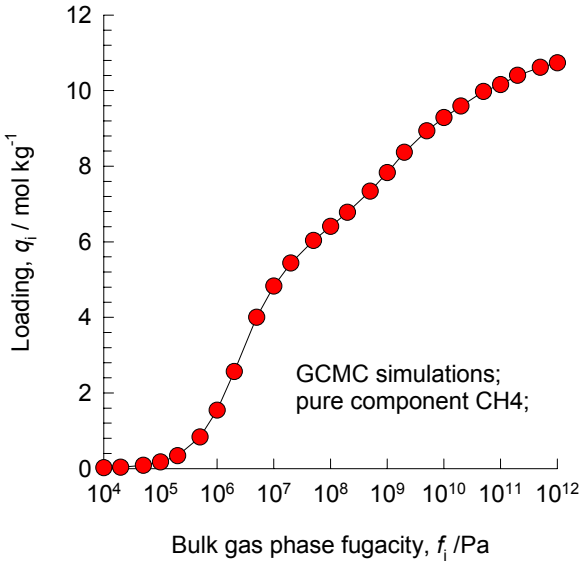
Loading, q_i / mol kg^{-1}
GCMC simulations;
pure component CH4;
Bulk gas phase fugacity, f_i /Pa

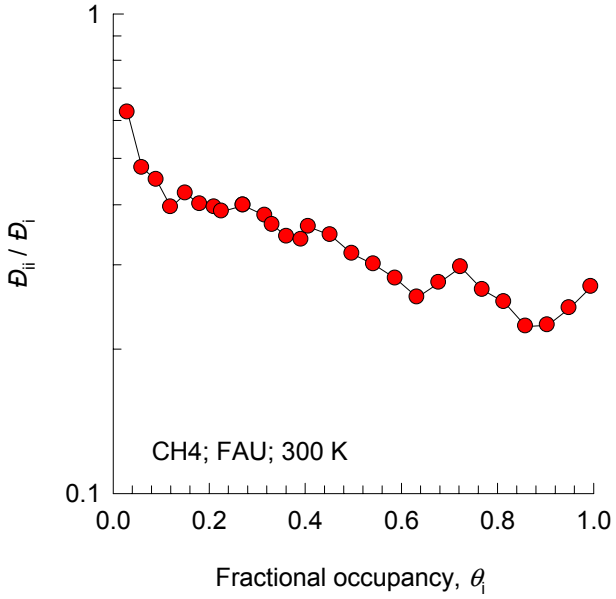
$Đ_{ii}$ / $Đ_i$
CH4; FAU; 300 K
Fractional occupancy, θ_i

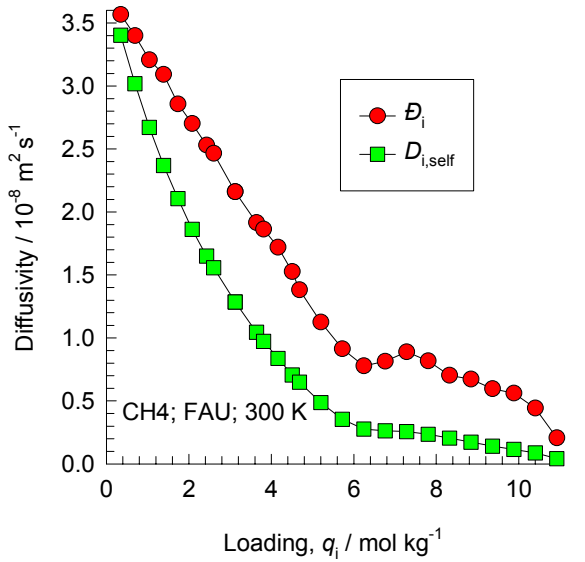
Diffusivity / 10^{-8} m^2 s^{-1}
$Đ_i$
$D_{i,self}$
CH4; FAU; 300 K
Loading, q_i / mol kg^{-1}

FAU, 300 K, CH4

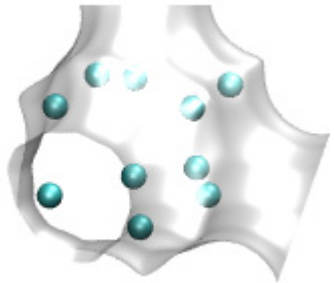

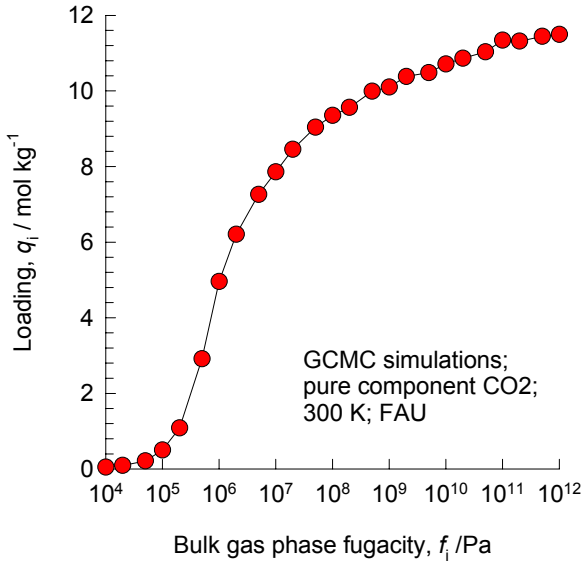
Loading, q_i / mol kg^{-1}
GCMC simulations;
pure component CO2;
300 K; FAU
Bulk gas phase fugacity, f_i /Pa

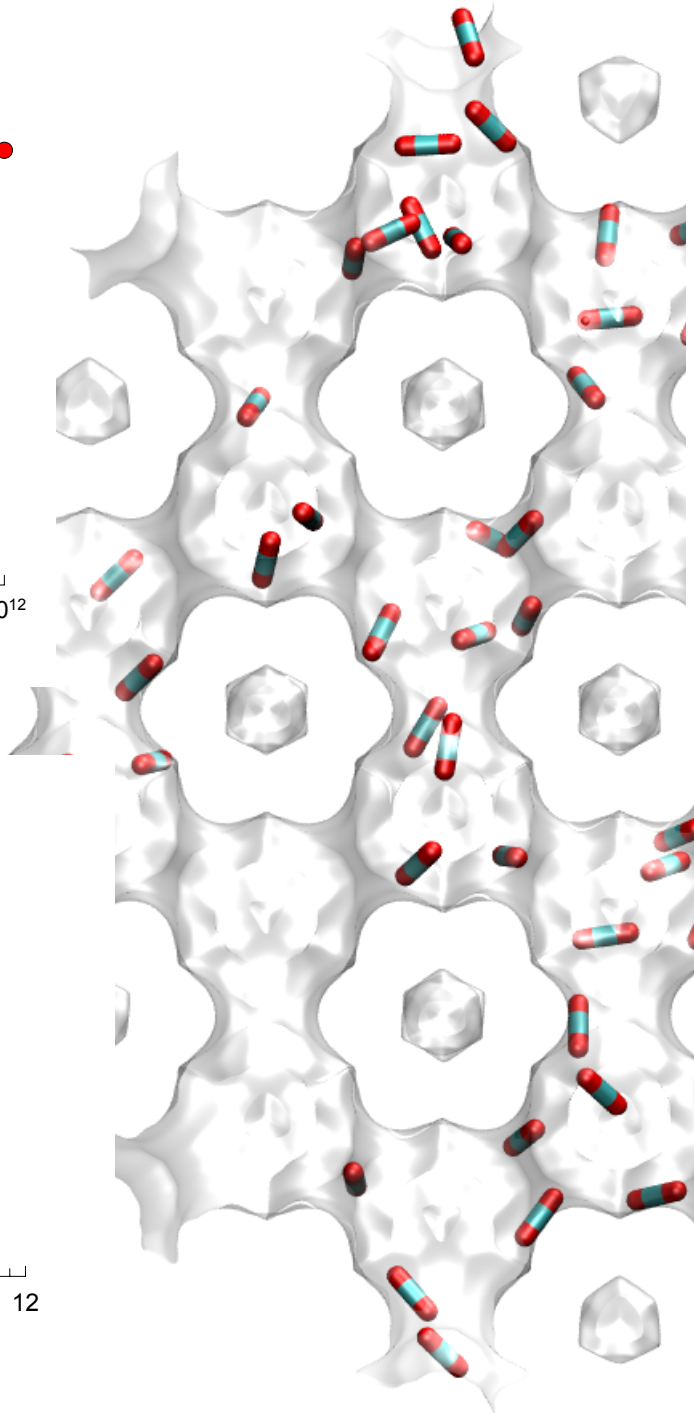

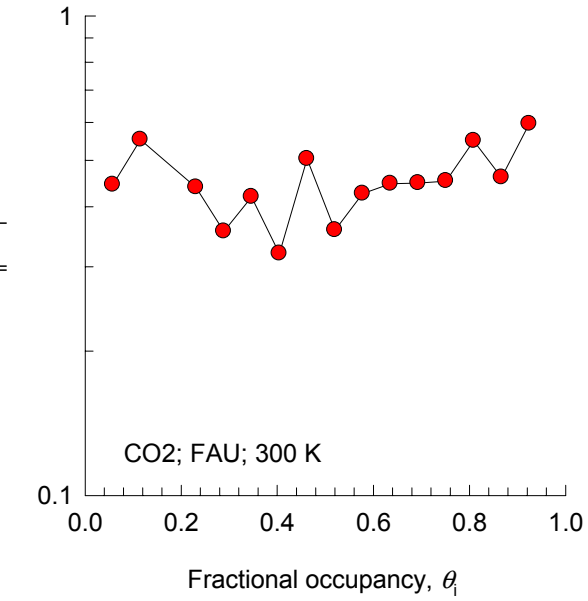
$Đ_{ii}$ / $Đ_i$
CO2; FAU; 300 K
Fractional occupancy, θ_i

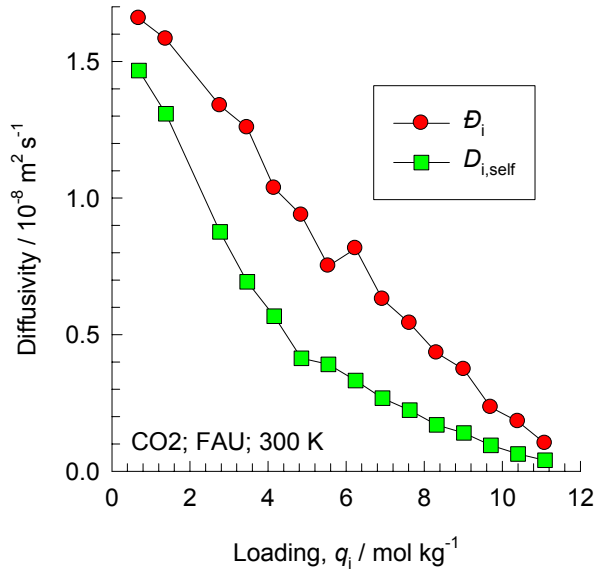
Diffusivity / 10^{-8} m^2 s^{-1}
$Đ_i$
$D_{i,self}$
CO2; FAU; 300 K
Loading, q_i / mol kg^{-1}

FAU, 300 K, CO2

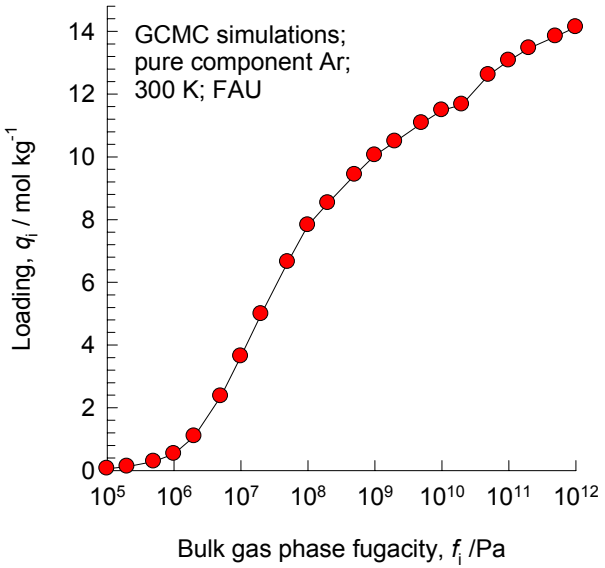
GCMC simulations;
pure component Ar;
300 K; FAU
Loading, q_i / mol kg^{-1}
Bulk gas phase fugacity, f_i /Pa

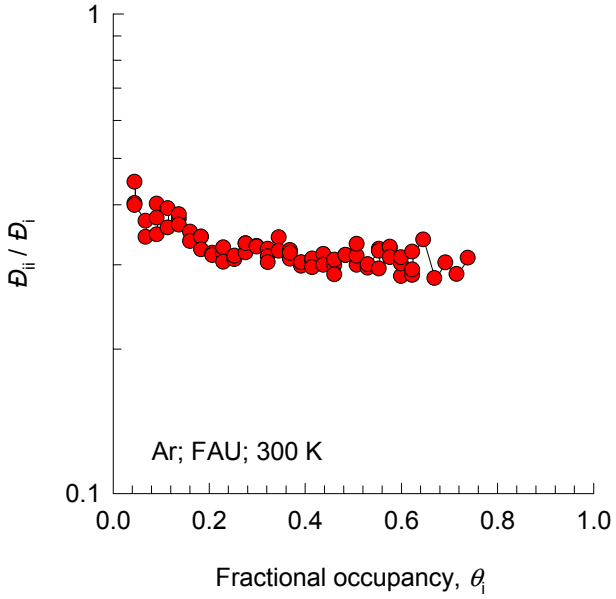
$Đ_{ii}$ / $Đ_i$
Ar; FAU; 300 K
Fractional occupancy, θ_i

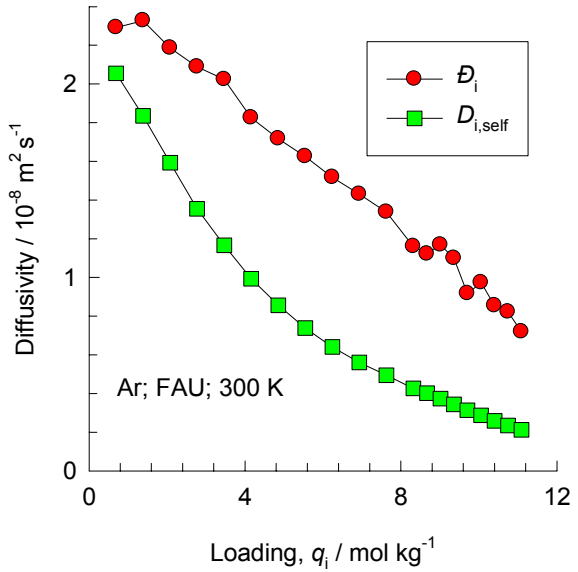
$Đ_i$
$D_{i,self}$
Ar; FAU; 300 K
Diffusivity / 10^{-8} m^2 s^{-1}
Loading, q_i / mol kg^{-1}

FAU, 300 K, Ar

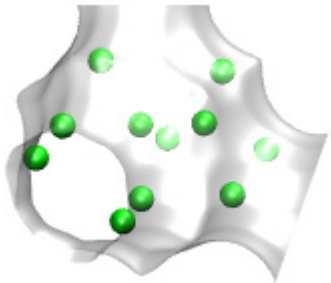

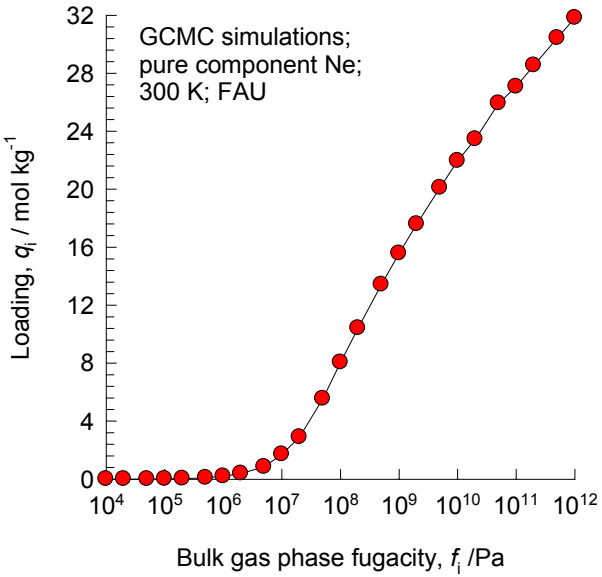
GCMC simulations;
pure component Ne;
300 K; FAU
Loading, q_i / mol kg^{-1}
Bulk gas phase fugacity, f_i /Pa

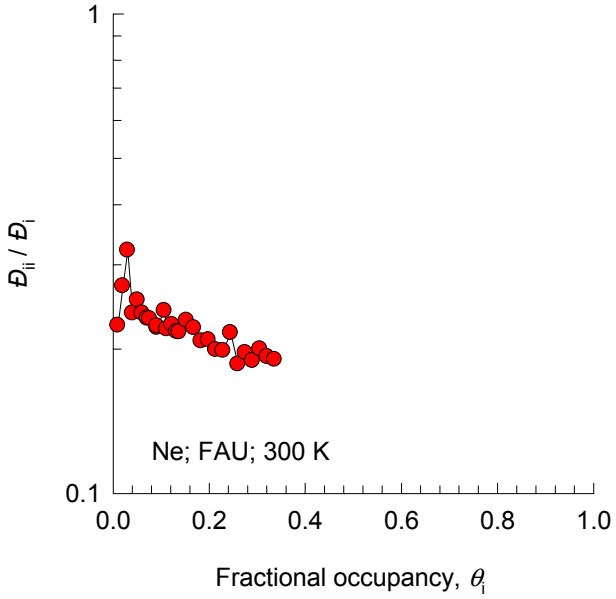
$Đ_{ii}$ / $Đ_i$
Ne; FAU; 300 K
Fractional occupancy, θ_i

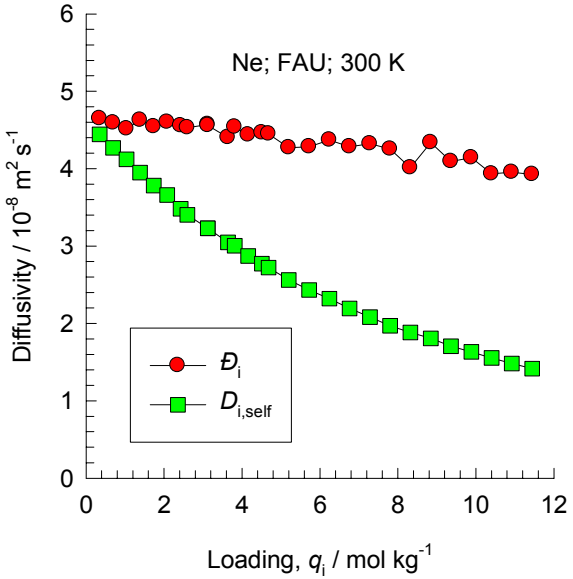
Ne; FAU; 300 K
Diffusivity / 10^{-8} m^2 s^{-1}
$Đ_i$
$D_{i,self}$
Loading, q_i / mol kg^{-1}

FAU, 300 K, Ne

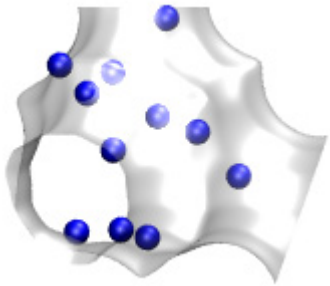

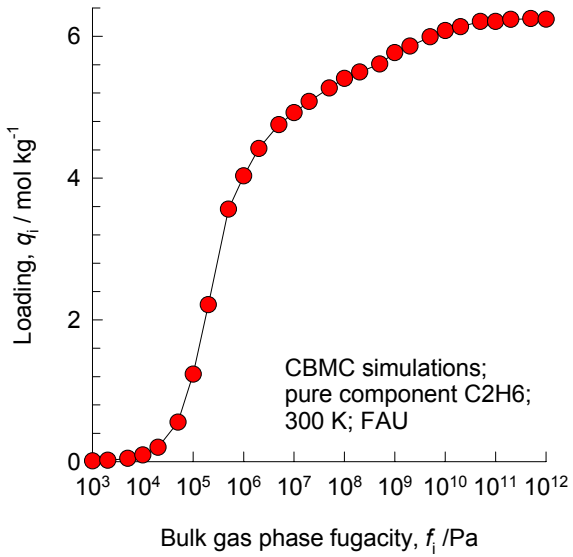
Loading, q_i / mol kg^{-1}
0
2
4
6
10^3 10^4 10^5 10^6 10^7 10^8 10^9 10^{10} 10^{11} 10^{12}
Bulk gas phase fugacity, f_i /Pa
CBMC simulations;
pure component C2H6;
300 K; FAU

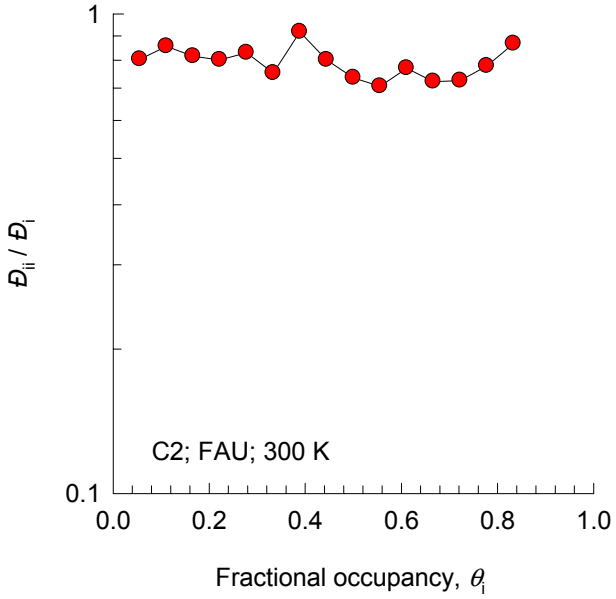
$Đ_{ii}$ / $Đ_i$
1
0.1
0.0
0.2
0.4
0.6
0.8
1.0
Fractional occupancy, θ_i
C2; FAU; 300 K

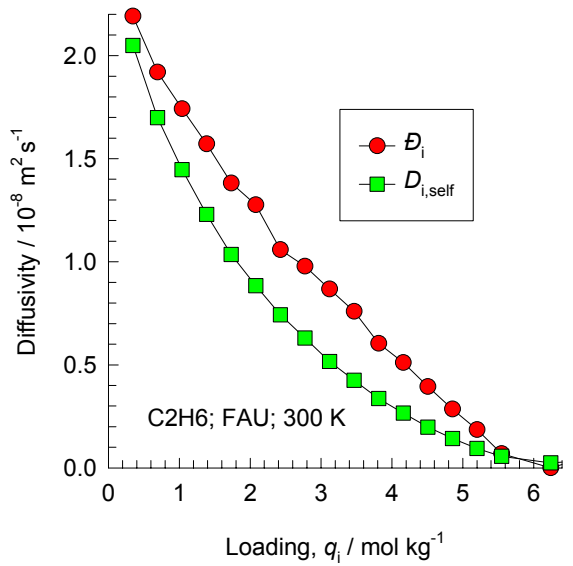
Diffusivity / 10^{-8} m^2 s^{-1}
0.0
0.5
1.0
1.5
2.0
0
1
2
3
4
5
6
Loading, q_i / mol kg^{-1}
$Đ_i$
$D_{i,self}$
C2H6; FAU; 300 K

FAU, 300 K, C2

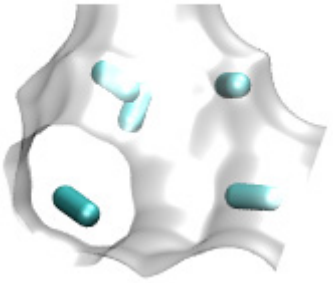

MFI (all silica)

10 ring channel
of MFI viewed along [100]

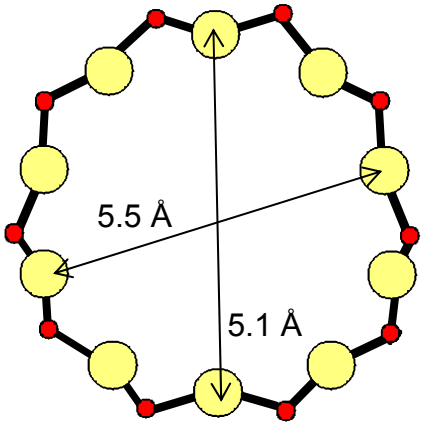

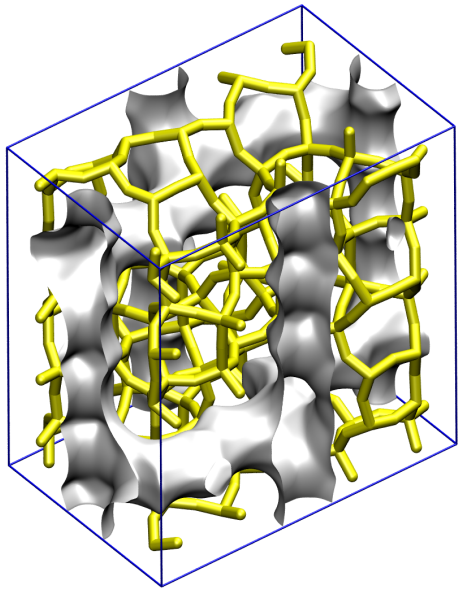

10 ring channel
of MFI viewed along [010]

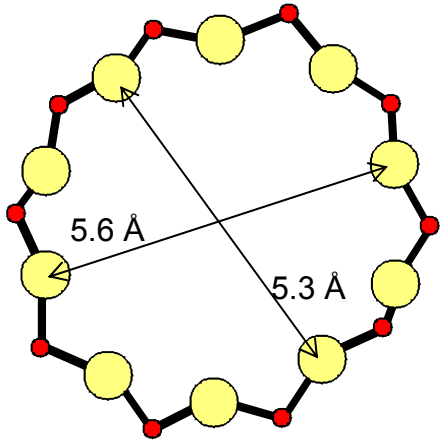

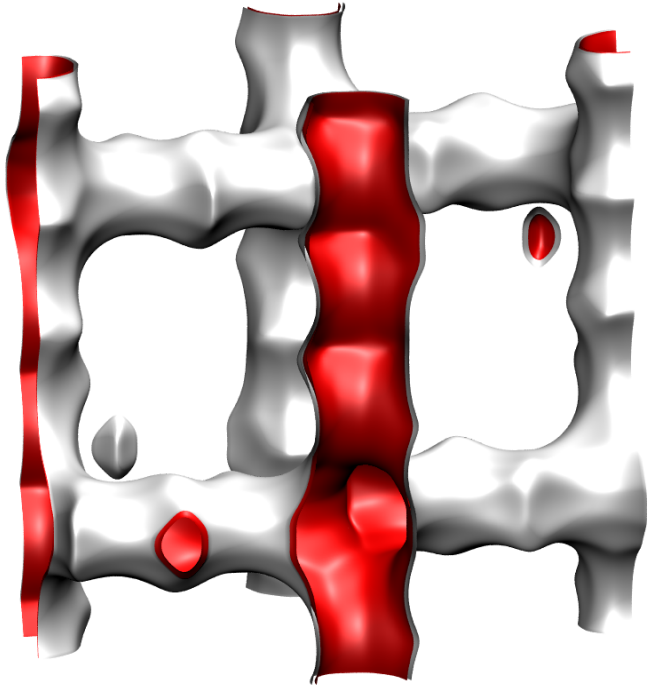

MFI, 300 K, CH4

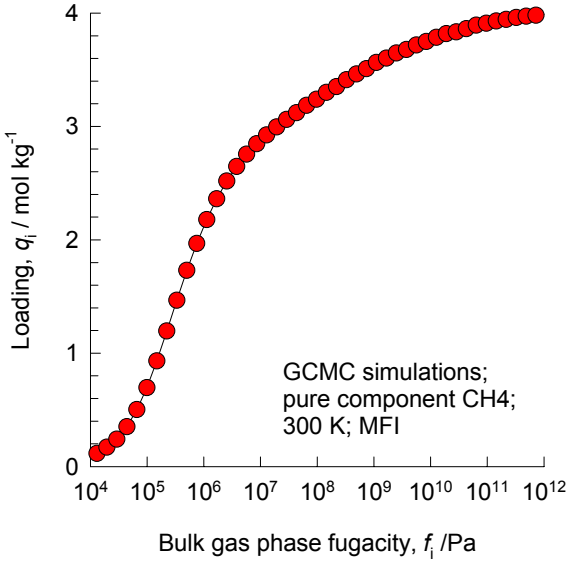
Loading, q_i / mol kg^{-1}
GCMC simulations;
pure component CH4;
300 K; MFI
Bulk gas phase fugacity, f_i /Pa

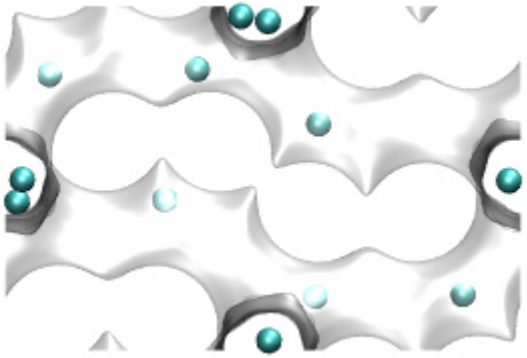

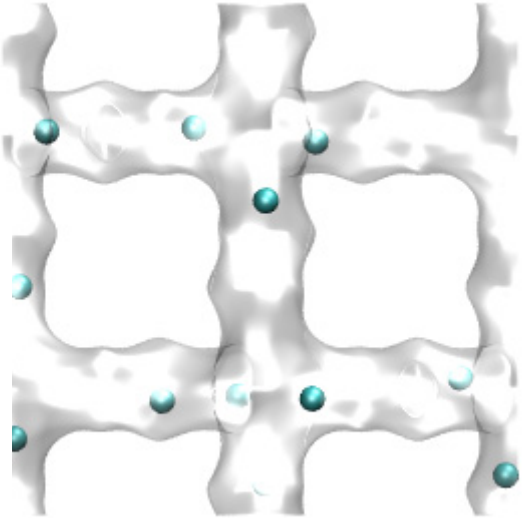

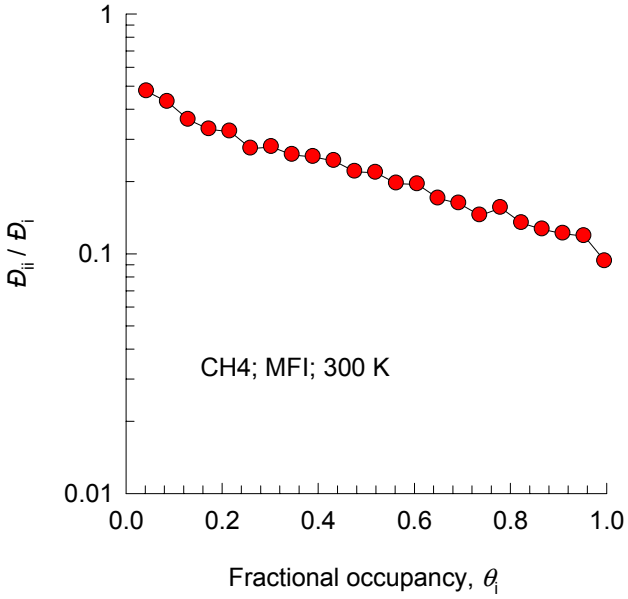
$Đ_{ii}$ / $Đ_i$
CH4; MFI; 300 K
Fractional occupancy, θ_i

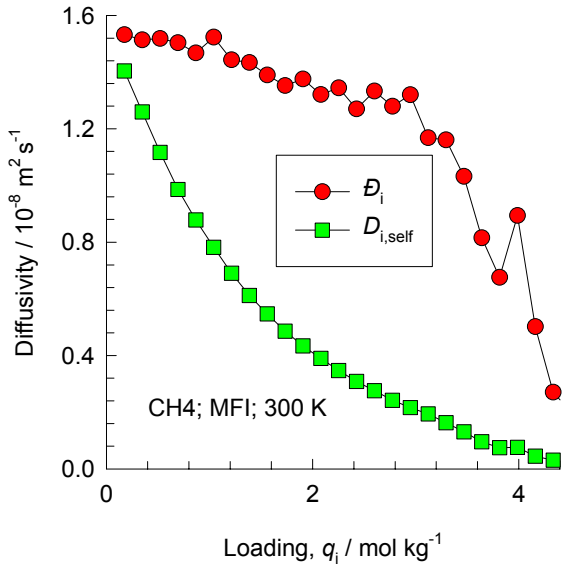
Diffusivity / 10^{-8} m^2 s^{-1}
$Đ_i$
$D_{i,self}$
CH4; MFI; 300 K
Loading, q_i / mol kg^{-1}

MFI, 300 K, CO2

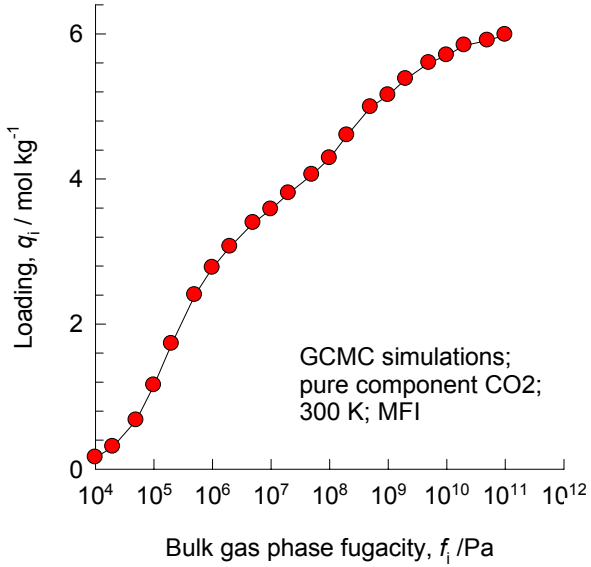
Loading, q_i / mol kg^{-1}
GCMC simulations;
pure component CO2;
300 K; MFI
Bulk gas phase fugacity, f_i /Pa

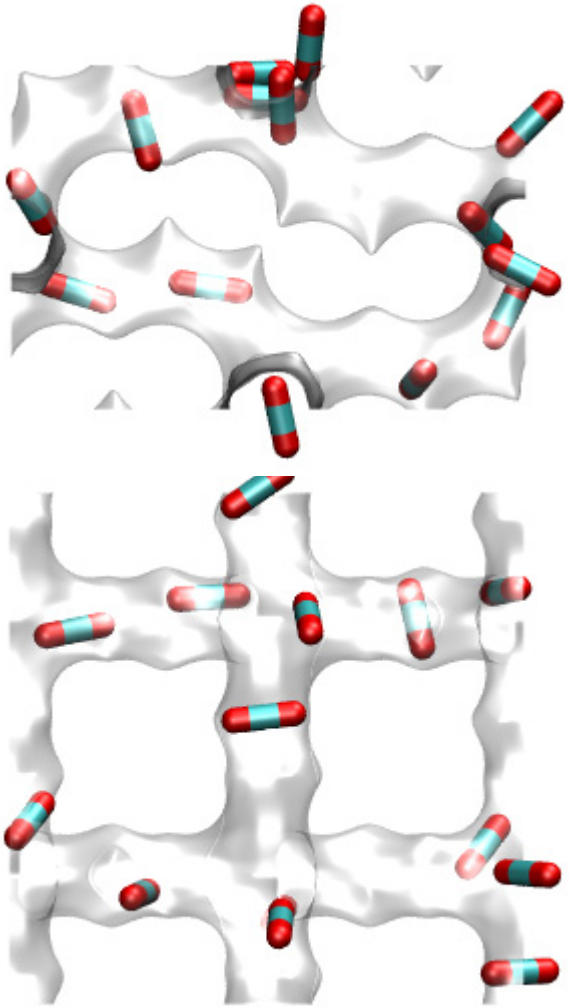

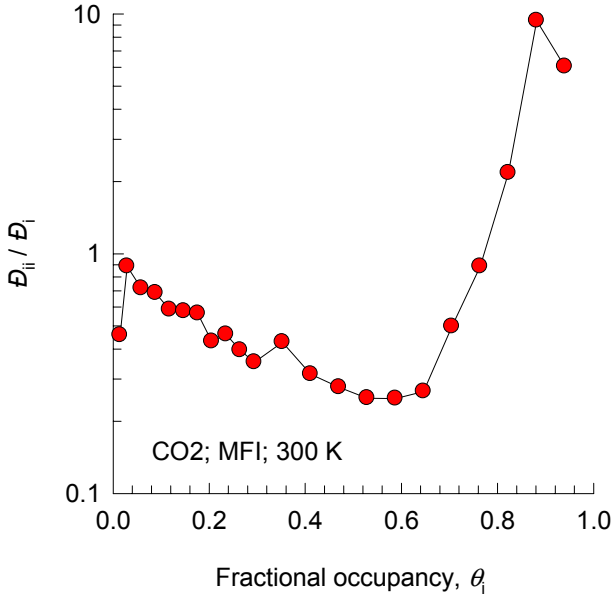
$Đ_{ii}$ / $Đ_i$
CO2; MFI; 300 K
Fractional occupancy, θ_i

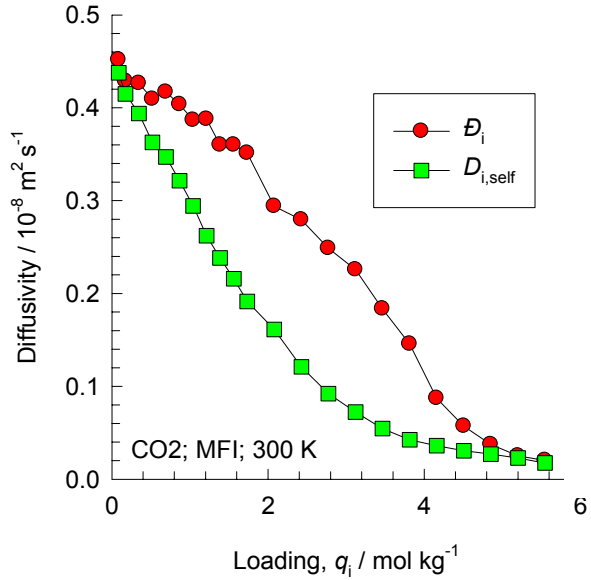
Diffusivity / 10^{-8} m^2 s^{-1}
$Đ_i$
$D_{i,self}$
CO2; MFI; 300 K
Loading, q_i / mol kg^{-1}

MFI, 300 K, Ar

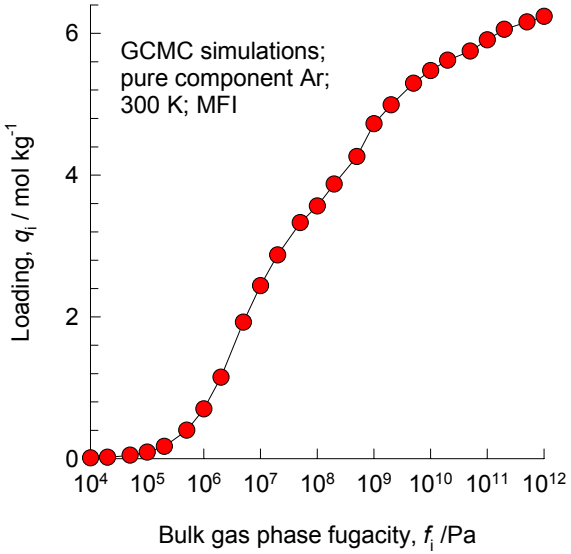
GCMC simulations;
pure component Ar;
300 K; MFI
Loading, q_i / mol kg^{-1}
Bulk gas phase fugacity, f_i /Pa

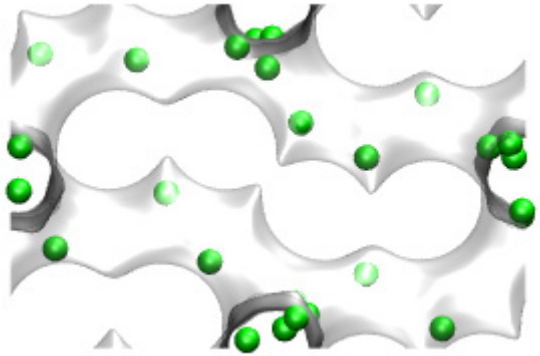

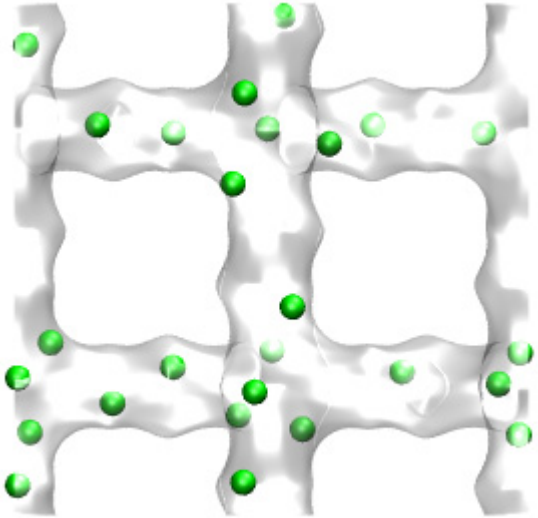

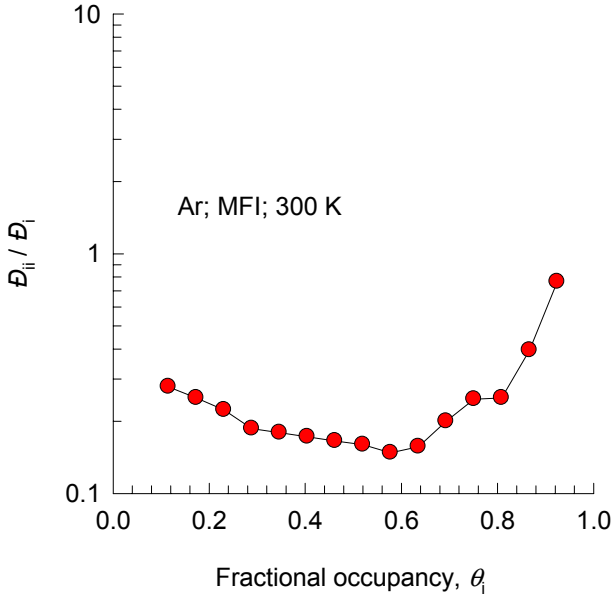
Ar; MFI; 300 K
$Đ_{ii}$ / $Đ_i$
Fractional occupancy, θ_i

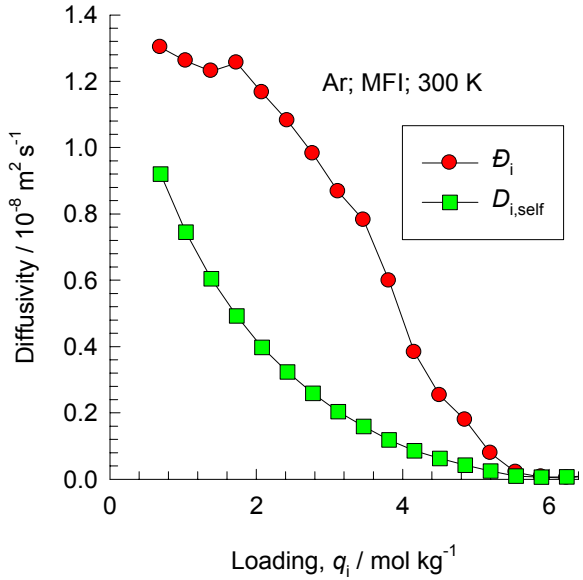
Ar; MFI; 300 K
$Đ_i$
$D_{i,self}$
Diffusivity / 10^{-8} m^2 s^{-1}
Loading, q_i / mol kg^{-1}

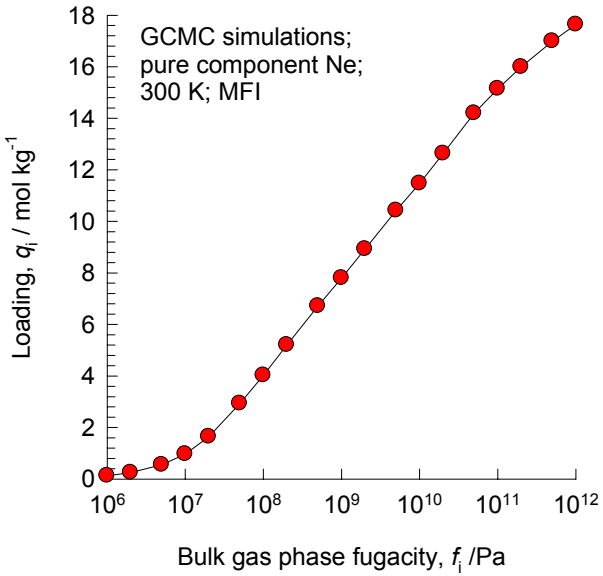
GCMC simulations;
pure component Ne;
300 K; MFI
Loading, q_i / mol kg^{-1}
Bulk gas phase fugacity, f_i /Pa

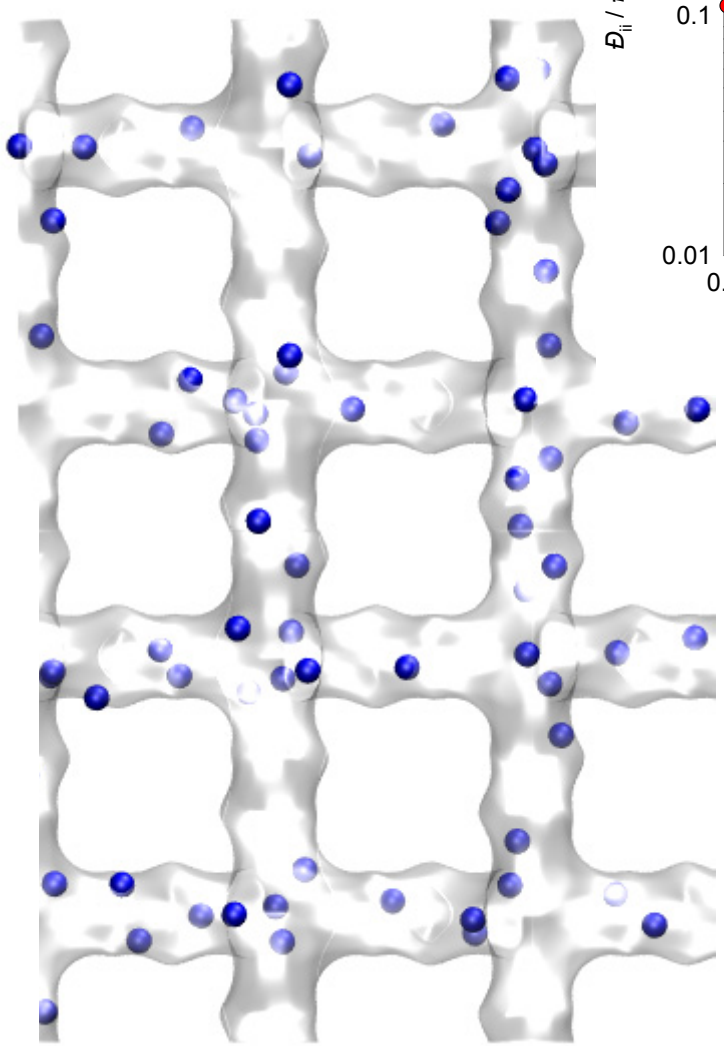

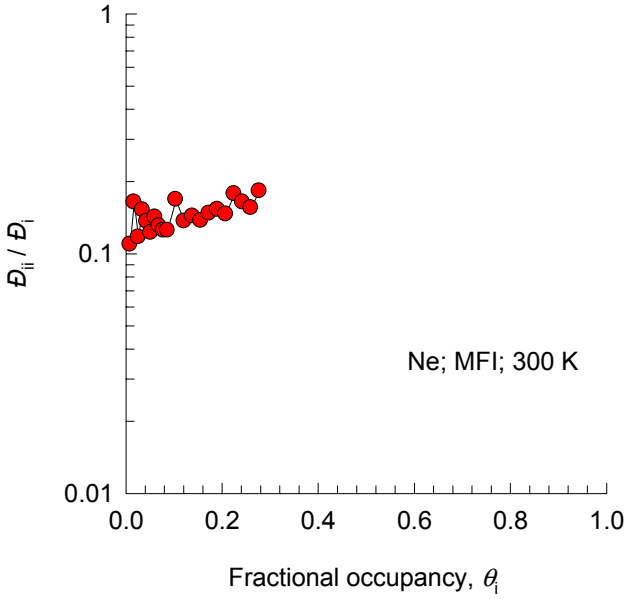
$Đ_{ii}$ / $Đ_i$
Ne; MFI; 300 K
Fractional occupancy, θ_i

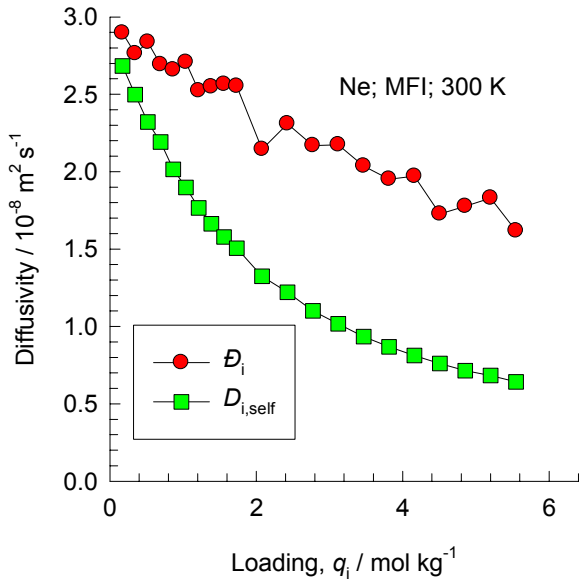
Ne; MFI; 300 K
$Đ_i$
$D_{i,self}$
Diffusivity / 10^{-8} m^2 s^{-1}
Loading, q_i / mol kg^{-1}

MFI, 300 K, Ne

LTA (all silica)

8-ring window of LTA

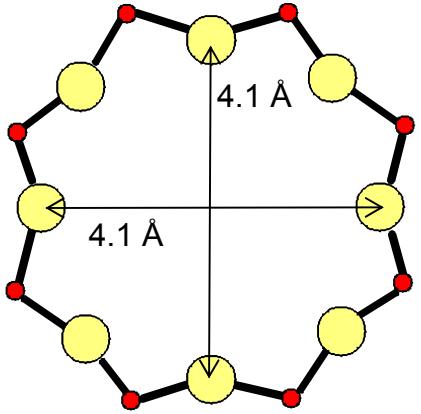

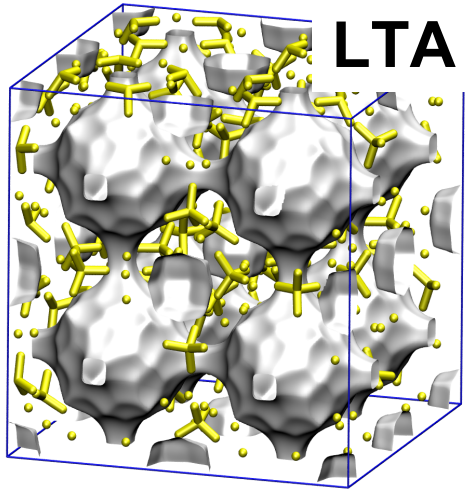

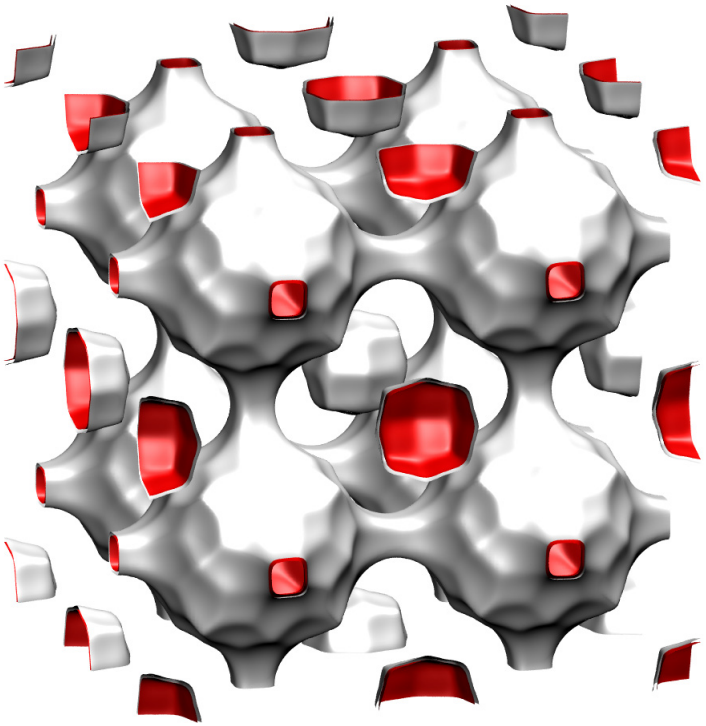

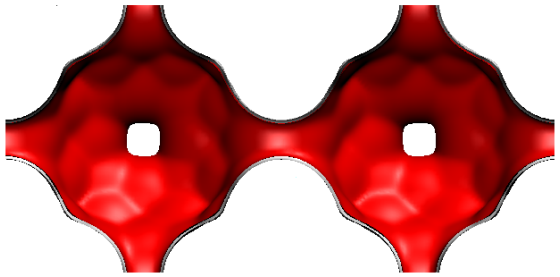

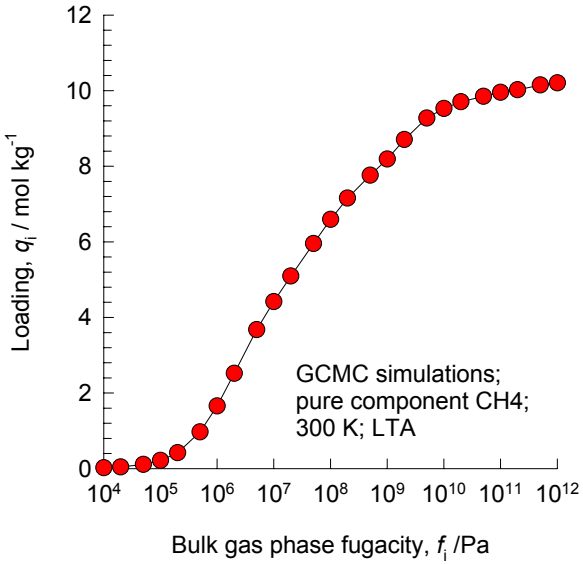
Loading, q_i / mol kg^{-1}
GCMC simulations;
pure component CH4;
300 K; LTA
Bulk gas phase fugacity, f_i /Pa

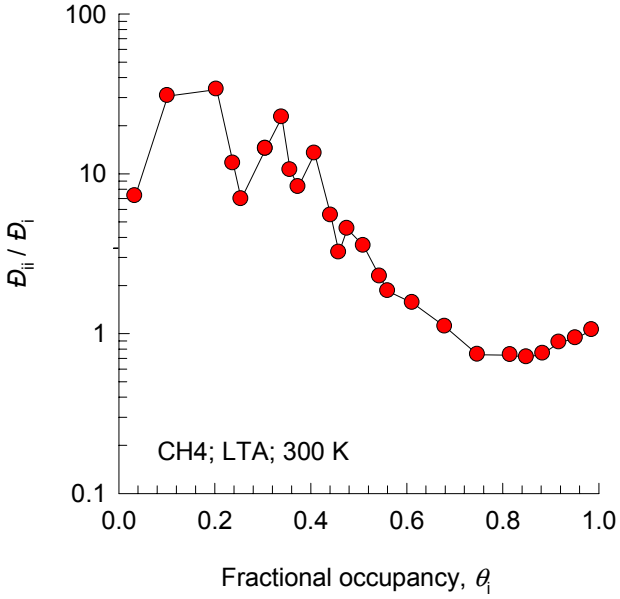
$Đ_{ii}$ / $Đ_i$
CH4; LTA; 300 K
Fractional occupancy, θ_i

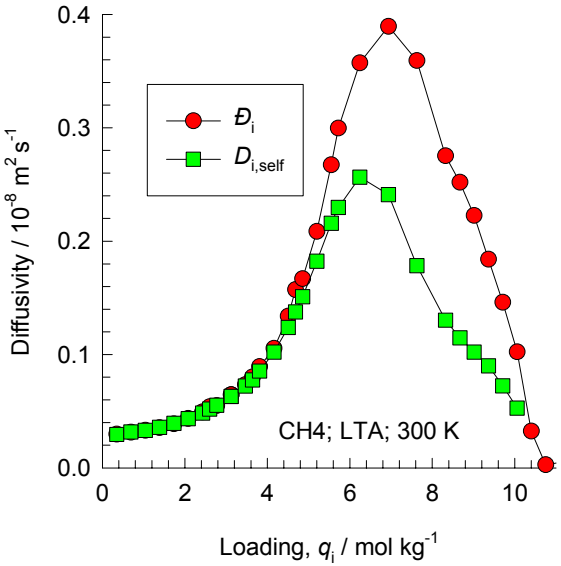
Diffusivity / 10^{-8} m^2 s^{-1}
$Đ_i$
$D_{i,self}$
CH4; LTA; 300 K
Loading, q_i / mol kg^{-1}

LTA, 300 K, CH4

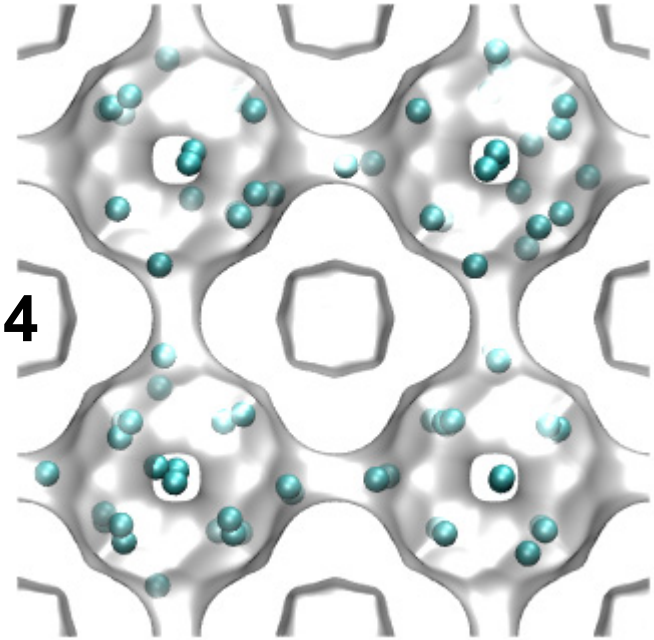

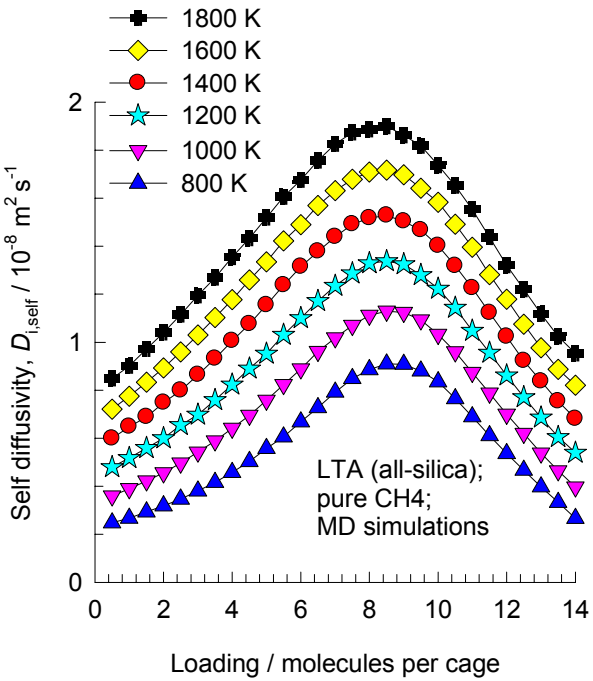

LTA, vary *T*, CH4

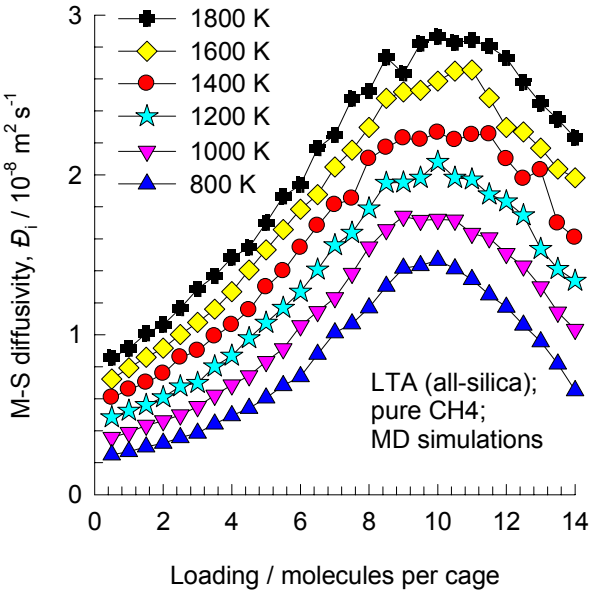

Self-diffusivities

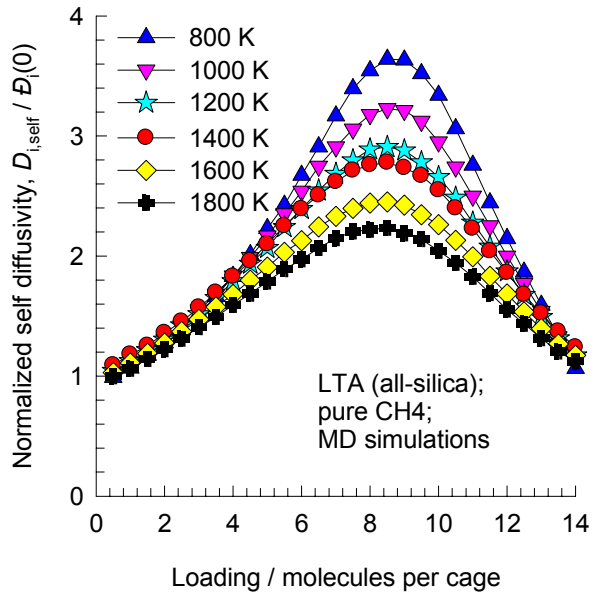

Loading dependence varies with temperature

Maxwell-Stefan diffusivities

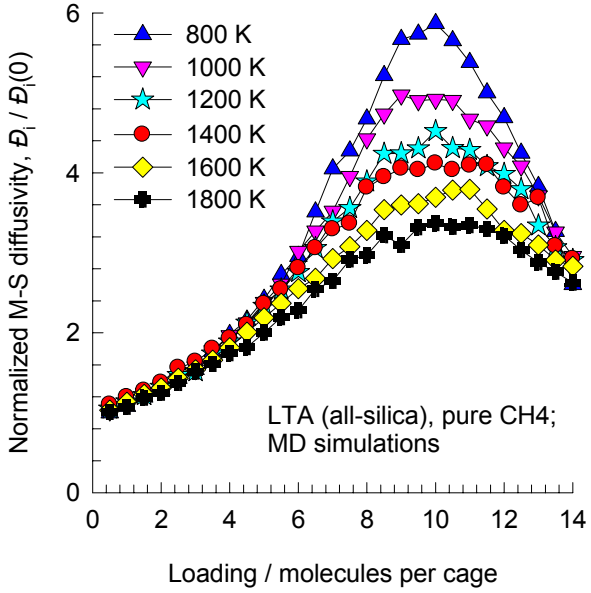

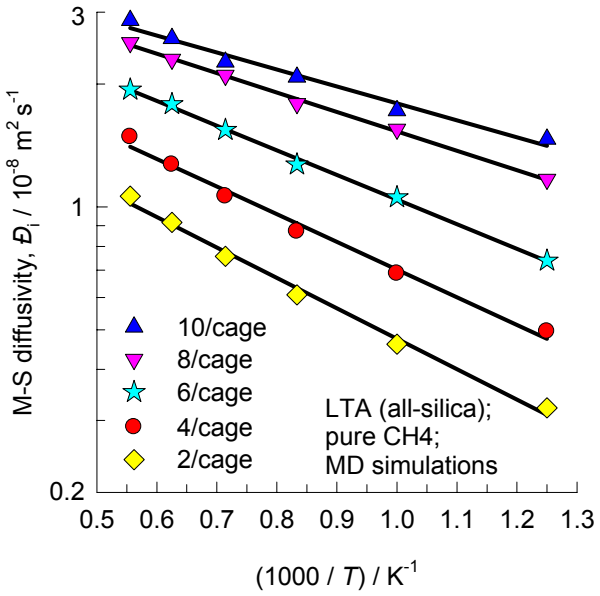

Arrhenius plot

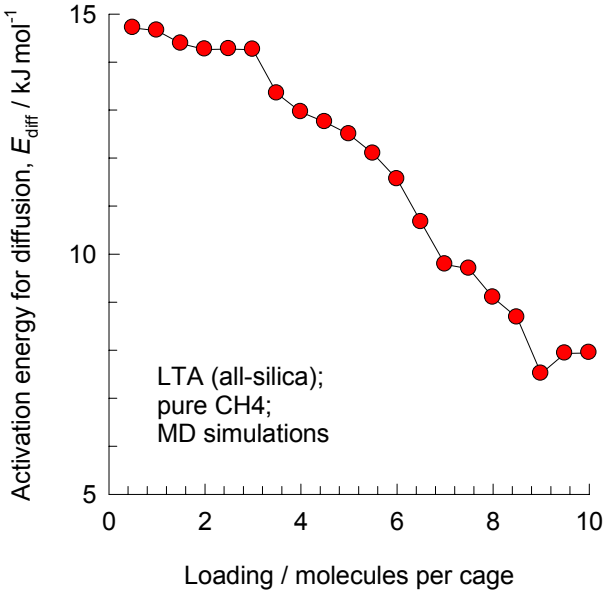

Activation energy is loading dependent

LTA, vary *T*, CH4

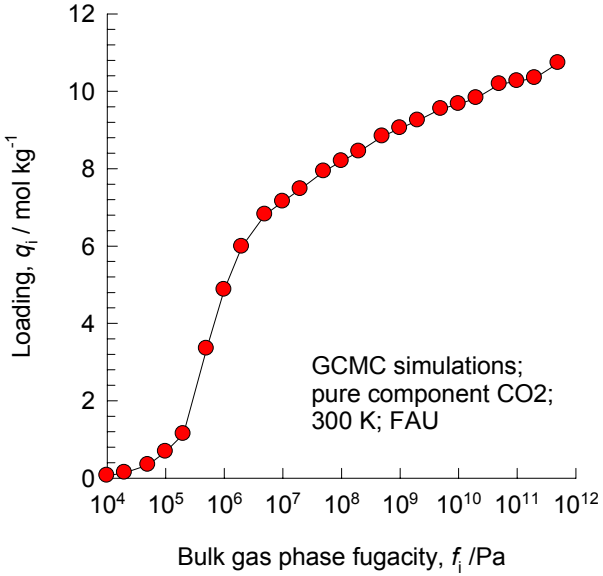
Loading, q_i / mol kg^{-1}
GCMC simulations;
pure component CO2;
300 K; FAU
Bulk gas phase fugacity, f_i /Pa

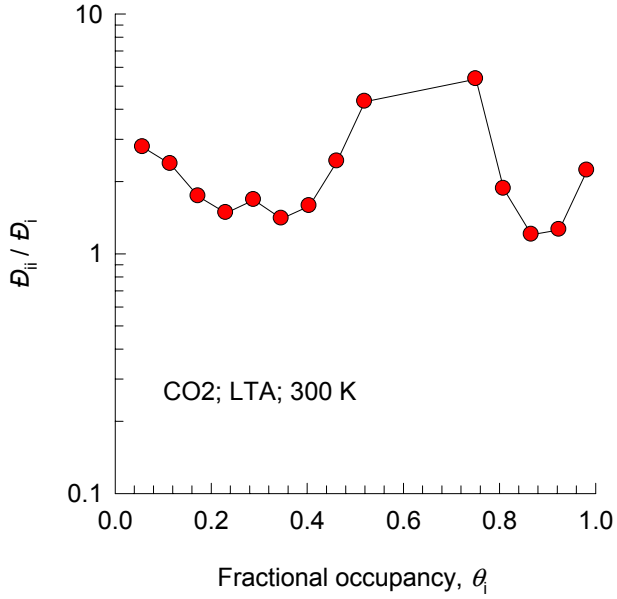
$Đ_{ii}$ / $Đ_i$
CO2; LTA; 300 K
Fractional occupancy, θ_i

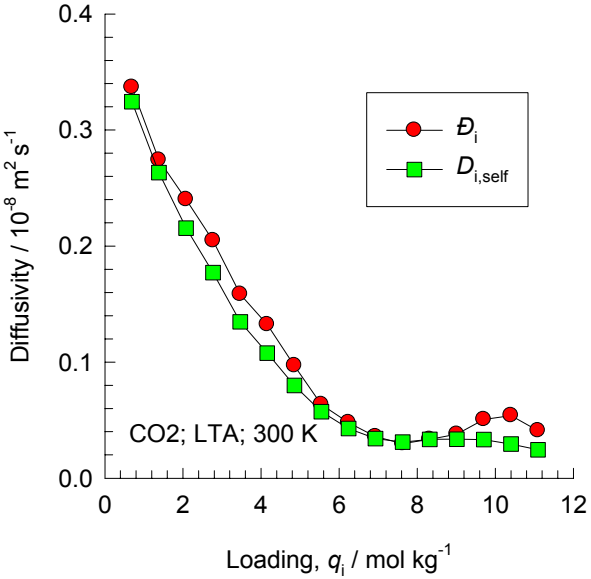
Diffusivity / 10^{-8} m^2 s^{-1}
$Đ_i$
$D_{i,self}$
CO2; LTA; 300 K
Loading, q_i / mol kg^{-1}

LTA, 300 K, CO2

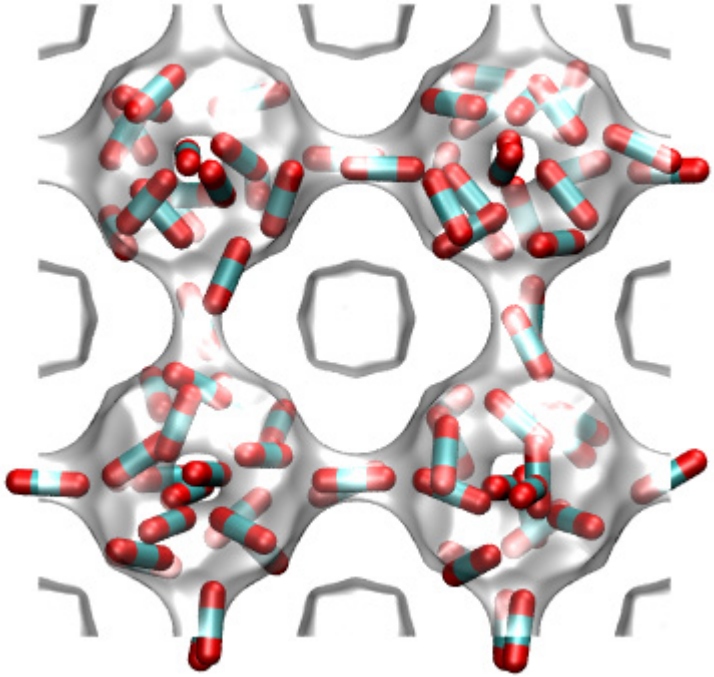

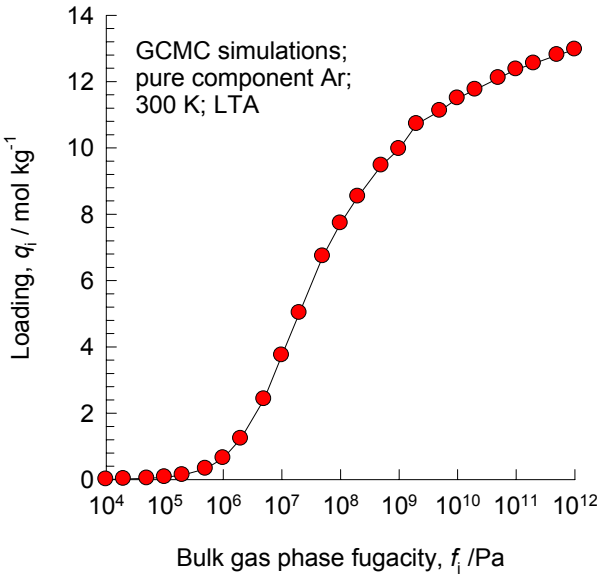
GCMC simulations;
pure component Ar;
300 K; LTA
Loading, q_i / mol kg^{-1}
Bulk gas phase fugacity, f_i /Pa

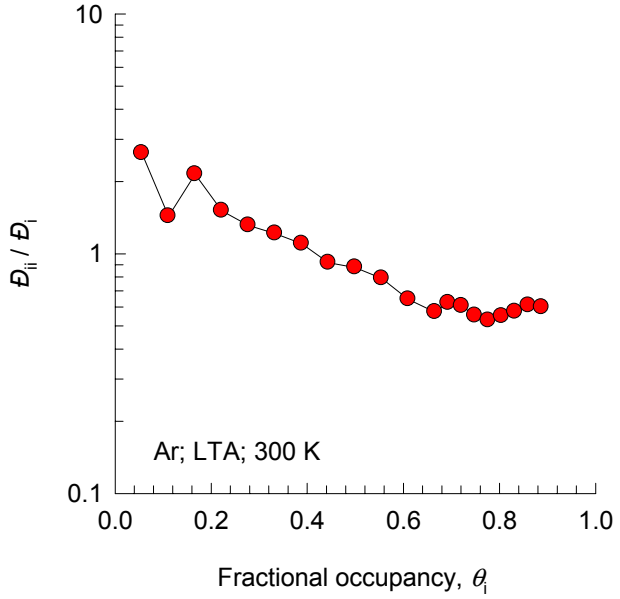
$Đ_i$ / $Đ_i$
Ar; LTA; 300 K
Fractional occupancy, θ_i

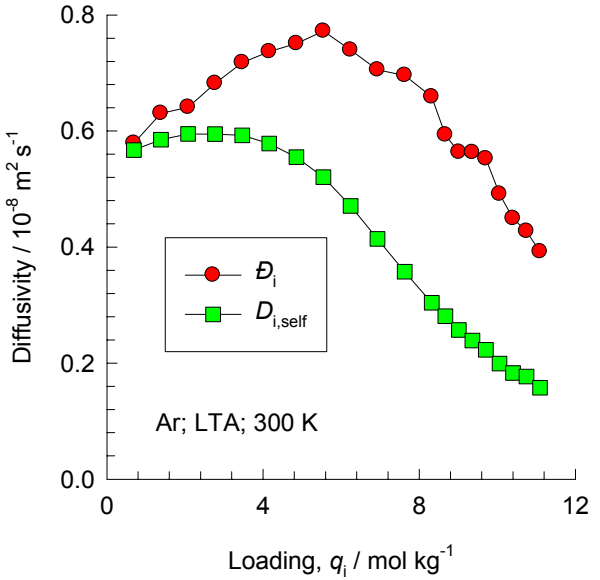
Diffusivity / 10^{-8} m^2 s^{-1}
$Đ_i$
$D_{i,self}$
Ar; LTA; 300 K
Loading, q_i / mol kg^{-1}

LTA, 300 K, Ar

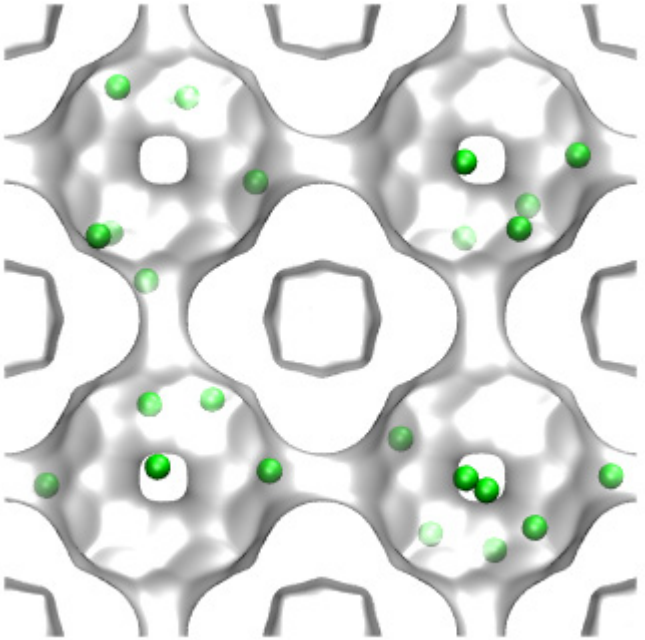

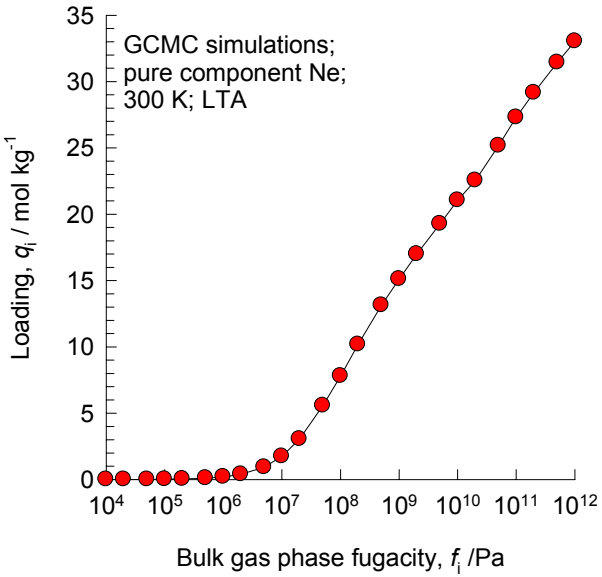
GCMC simulations;
pure component Ne;
300 K; LTA
Loading, q_i / mol kg^{-1}
Bulk gas phase fugacity, f_i /Pa

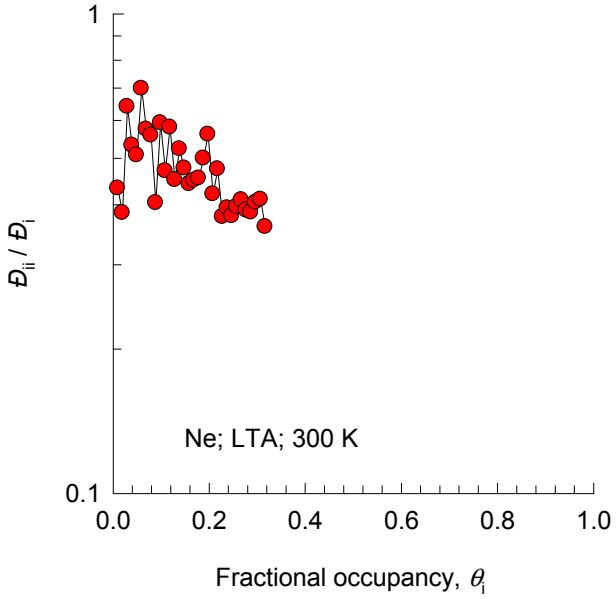
Ne; LTA; 300 K
$Đ_{ii}$ / $Đ_i$
Fractional occupancy, θ_i

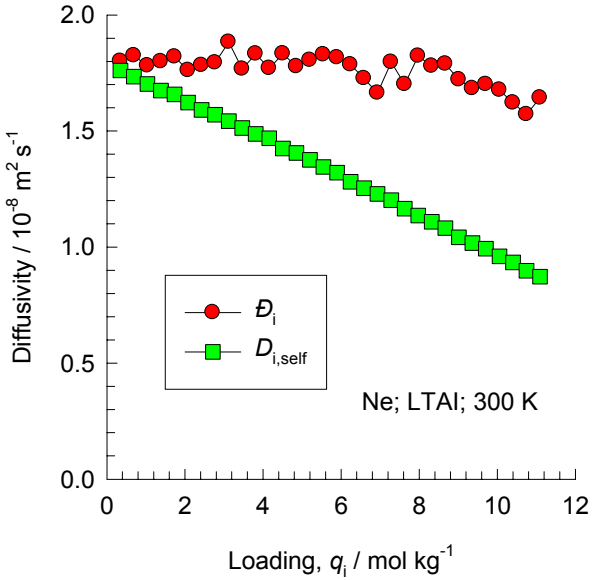
$Đ_i$
$D_{i,self}$
Ne; LTAI; 300 K
Diffusivity / 10^{-8} m^2 s^{-1}
Loading, q_i / mol kg^{-1}

LTA, 300 K, Ne

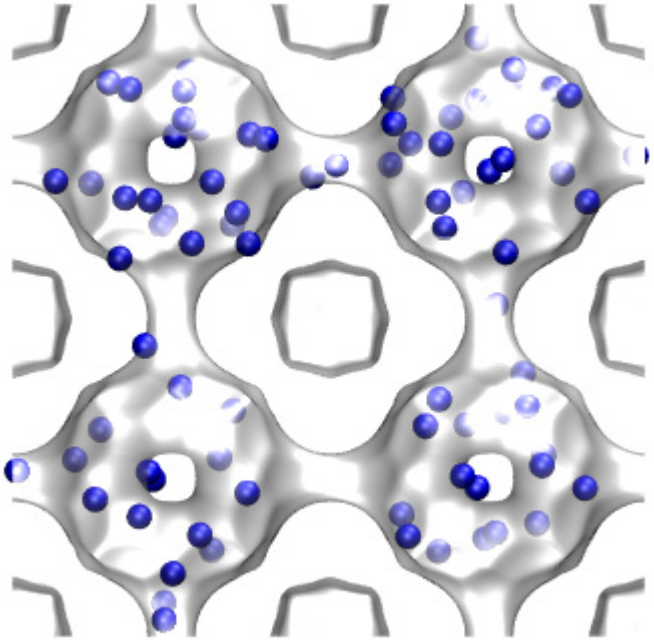

LTA, 300 K, N2

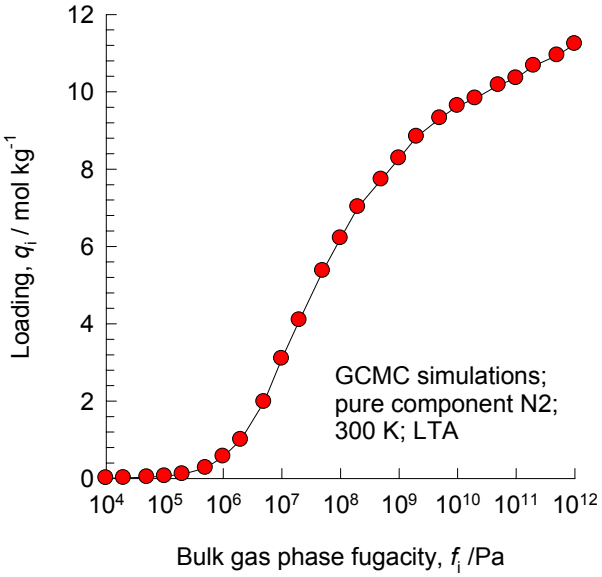
Loading, q_i / mol kg^{-1}
Bulk gas phase fugacity, f_i /Pa
GCMC simulations;
pure component N2;
300 K; LTA

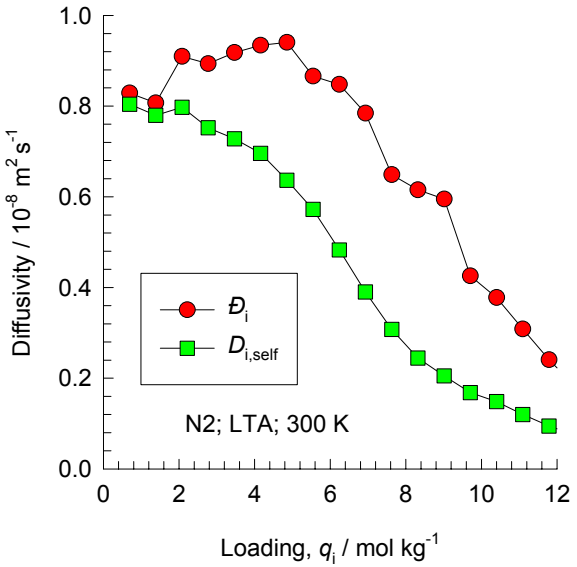
Diffusivity / 10^{-8} m^2 s^{-1}
Loading, q_i / mol kg^{-1}
$Đ_i$
$D_{i,self}$
N2; LTA; 300 K

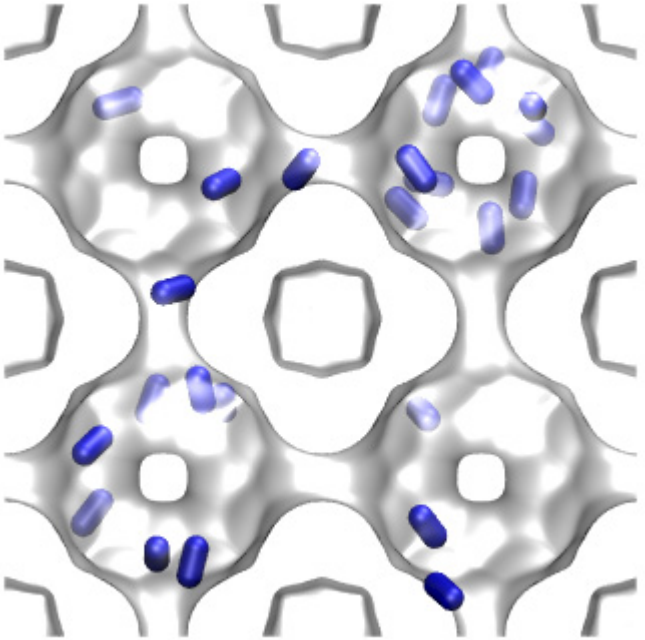

LTA, 300 K, Kr

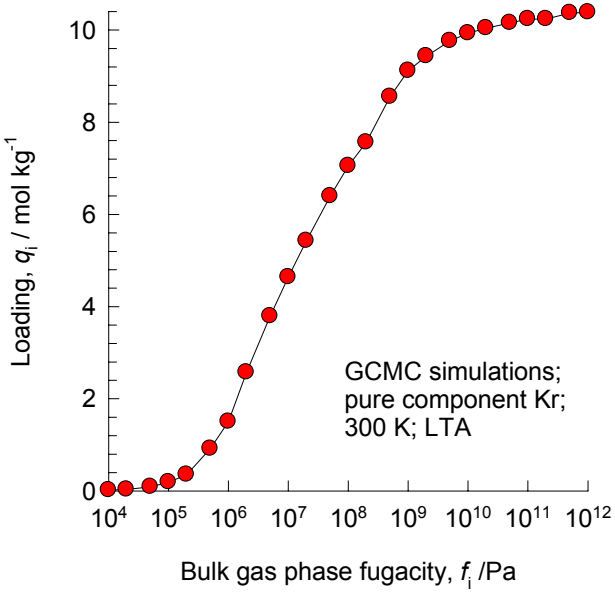
Loading, q_i / mol kg^{-1}
Bulk gas phase fugacity, f_i /Pa
GCMC simulations;
pure component Kr;
300 K; LTA

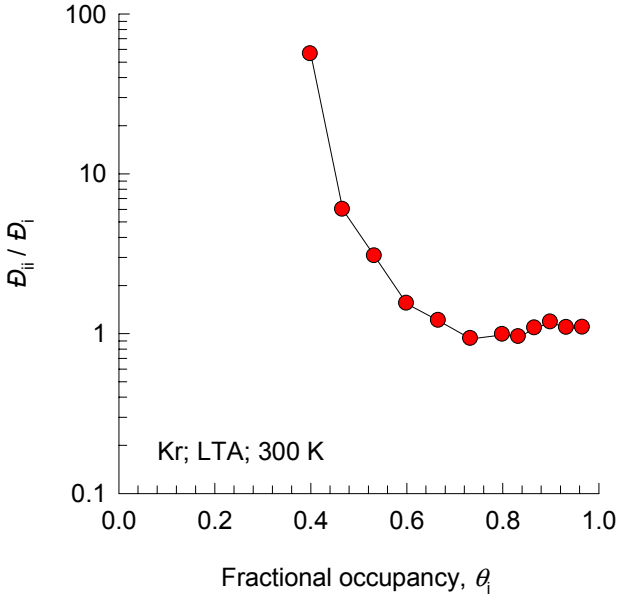
$Đ_{ii}$ / $Đ_i$
Fractional occupancy, θ_i
Kr; LTA; 300 K

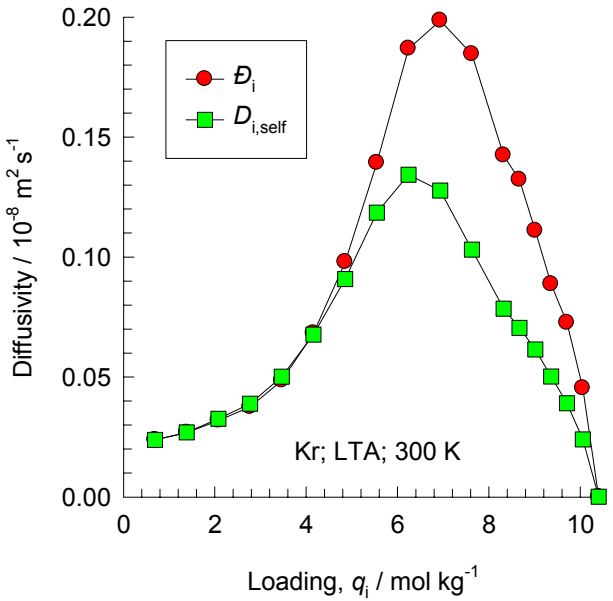
Diffusivity / 10^{-8} m^2 s^{-1}
Loading, q_i / mol kg^{-1}
$Đ_i$
$D_{i,self}$
Kr; LTA; 300 K

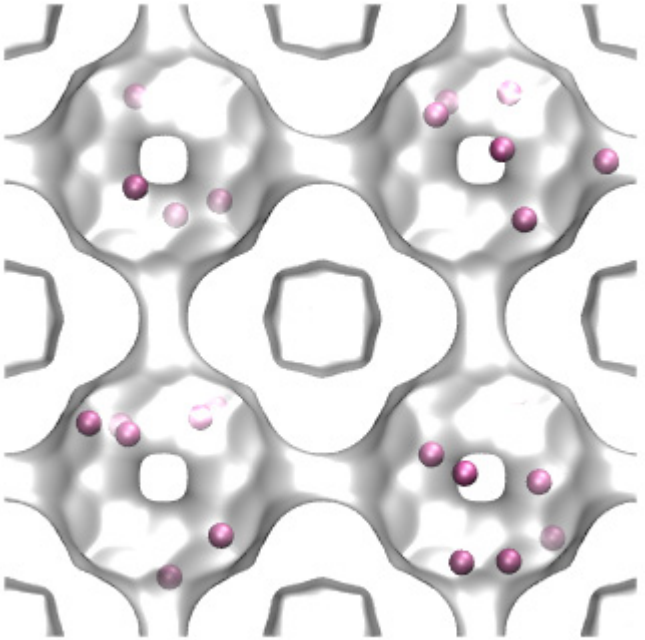

CHA (all silica)

8-ring window of CHA

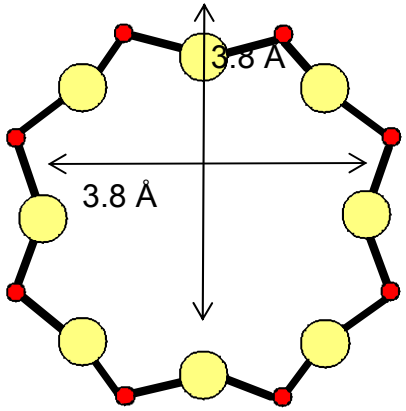

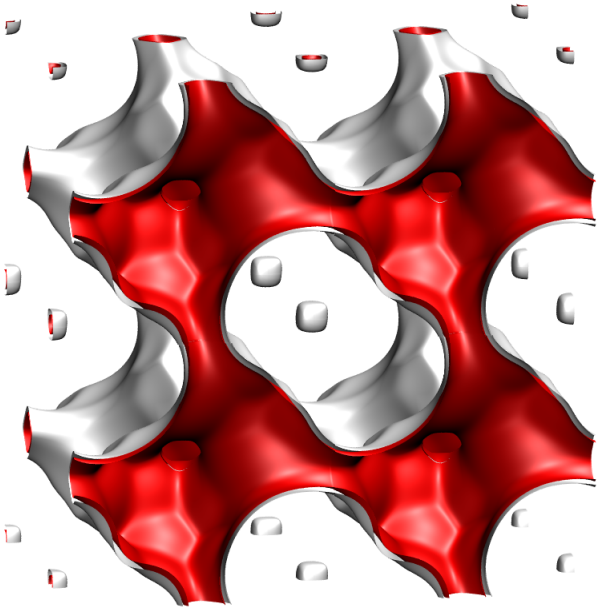

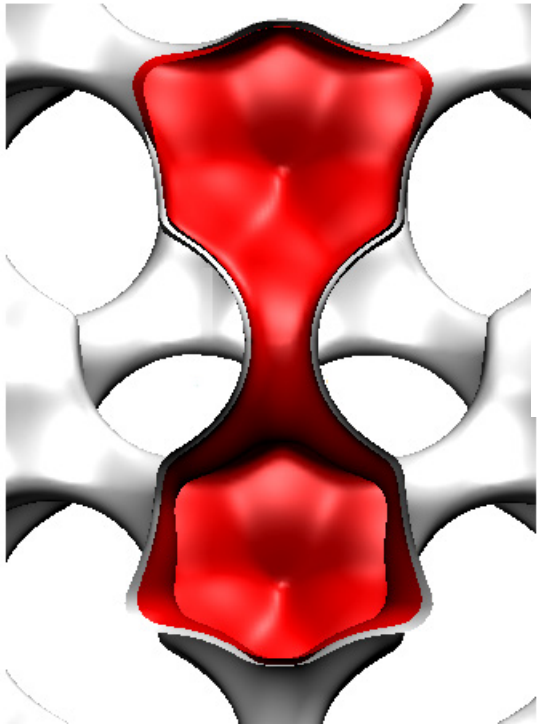

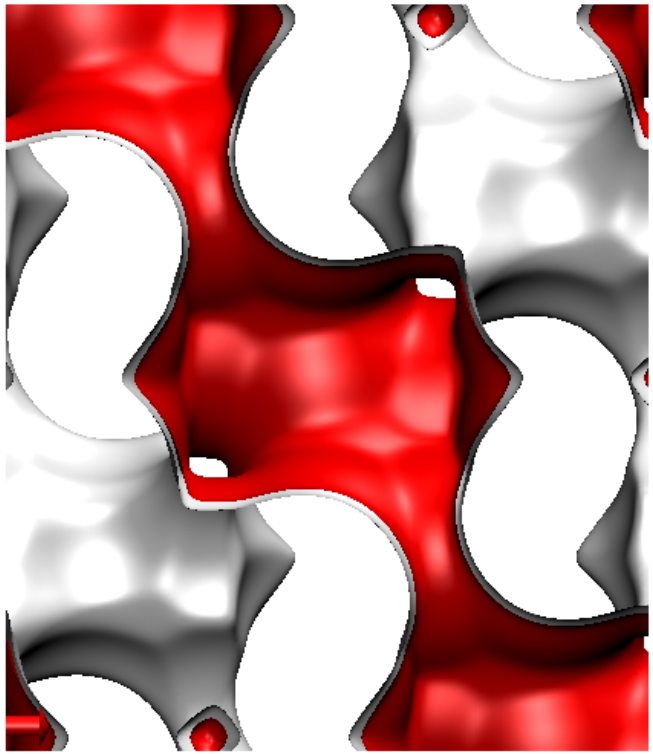

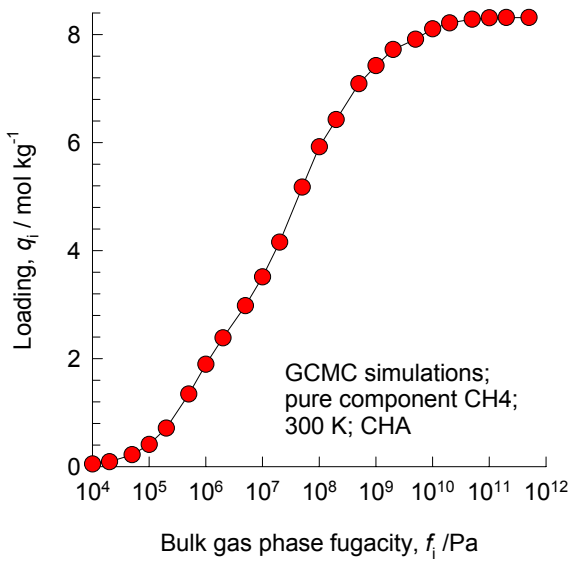
Loading, q_i / mol kg^{-1}
0
2
4
6
8
10^4 10^5 10^6 10^7 10^8 10^9 10^{10} 10^{11} 10^{12}
Bulk gas phase fugacity, f_i /Pa
GCMC simulations;
pure component CH4;
300 K; CHA

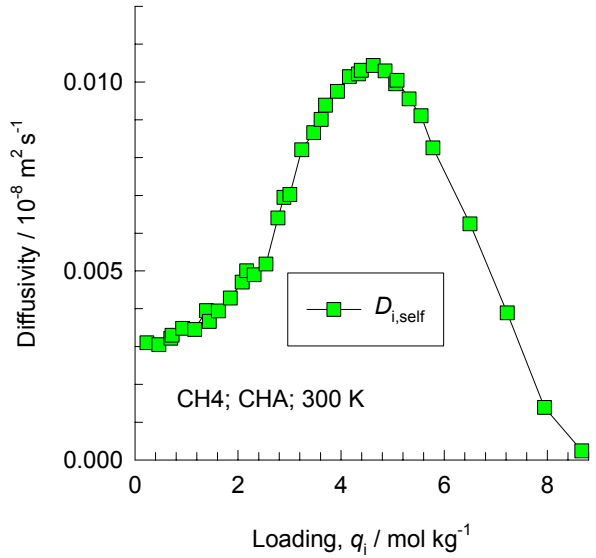
Diffusivity / 10^{-8} m^2 s^{-1}
0.000
0.005
0.010
0
2
4
6
8
Loading, q_i / mol kg^{-1}
$D_{i,self}$
CH4; CHA; 300 K

CHA, 300 K, CH4

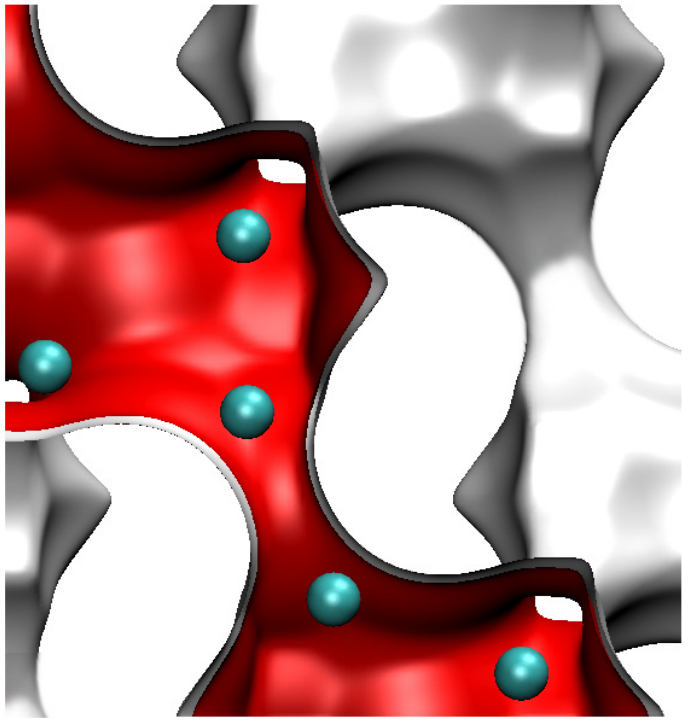

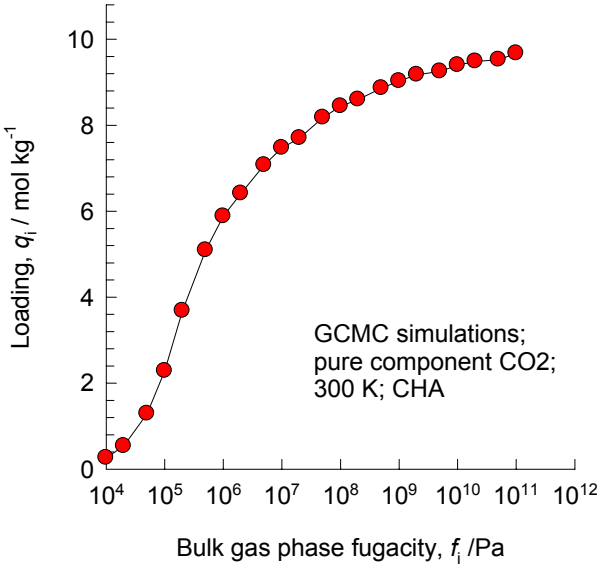
Loading, q_i / mol kg^{-1}
Bulk gas phase fugacity, f_i /Pa
GCMC simulations;
pure component CO2;
300 K; CHA

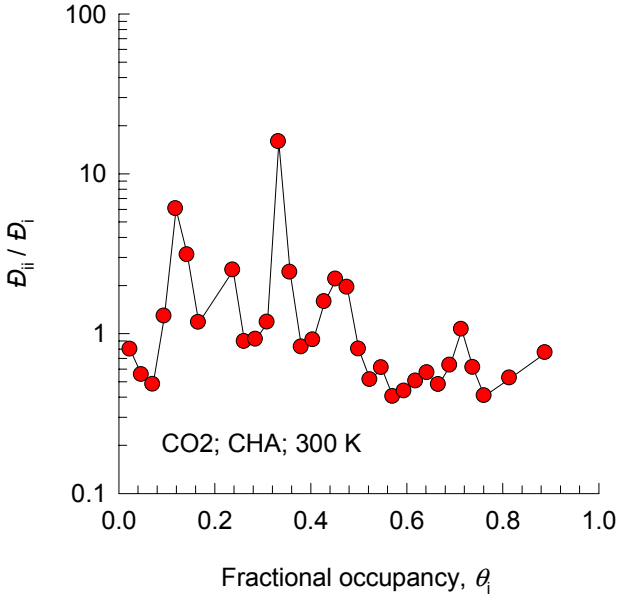
$Đ_{ii}$ / $Đ_i$
Fractional occupancy, θ_i
CO2; CHA; 300 K

CHA, 300 K, CO2

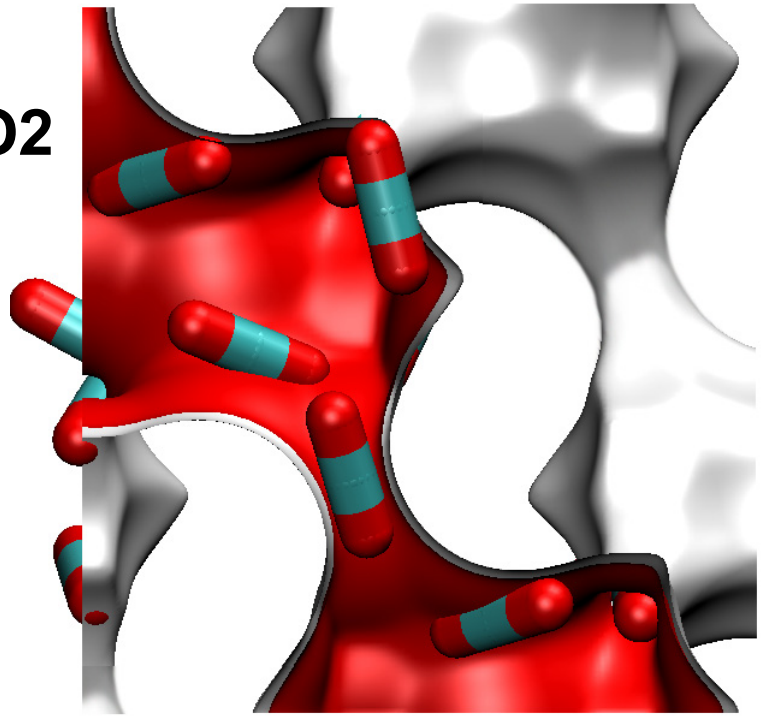

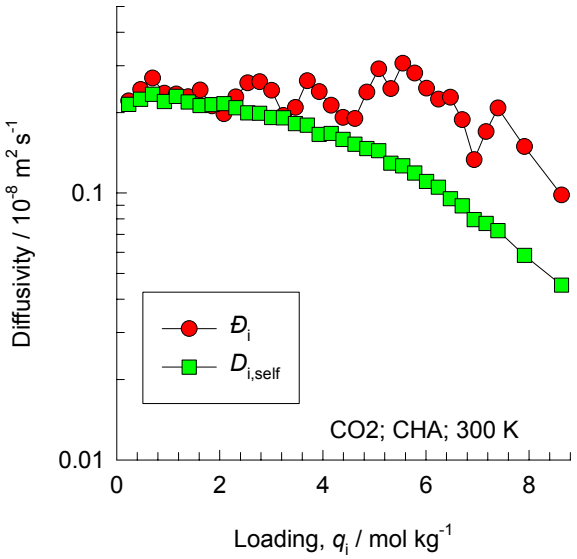
Diffusivity / 10^{-8} m^2 s^{-1}
Loading, q_i / mol kg^{-1}
$Đ_i$
$D_{i,self}$
CO2; CHA; 300 K

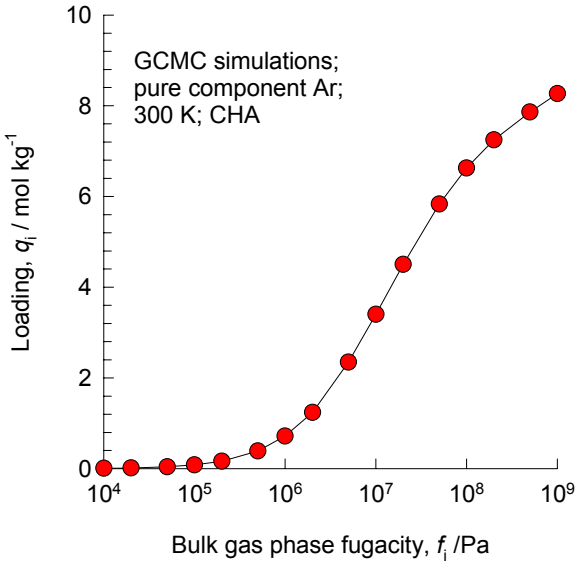
GCMC simulations;
pure component Ar;
300 K; CHA
Loading, q_i / mol kg^{-1}
Bulk gas phase fugacity, f_i /Pa

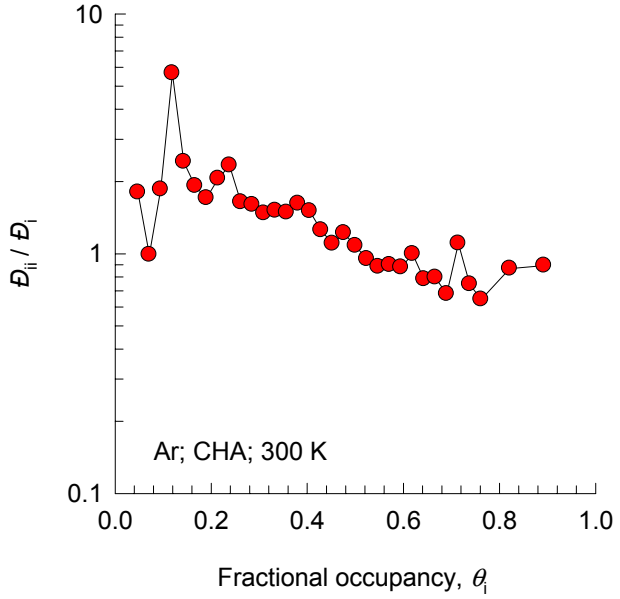
Ar; CHA; 300 K
$Đ_{ii} / Đ_i$
Fractional occupancy, θ_i

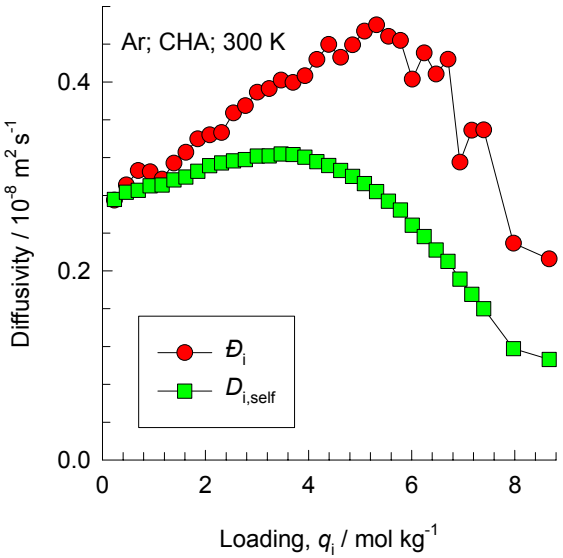
Ar; CHA; 300 K
$Đ_i$
$D_{i,self}$
Diffusivity / 10^{-8} m^2 s^{-1}
Loading, q_i / mol kg^{-1}

CHA, 300 K, Ar

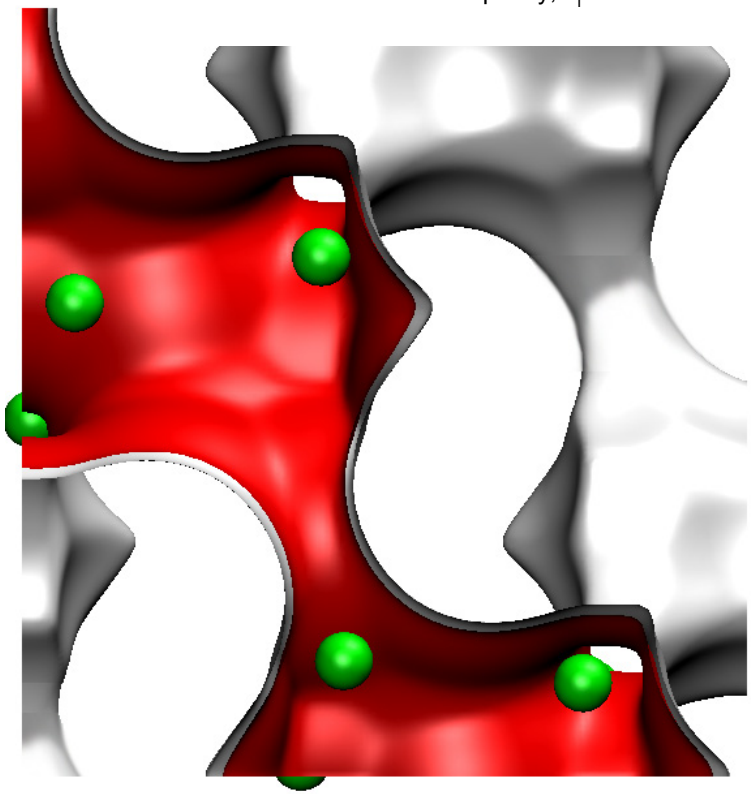

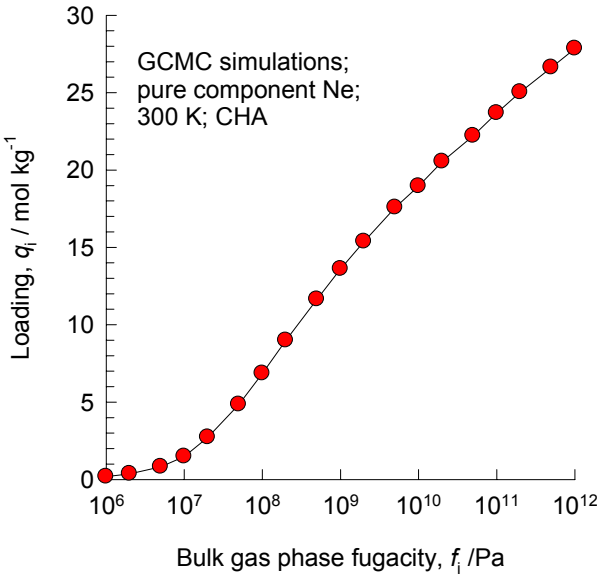
GCMC simulations;
pure component Ne;
300 K; CHA
Loading, q_i / mol kg^{-1}
Bulk gas phase fugacity, f_i /Pa

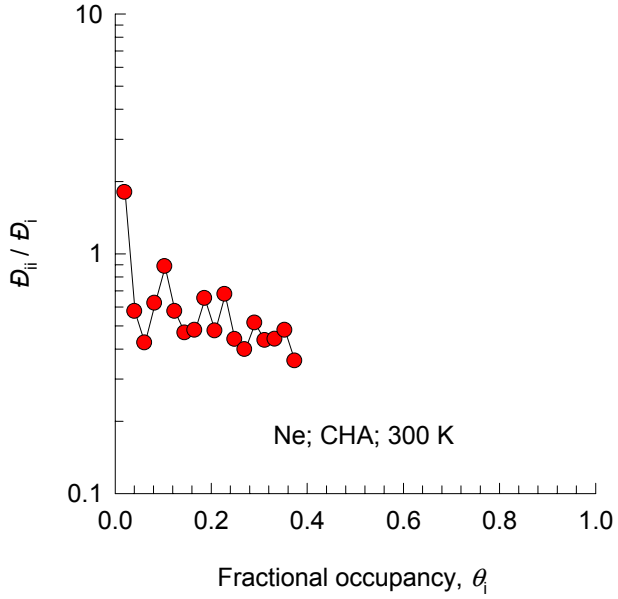
$Đ_{ii}$ / $Đ_i$
Ne; CHA; 300 K
Fractional occupancy, θ_i

CHA, 300 K, Ne

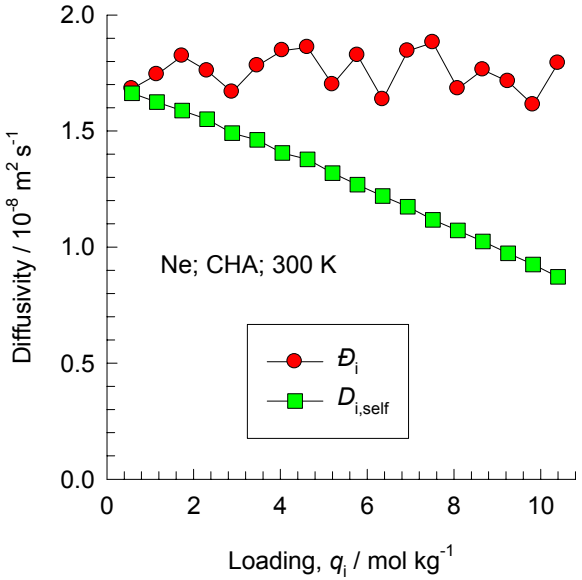
Ne; CHA; 300 K
$Đ_i$
$D_{i,self}$
Diffusivity / 10^{-8} m^2 s^{-1}
Loading, q_i / mol kg^{-1}

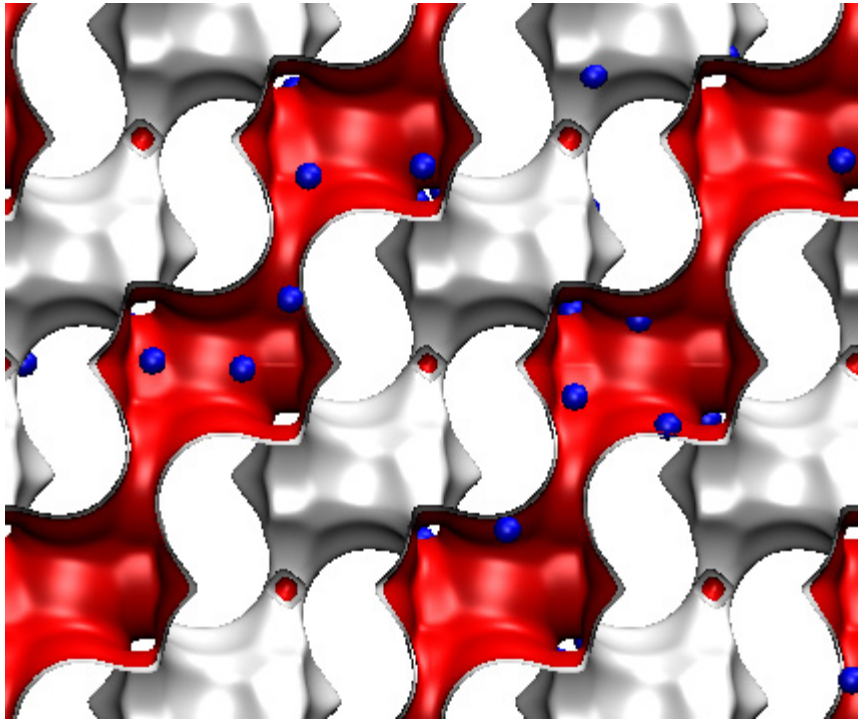

CHA, 300 K, H2

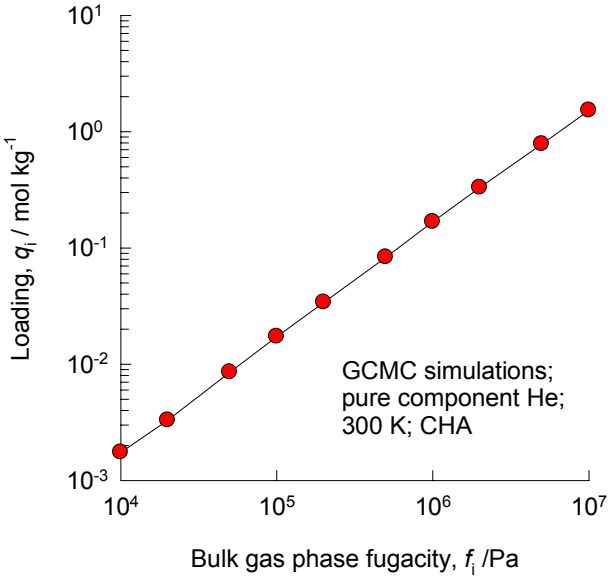
Loading, q_i / mol kg^{-1}
10^{1}
10^{0}
10^{-1}
10^{-2}
10^{-3}
GCMC simulations;
pure component He;
300 K; CHA
10^{4}
10^{5}
10^{6}
10^{7}
Bulk gas phase fugacity, f_i /Pa

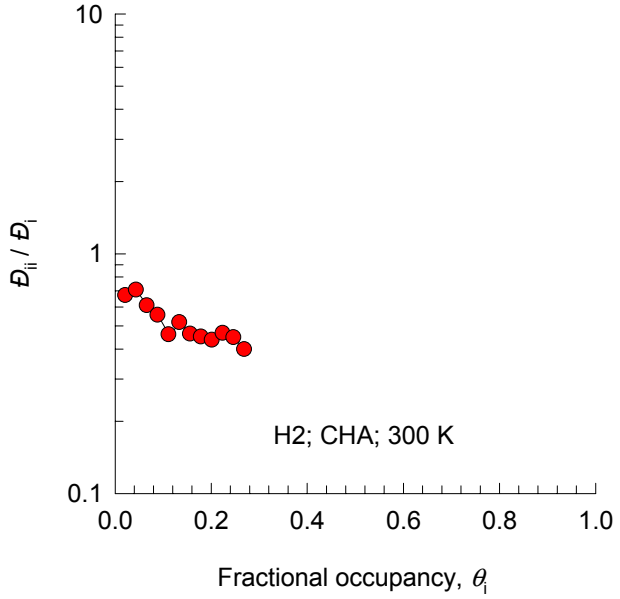
$Đ_{ii}$ / $Đ_i$
10
1
0.1
H2; CHA; 300 K
0.0
0.2
0.4
0.6
0.8
1.0
Fractional occupancy, θ_i

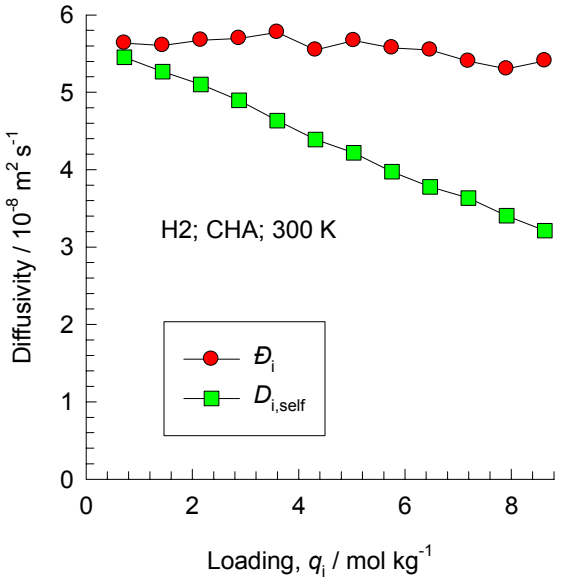
Diffusivity / 10^{-8} m^2 s^{-1}
6
5
4
3
2
1
0
H2; CHA; 300 K
$Đ_i$
$D_{i,self}$
0
2
4
6
8
Loading, q_i / mol kg^{-1}

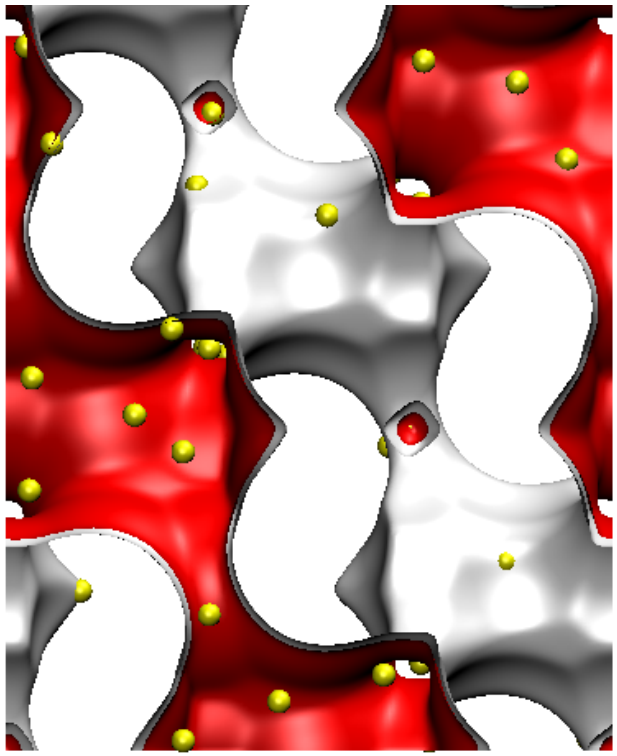

DDR (all silica)

8-ring window of DDR

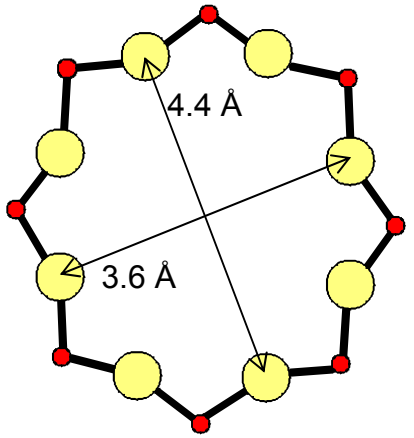

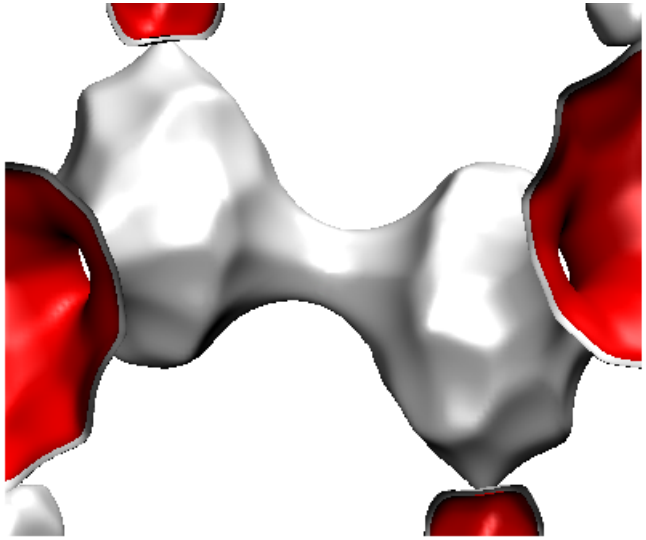

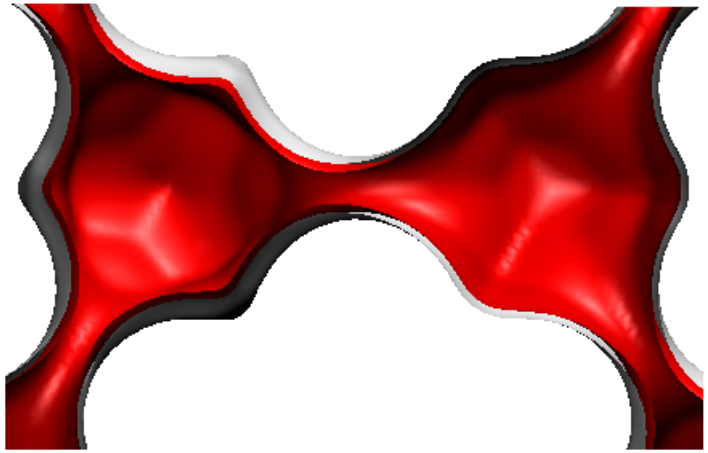

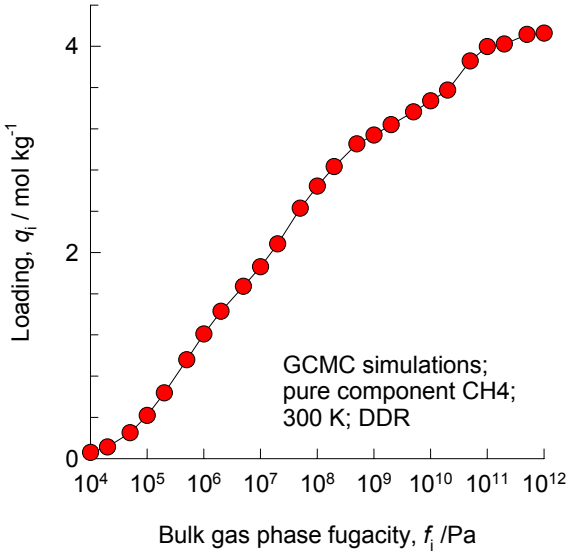
Loading, q_i / mol kg^{-1}
0
2
4
10^4 10^5 10^6 10^7 10^8 10^9 10^{10} 10^{11} 10^{12}
Bulk gas phase fugacity, f_i /Pa
GCMC simulations;
pure component CH4;
300 K; DDR

DDR, 300 K, CH4

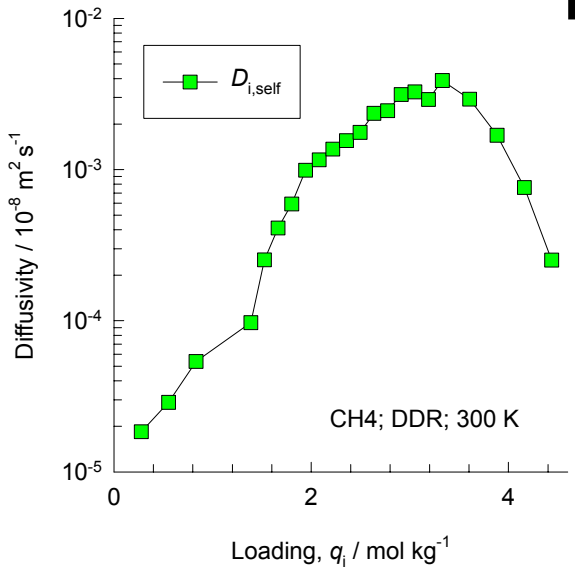
Diffusivity / 10^{-8} m^2 s^{-1}
10^{-2}
10^{-3}
10^{-4}
10^{-5}
$D_{i,self}$
CH4; DDR; 300 K
0
2
4
Loading, q_i / mol kg^{-1}

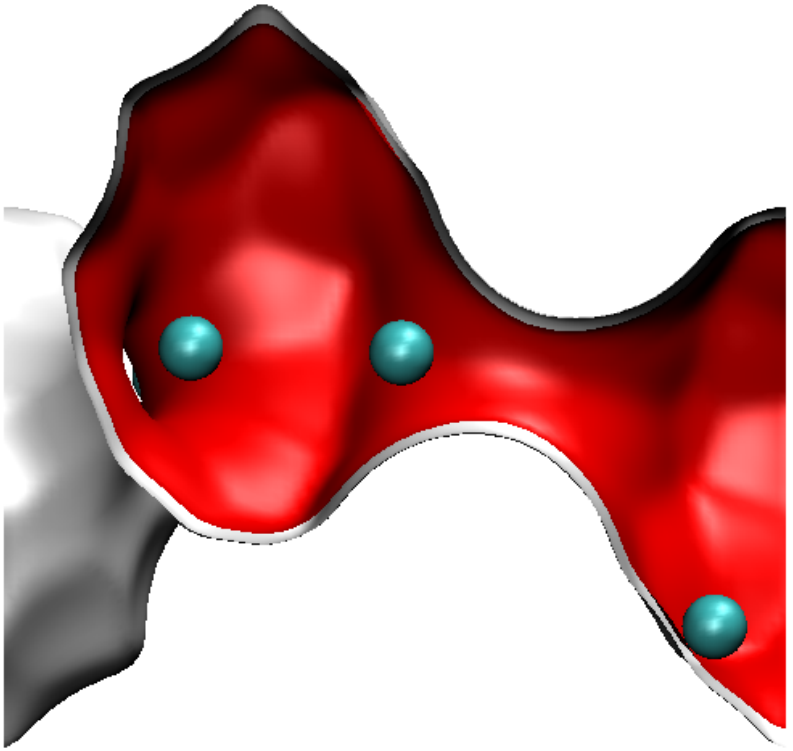

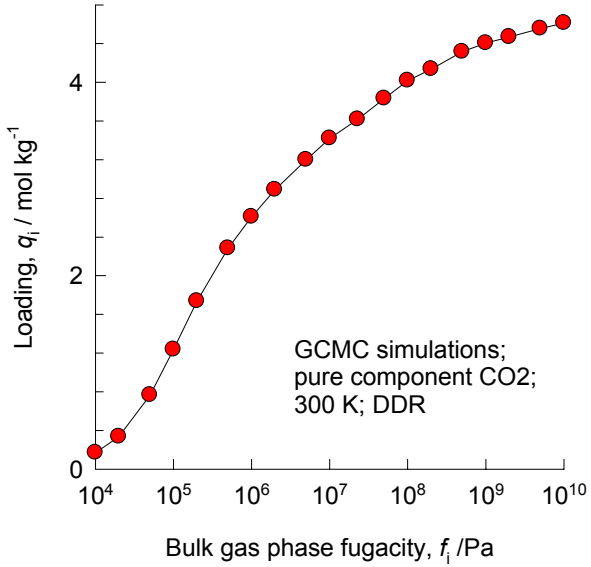
Loading, q_i / mol kg^{-1}
0
2
4
10^4
10^5
10^6
10^7
10^8
10^9
10^{10}
GCMC simulations;
pure component CO2;
300 K; DDR
Bulk gas phase fugacity, f_i /Pa

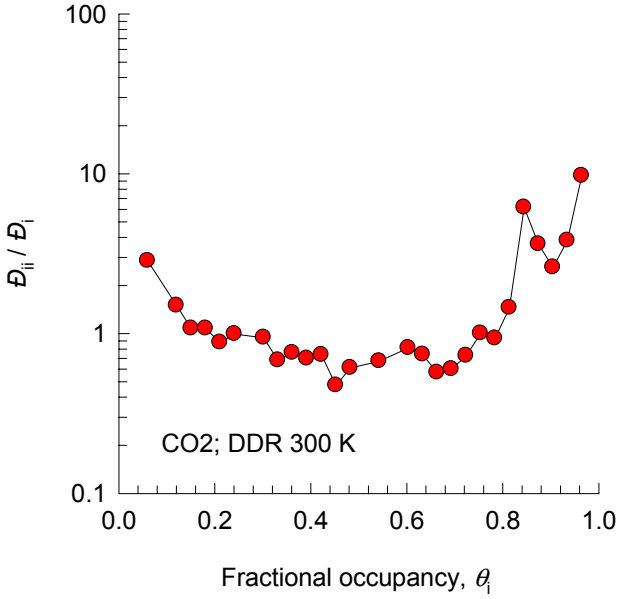
100
10
1
0.1
$Đ_{ii}$ / $Đ_i$
0.0
0.2
0.4
0.6
0.8
1.0
CO2; DDR 300 K
Fractional occupancy, θ_i

DDR, 300 K, CO2

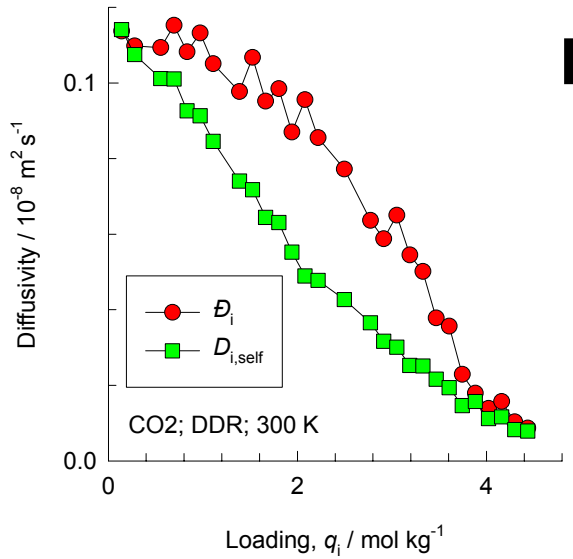
Diffusivity / 10^{-8} m^2 s^{-1}
0.1
0.0
$Đ_i$
$D_{i,self}$
CO2; DDR; 300 K
0
2
4
Loading, q_i / mol kg^{-1}

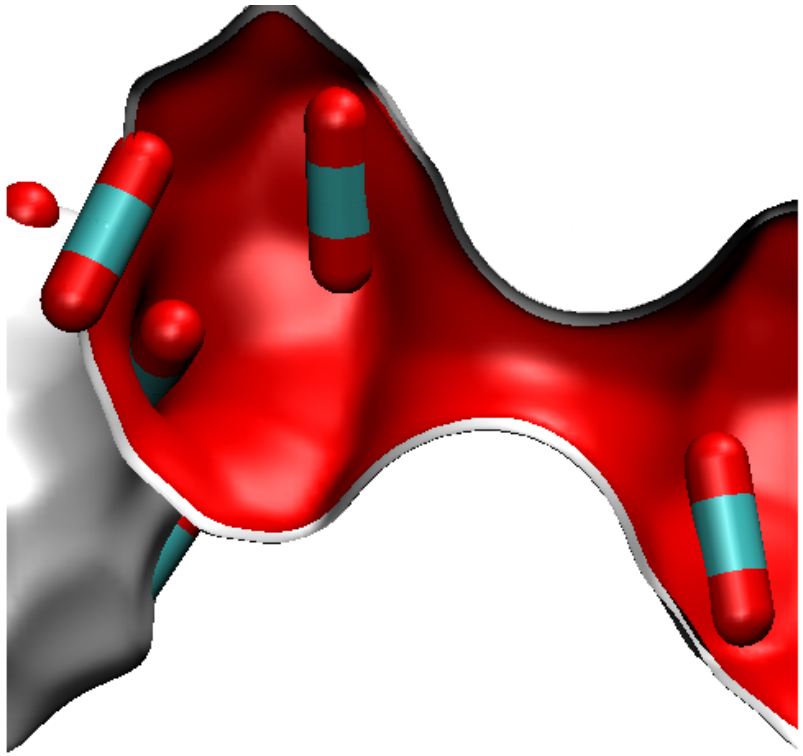

DDR, 300 K, N2

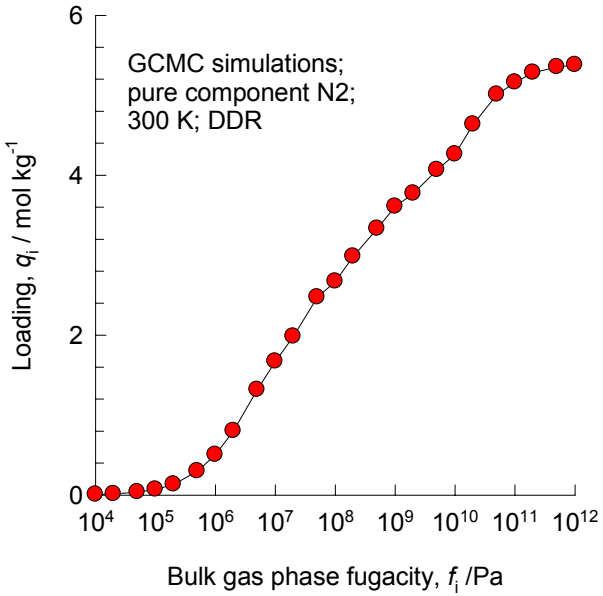
GCMC simulations;
pure component N2;
300 K; DDR
Loading, q_i / mol kg^{-1}
Bulk gas phase fugacity, f_i /Pa

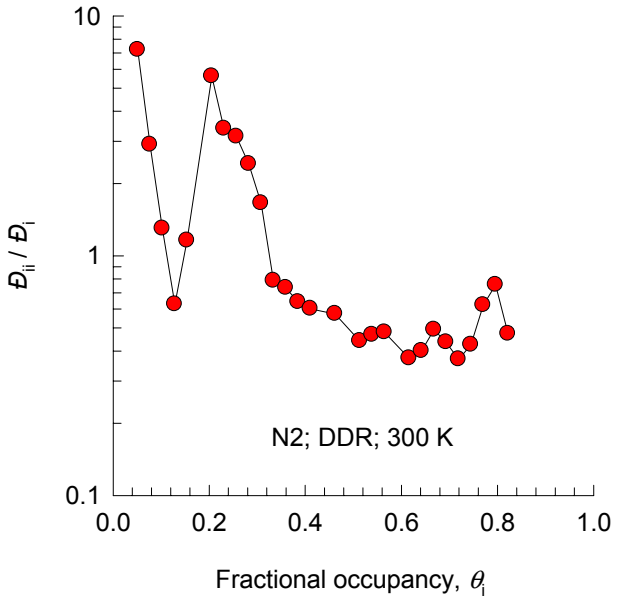
N2; DDR; 300 K
$Đ_{ii} / Đ_i$
Fractional occupancy, θ_i

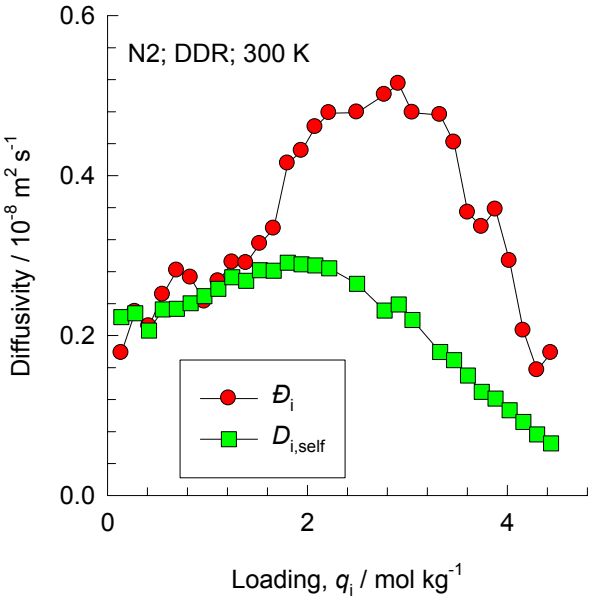
N2; DDR; 300 K
$Đ_i$
$D_{i,self}$
Diffusivity / 10^{-8} m^2 s^{-1}
Loading, q_i / mol kg^{-1}

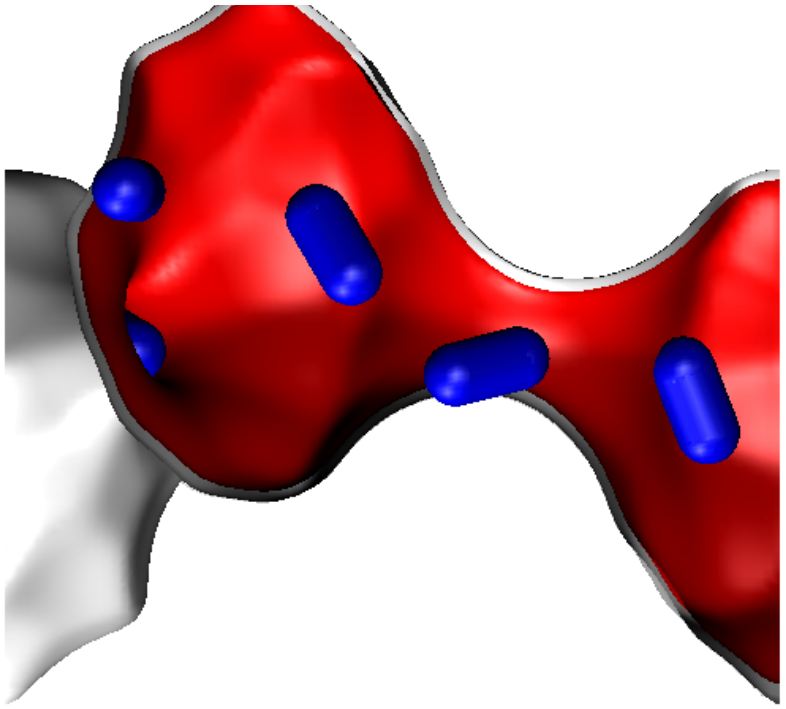

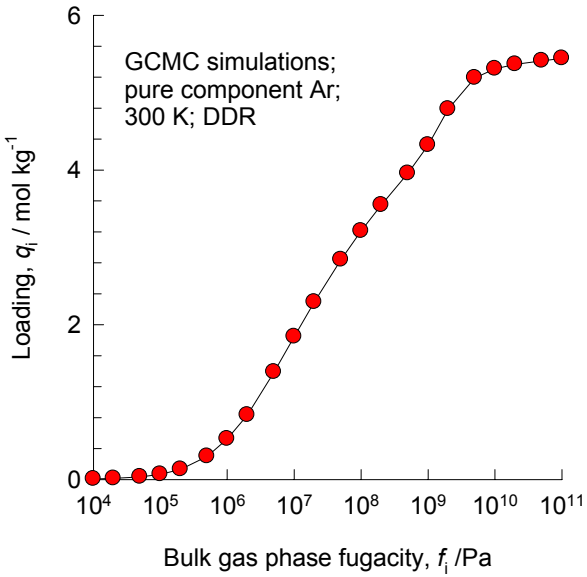
GCMC simulations;
pure component Ar;
300 K; DDR
Loading, q_i / mol kg^{-1}
Bulk gas phase fugacity, f_i /Pa

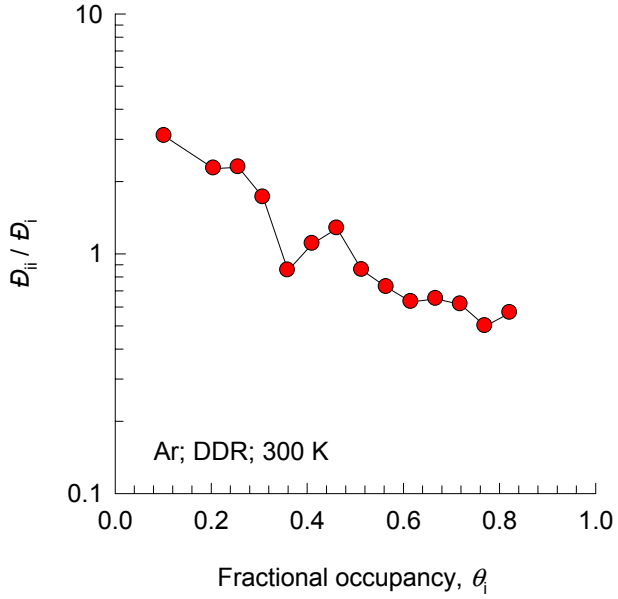
Ar; DDR; 300 K
$Đ_{ii}$ / $Đ_i$
Fractional occupancy, θ_i

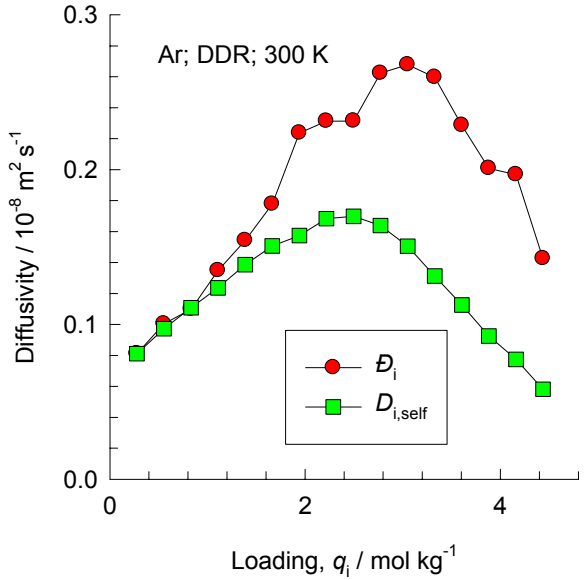
Ar; DDR; 300 K
$Đ_i$
$D_{i,self}$
Diffusivity / 10^{-8} m^2 s^{-1}
Loading, q_i / mol kg^{-1}

DDR, 300 K, Ar

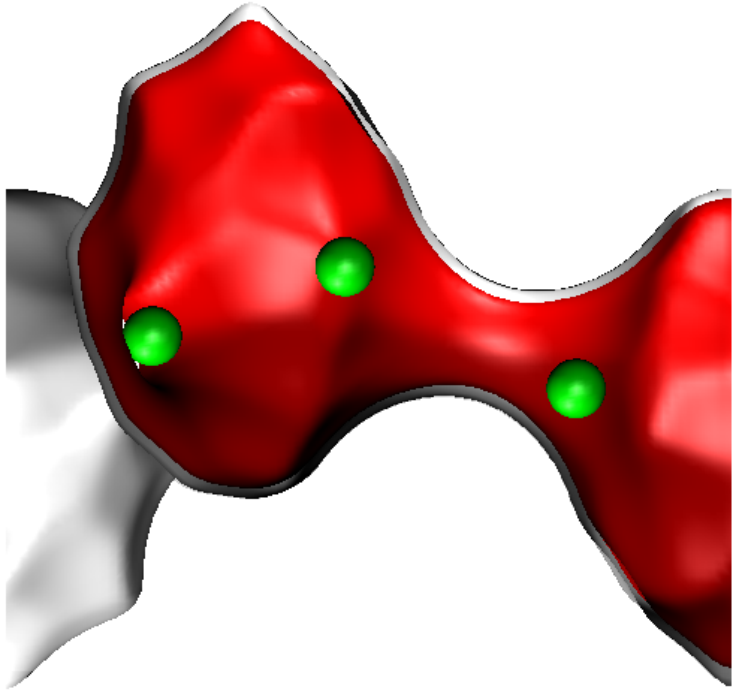

DDR, 300 K, Ne

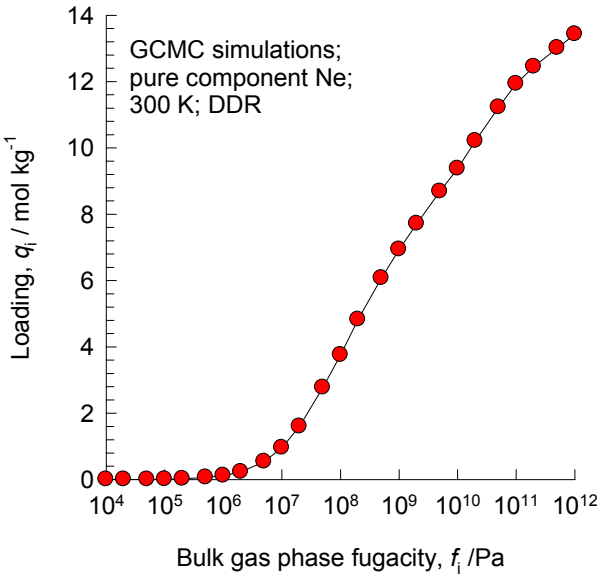
GCMC simulations;
pure component Ne;
300 K; DDR
Loading, q_i / mol kg^{-1}
Bulk gas phase fugacity, f_i /Pa

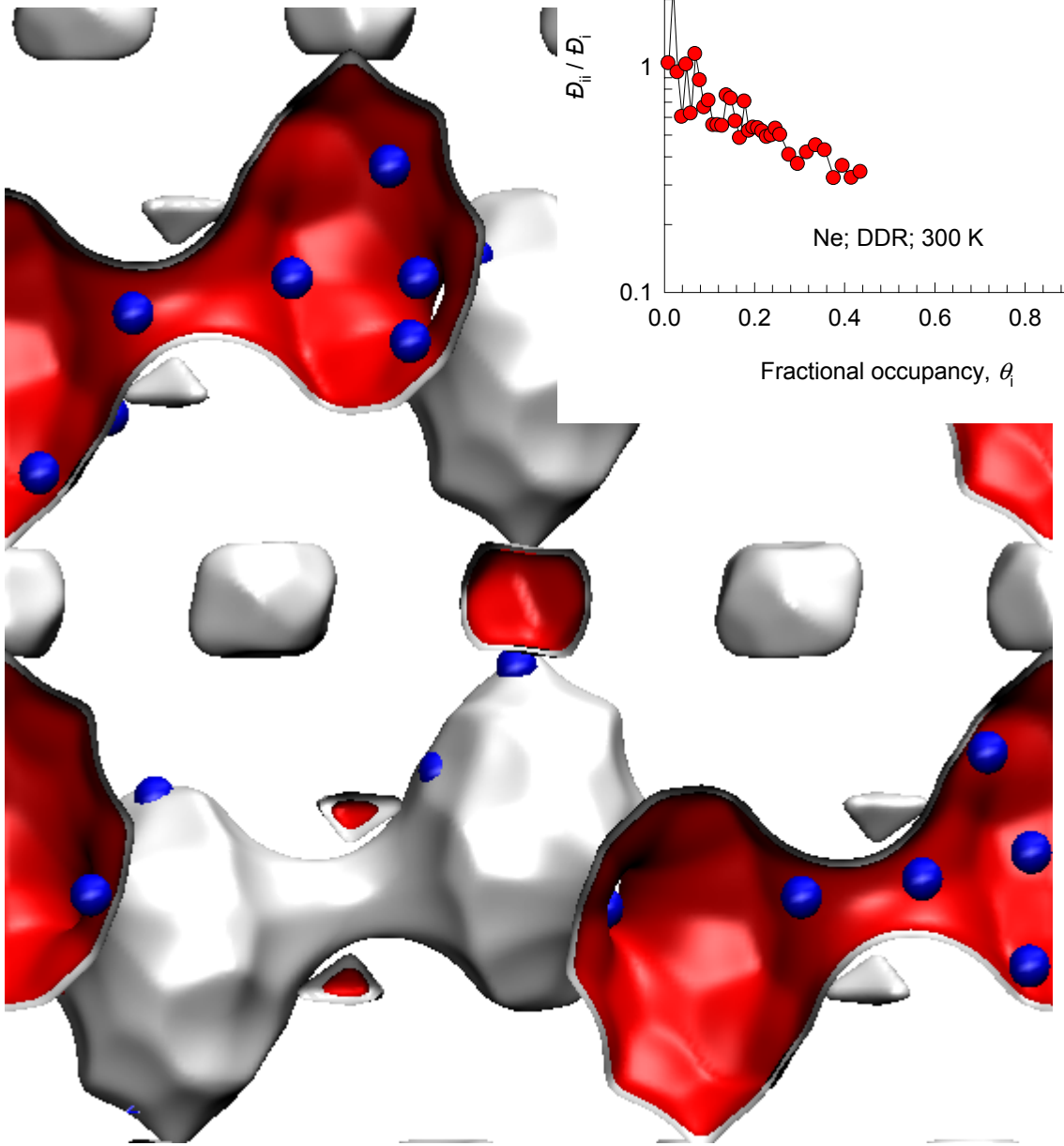

$Đ_{ii}$ / $Đ_i$
Ne; DDR; 300 K
Fractional occupancy, θ_i

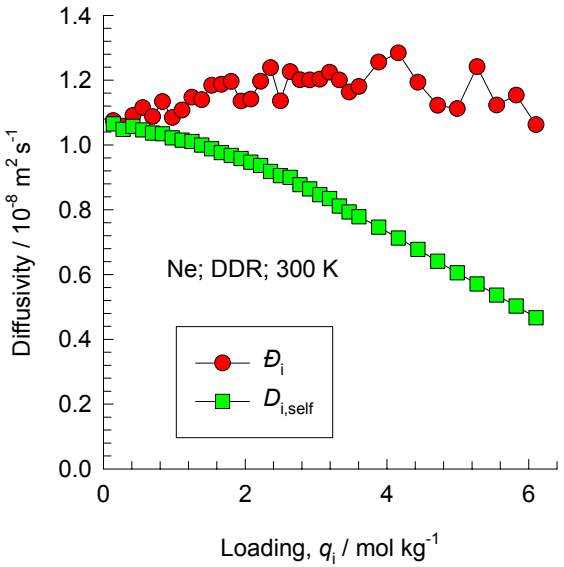
Diffusivity / 10^{-8} m^2 s^{-1}
Ne; DDR; 300 K
$Đ_i$
$D_{i,self}$
Loading, q_i / mol kg^{-1}

DDR, 300 K, O2

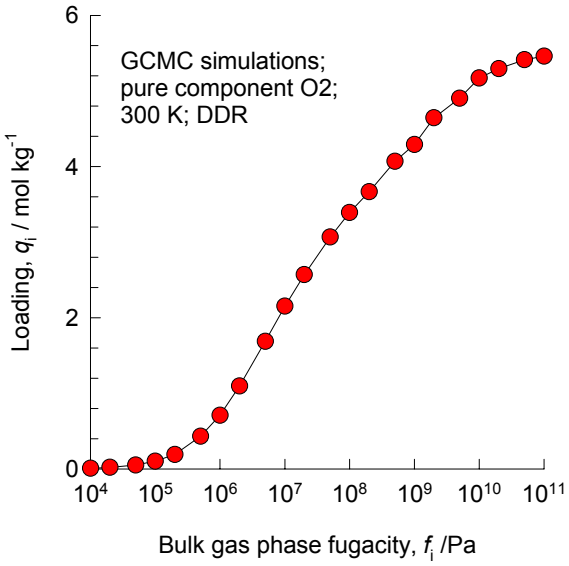
GCMC simulations;
pure component O2;
300 K; DDR
Loading, q_i / mol kg^{-1}
Bulk gas phase fugacity, f_i /Pa

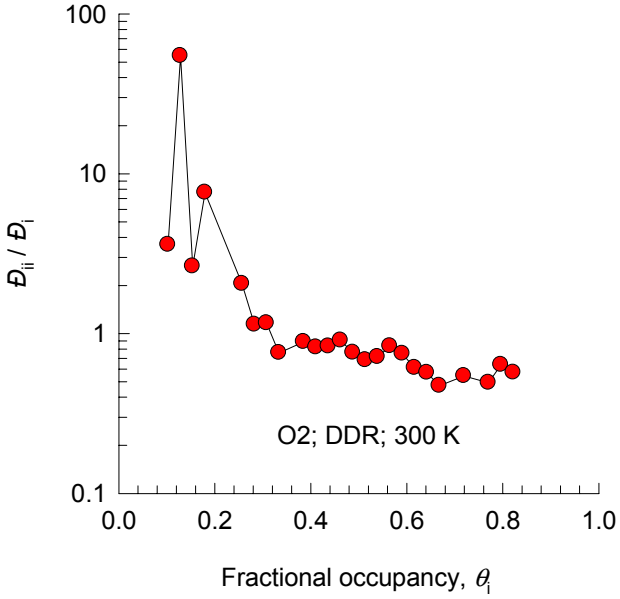
O2; DDR; 300 K
$Đ_{ii}$ / $Đ_i$
Fractional occupancy, θ_i

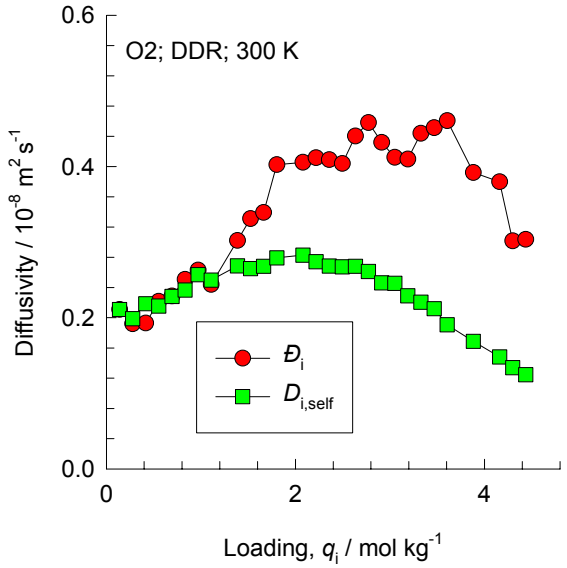
O2; DDR; 300 K
$Đ_i$
$D_{i,self}$
Diffusivity / 10^{-8} m^2 s^{-1}
Loading, q_i / mol kg^{-1}

MOR

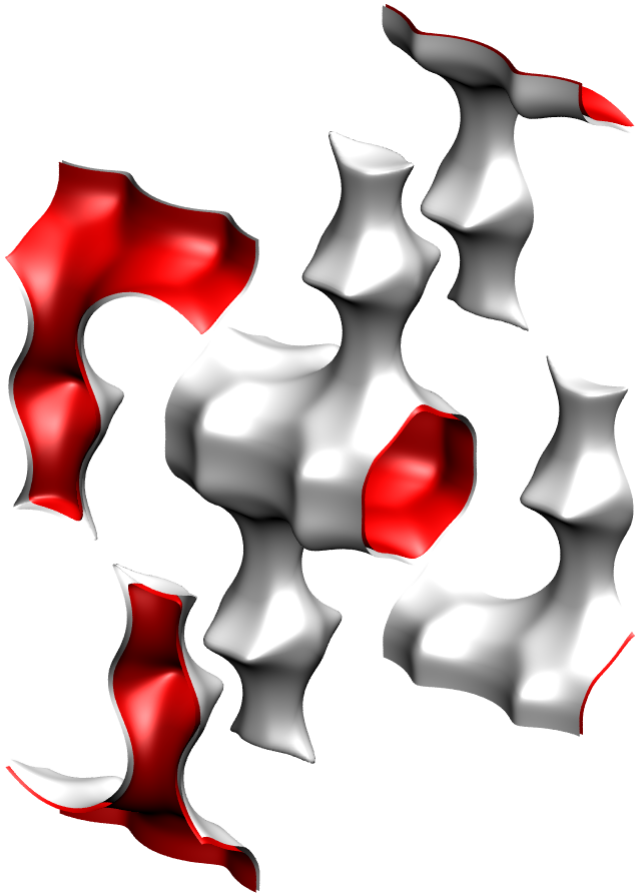

12-ring
main channels

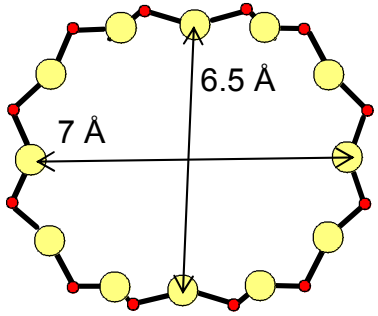

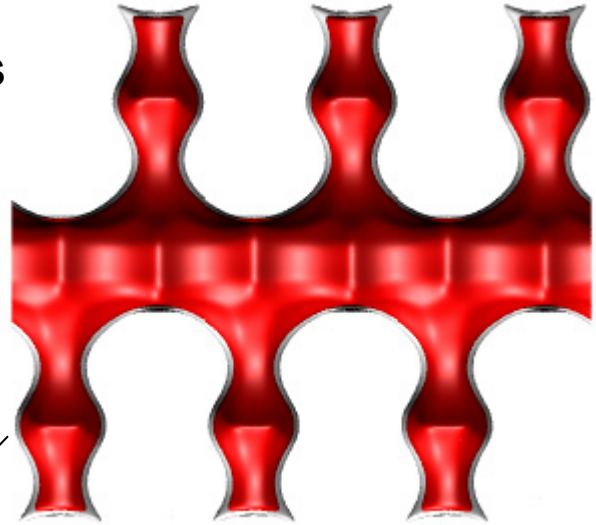

8-ring
side pockets

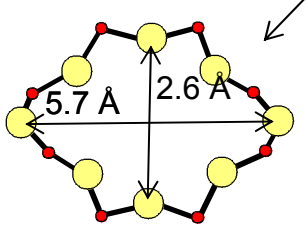

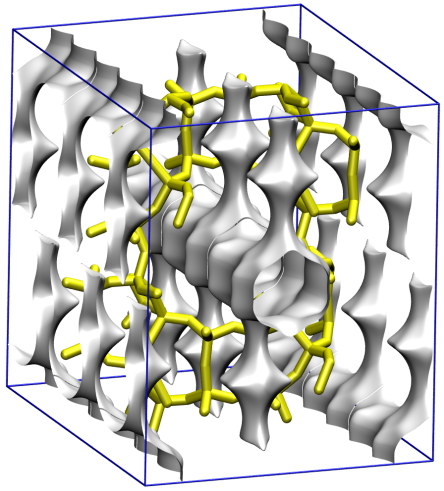

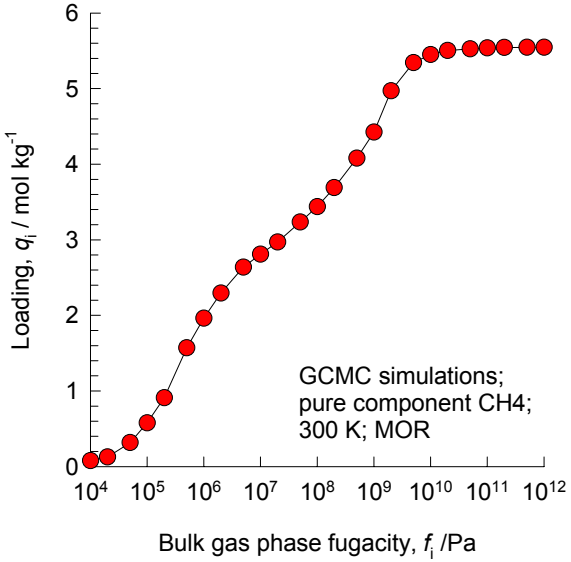

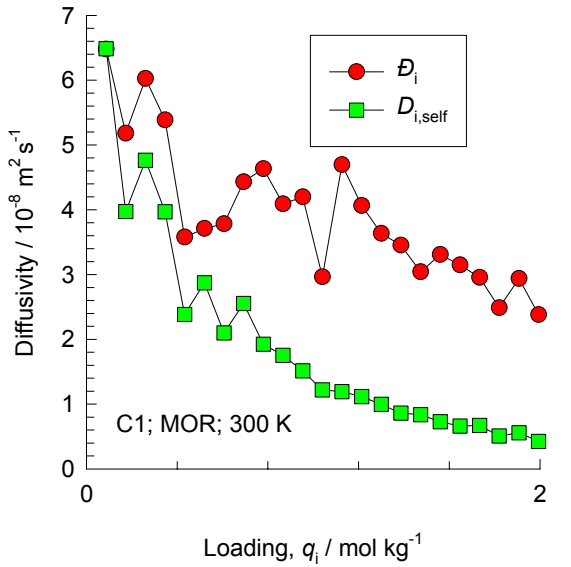

MOR, 300 K, pure C1

f_i=1000 kPa

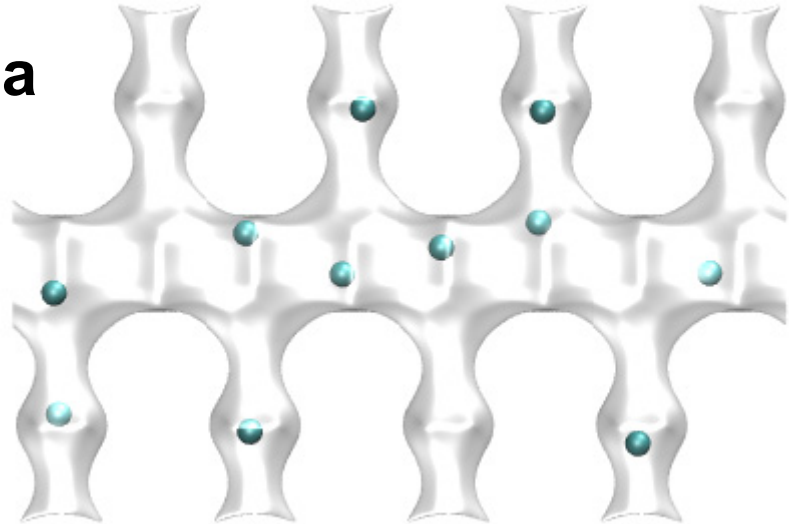

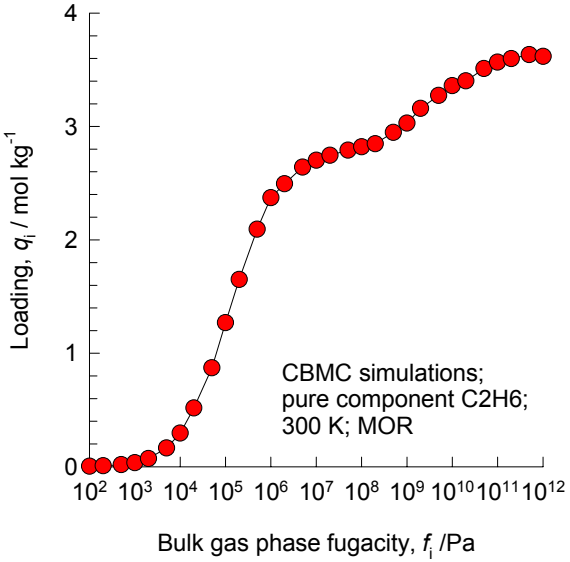

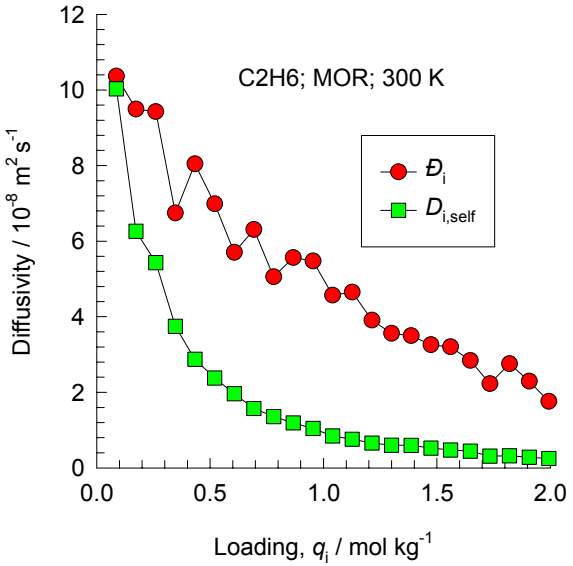

MOR, 300 K, pure C2

f_i=1000 kPa

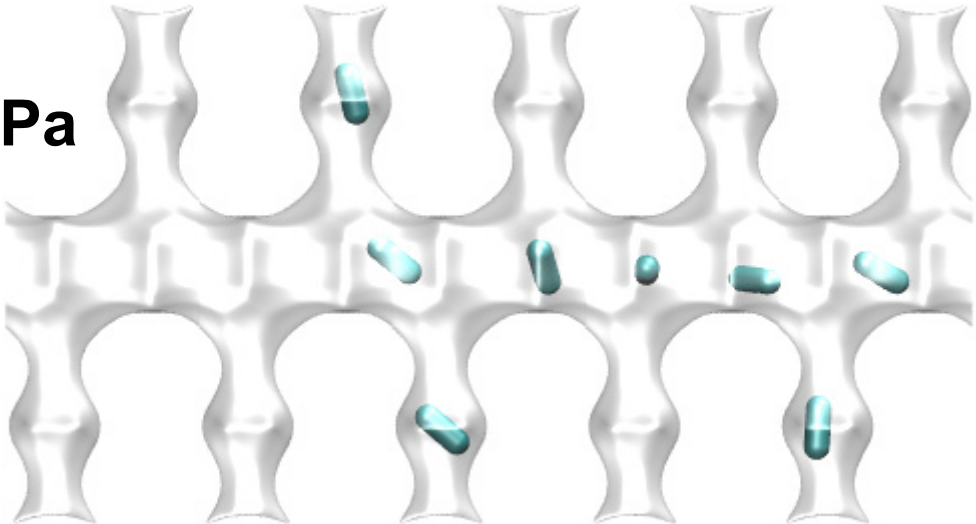

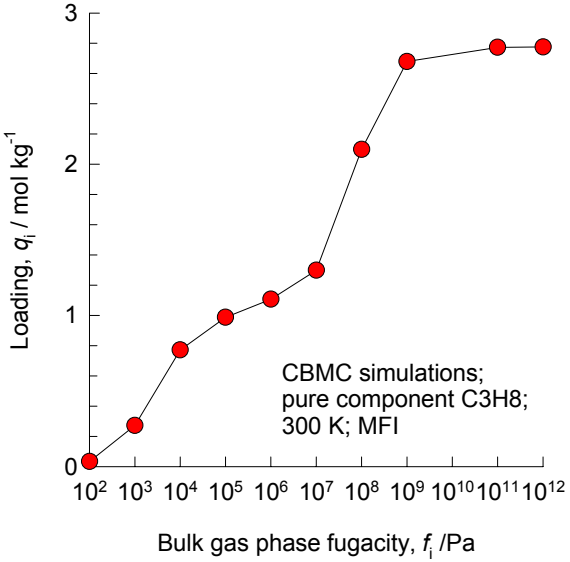

MOR, 300 K, pure C3

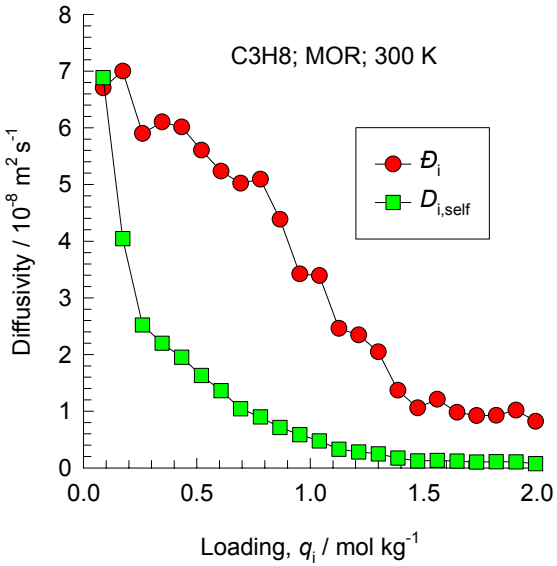

f_i=1000 kPa

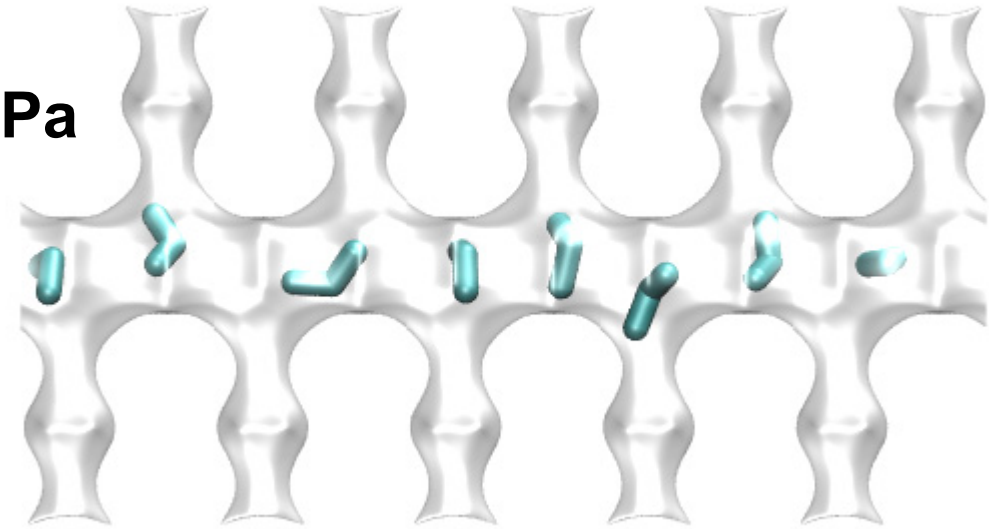

MOR, 300 K, pure components: location in side pockets

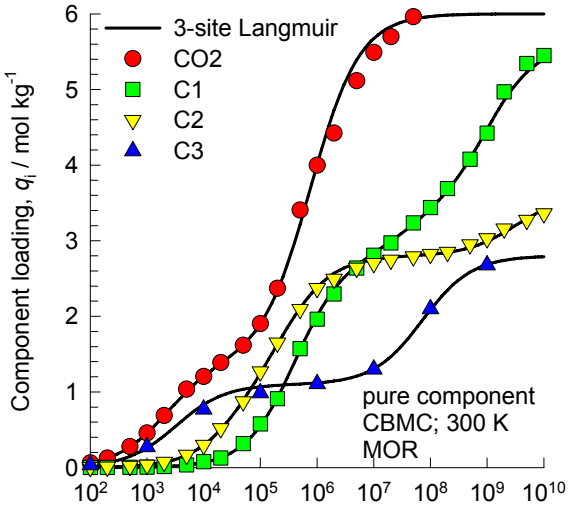

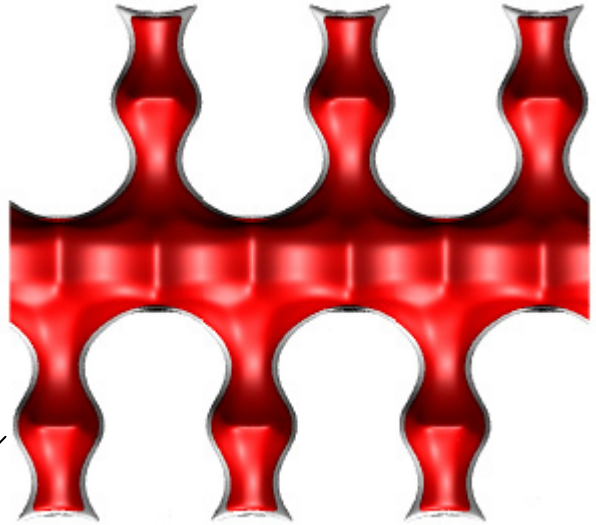

8-ring
side pockets

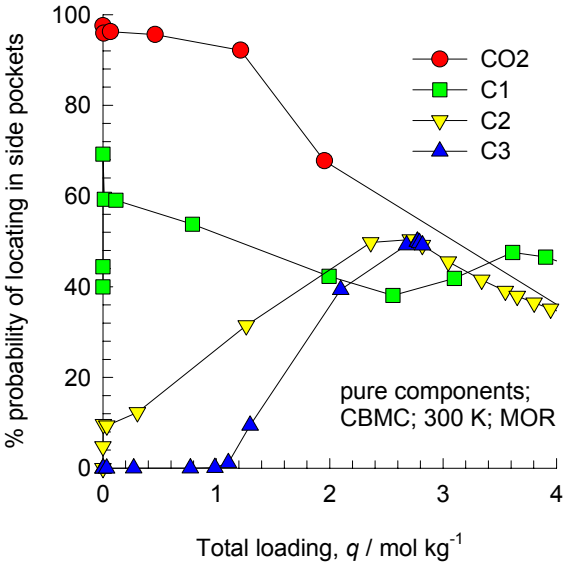

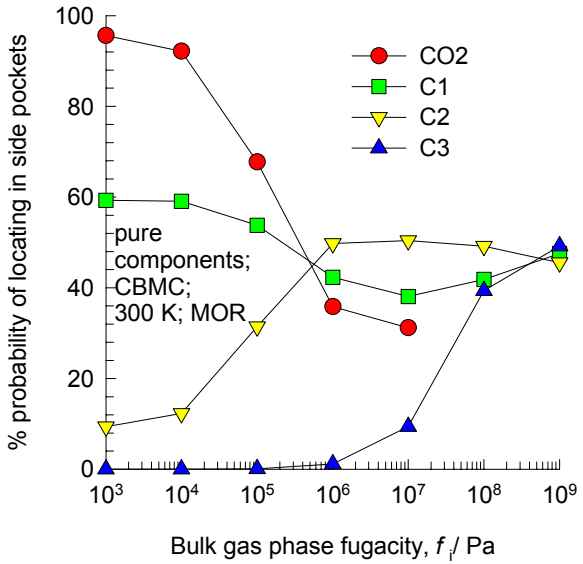

TON (all silica)

10-ring
channel of TON

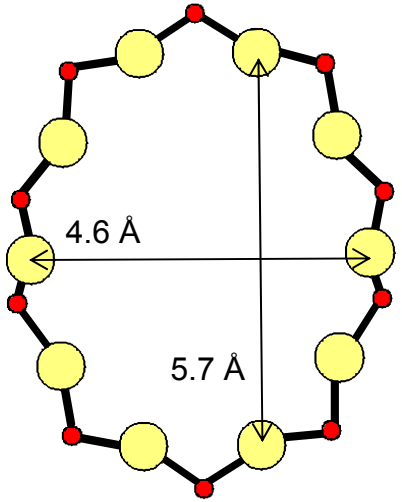

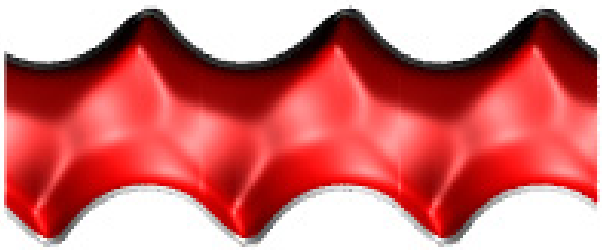

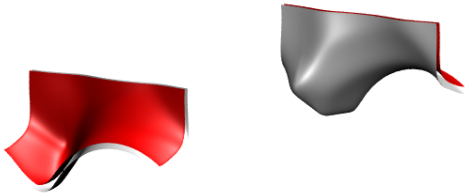

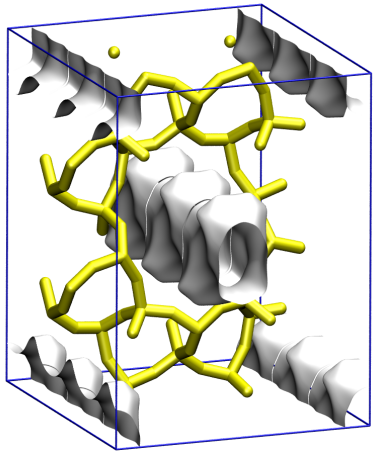

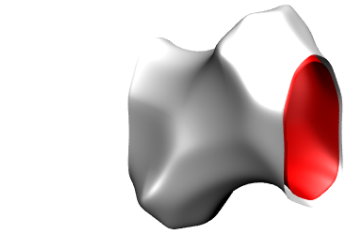

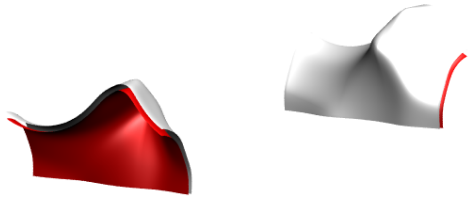

TON, 300 K, CH4

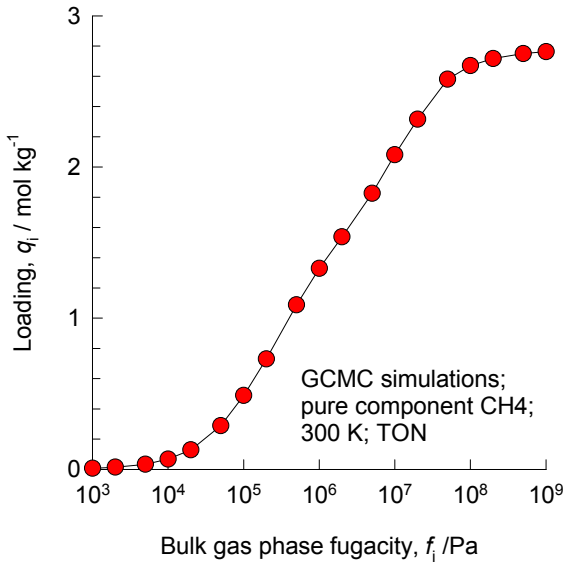
Loading, q_i / mol kg^{-1}
0
1
2
3
10^3
10^4
10^5
10^6
10^7
10^8
10^9
GCMC simulations;
pure component CH4;
300 K; TON
Bulk gas phase fugacity, f_i /Pa

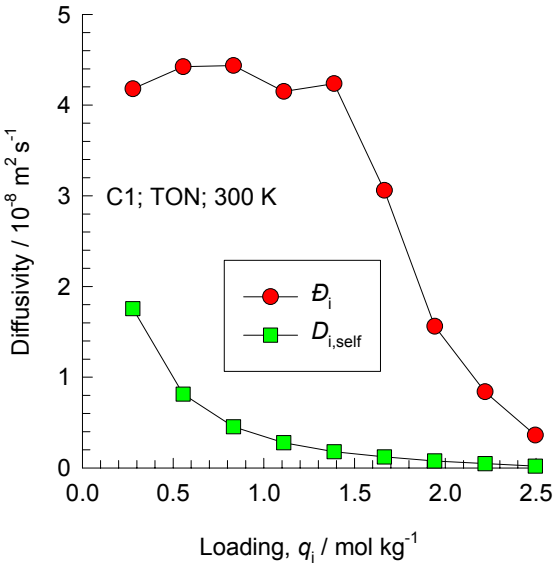
Diffusivity / 10^{-8} m^2 s^{-1}
0
1
2
3
4
5
0.0
0.5
1.0
1.5
2.0
2.5
C1; TON; 300 K
Đ$_i$
$D_{i,self}$
Loading, q_i / mol kg^{-1}

TON, 300 K, C2

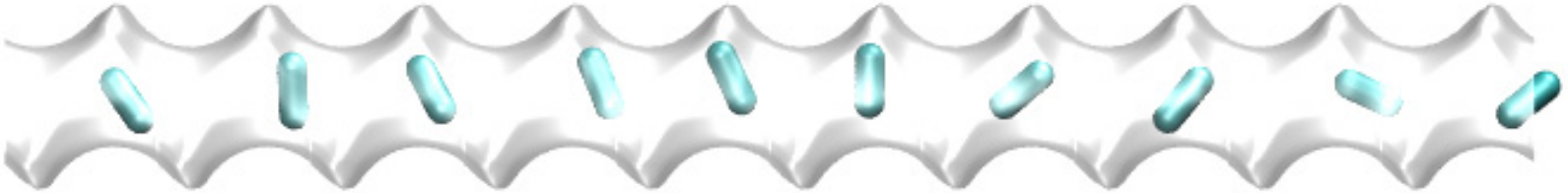

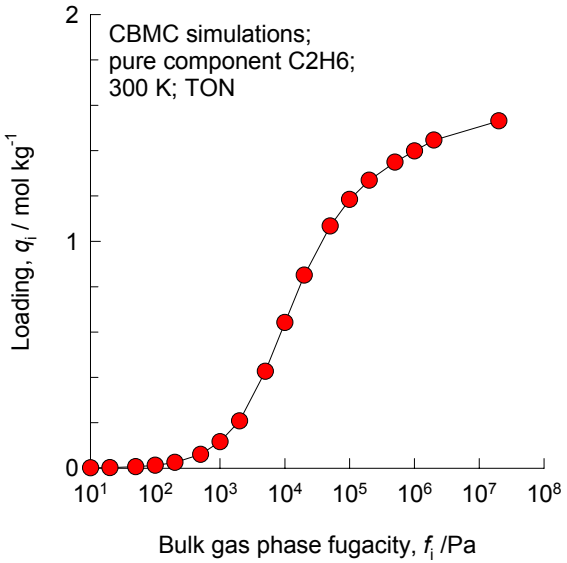
CBMC simulations;
pure component C2H6;
300 K; TON
Loading, q_i / mol kg^{-1}
Bulk gas phase fugacity, f_i /Pa
0
1
2
10^1
10^2
10^3
10^4
10^5
10^6
10^7
10^8

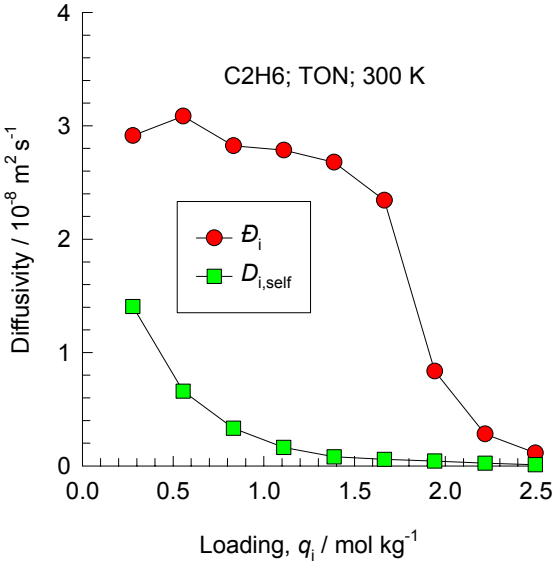
C2H6; TON; 300 K
Diffusivity / 10^{-8} m^2 s^{-1}
Loading, q_i / mol kg^{-1}
$Đ_i$
$D_{i,self}$
0
1
2
3
4
0.0
0.5
1.0
1.5
2.0
2.5

ETS-4

12-ring
channel of ETS-4

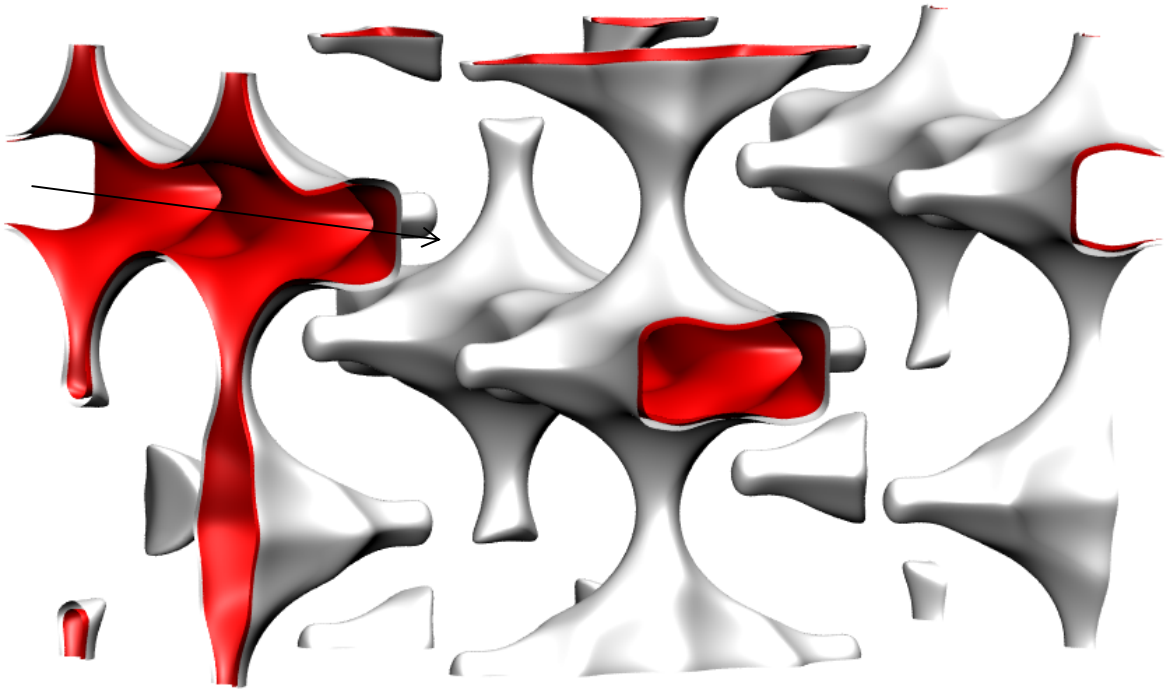

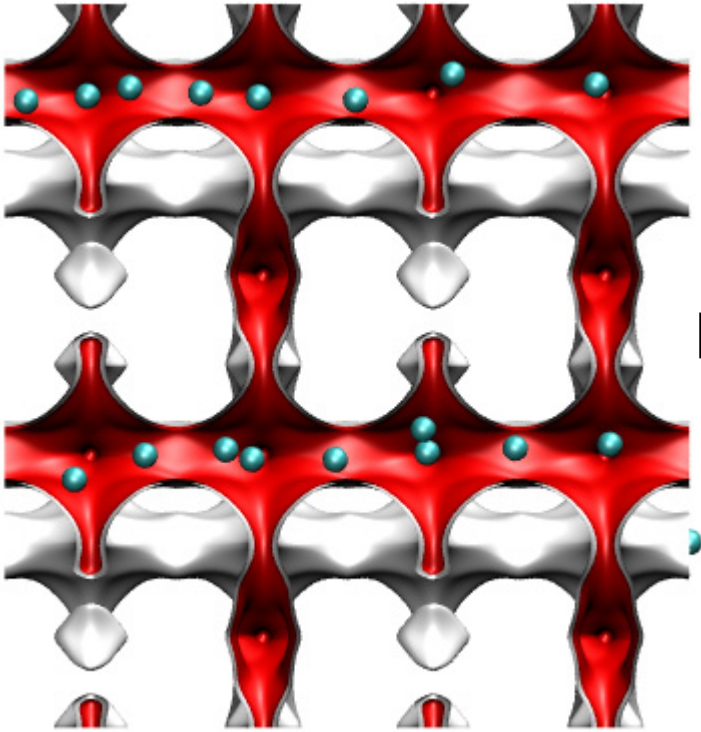

12-ring channels
(diffusion is considered only
in this direction

ETS-4, 300 K, CH4

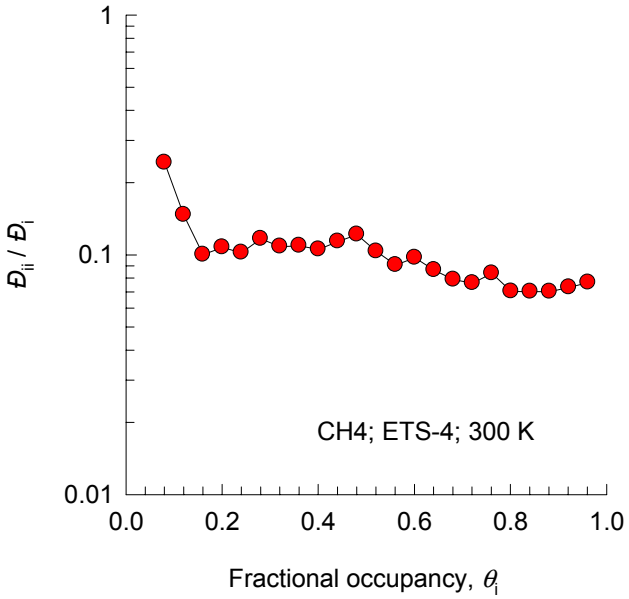

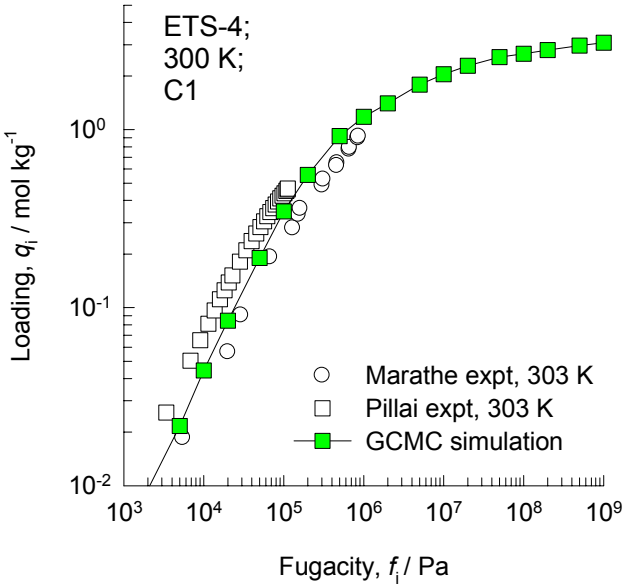

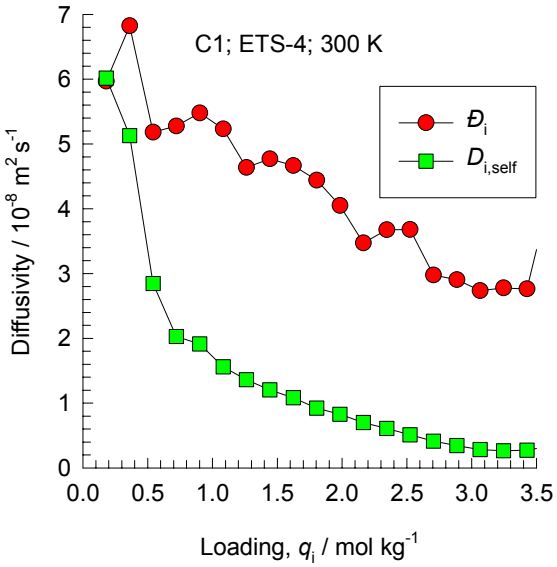

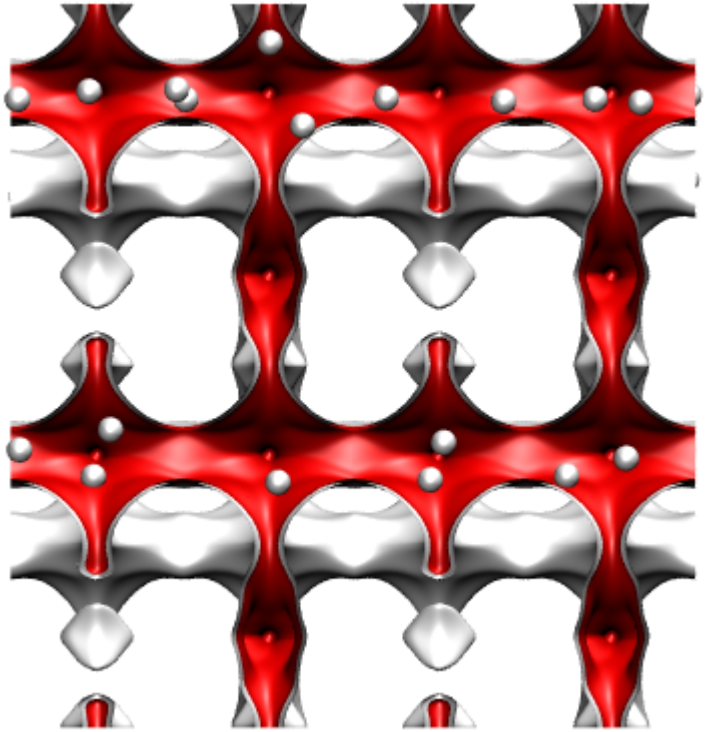

12-ring channels
(diffusion is considered only
in this direction

ETS-4, 300 K, Ar

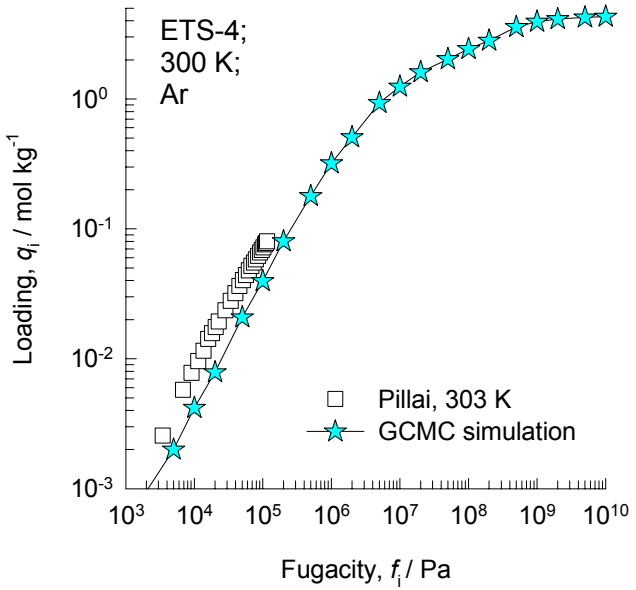

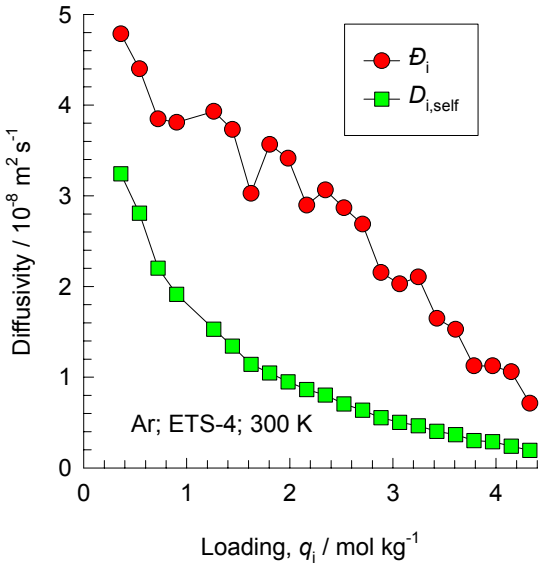

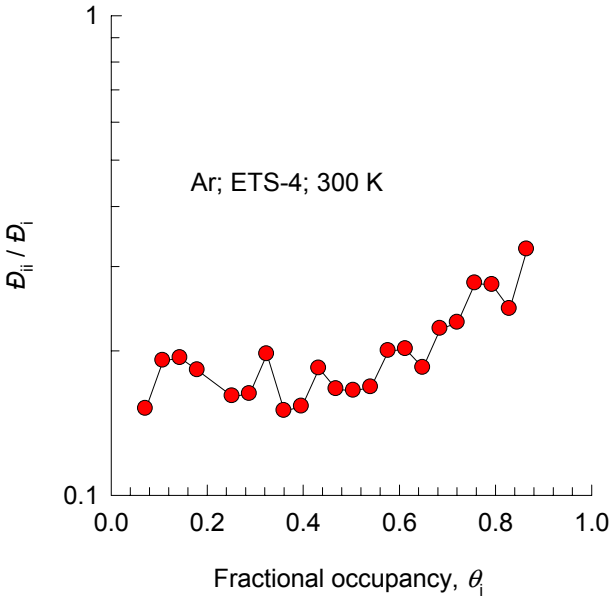

12-ring channels (diffusion is considered only in this direction

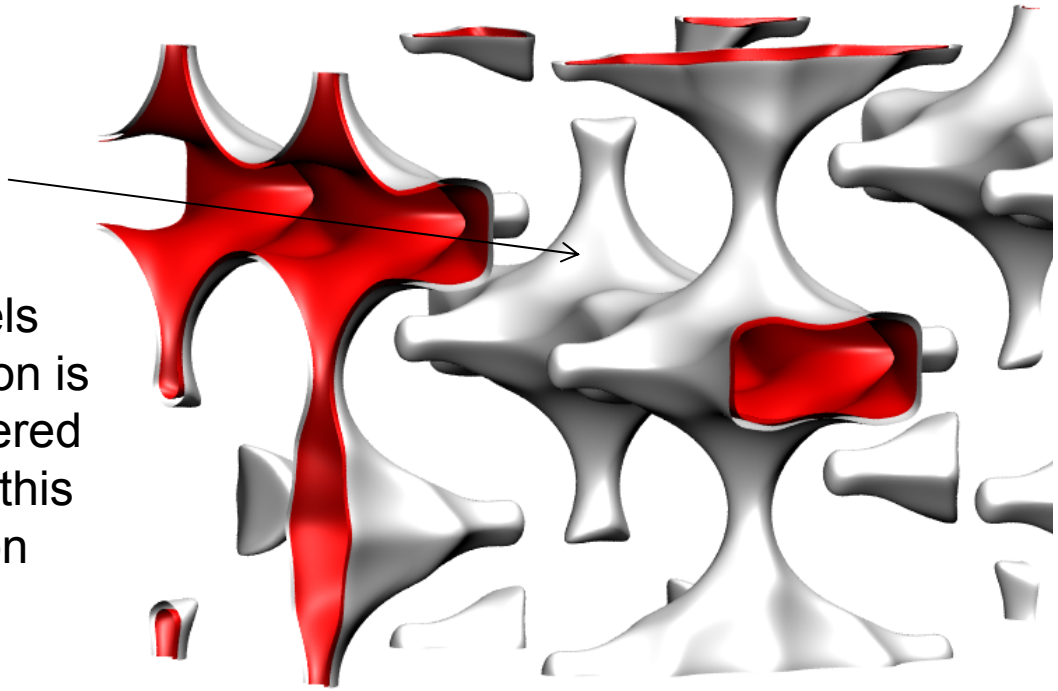

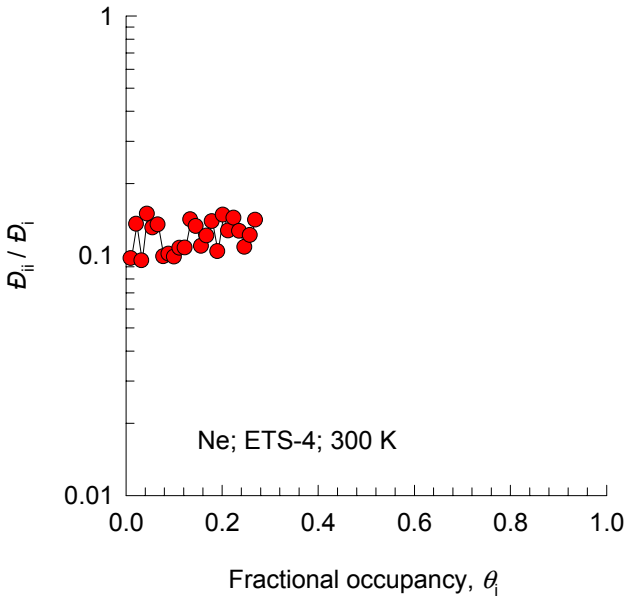

ETS-4, 300 K, Ne

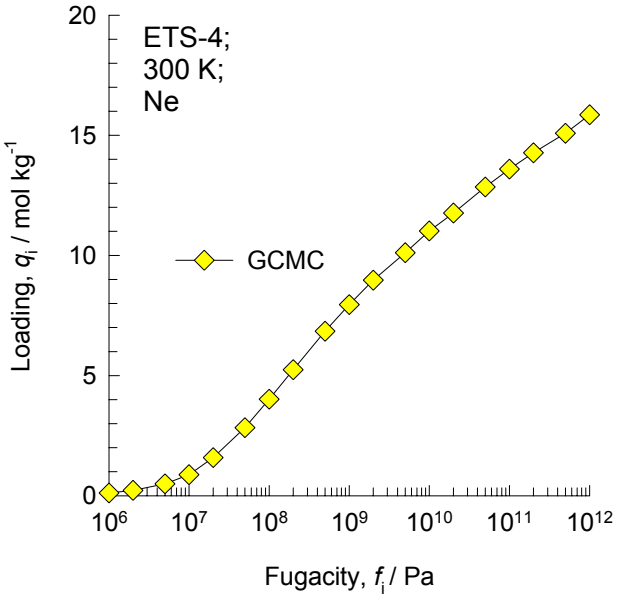

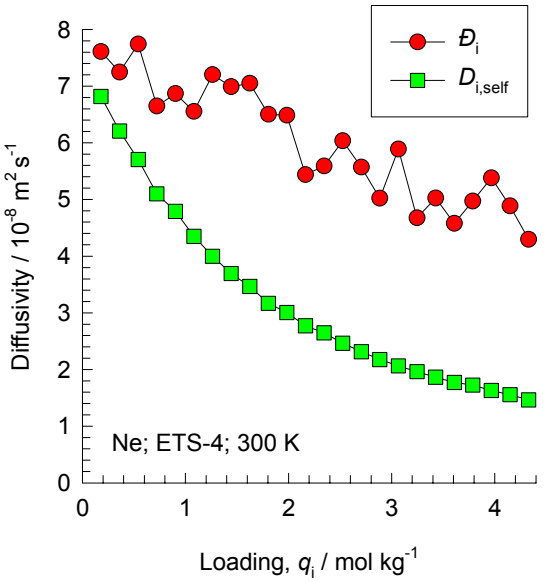

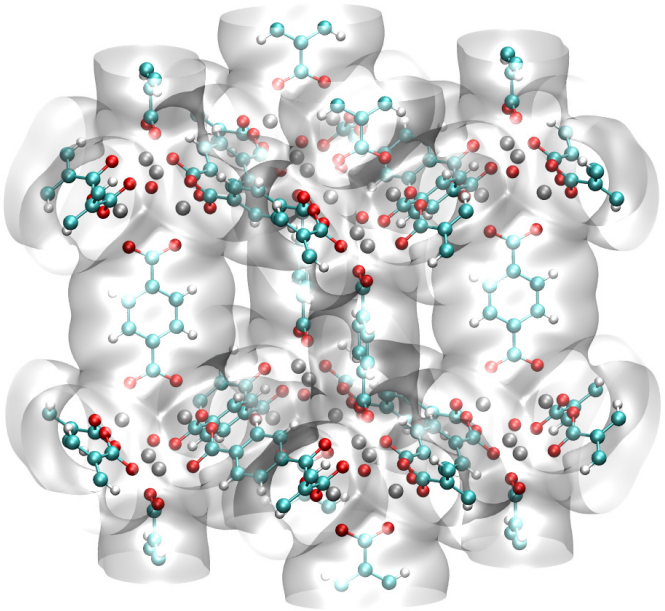

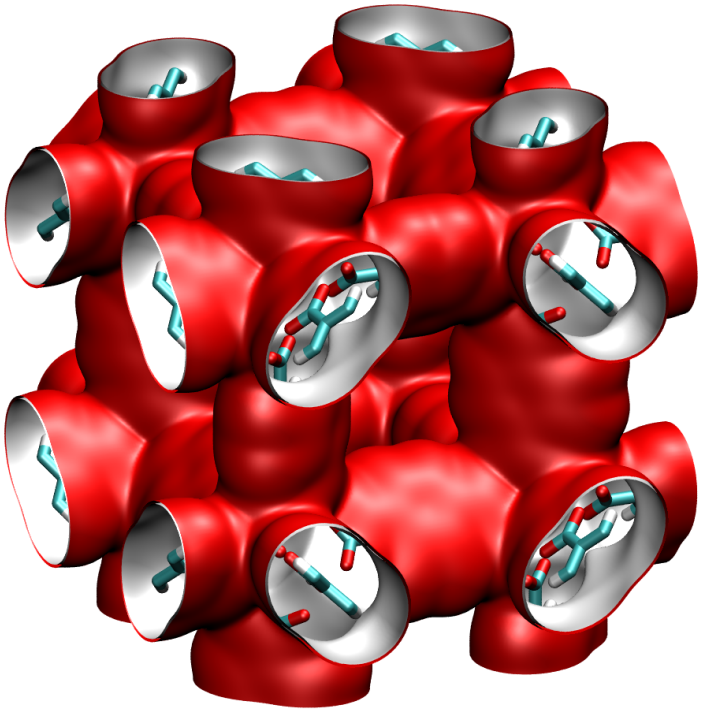

IRMOF-1

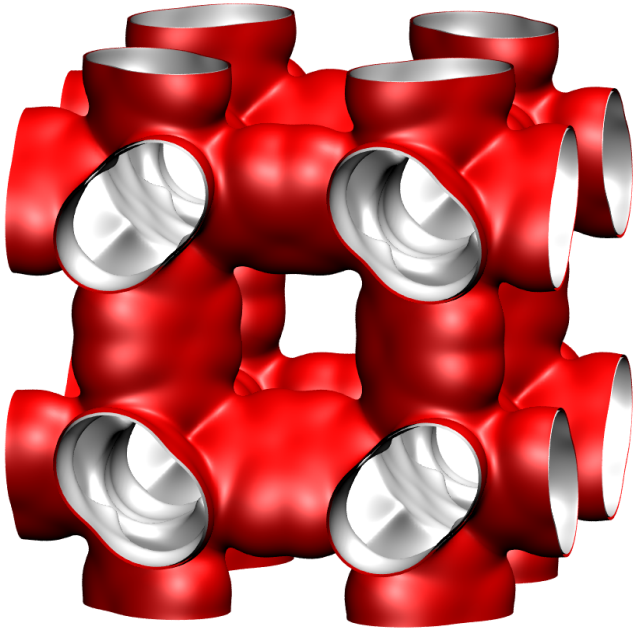

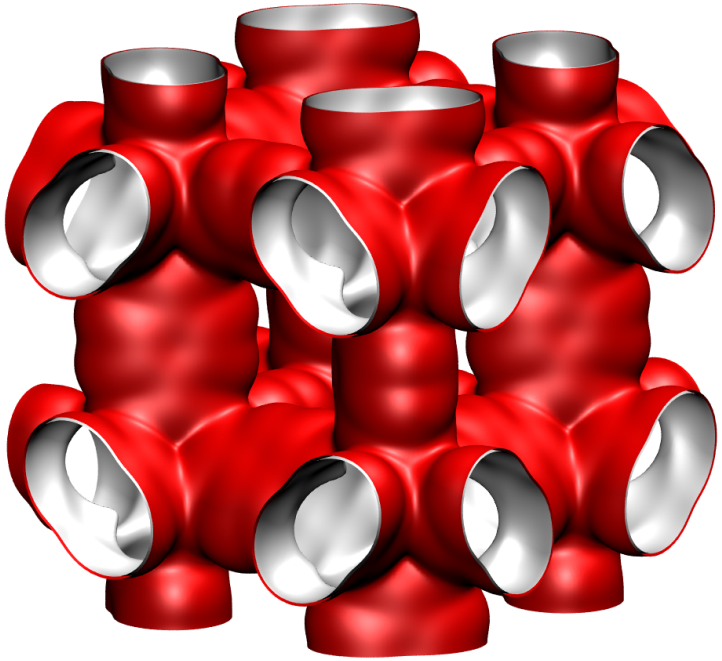

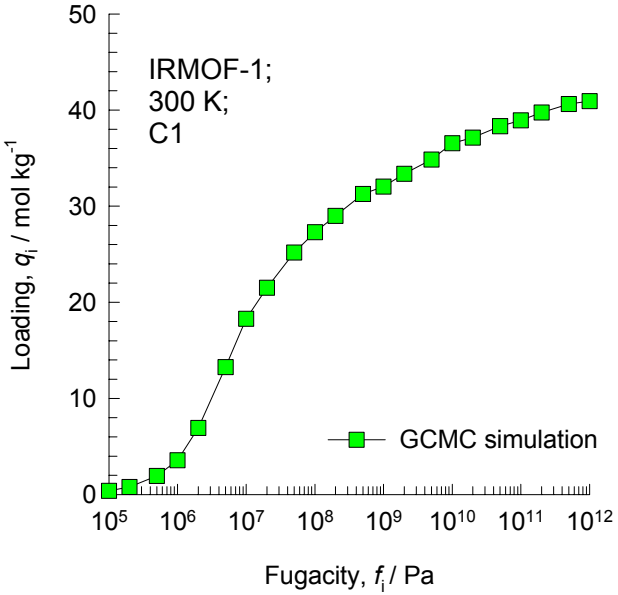

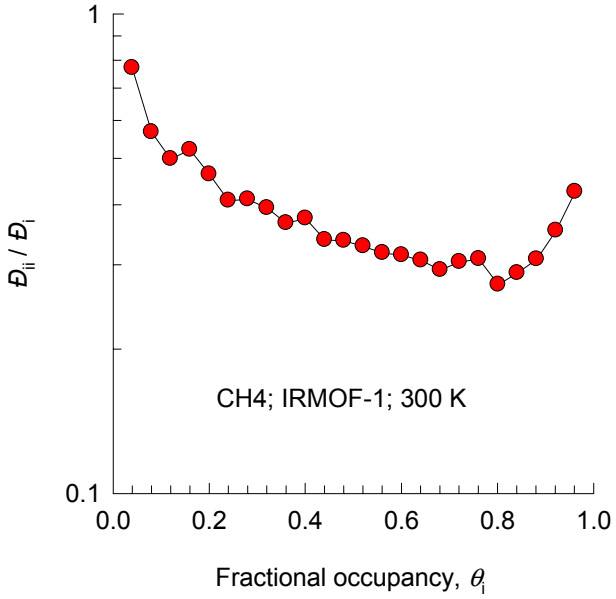

IRMOF-1, 300 K, CH4

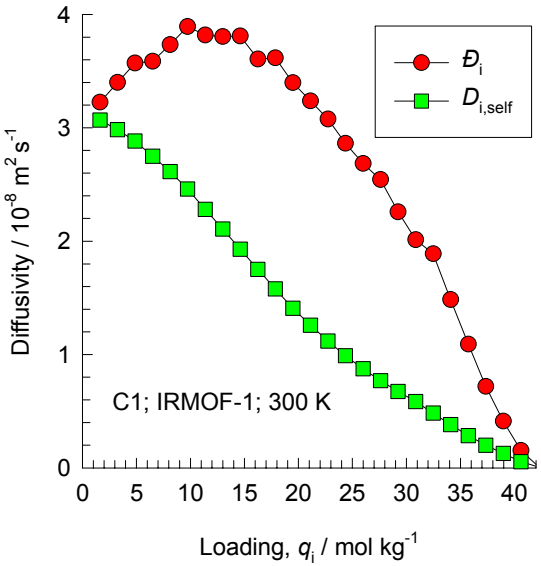

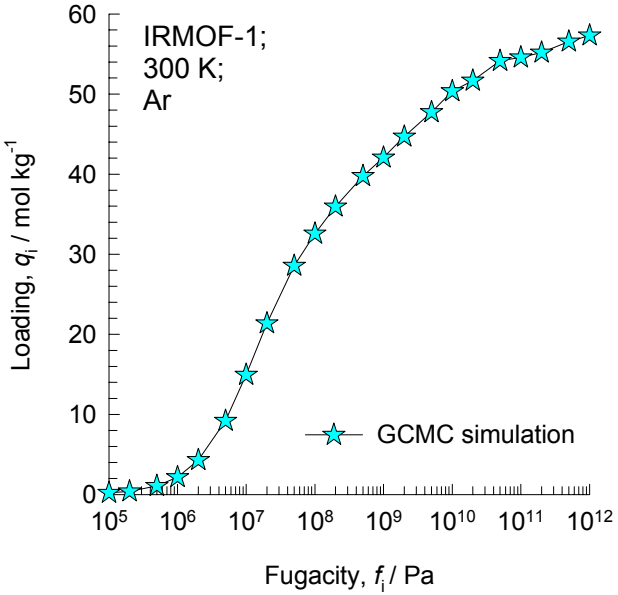

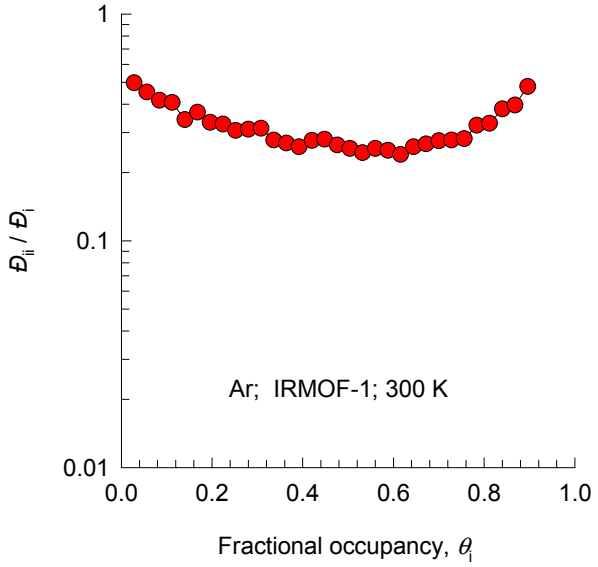

IRMOF-1, 300 K, Ar

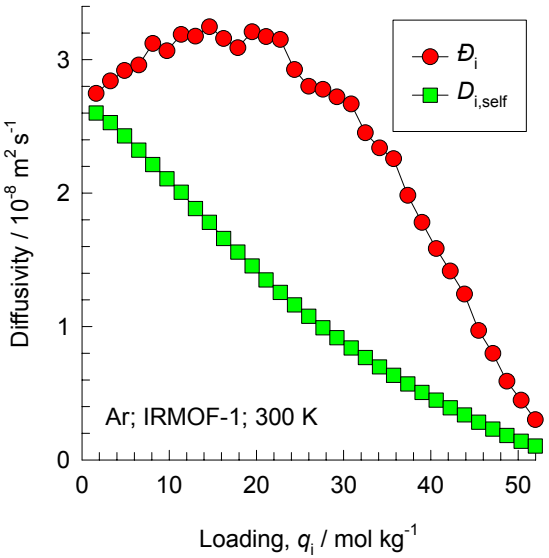

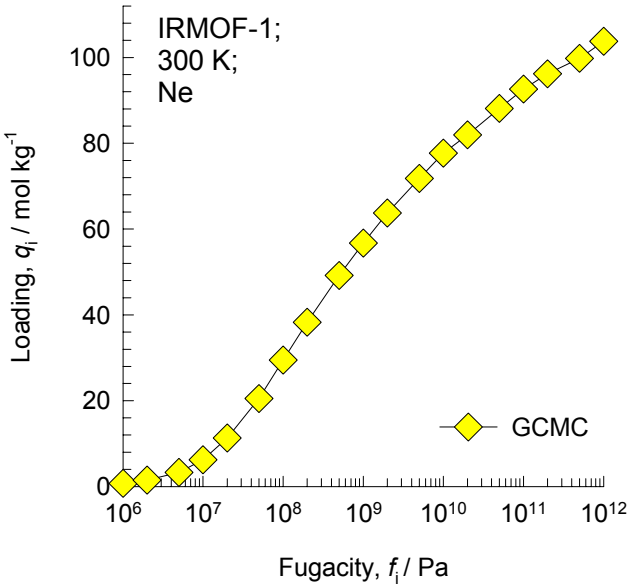

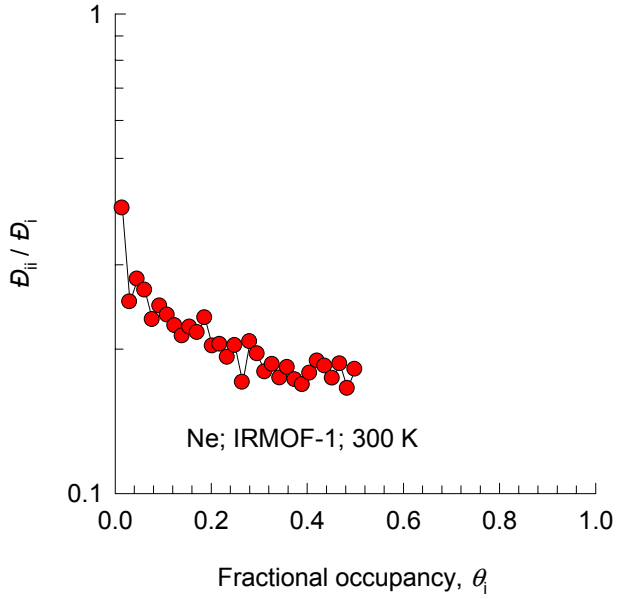

IRMOF-1, 300 K, Ne

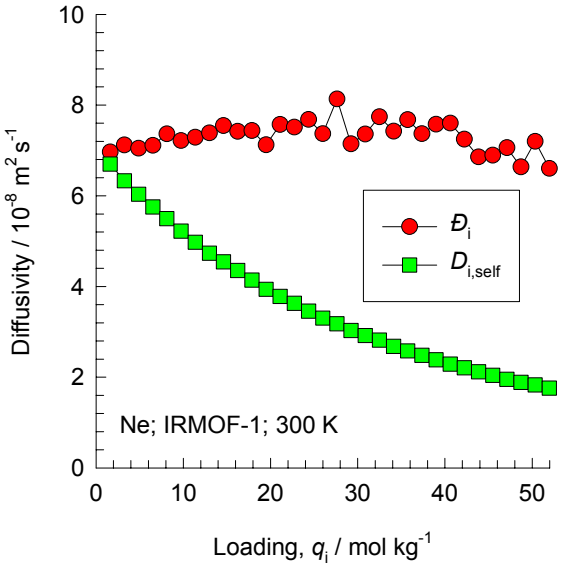

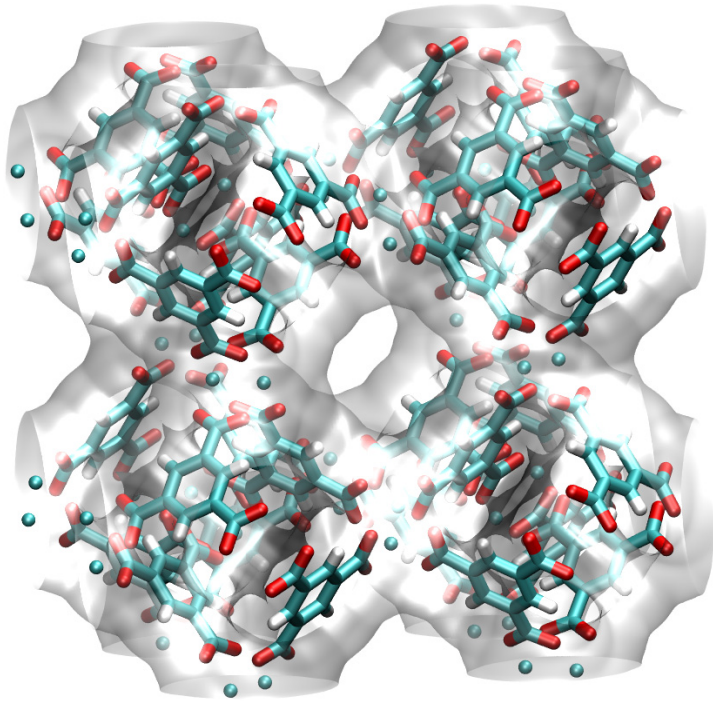

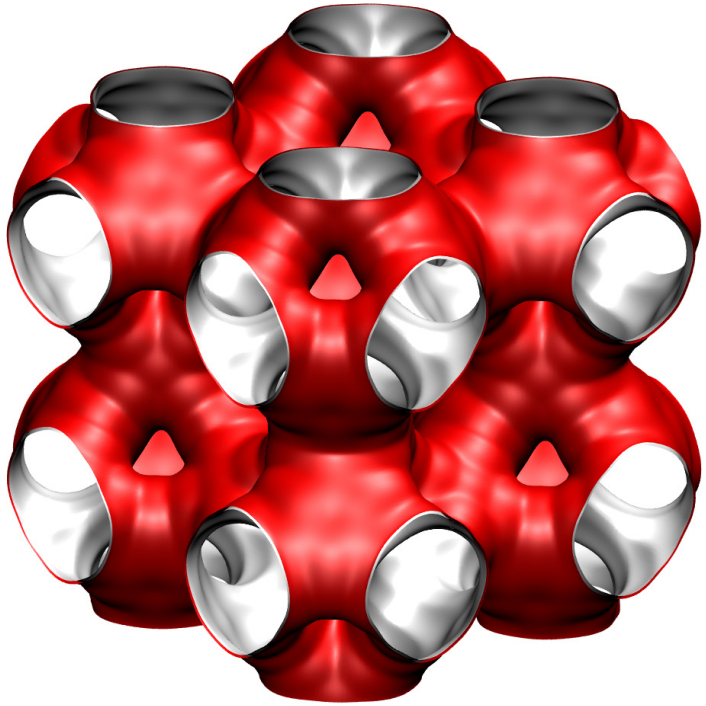

CuBTC

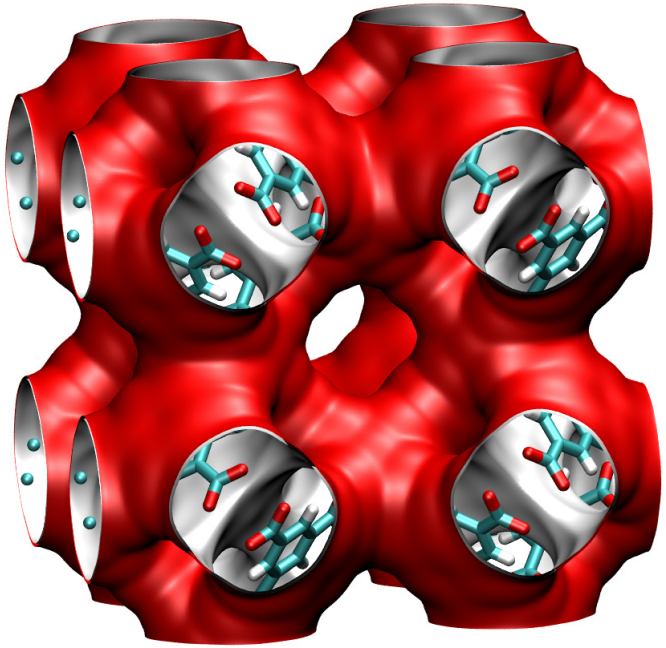

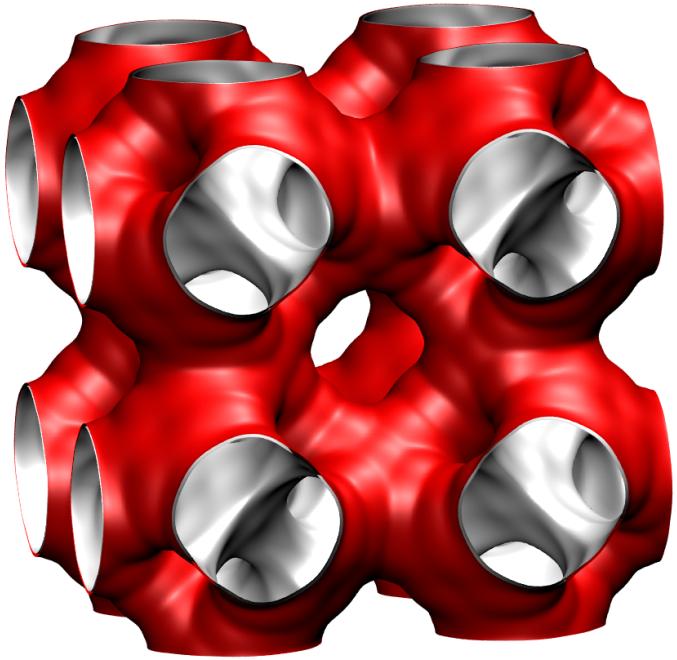

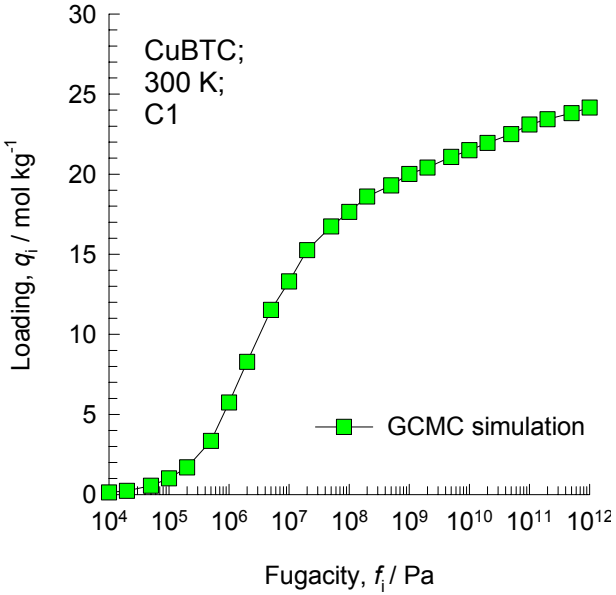

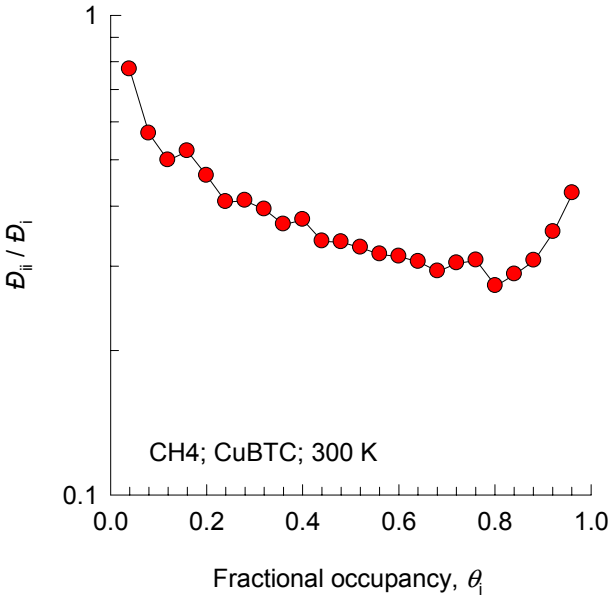

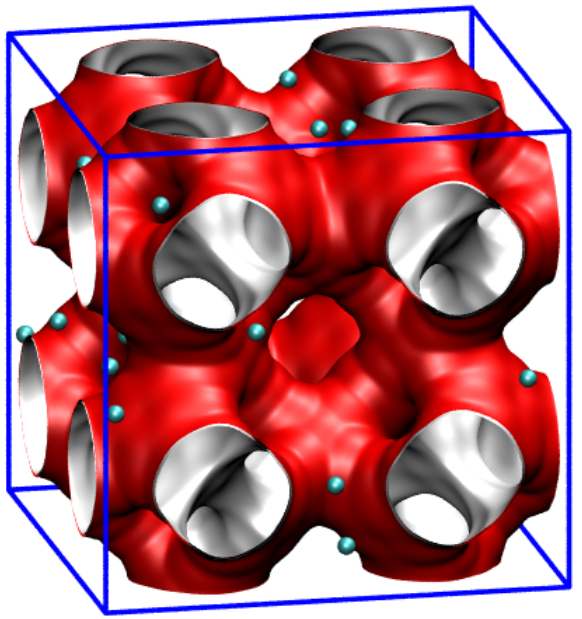

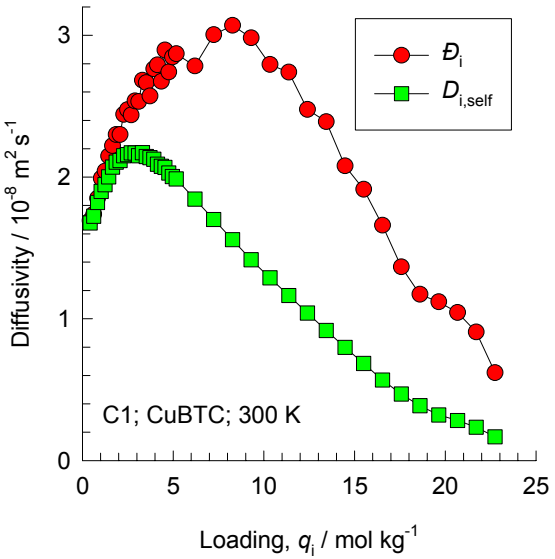

CuBTC, 300 K, CH4

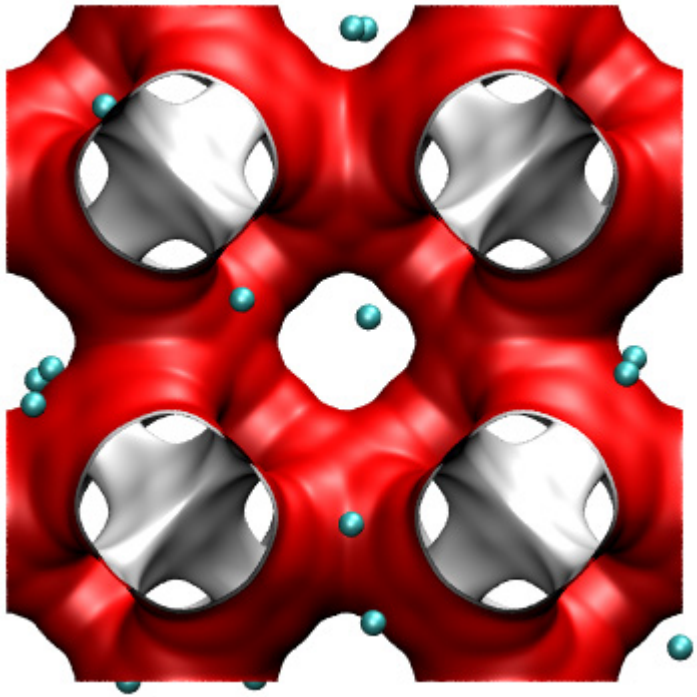

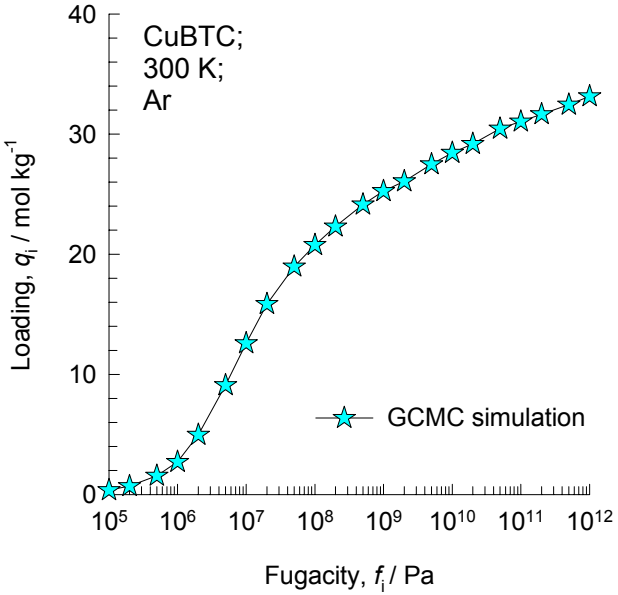

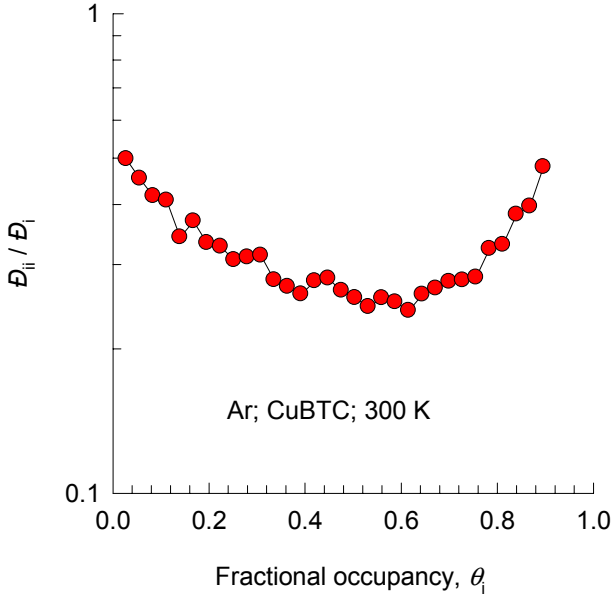

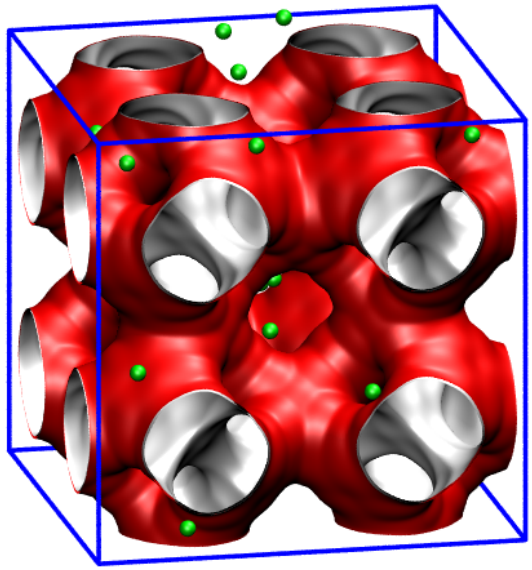

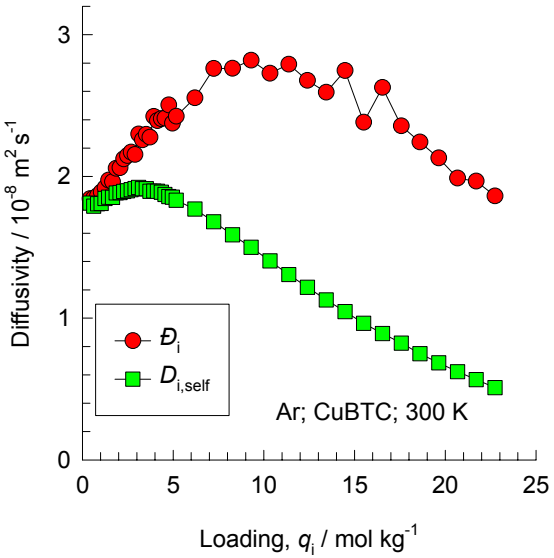

CuBTC, 300 K, Ar

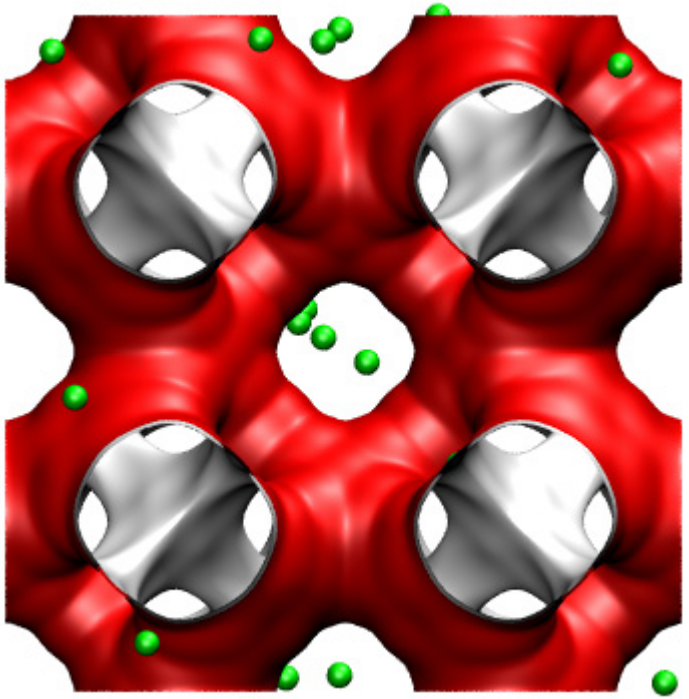

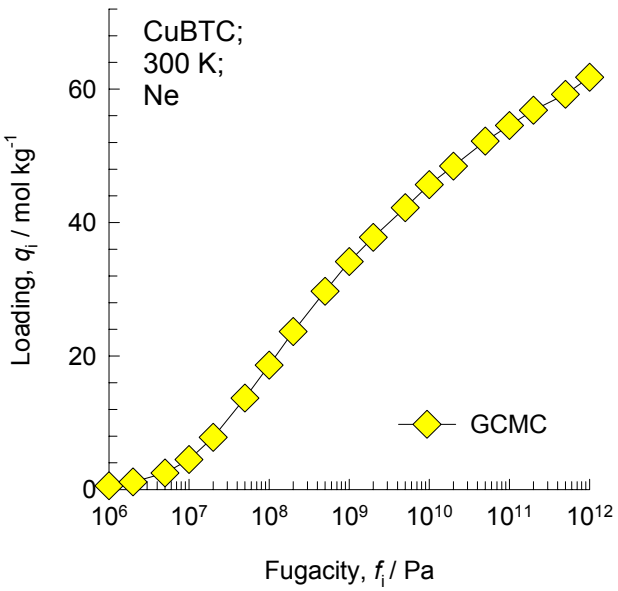

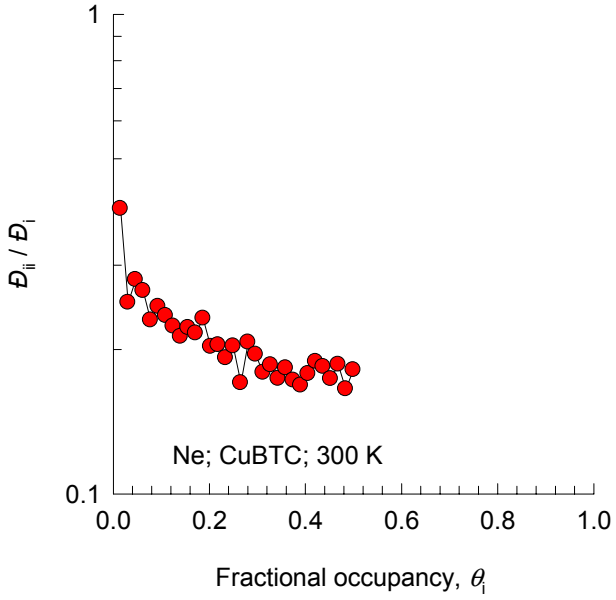

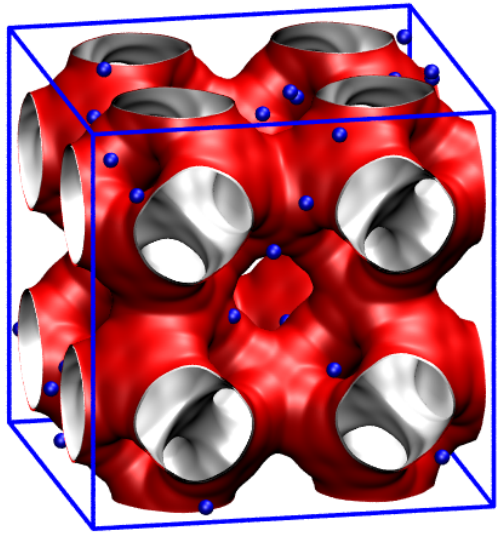

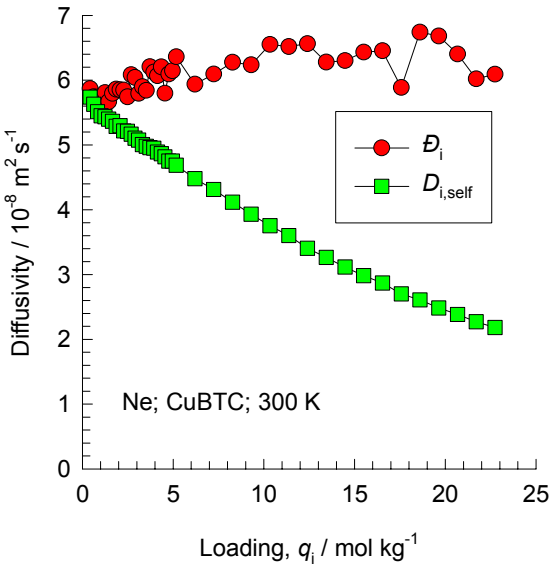

CuBTC, 300 K, Ne

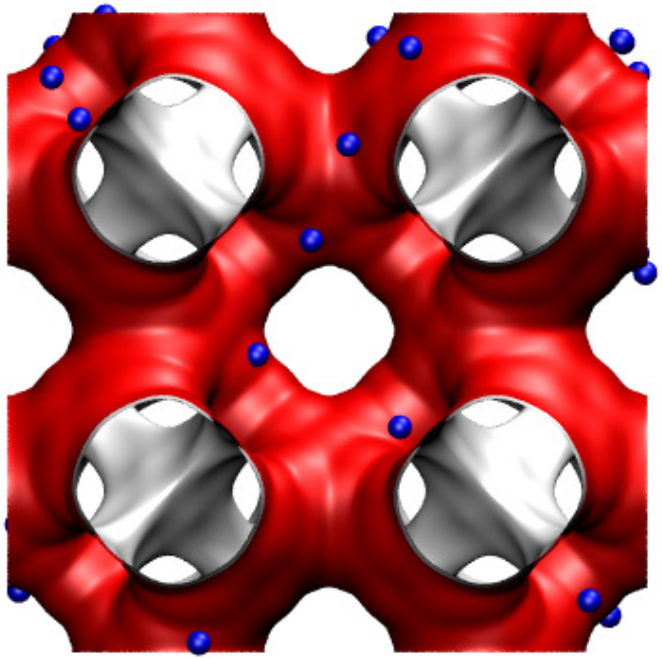

Appendix A4

MD mixture diffusion simulations in zeolites, ETS-4, IRMOF-1, and CuBTC

Ne-Ar mixture

AFI

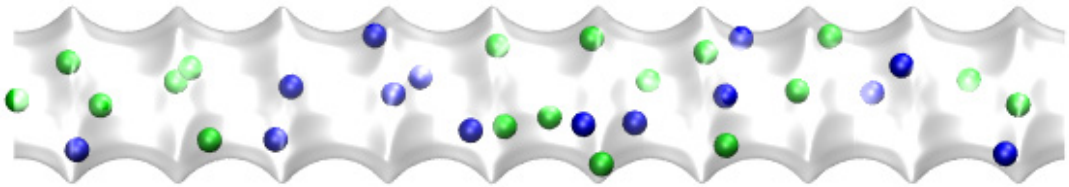

FAU

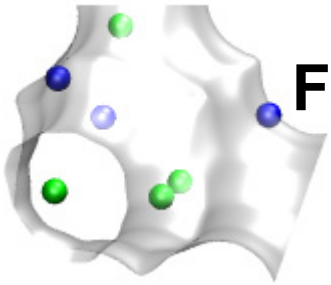

MFI

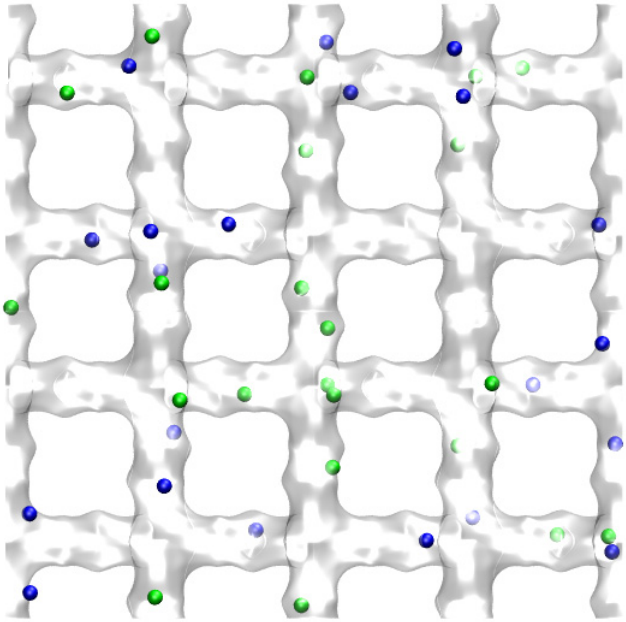

LTA

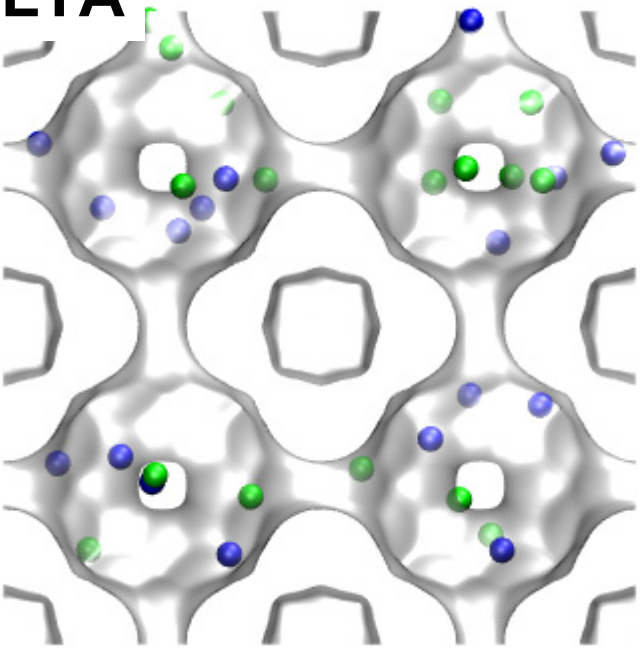

DDR

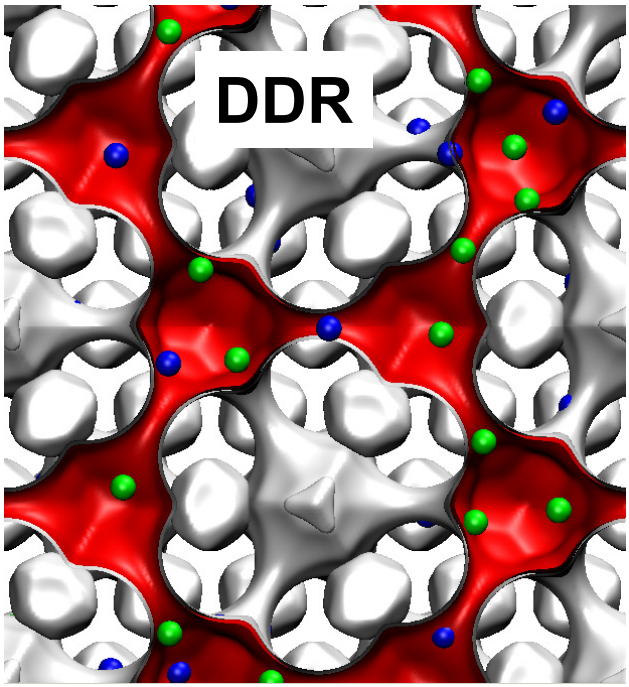

CHA

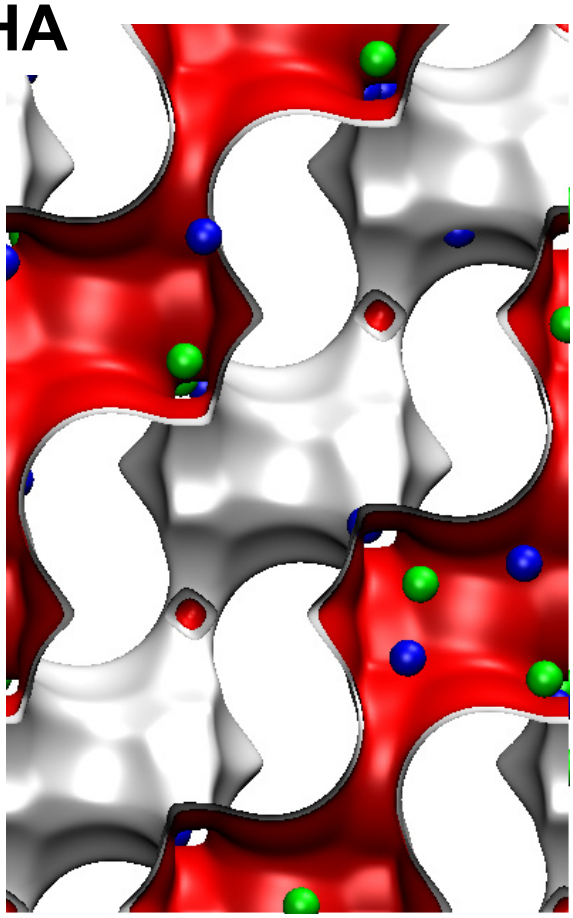

Ne-Ar mixtures at 300 K; equimolar mixture
Self diffusivities

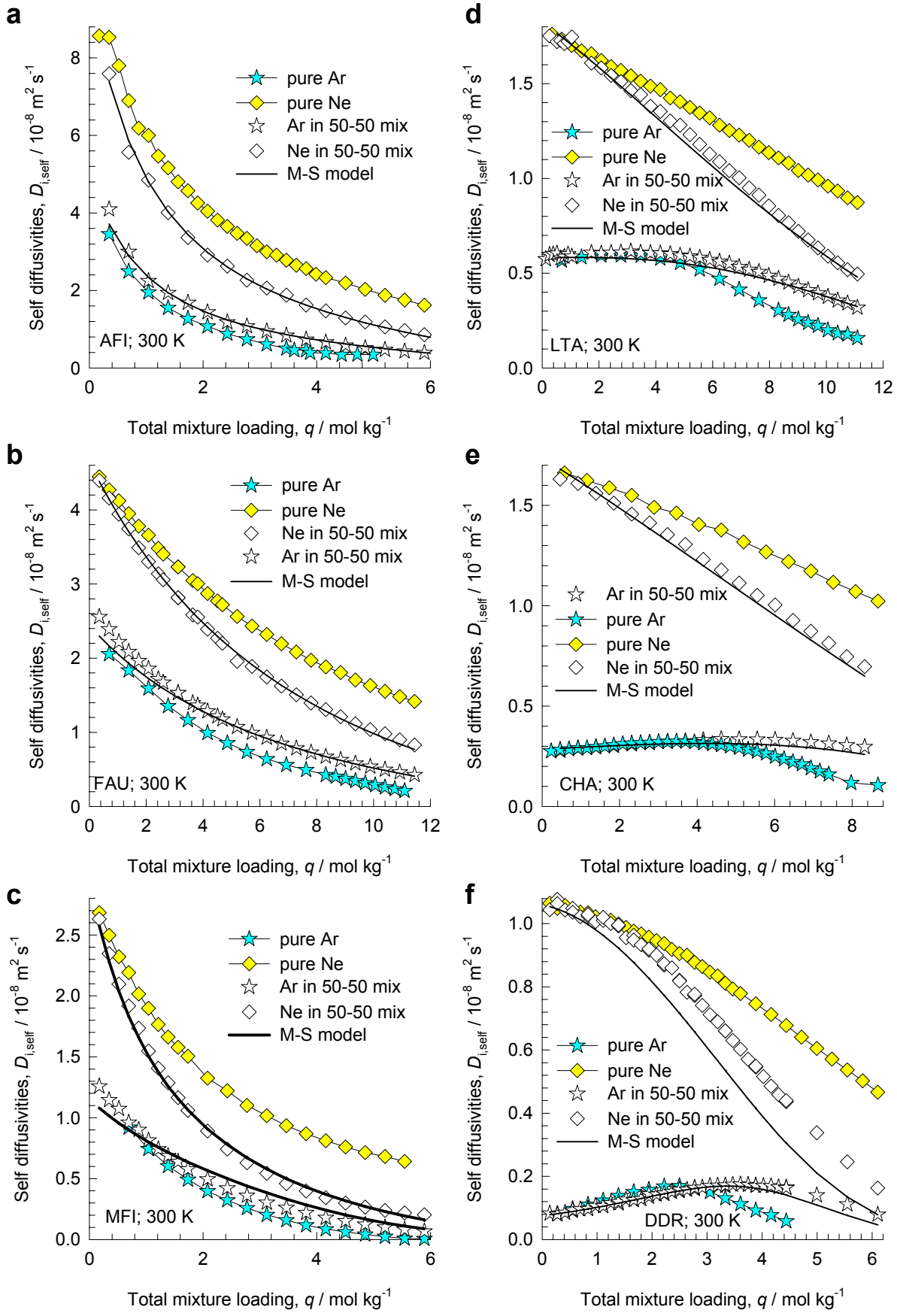

Ne-Ar mixtures at 300 K; equimolar mixture M-S diffusivities

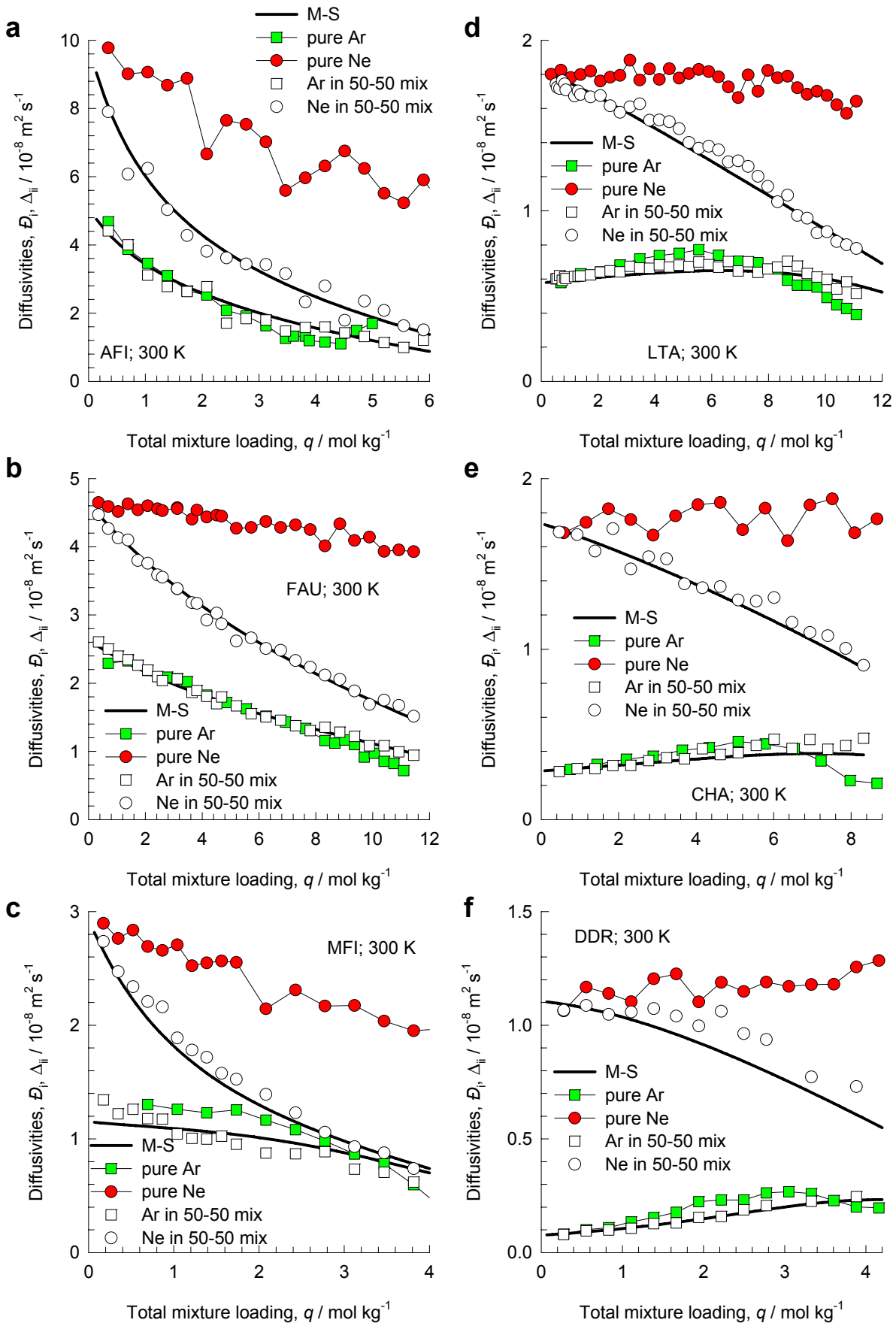

Ne-Ar mixtures at 300 K; equimolar mixture
Onsager matrix, ratios

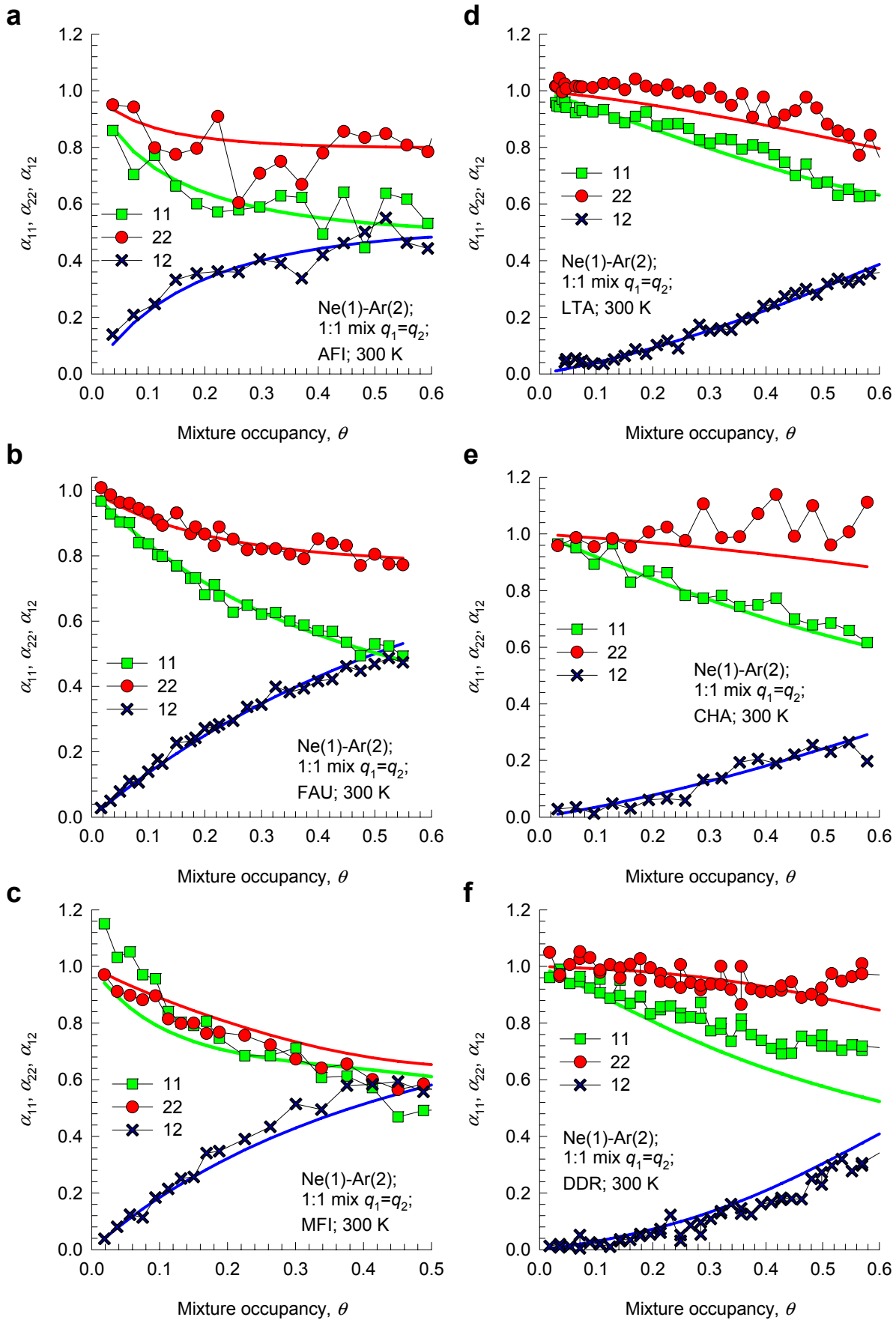

Ne-Ar mixtures at 300 K; varying x2, const qt
Self diffusivities

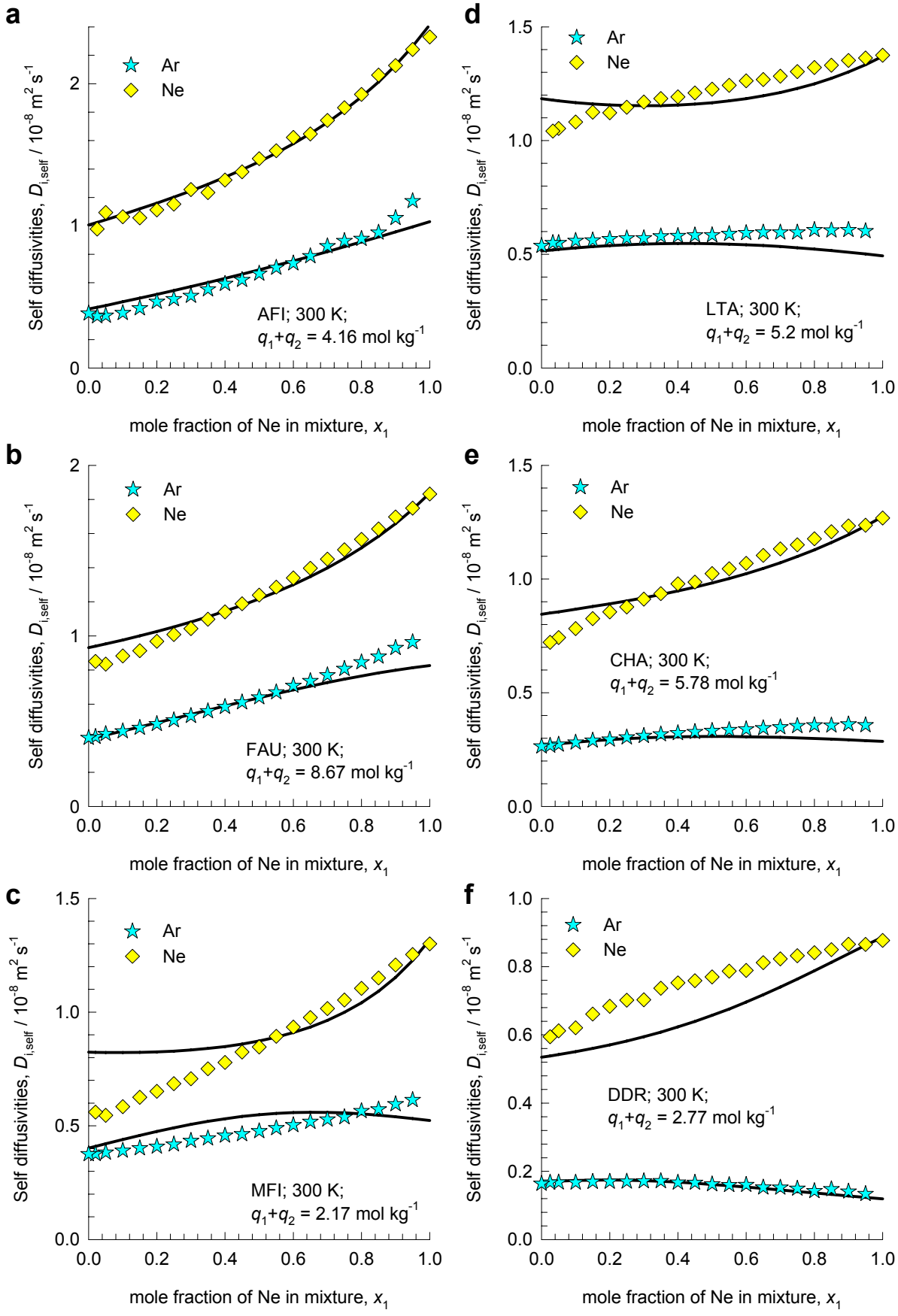

Ne-Ar mixtures at 300 K; varying x2, const qt M-S diffusivities

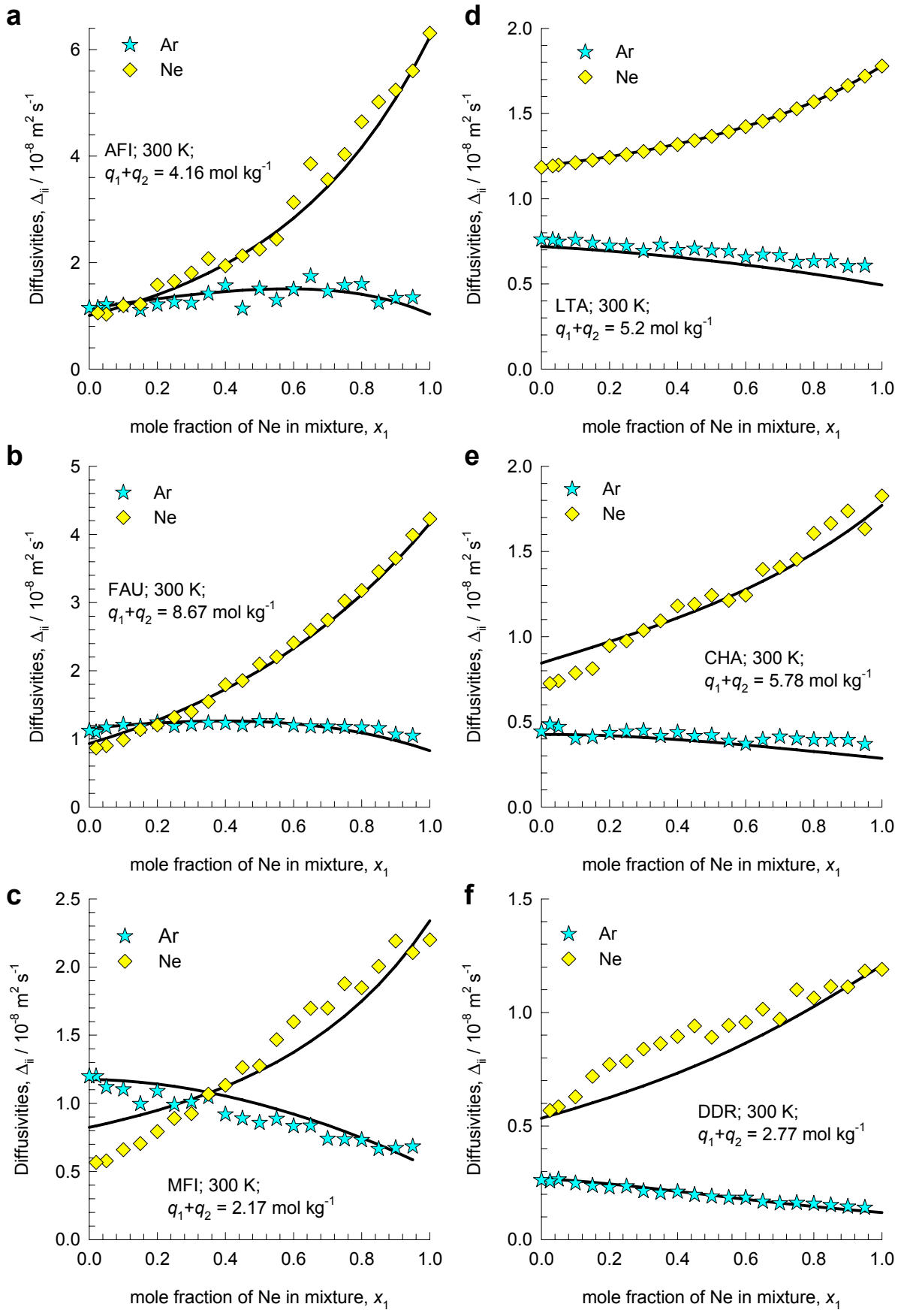

Ne-Ar mixtures at 300 K; varying x2, const qt
Onsager matrix, ratios

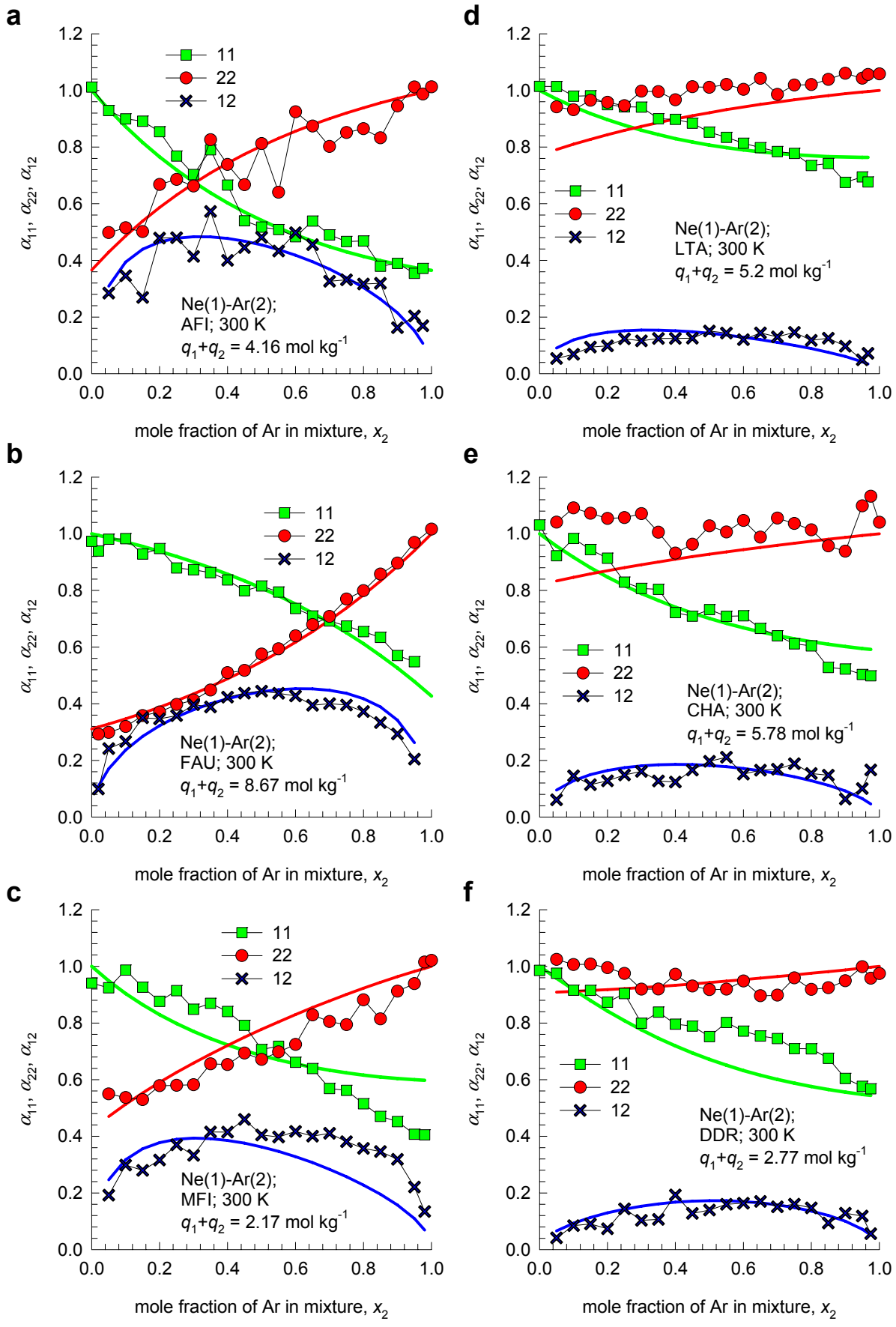

Ne-Ar mixtures in ETS-4 300 K; equimolar mixture

12-ring channels (diffusion is considered only in this direction

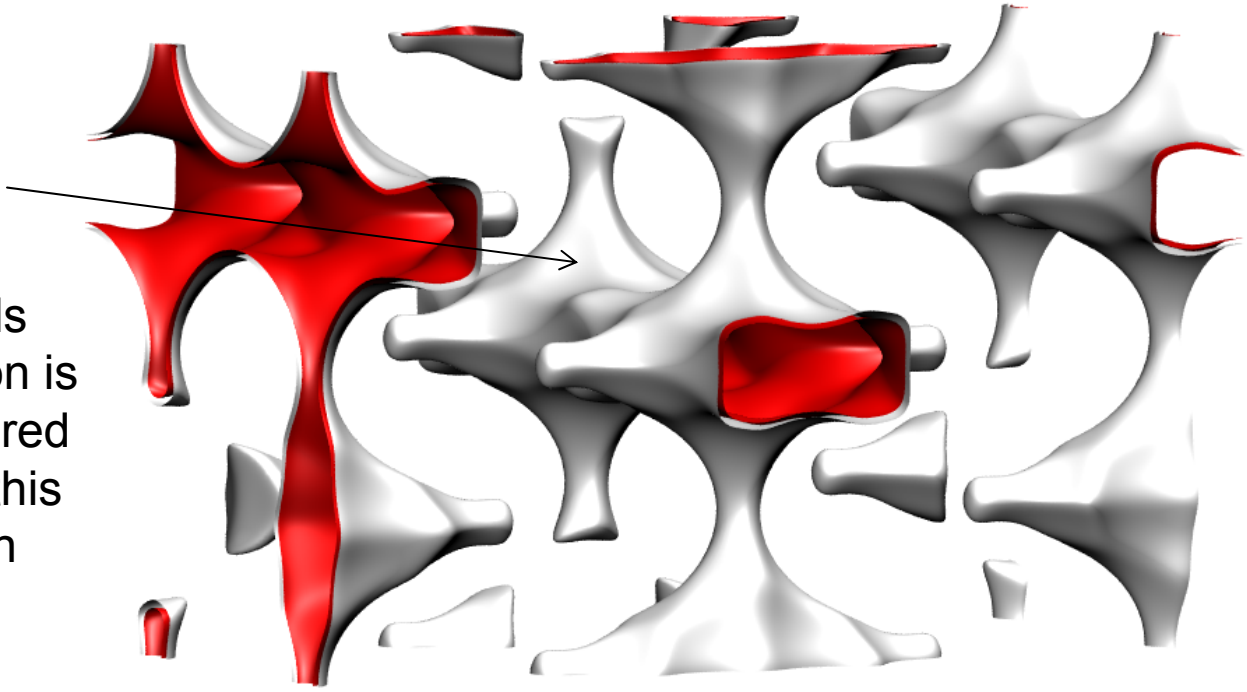

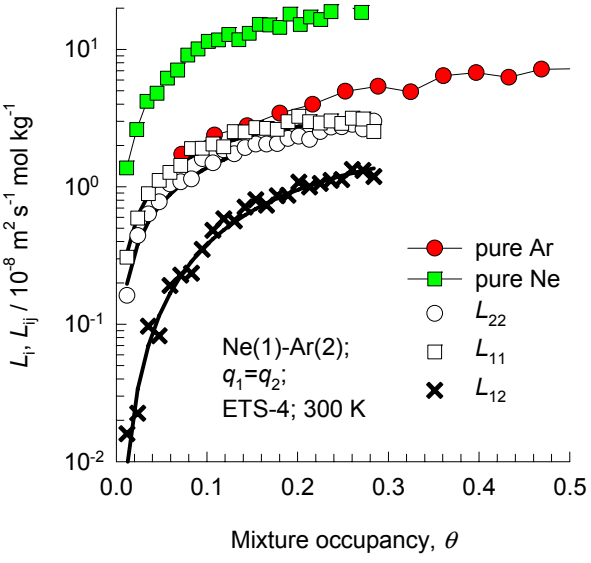

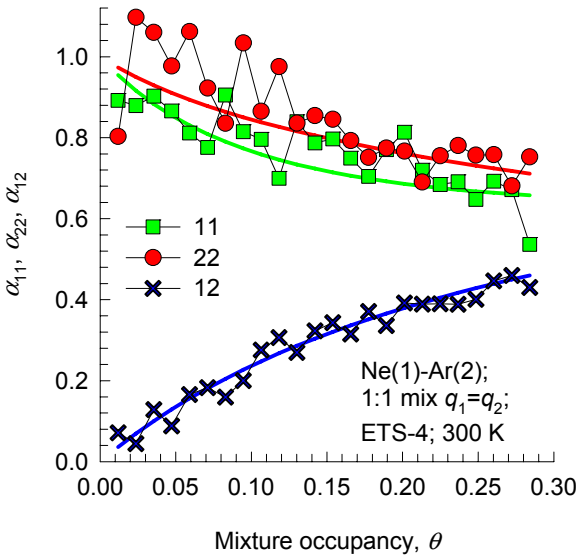

Ne-Ar mixtures in IRMOF-1 at 300 K; equimolar mixture

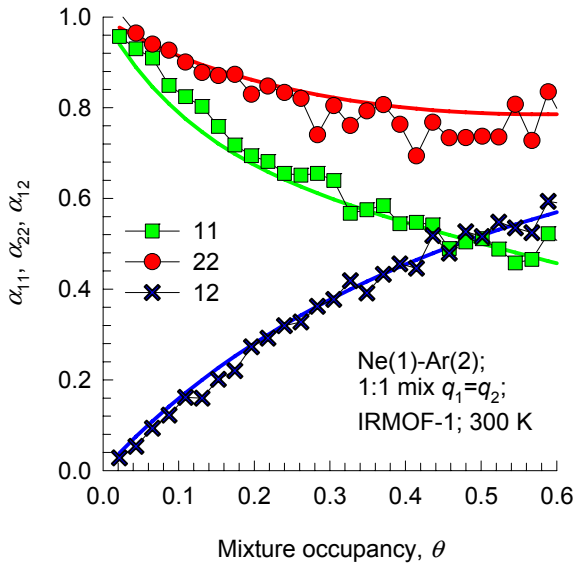

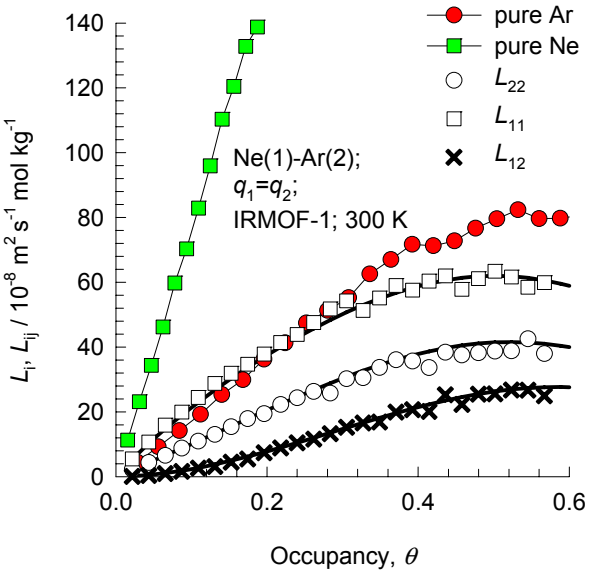

Ne-Ar mixtures in CuBTC at 300 K; equimolar mixture

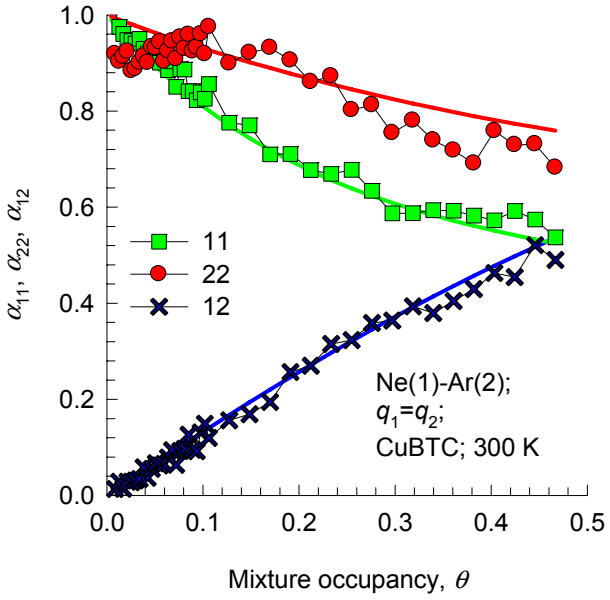

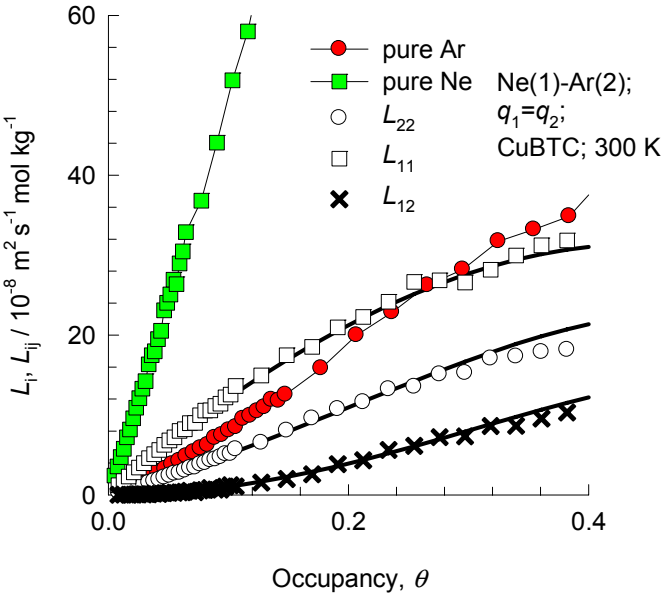

Ne-CO2 mixture

AFI

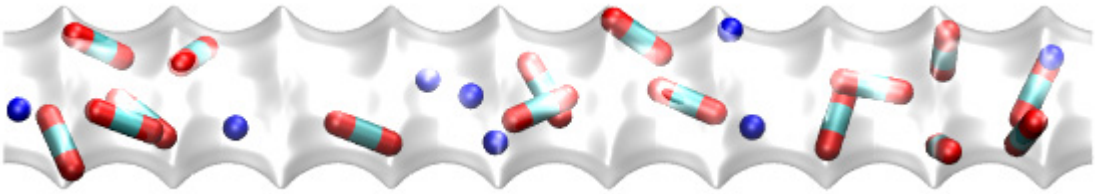

FAU

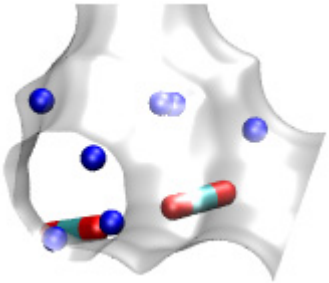

MFI

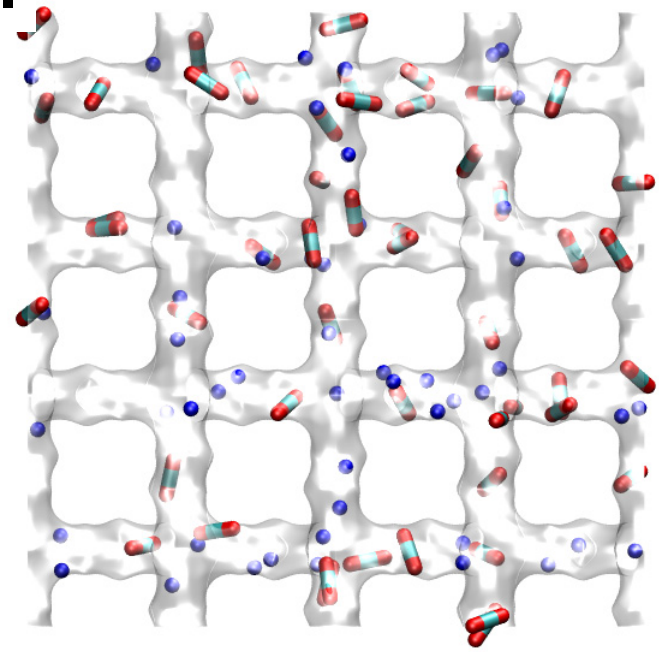

LTA

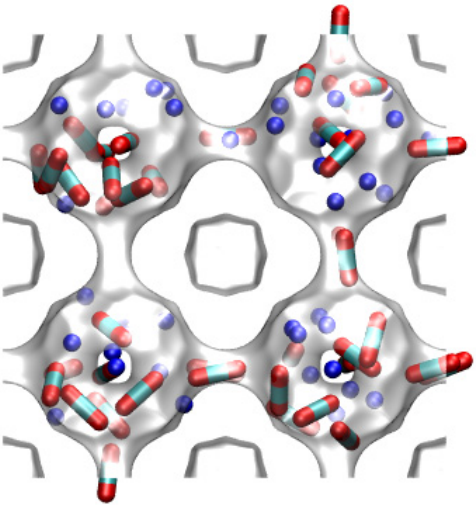

CHA

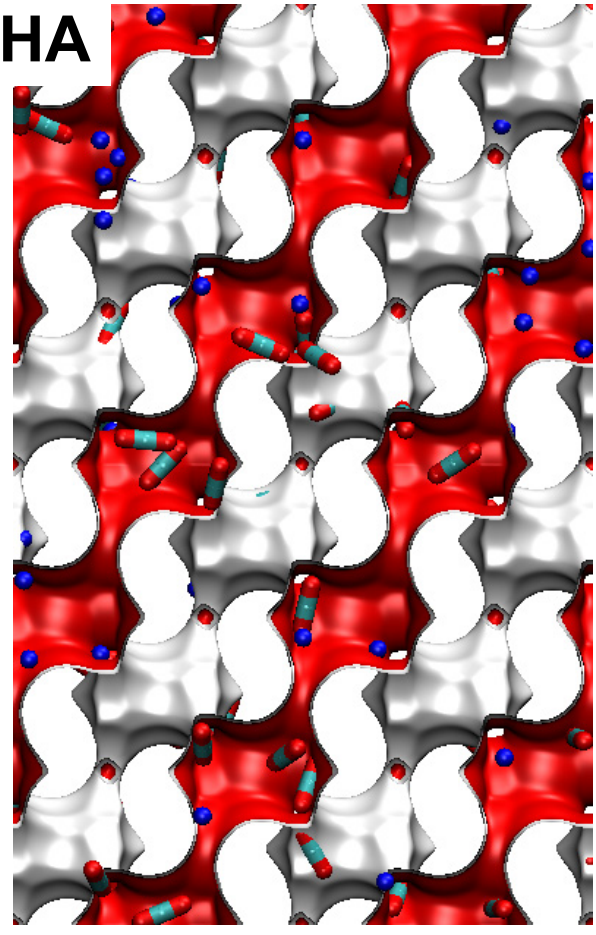

DDR

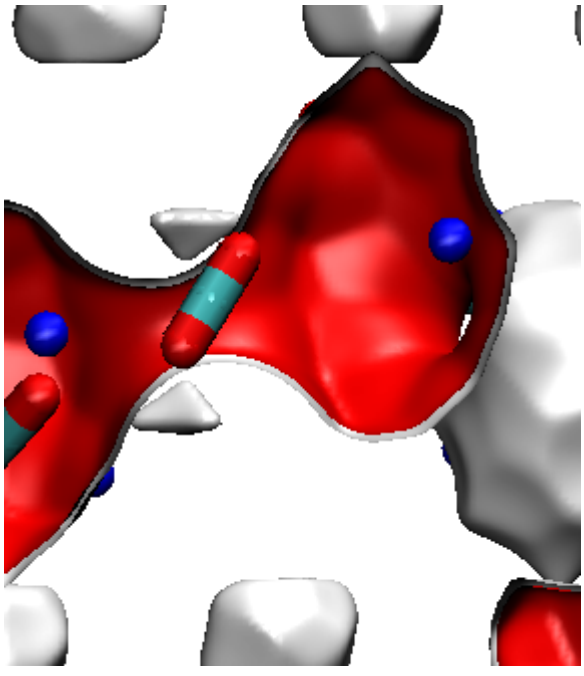

Ne-CO2 mixtures at 300 K; equimolar mixture
Self diffusivities

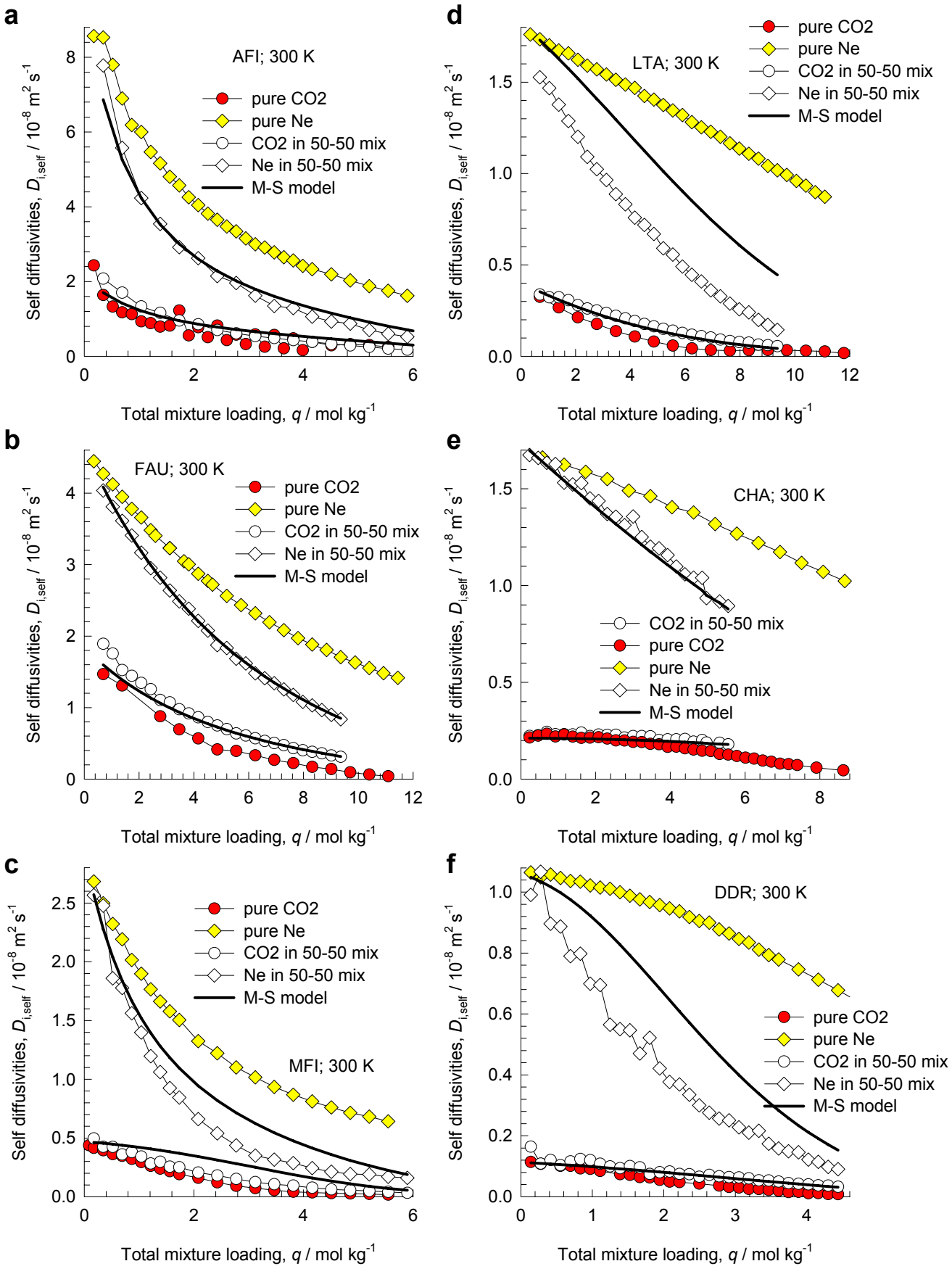

Ne-CO2 mixtures at 300 K; equimolar mixture M-S diffusivities

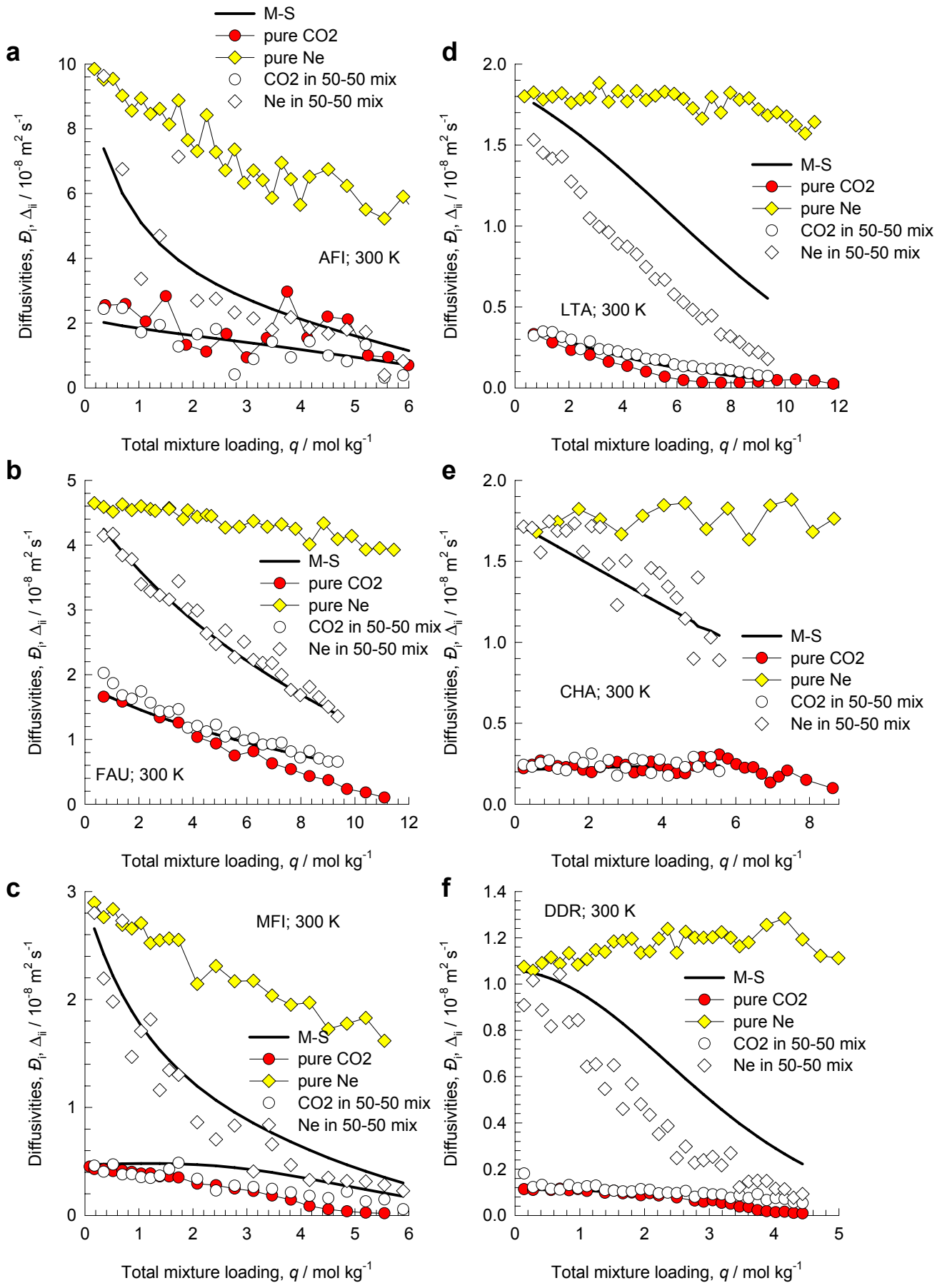

Ne-CO2 mixtures at 300 K; equimolar mixture Onsager matrix, ratios

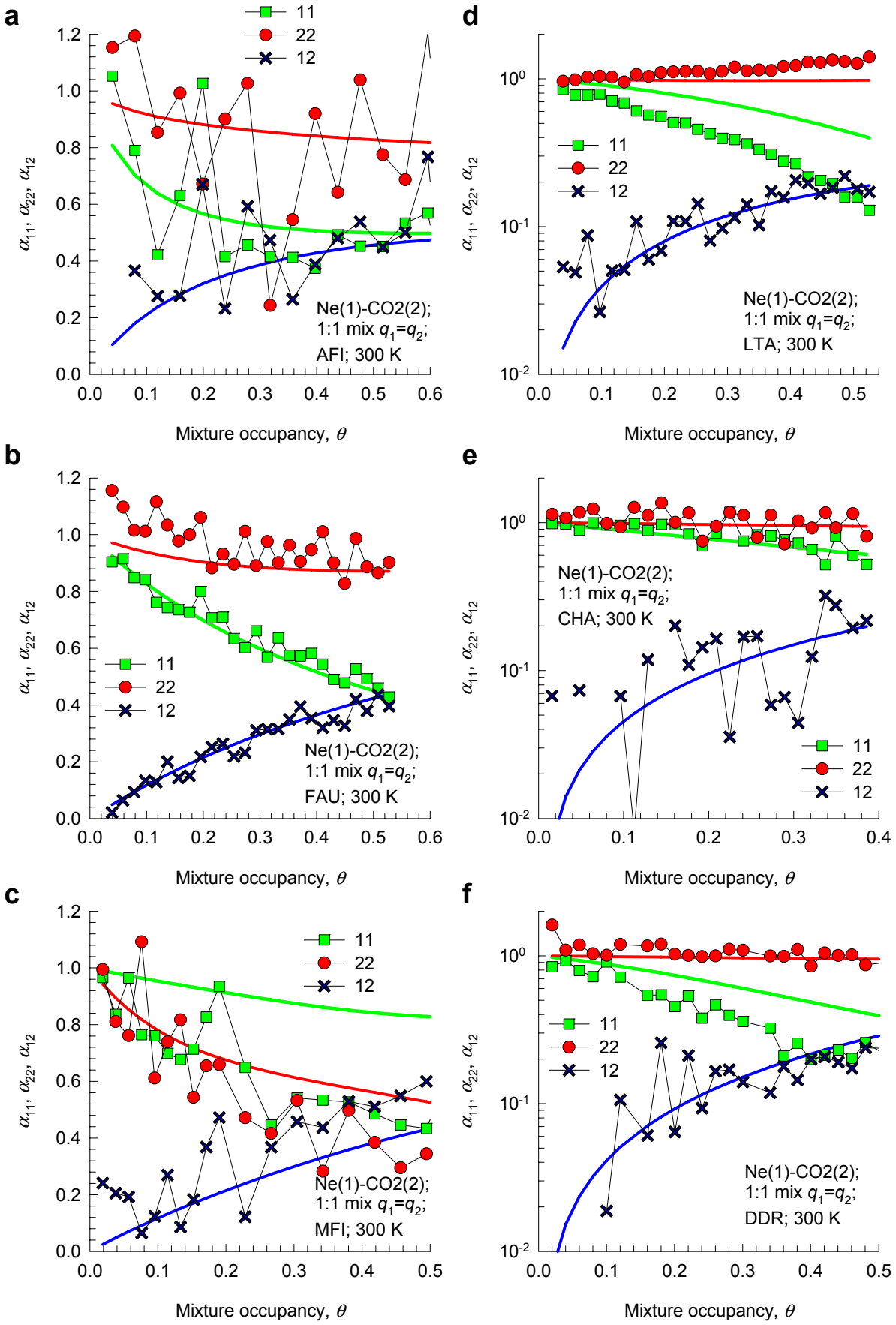

Ne-CO2 mixtures at 300 K; varying x2, const qt
Self diffusivities

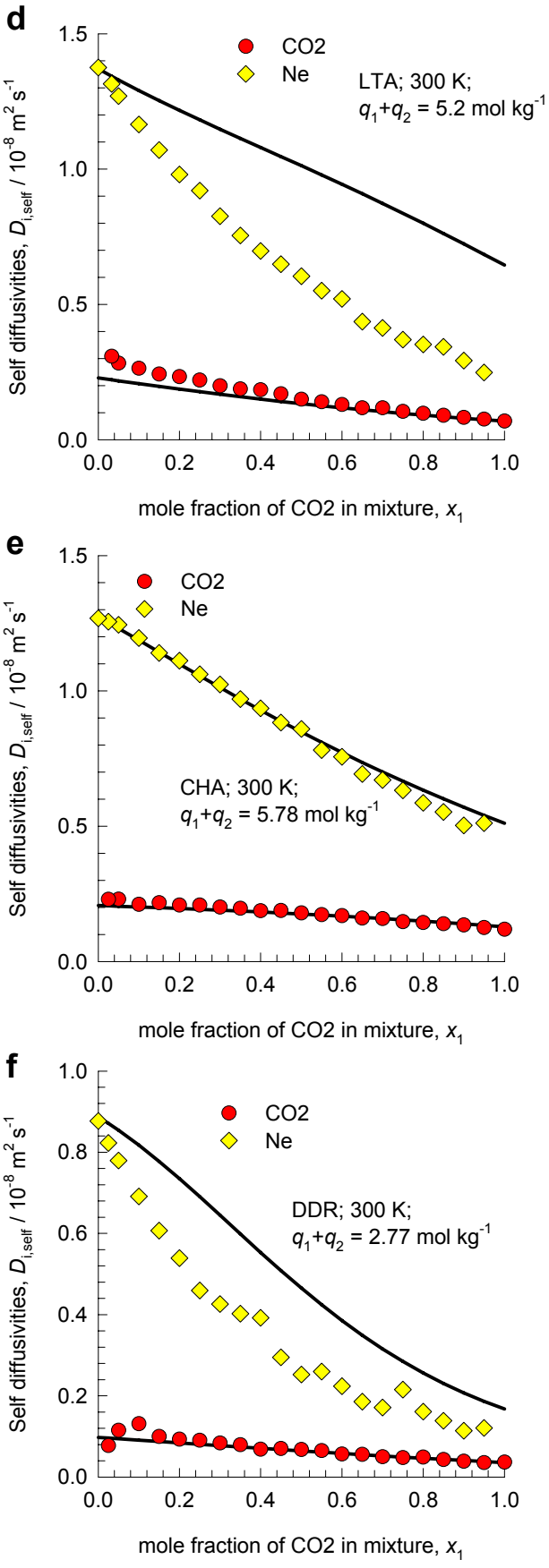

Ne-CO2 mixtures at 300 K; varying x2, const qt M-S diffusivities

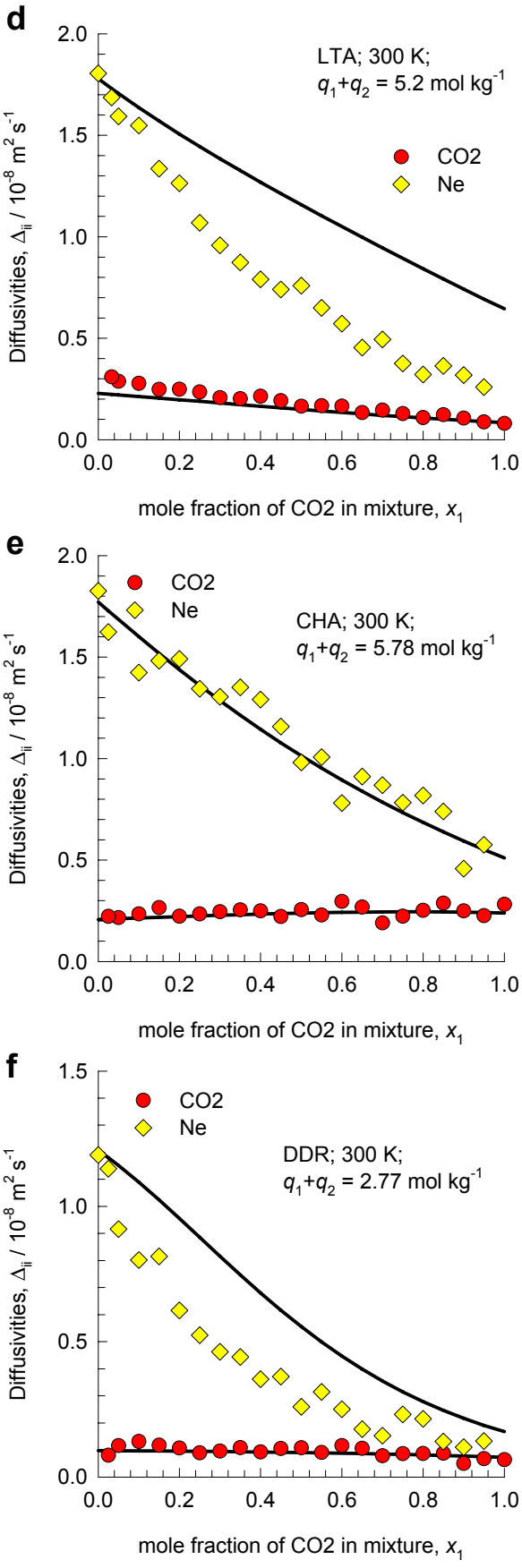

Ne-CO2 mixtures at 300 K; varying x2, const qt
Onsager matrix, ratios

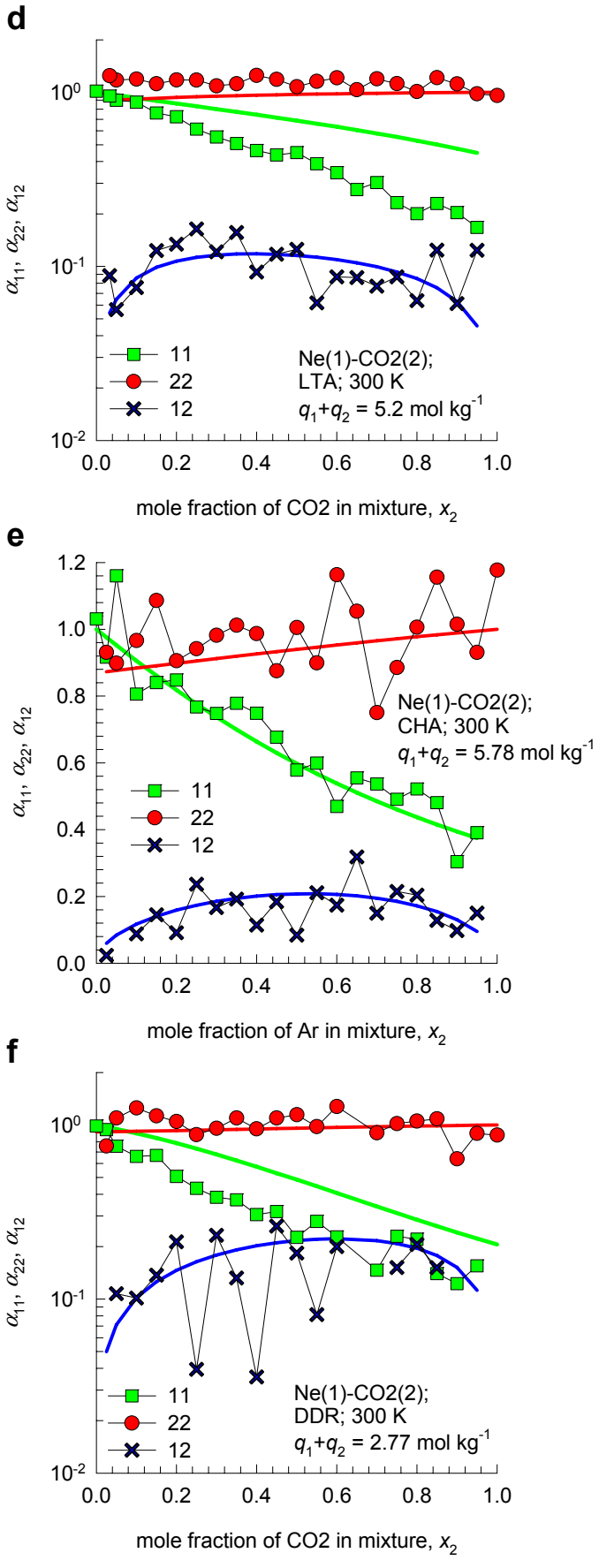

CO2-Ar mixture

LTA

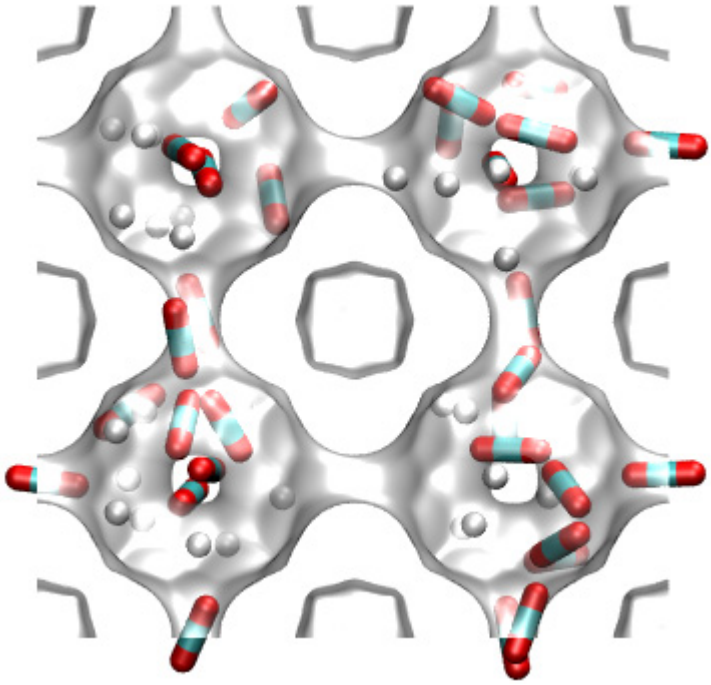

DDR

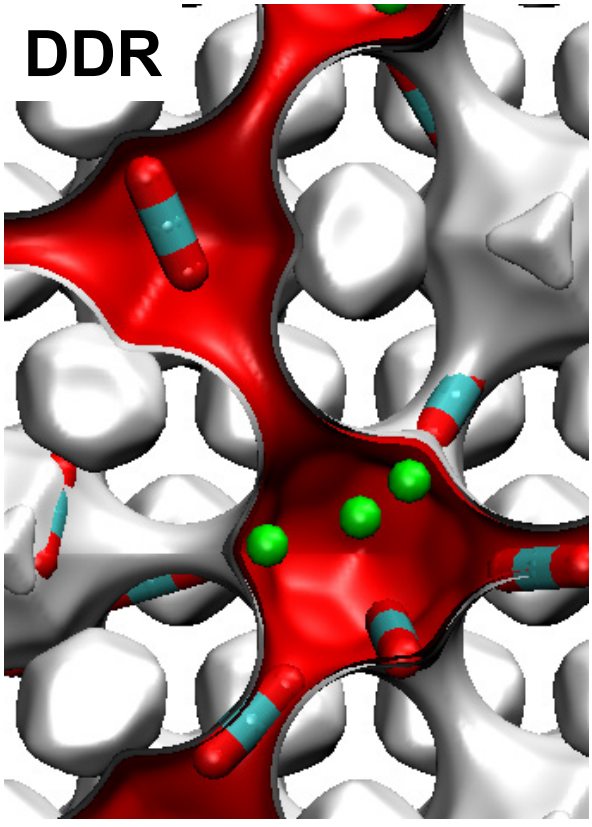

CHA

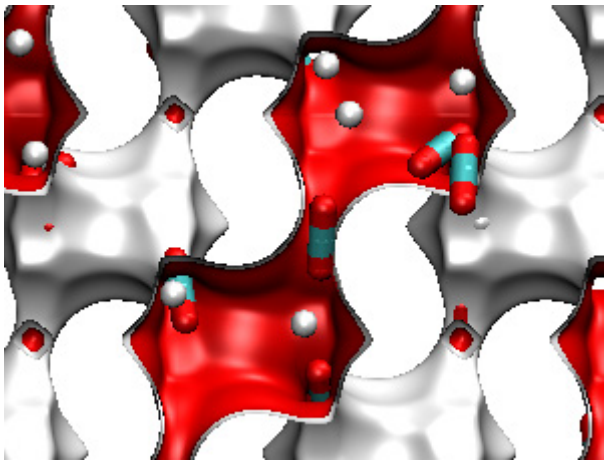

CO2-Ar mixtures at 300 K; equimolar mixture
Self diffusivities

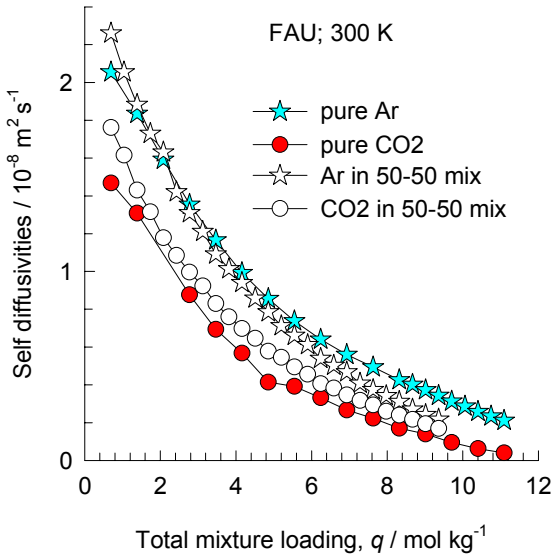

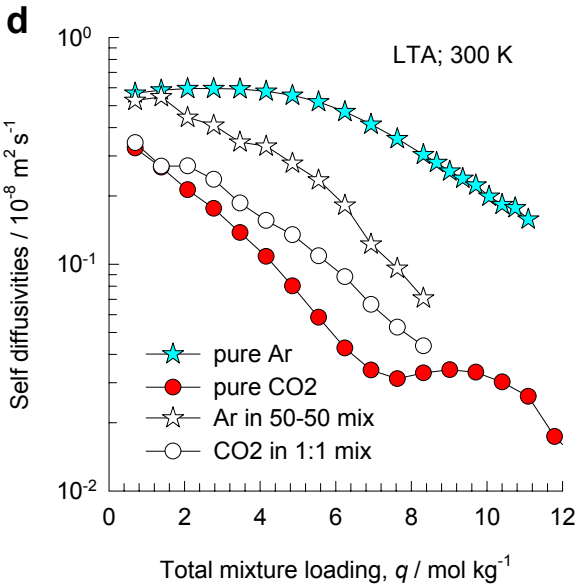

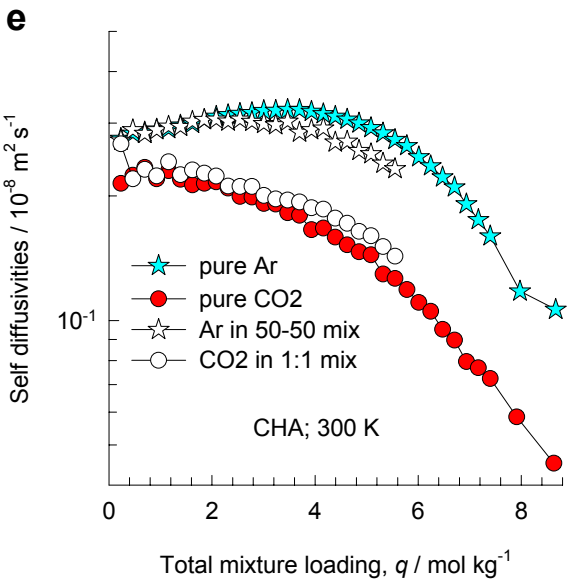

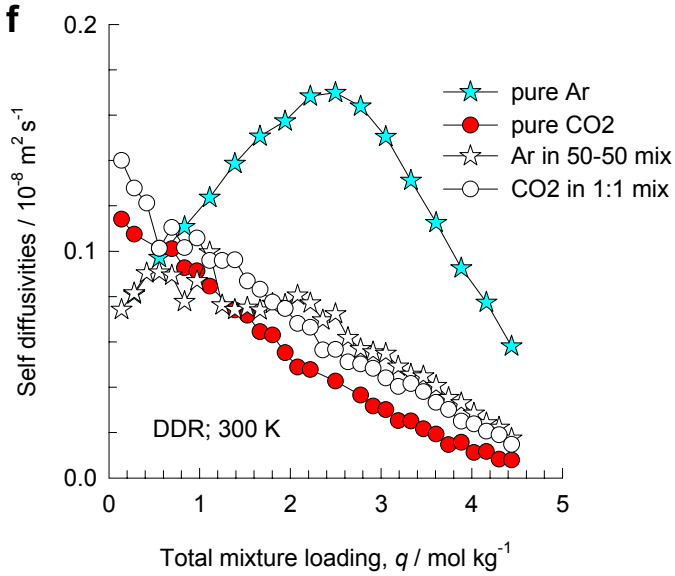

CO2-Ar mixtures at 300 K; equimolar mixture M-S diffusivities

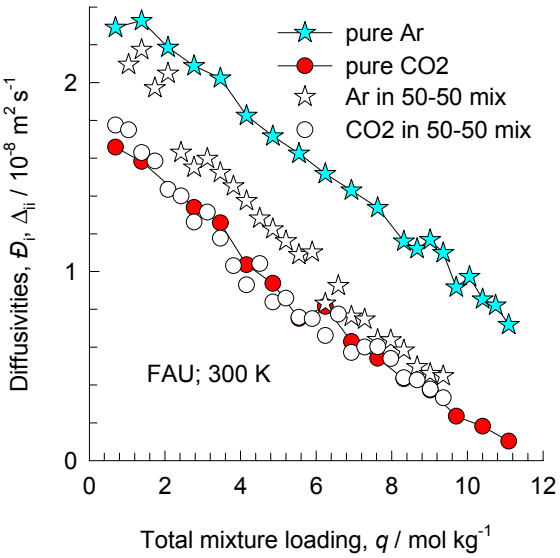

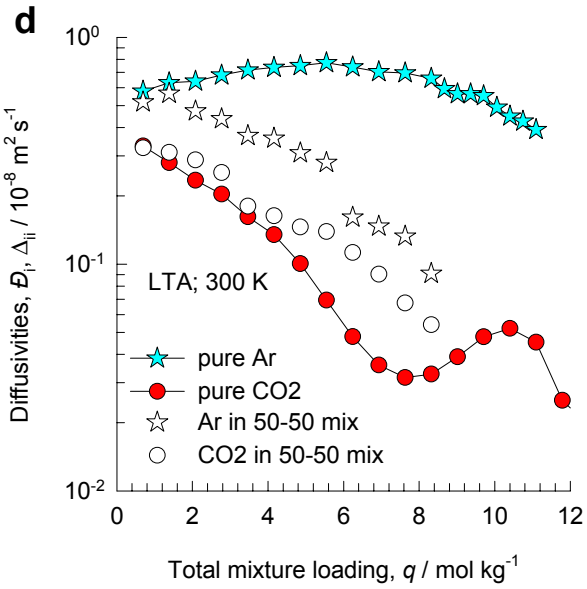

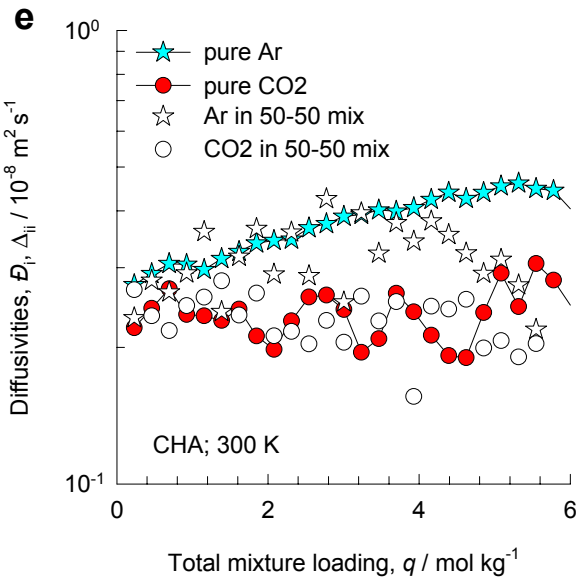

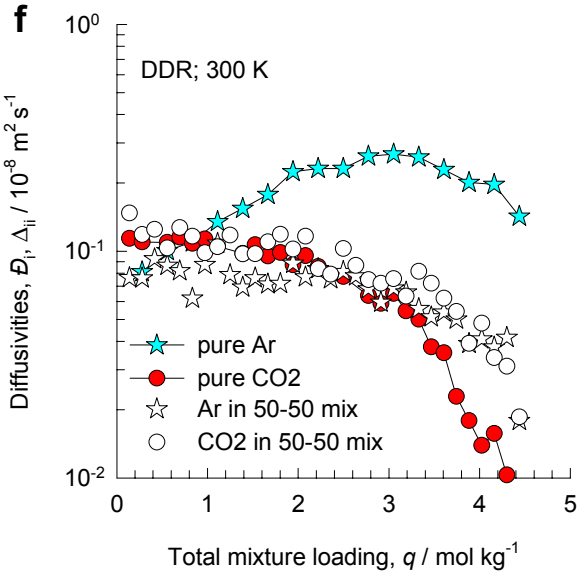

C1-Ar mixtures at 300 K; equimolar mixture Self-diffusivities

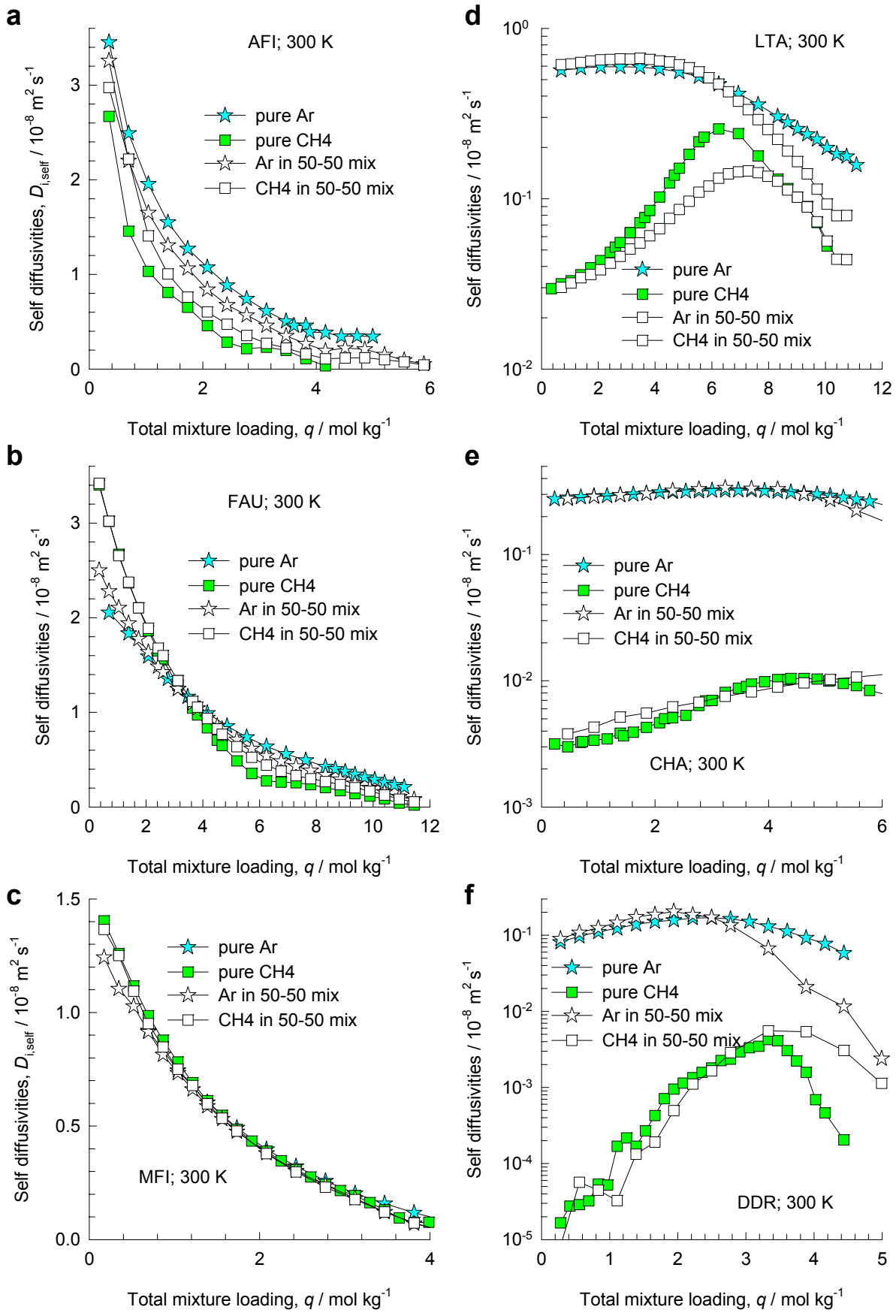

C1-Ar mixtures at 300 K; equimolar mixture M-S diffusivities

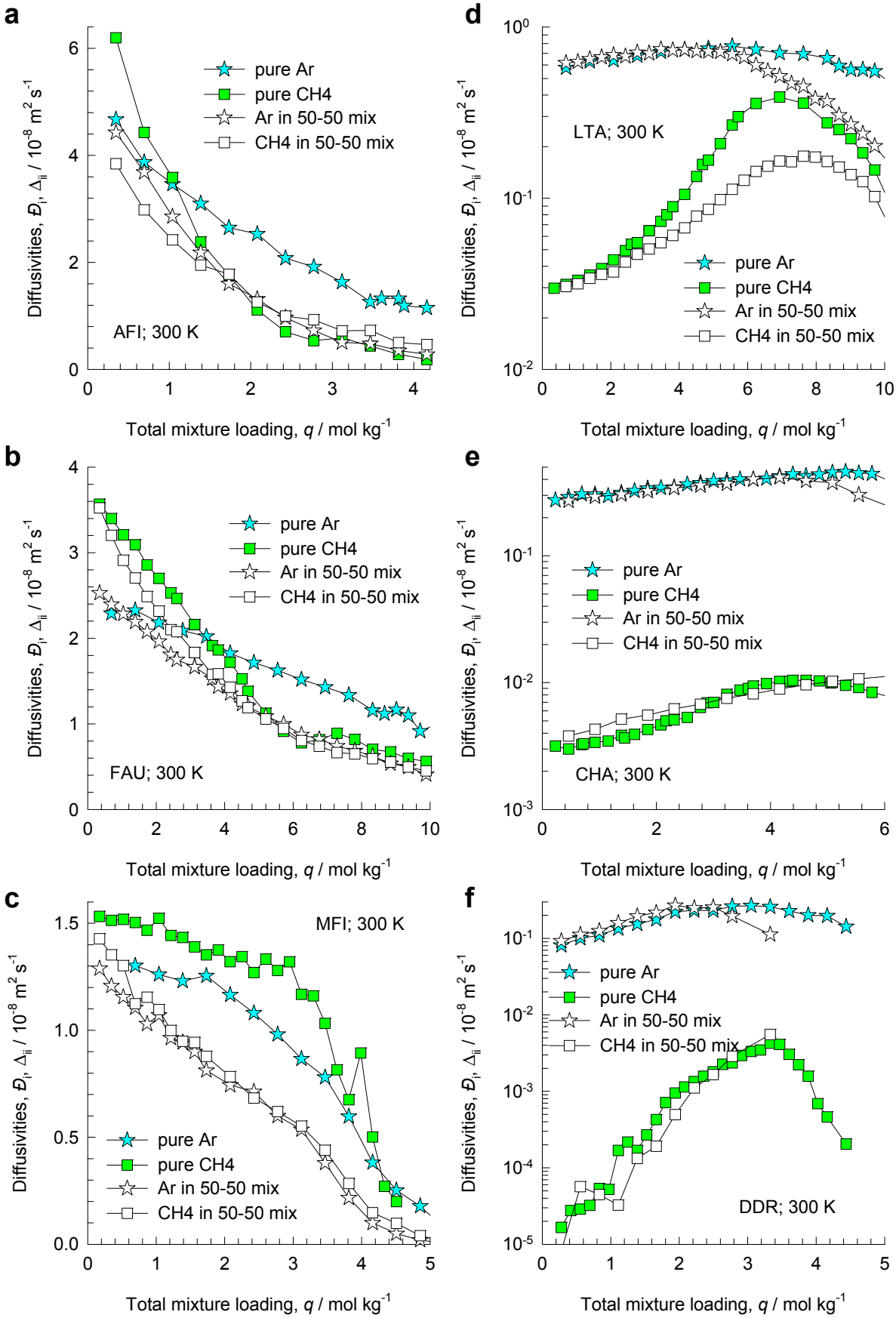

C1-Ar mixtures at 300 K; equimolar mixture Onsager matrix, ratios

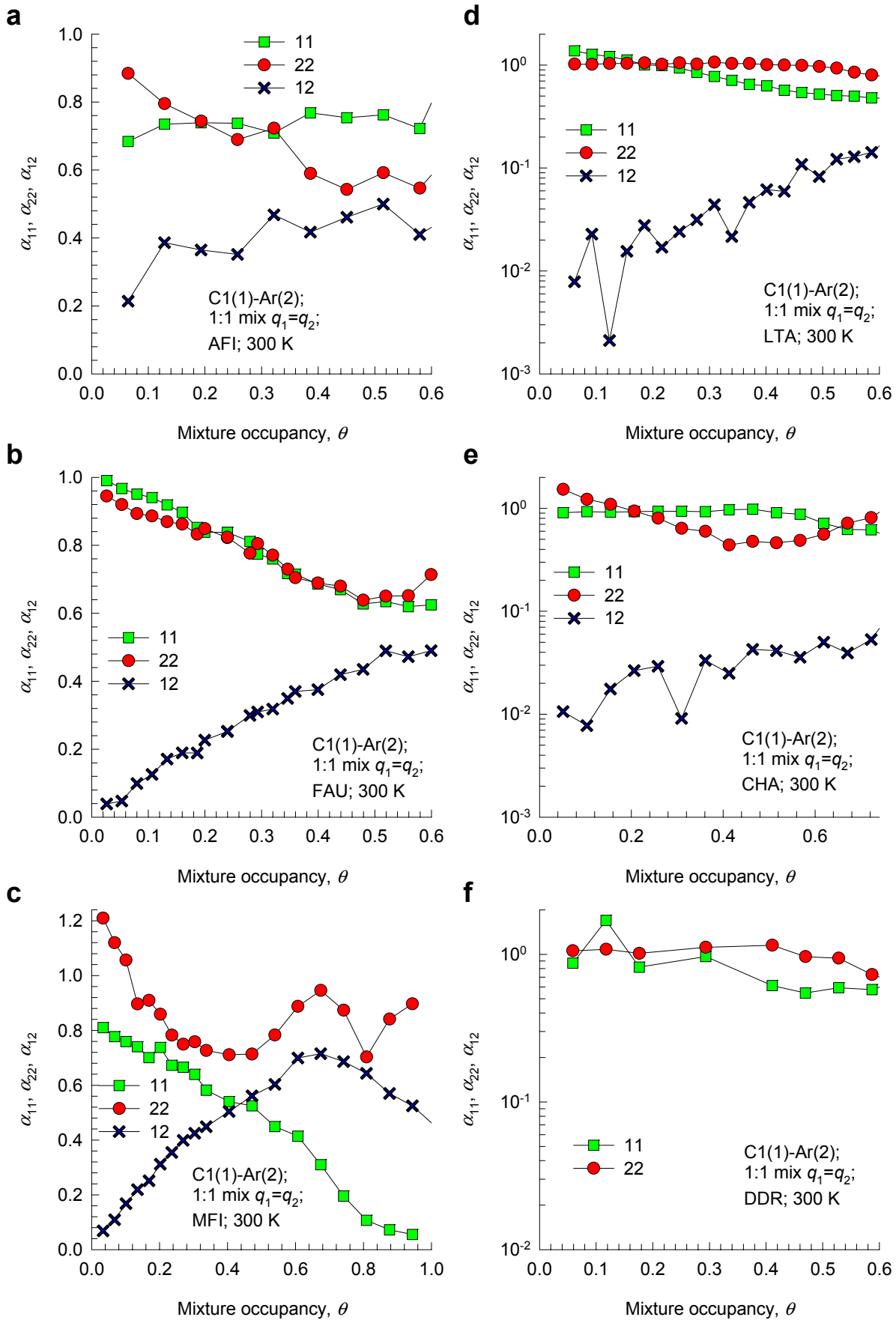

C1-Ar mixtures in ETS-4 300 K; equimolar mixture

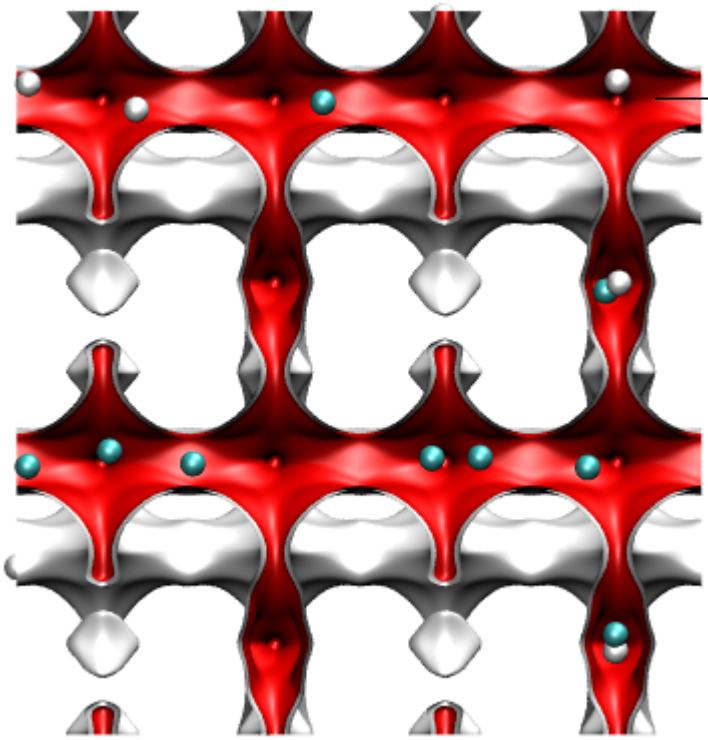

12-ring channels
(diffusion is considered only in this direction

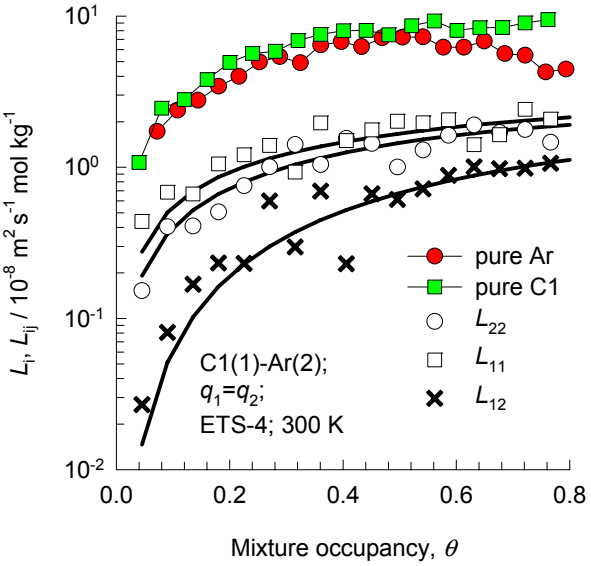

C1-Ar mixtures in IRMOF-1 at 300 K; equimolar mixture

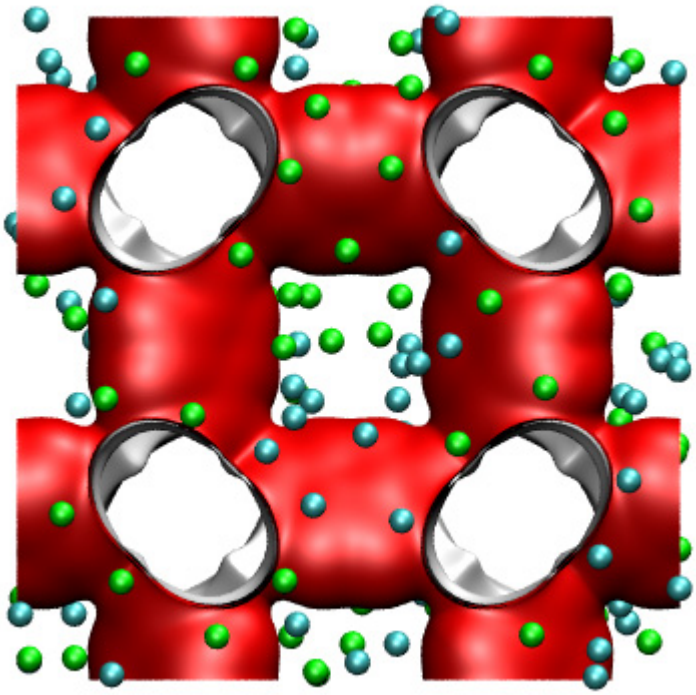

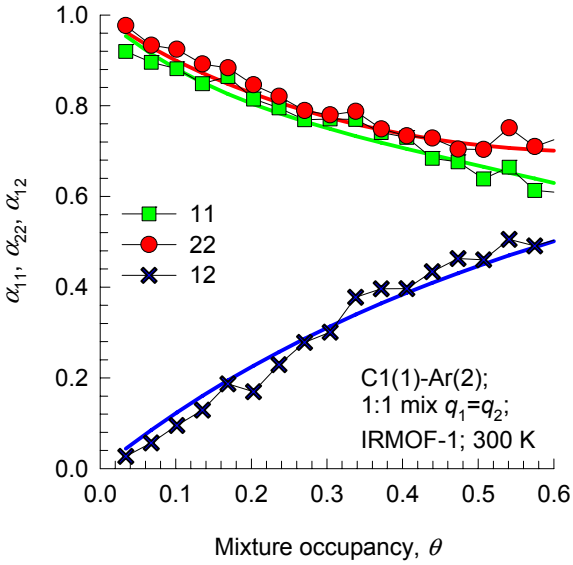

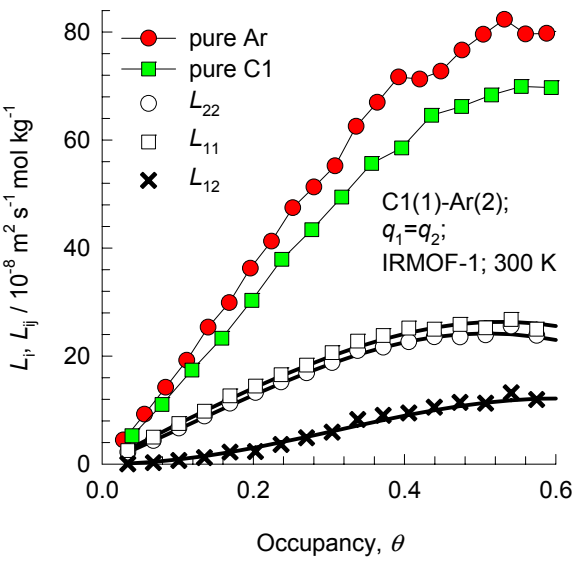

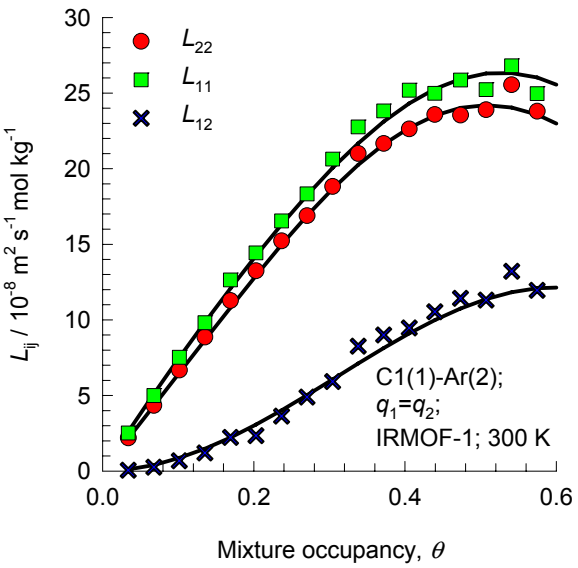

C1-Ar mixtures in CuBTC at 300 K; equimolar mixture

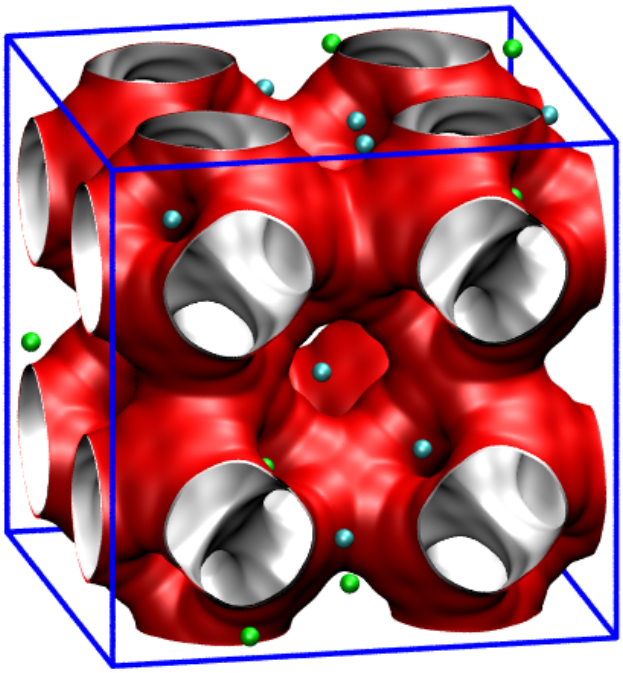

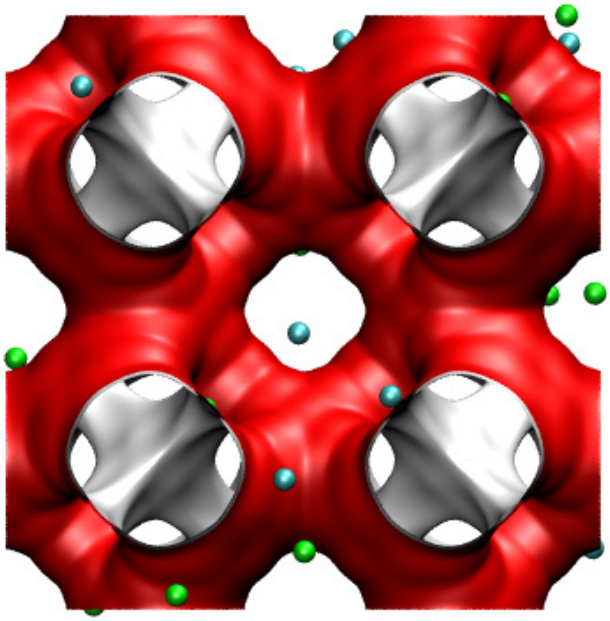

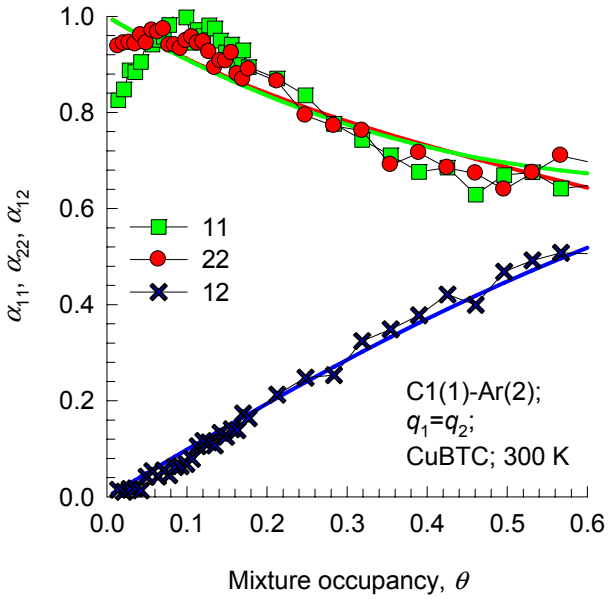

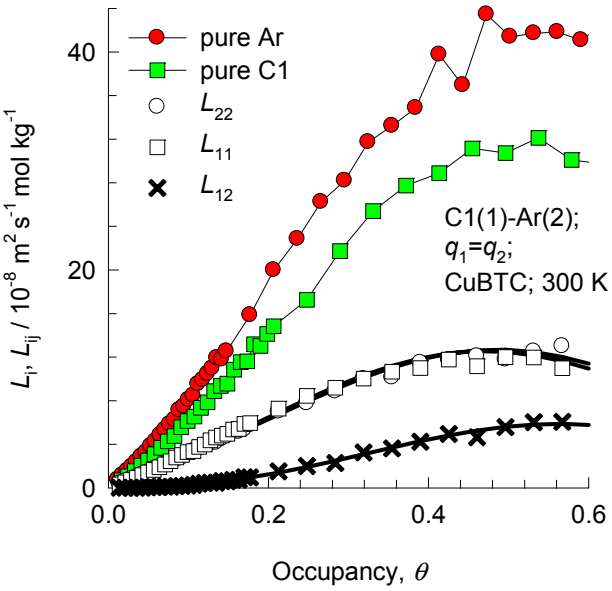

Ar-Kr mixtures in LTA at 300 K; Self and M-S diffusivities

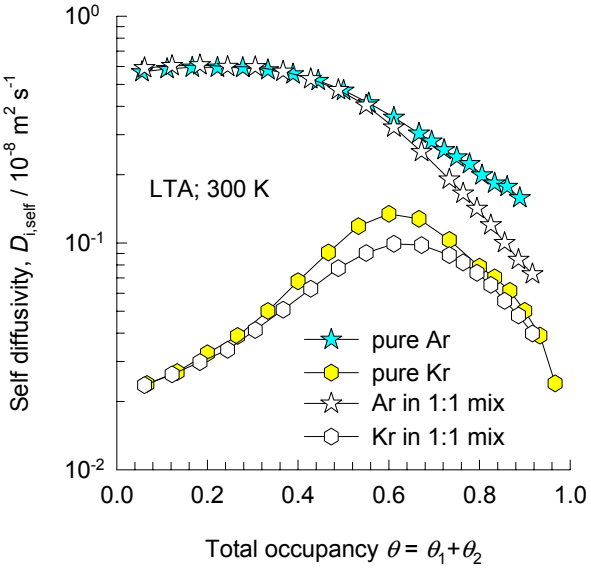

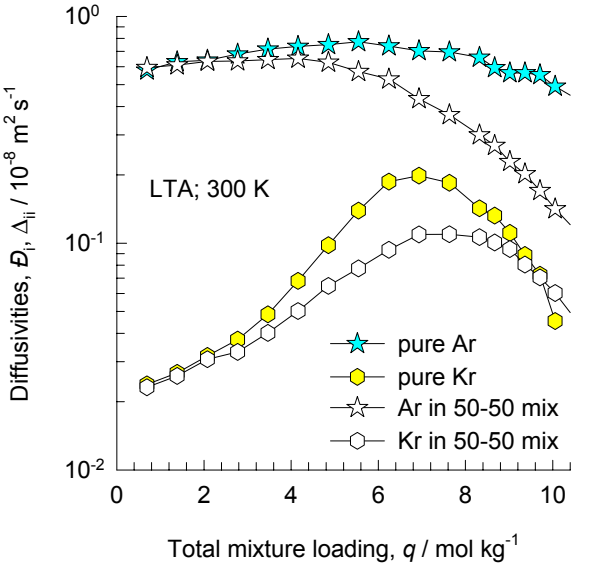

N2-CH4 mixtures in LTA at 300 K; Self and M-S diffusivities

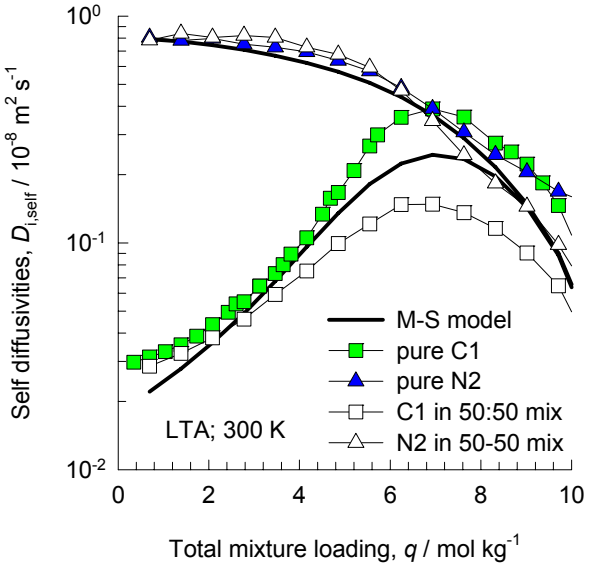

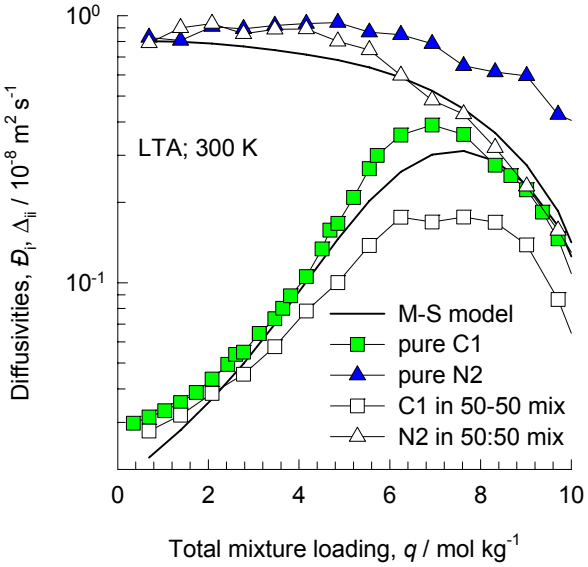

CO2-O2 mixtures in DDR at 300 K; Self and M-S diffusivities

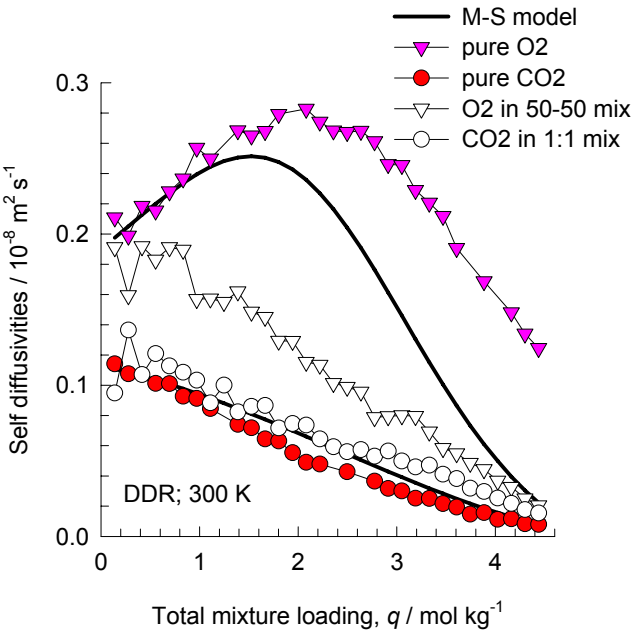

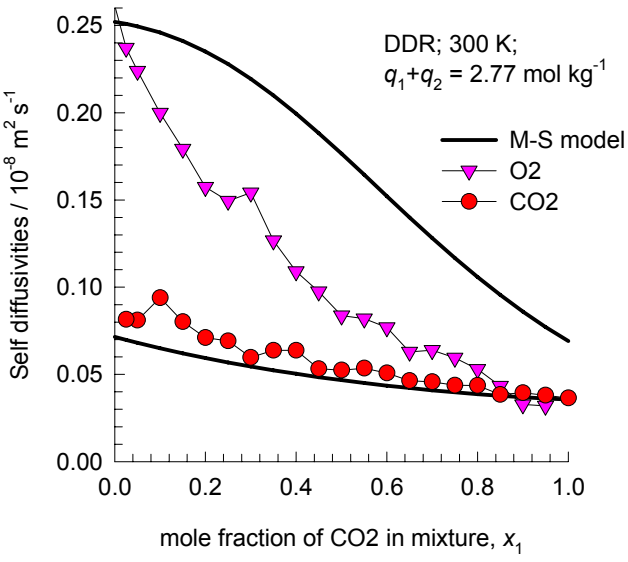

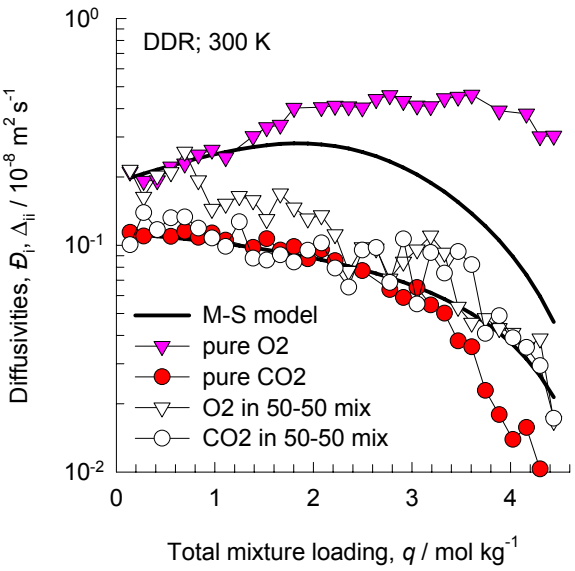

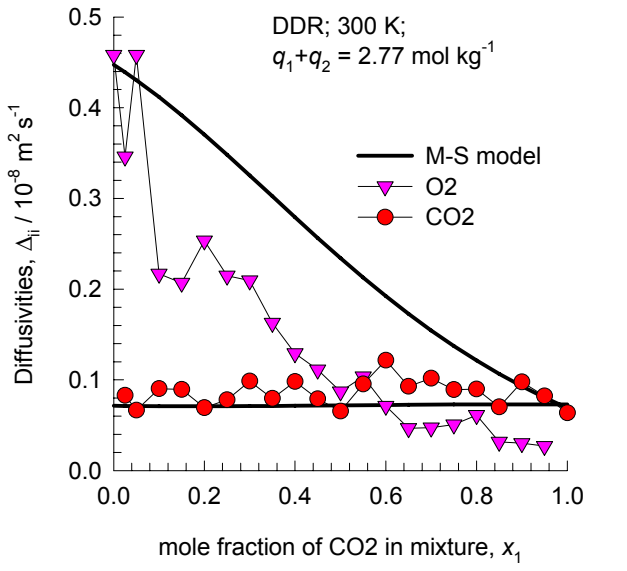

CO2-N2 mixtures in DDR at 300 K; Self and M-S diffusivities

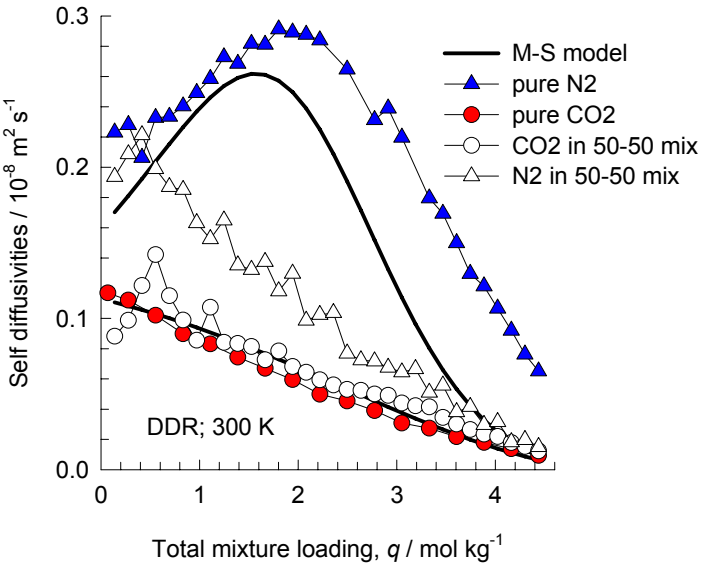

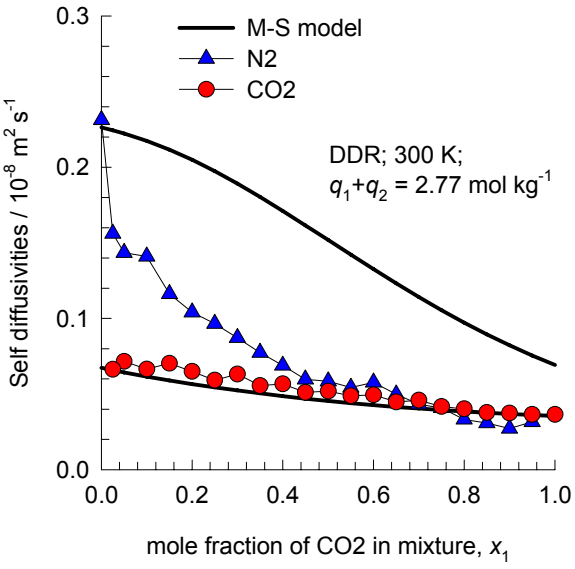

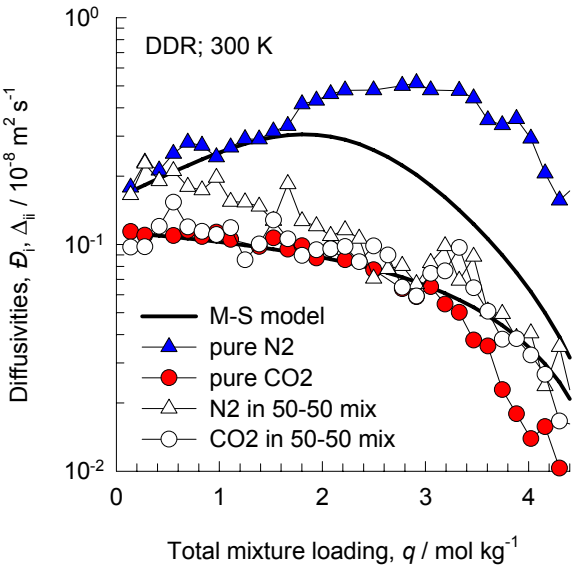

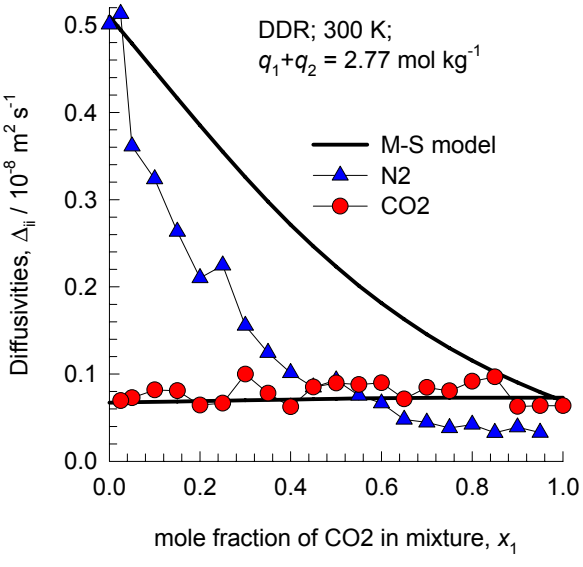

N2-O2 mixtures in DDR at 300 K; Self and M-S diffusivities

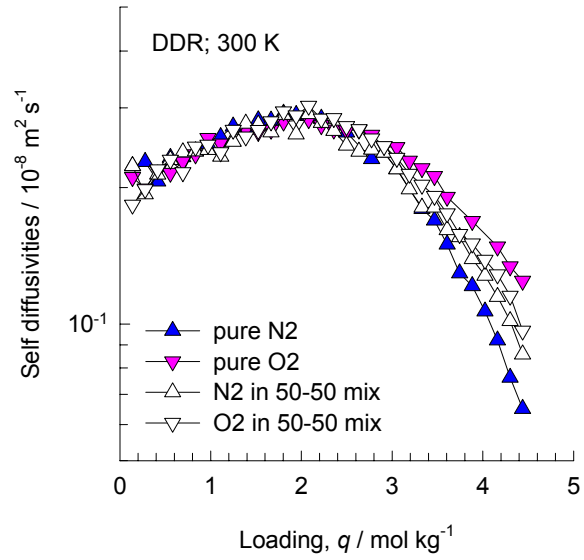

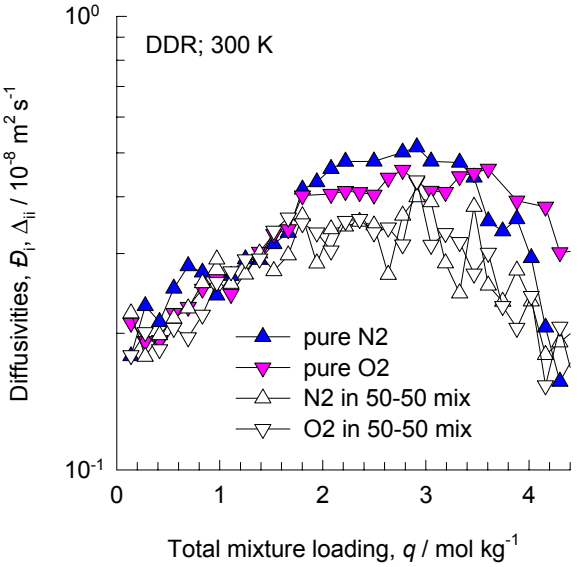

C1-C3 mixtures in AFI at 300 K; Self and M-S diffusivities

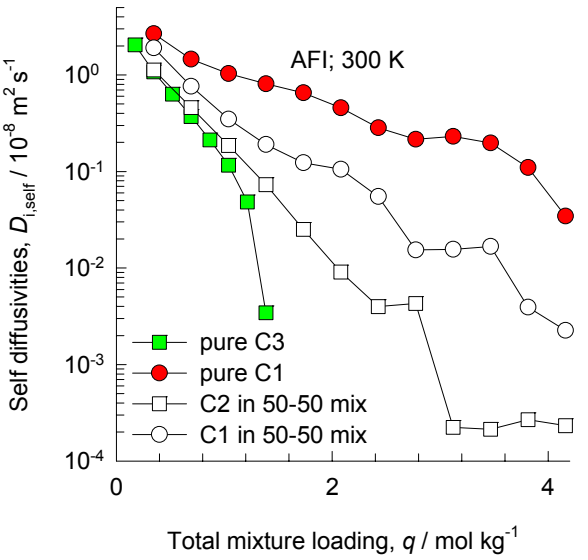

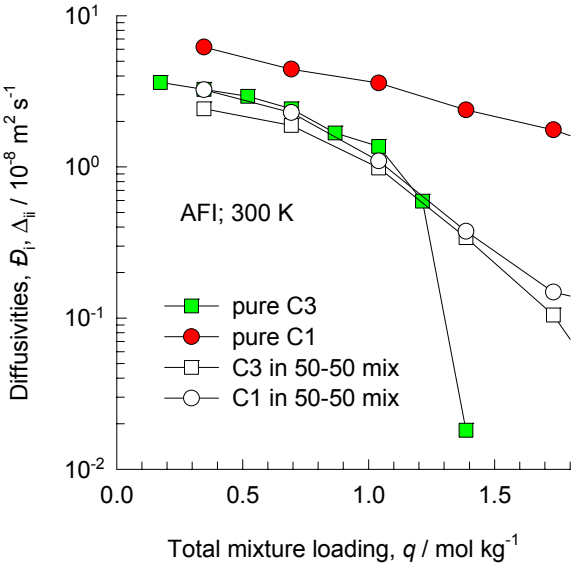

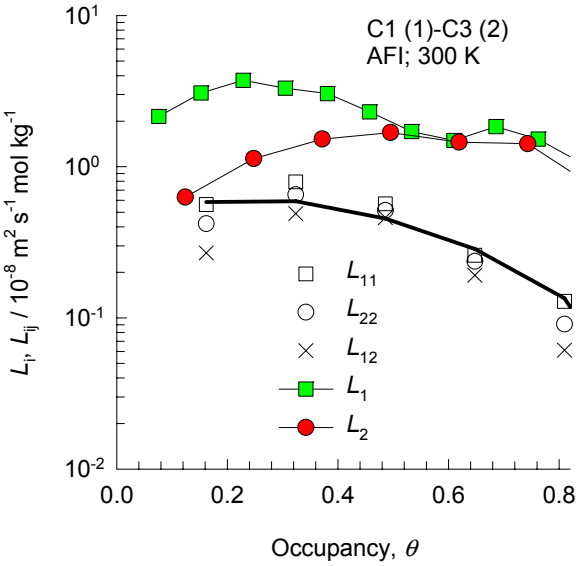

C1-C2 mixtures in FAU at 300 K; Self and M-S diffusivities

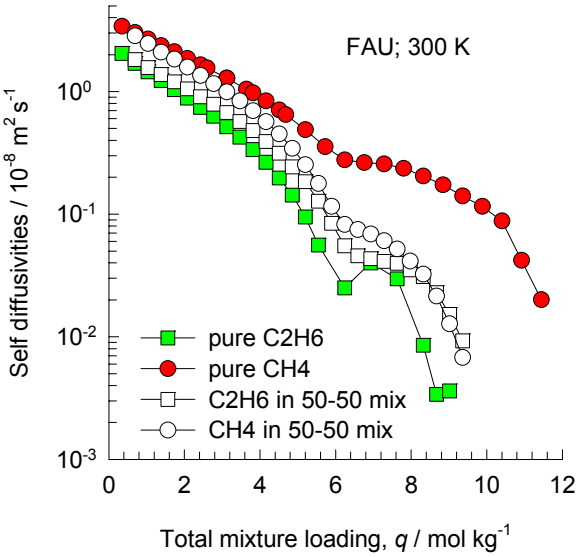

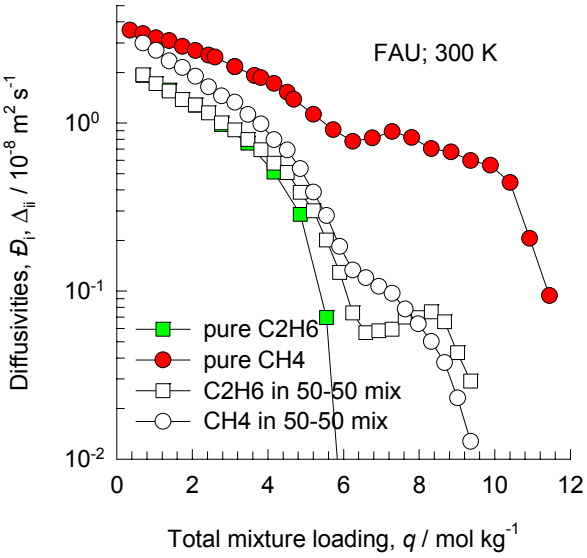

C1-C2 mixtures in MOR at 300 K; Self and M-S diffusivities

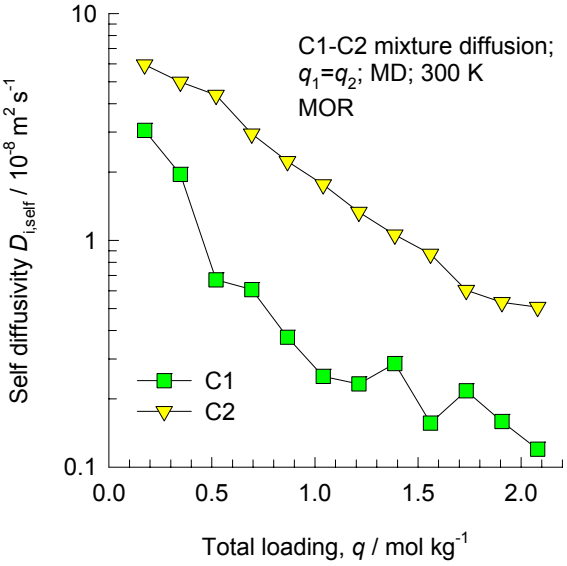

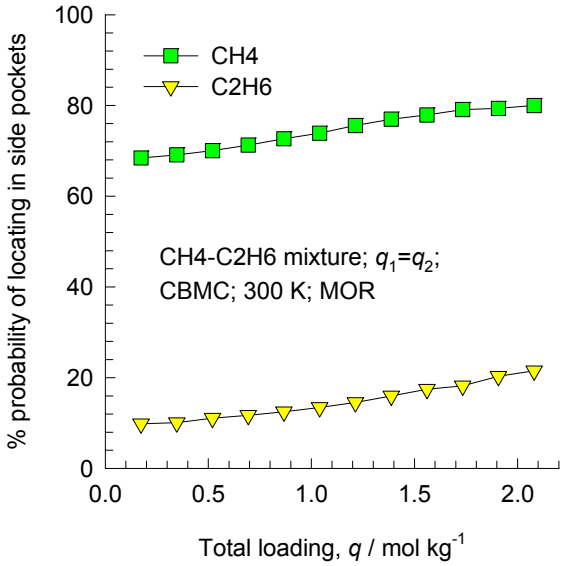

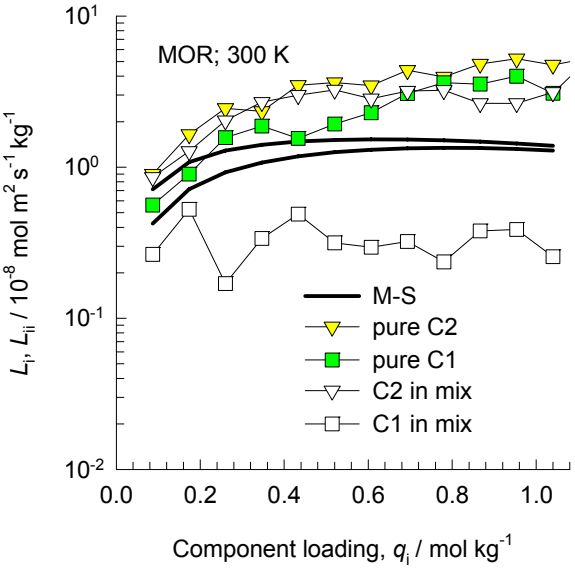

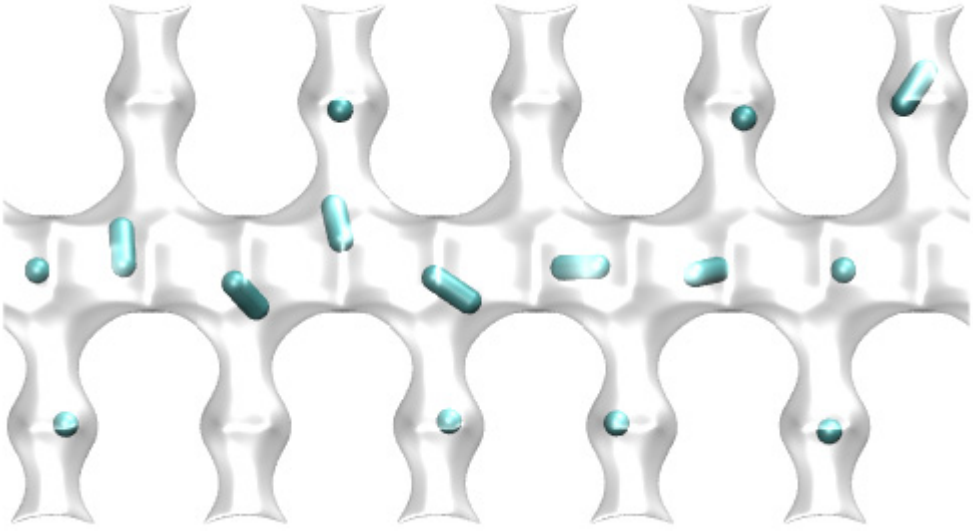

C1-C3 mixtures in MOR at 300 K; Self and M-S diffusivities

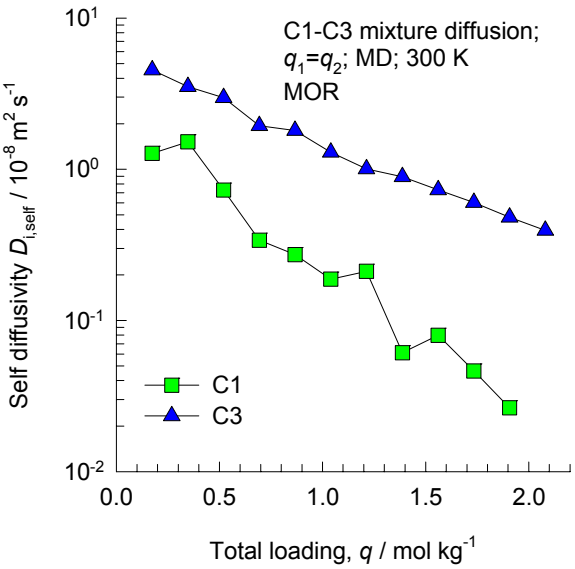

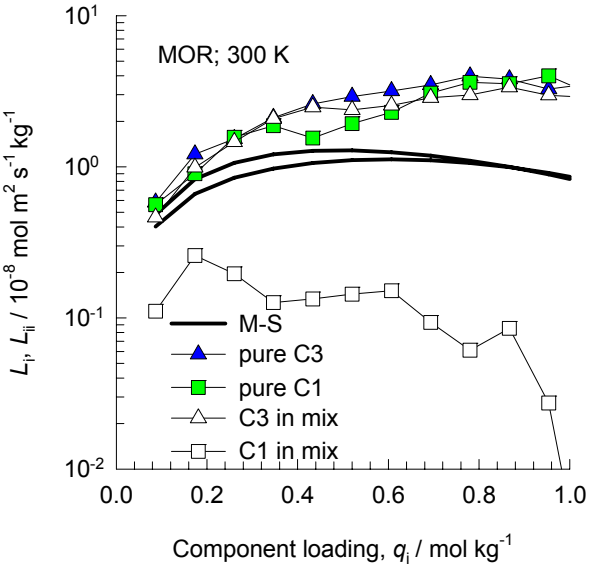

M-S diffusivity of Ne

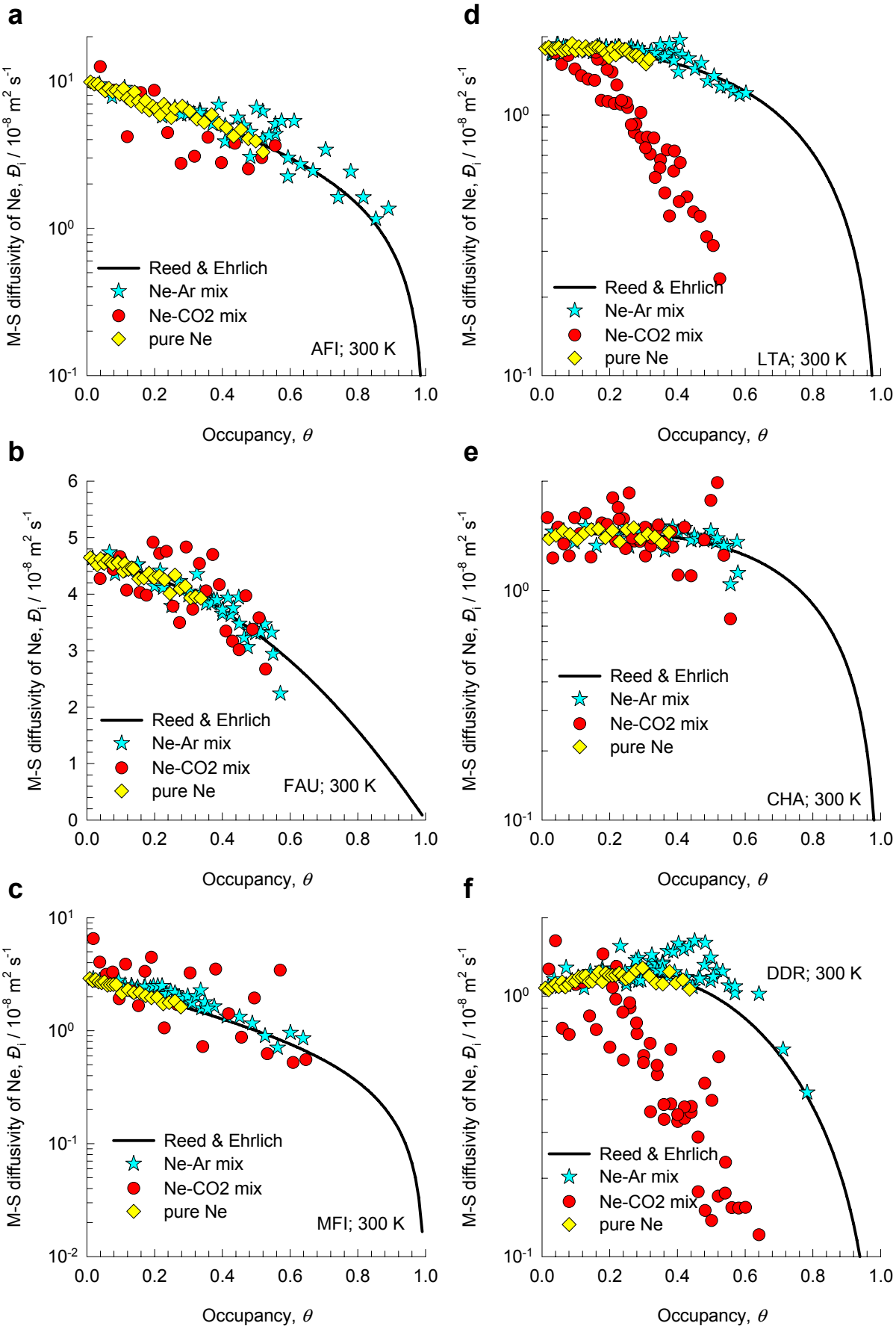

M-S diffusivity of Ar

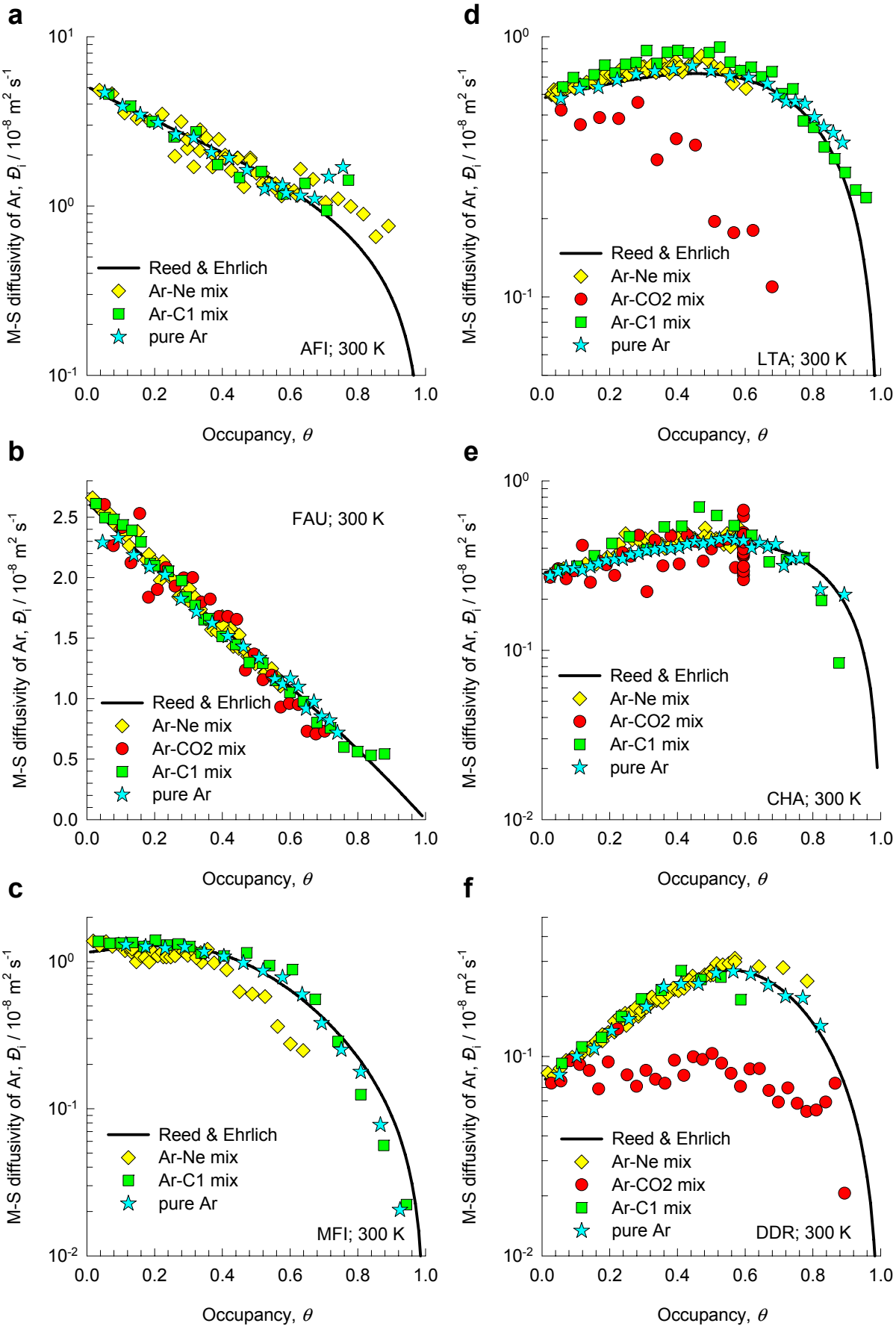

M-S diffusivity of C1

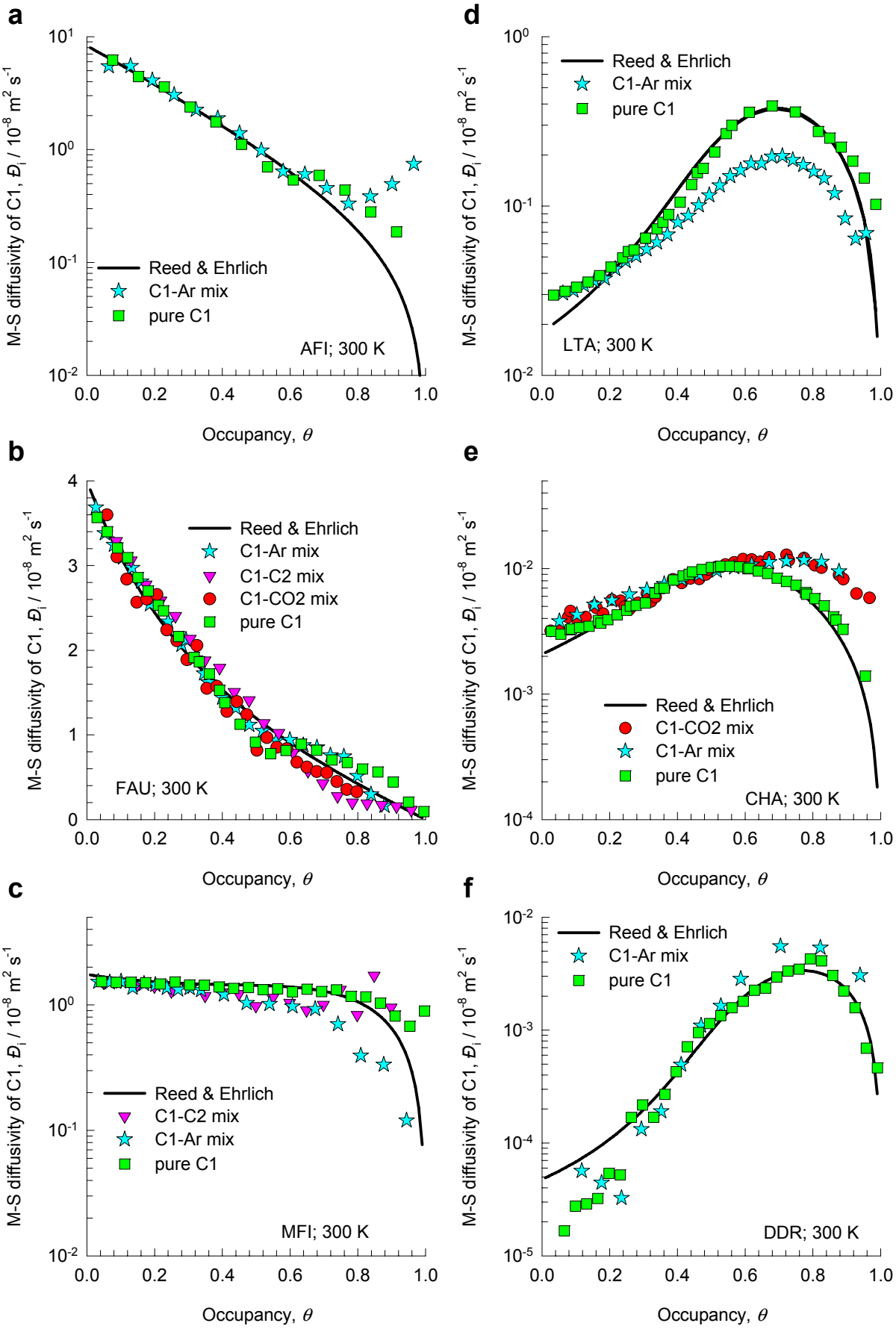

M-S diffusivity of CO2

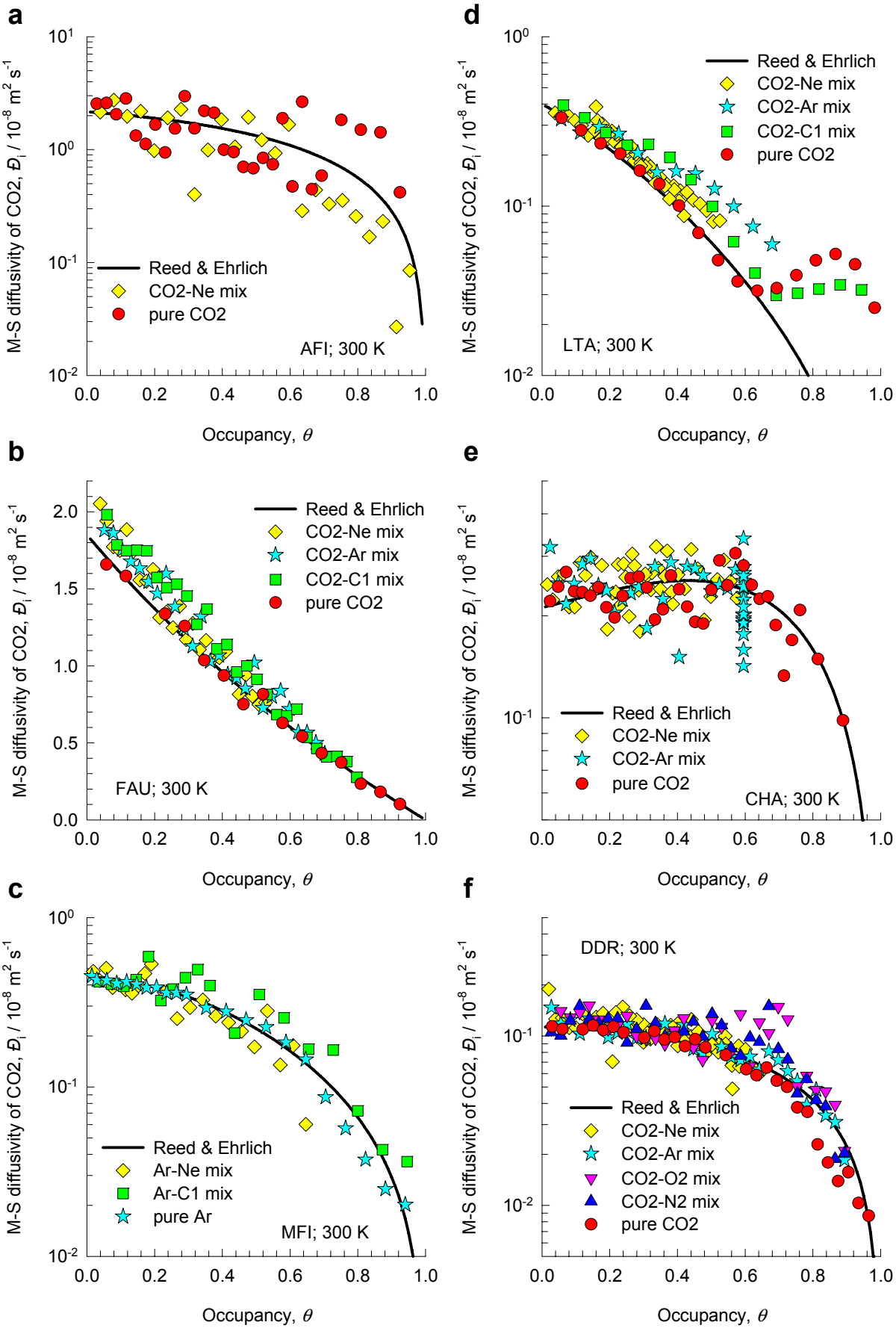

M-S diffusivity of N2

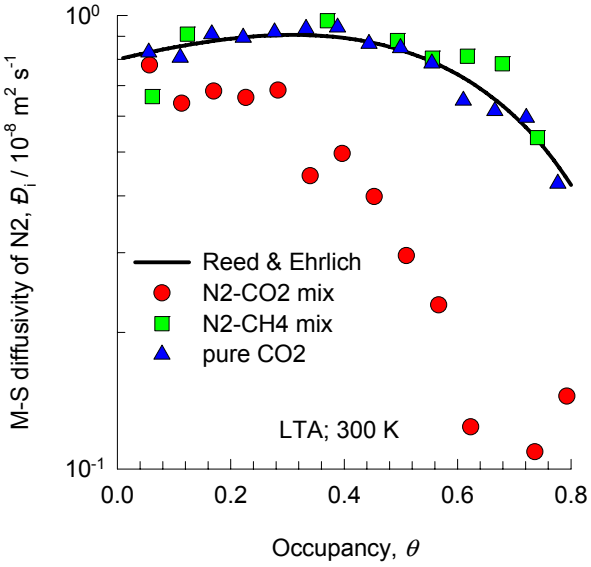

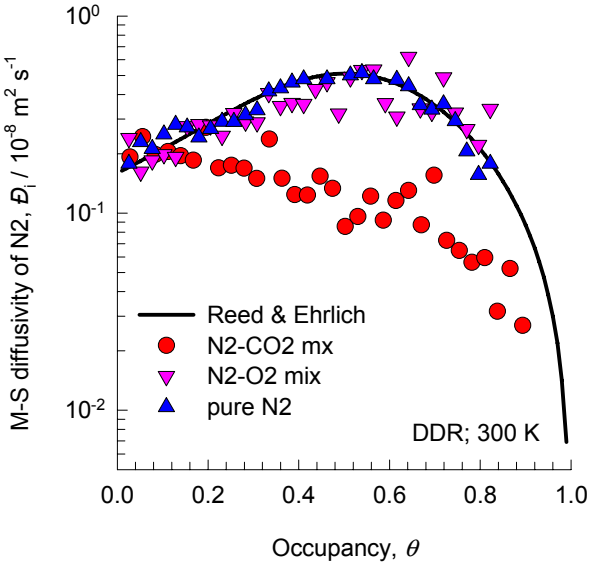

M-S diffusivity of O2

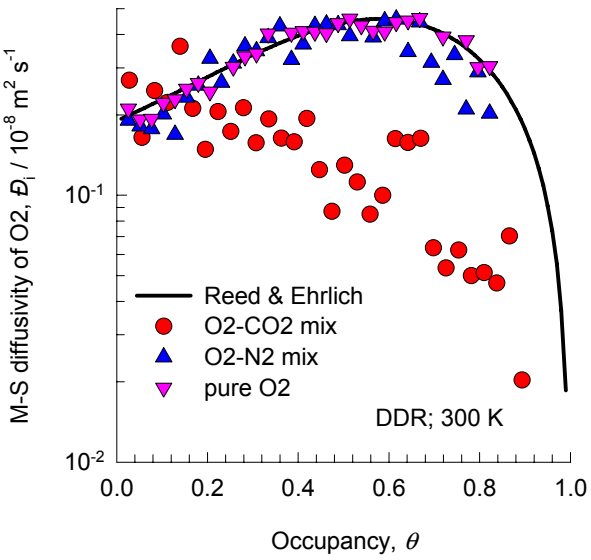

Appendix A5. Simulations of diffusion in CNTs

MD simulations to study diffusion of both pure components (methane (C1), ethane (C2), propane (C3), n-butane (nC4), iso-butane (iC4), hydrogen (H2), argon (Ar), and neon (Ne)) and binary mixtures (C1-C2, C1-C3, C1-nC4, C1-iC4, C1-H2, Ar-Ne) for a variety of loadings in CNTs of both zig-zag ((20,0)) and armchair (10,10) configurations; see Figures 1 and 2. Figure 3 shows some typical snapshots of molecules in the armchair CNT.

Additionally, CBMC simulations were carried out to determine the sorption isotherms for pure components; this information is required for determination of saturation capacities and interpretation of the diffusion data.

1. CBMC and MD Simulation methodologies

Simulations have been carried out for diffusion, and adsorption, of pure components (n = 1) and binary (n = 2) mixtures containing C1, C2, C3, nC4, iC4, H2, Ar, and Ne in both zig-zag and armchair CNT configurations; the various campaigns are specified in Table 1. We use the united atom model. The force field for the alkanes are the same as those reported by Dubbeldam et al.[1]. We consider the CH_x groups as single, chargeless interaction centers with their own effective potentials. The beads in the chain are connected by harmonic bonding potentials. A harmonic cosine bending potential models the bond bending between three neighboring beads, a Ryckaert-Bellemans potential controls the torsion angle. The beads in a chain separated by more than three bonds interact with each other through a Lennard-Jones potential. The force field for the CNT wall, Ar, Ne and H_2 are given in Table 2. The force field for the C wall is the same as that developed for graphite[2-5]. The force field for H_2 is taken from the literature[6]. The force field for Ar and Ne correspond to those used by Ackerman et al.[4], The force fields for alkanes have been given in detail in an earlier publication[1]. The solid-fluid potentials were derived from the Lorentz-Berthelot combining rules $\sigma_{ij} = (\sigma_i + \sigma_j)/2$; $\varepsilon_{ij} = \sqrt{\varepsilon_i \varepsilon_j}$.

The Lennard-Jones potentials are shifted and cut at 1.2 nm. We assume that the nanotubes are completely rigid, with all carbon atoms fixed in their ideal lattice positions. The recent study of Chen et al.[7] has confirmed that the accounting for the flexibility for the CNT tube wall has only a small influence on the diffusivities when the pressure is above about 1 bar.

Pure component adsorption isotherms were determined using Configurational-Bias Monte Carlo (CBMC) simulations following the procedure described in earlier publications[1, 8, 9] and a simulation box consisting of a single CNT, with the length of 36 unit cells; the unit cell dimensions for the various CNTs simulated are specified in Table 3.

CBMC simulation results for pure component isotherms in various CNT configurations are summarized in Figures 4, 5, 6, 7, 8, and 9. From these isotherms we determine the saturation capacities $q_{i,sat}$ as listed in Table 4 for each species *i* in a particular CNT configuration.

The MD simulation methodology and code was the same as that for zeolites, described in Appendix A1. The MD simulations were carried out for a variety of molecular loadings within the CNT. For 1D transport of molecules within CNTs of different configurations, it is convenient to express the loadings in terms of molecules per tube length, q_i. For zig-zag CNTs a minimum tube length of 36 unit cells, and for the armchair configuration a minimum tube length of 72 unit cells were used. To get accurate statistics for diffusivity determinations at low loadings, a minimum number of 40 molecules were used, resulting in simulation boxes with tube lengths of a few hundred unit cells for low loadings. All simulations were carried out on clusters of PCs equipped with Intel Xeon processors running at 3.4 GHz on the Linux operating system.

The elements Δ_{ij} were determined using

$$\Delta_{ij} = \frac{1}{2n_j} \lim_{\Delta t \to \infty} \frac{1}{\Delta t} \left\langle \left(\sum_{l=1}^{n_i} \left(\mathbf{r}_{l,i}(t+\Delta t) - \mathbf{r}_{l,i}(t) \right) \right) \bullet \left(\sum_{k=1}^{n_j} \left(\mathbf{r}_{k,j}(t+\Delta t) - \mathbf{r}_{k,j}(t) \right) \right) \right\rangle \qquad (1)$$

In this expression, n_i and n_j represent the number of molecules of species *i* and *j* respectively, and $\mathbf{r}_{l,i}(t)$ is the position of molecule *l* of species *i* at any time *t*. In this context we note a typographical error in eq (1) as *printed* in our earlier publication [10] wherein the denominator in the right member had n_i

instead of n_j. The simulation results presented in this publication are, however, correct as the proper formula given in eq (1) was used. From the definition $q_i = \frac{n_i A_{CNT}}{V}$, where V is the volume of the simulation box and A_{CNT} is the cross-sectional area of CNT tube, we can determine the molecular loadings in the units of molecules per length of tube. The Onsager Reciprocal Relations $L_{ij} = L_{ji}$ yields

$$\Delta_{ij} q_j = \Delta_{ji} q_i \tag{2}$$

For single component diffusion, n=1, Δ_{11} can be identified with the M-S, or "corrected" diffusivity $Đ_1$.

Animations based on the MD simulations showing the motion of molecules can be viewed by downloading the movies from our website [11].

Figures 4, 5, 6, 7, 8, and 9 contain MD simulated data for pure component diffusivities $Đ_i$ and the elements Δ_{ij} for the various campaigns specified in Table 1.

For describing the loading dependence of the M-S diffusivity we use the model due to Reed and Ehrlich[12, 13] that has been applied in the case of zeolite diffusion.[13-15], and described in Appendix A2. The fitted parameters ϕ_1 for various molecule-CNT combinations are listed in Table 4.

The Reed and Ehrlich model fits are shown by continuous solid lines in Figures 4, 5, 6, 7, 8, and 9.

2. Notation

A_{CNT}	cross-sectional area of CNT, m^2
q_i	molecular loading, molecules per unit length of CNT
$q_{i,sat}$	saturation loading, molecules per unit length of CNT

Other symbols as listed in Appendix A1.

3. Literature cited

[1] D. Dubbeldam, S. Calero, T.J.H. Vlugt, R. Krishna, T.L.M. Maesen, B. Smit, United Atom Forcefield for Alkanes in Nanoporous Materials, J. Phys. Chem. B 108 (2004) 12301-12313.

[2] W.A. Steele, The Interaction of Gases With Solid Surfaces, Pergamon Press, Oxford, 1974.

[3] A.I. Skoulidas, D.M. Ackerman, J.K. Johnson, D.S. Sholl, Rapid transport of gases in carbon nanotubes, Phys. Rev. Lett. 89 (2002) 185901.

[4] D.M. Ackerman, A.I. Skoulidas, D.S. Sholl, J.K. Johnson, Diffusivities of Ar and Ne in carbon nanotubes, Mol. Simulation 29 (2003) 677-684.

[5] T. Düren, F.J. Keil, N.A. Seaton, Composition dependent transport diffusion coefficients of CH_4/CF_4 mixtures in carbon nanotubes by non-equilibrium molecular dynamics simulations, Chem. Eng. Sci. 57 (2002) 1343-1354.

[6] V. Buch, Path integral simulations of mixed para-D2 and ortho-D2 clusters: The orientational effects, J. Chem. Phys. 100 (1994) 7610-7629.

[7] H. Chen, J.K. Johnson, D.S. Sholl, Transport of Gases is Rapid in Carbon Nanotubes, J. Phys. Chem. B 110 (2006) 1971-1975.

[8] D. Dubbeldam, S. Calero, T.J.H. Vlugt, R. Krishna, T.L.M. Maesen, E. Beerdsen, B. Smit, Force Field Parametrization through Fitting on Inflection Points in Isotherms, Phys. Rev. Lett. 93 (2004) 088302.

[9] S. Calero, D. Dubbeldam, R. Krishna, B. Smit, T.J.H. Vlugt, J.F.M. Denayer, J.A. Martens, T.L.M. Maesen, Understanding the role of sodium during adsorption. A force field for alkanes in sodium exchanged faujasites, J. Am. Chem. Soc. 126 (2004) 11377-11386.

[10] R. Krishna, J.M. van Baten, Describing binary mixture diffusion in carbon nanotubes with the Maxwell-Stefan equations. An investigation using molecular dynamics simulations, Ind. Eng. Chem. Res. 45 (2006) 2084-2093.

[11] J.M. van Baten, R. Krishna, MD animations of diffusion in nanoporous materials, University of Amsterdam, Amsterdam, http://www.science.uva.nl/research/cr/animateMD/, 6 January 2008.

[12] D.A. Reed, G. Ehrlich, Surface diffusion, atomic jump rates and thermodynamics, Surf. Sci. 102 (1981) 588-609.

[13] R. Krishna, D. Paschek, R. Baur, Modelling the occupancy dependence of diffusivities in zeolites, Microporous Mesoporous Mater. 76 (2004) 233-246.

[14] R. Krishna, J.M. van Baten, Diffusion of alkane mixtures in zeolites. Validating the Maxwell-Stefan formulation using MD simulations, J. Phys. Chem. B 109 (2005) 6386-6396.

[15] J.M. van Baten, R. Krishna, Entropy effects in adsorption and diffusion of alkane isomers in mordenite: An investigation using CBMC and MD simulations, Microporous Mesoporous Mater. 84 (2005) 179-191.

Table 1. MD simulation campaigns with various alkanes in various CNT topologies. Each simulation was run for 5 ns and the MSD data were fitted for the 0.5 – 5 ns time range.

CNT	*n*	Components	Campaign
Zig-zag (20,0)	1	C1, C2, C3, nC4, iC4	Pure, varying molecular loadings q_i
	2	C1/C2, C1/C3, C1/nC4, C1/iC4	50-50 mixtures, varying $(q_1 + q_2)$
	2	C1/C2	Varying x_i, keeping constant
Armchair (10,10)	1	C1, H2, Ar, Ne	pure, varying molecular loadings q_i
	2	C1/H2, and Ar/Ne	50-50 mixtures, varying $(q_1 + q_2)$
	2	C1/H2	Varying x_i, keeping $(q_1 + q_2)$ constant

Table 2. Lennard-Jones parameters. The units of σ are in nm, and those of (ε / k_B) in K.

Site	σ	(ε / k_B)
Ar	0.342	124.07
Ne	0.2789	35.7
H2	0.296	34.2
C(wall)	0.34	28

Table 3. Dimensions (in nm) of CNTs used in the simulations. The diameter represents the center-to-center distance of C atoms on the CNT wall.

CNT	Diameter	Unit Cell Length
Zig-zag (20,0)	1.5674	0.426
Armchair (10,10)	1.3579	0.246

Table 4. Pure component saturation capacities and diffusion data. The data on $q_{i,sat}$ are in molecules per nm. The zero-loading diffusivities $Đ_i(0)$ are in units of 10^{-8} m^2 s^{-1}.

Zeolite	Molecule	Saturation capacity, $q_{i,sat}$ / molecules/nm	$Đ_i(0)$ / 10^{-8} m^2 s^{-1}	z	ϕ_i
CNT(20,0)	C1	20	7500	2	$0.04\exp(3.3\theta_i)$
CNT(20,0)	C2	14	2500	2	$0.17\exp(3.0\theta_i)$
CNT(20,0)	C3	9	950	2	$0.7\exp(2.0\theta_i)$
CNT(20,0)	nC4	8	720	2	$0.9\exp(1.5\theta_i)$
CNT(20,0)	iC4	7	720	2	$0.9\exp(1.5\theta_i)$
CNT(10,10)	C1	13	7500	2	$0.35\exp(2.5\theta_i)$
CNT(10,10)	H2	40	9200	2	$0.2\exp(2.6\theta_i)$
CNT(10,10)	Ar	25	2860	2	$0.54\exp(0.7\theta_i)$
CNT(10,10)	Ne	50	1870	2	$0.34\exp(1.06\theta_i)$

4. Captions for Figures

Figure 1. Zig-zag configuration CNT(20,0)

Figure 2. Armchair configuration CNT (10,10)

Figure 3. Snapshots of molecules in CNT (10,10).

Figure 4. Isotherm and diffusion data for C1-C2 mixture in CNT (20,0)

Figure 5. Isotherm and diffusion data for C1-C3 mixture in CNT (20,0)

Figure 6. Isotherm and diffusion data for C1-nC4 mixture in CNT (20,0)

Figure 7. Isotherm and diffusion data for C1-iC4 mixture in CNT (20,0)

Figure 8. Isotherm and diffusion data for C1-H2 mixture in CNT (10,10)

Figure 9. Isotherm and diffusion data for Ar-Ne mixture in CNT (10,10)

CNT (20,0)

Figure 1

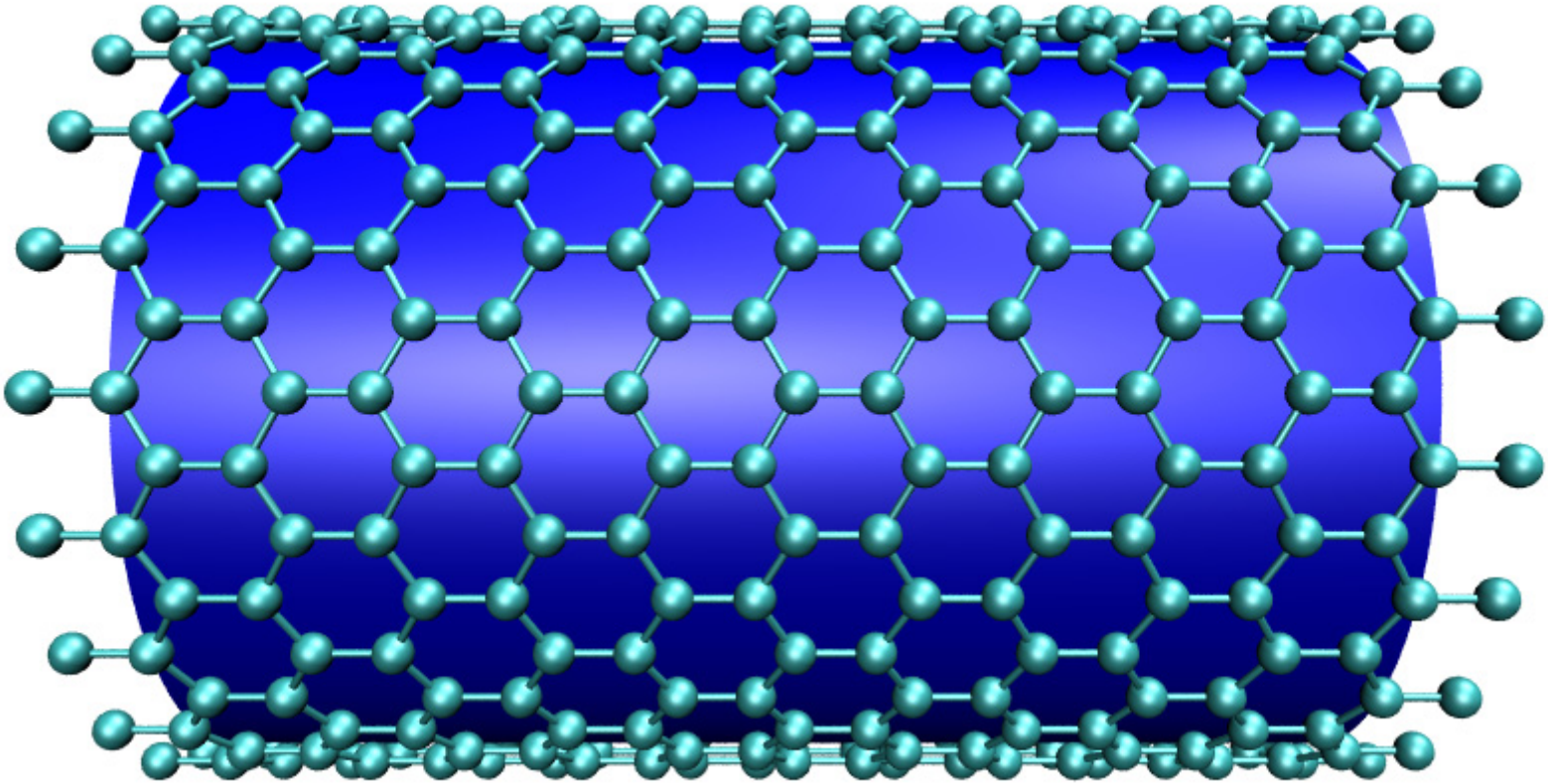

CNT (10,10)

Figure 2

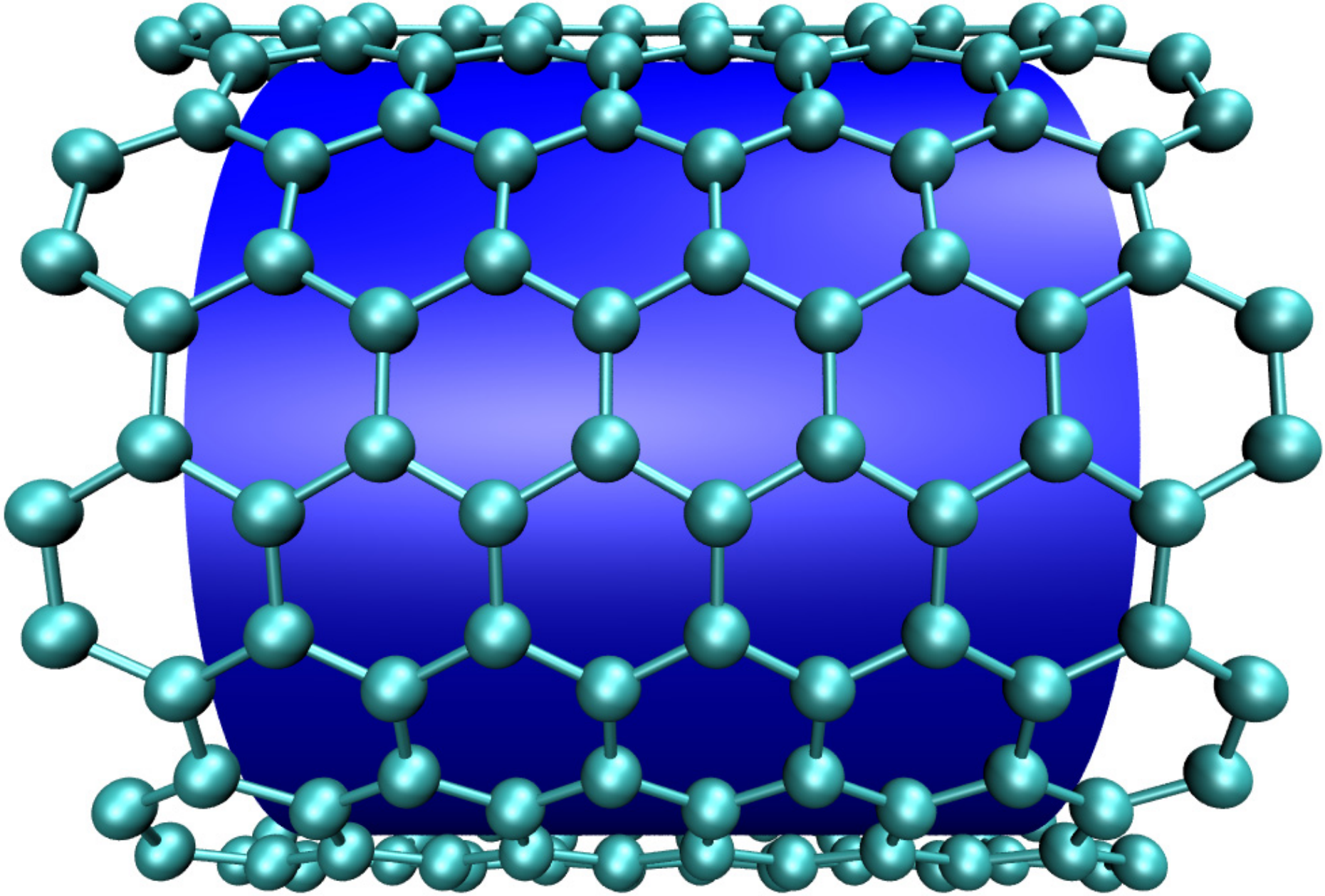

CNT (10,10)

Figure 3

Snapshot of equimolar C1-C2 mixture

Snapshot of Ar

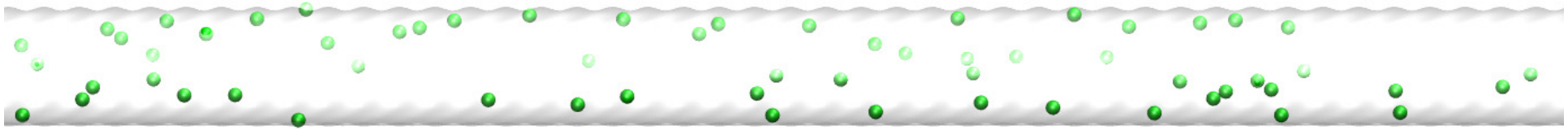

Snapshot of Ne

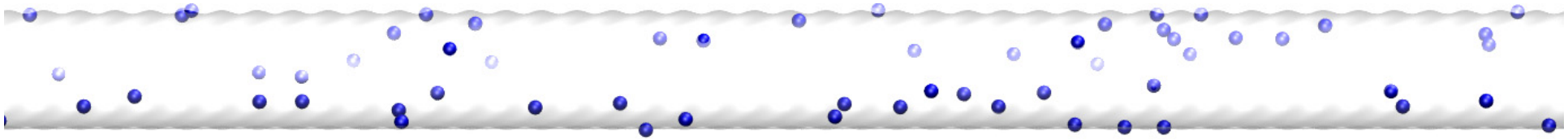

Snapshot of equimolar Ar-Ne mixture

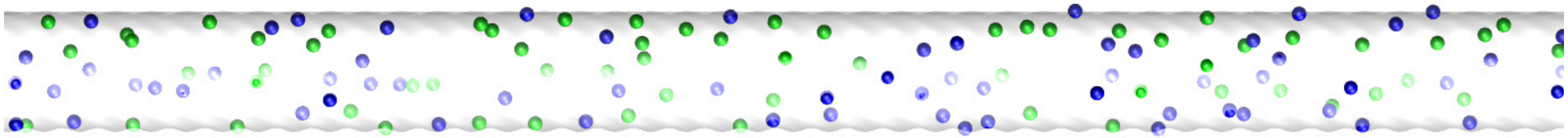

CNT (20,0); C1, C2, and C1-C2 mixture, 300 K

Figure 4

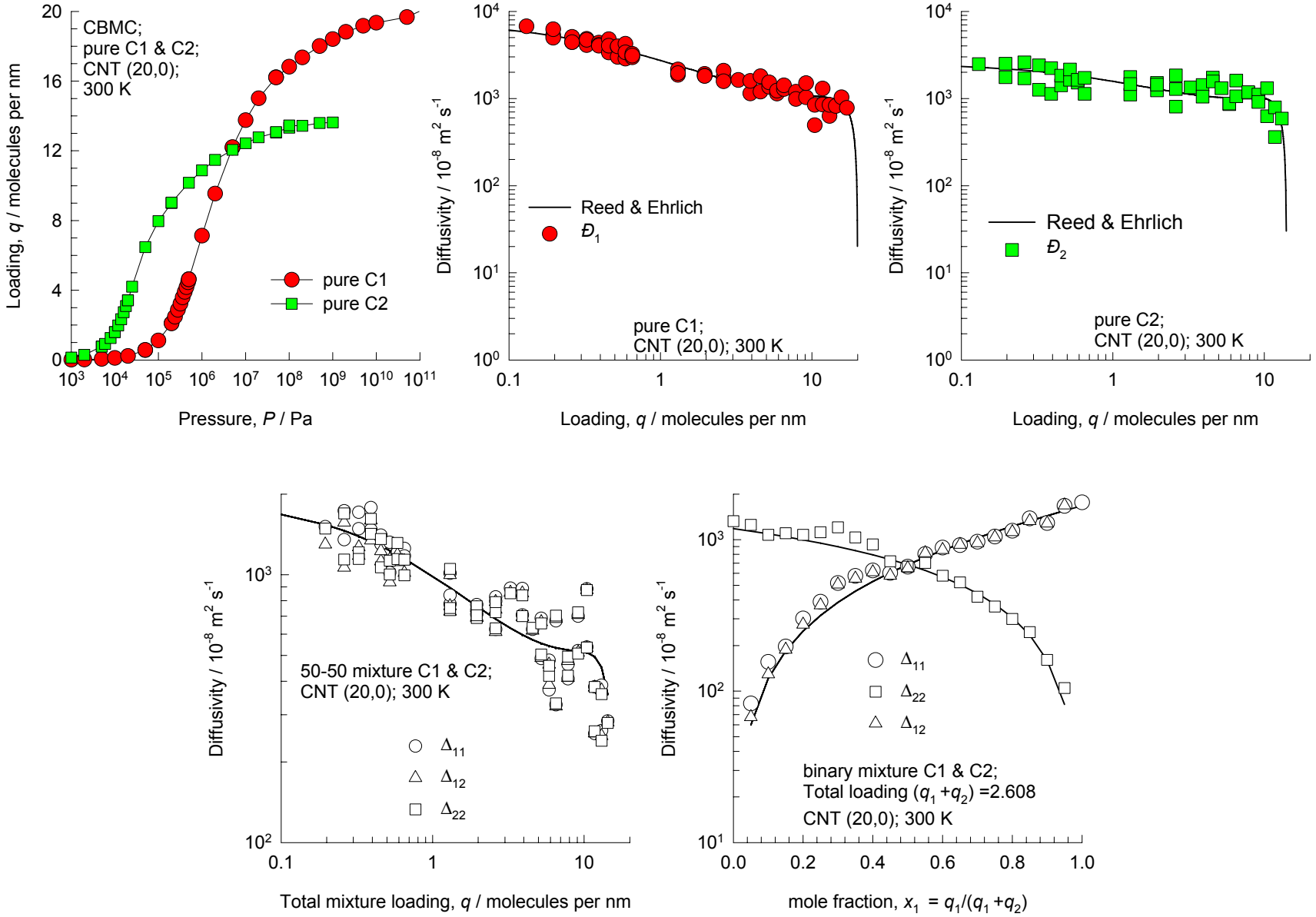

CNT (20,0); C1, C3, and C1-C3 mixture, 300 K

Figure 5

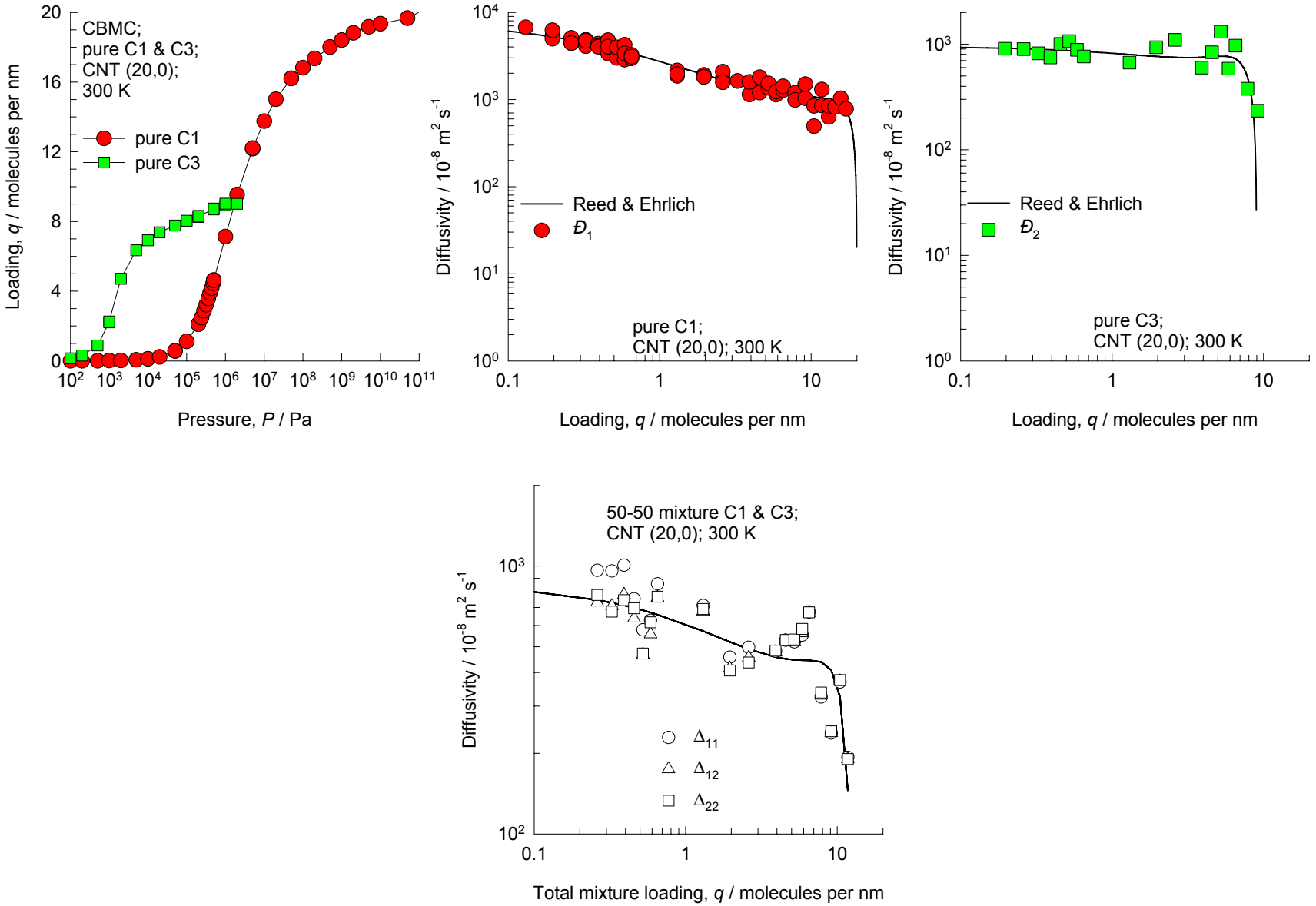

CNT (20,0); C1, nC4, and C1-nC4 mixture, 300 K

Figure 6

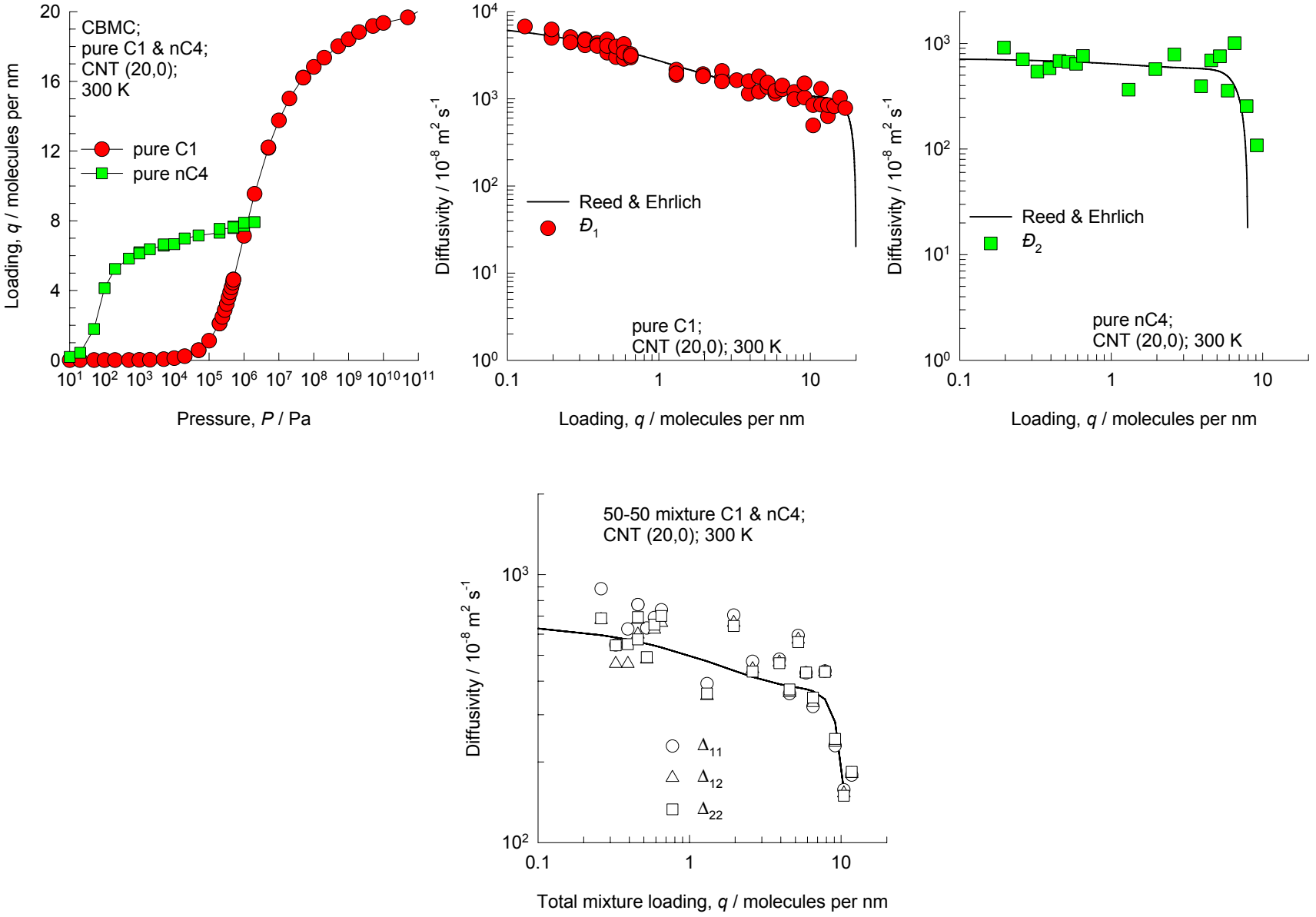

CNT (20,0); C1, iC4, and C1-iC4 mixture, 300 K

Figure 7

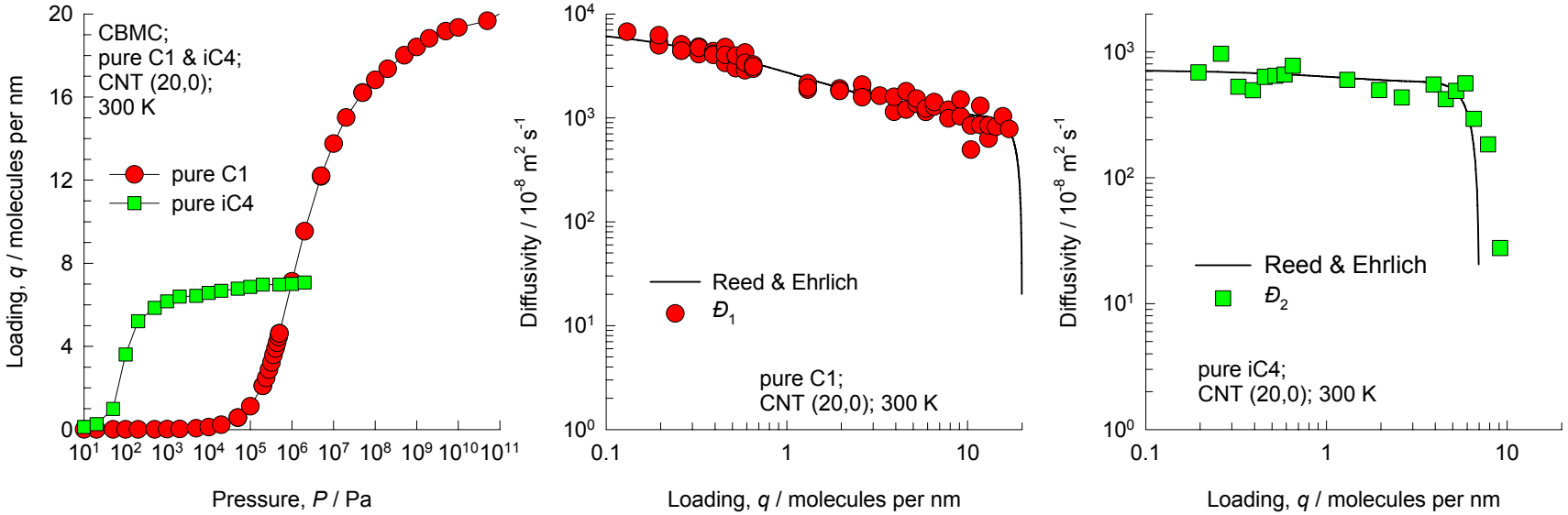

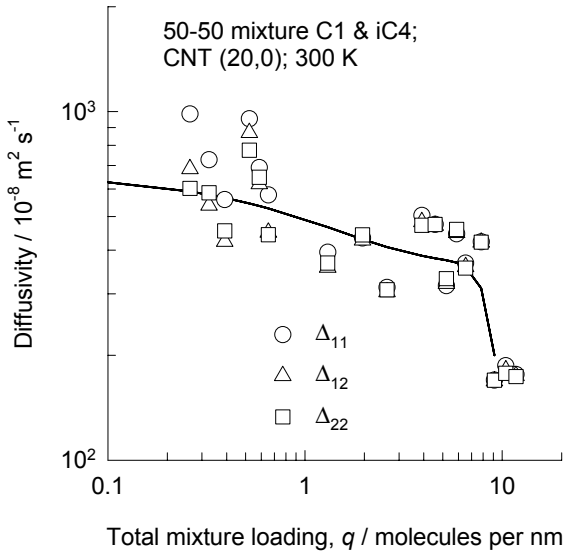

CNT (10,10); C1, H2, and C1-H2 mixture, 300 K

Figure 8

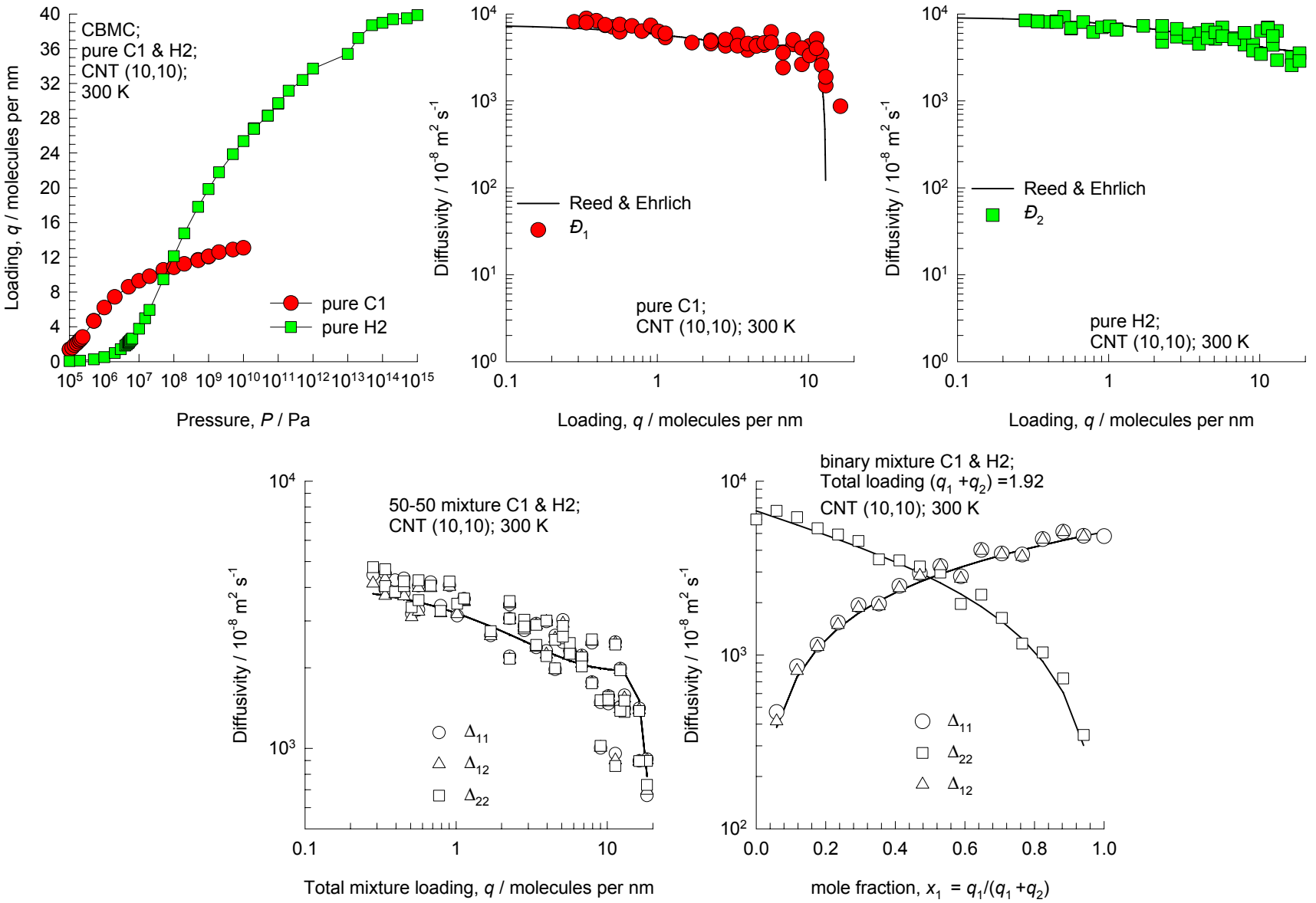

CNT (10,10); Ar, Ne, and Ar-Ne mixture, 300 K

Figure 9